

**Time resolved photoelectron spectroscopy for  
femtosecond characterization of X-ray  
free-electron laser pulses**

**Dissertation**

**zur Erlangung des Doktorgrades  
des Fachbereichs Physik  
der Universität Hamburg**

vorgelegt von

Dipl.-Phys. Ivanka Grguraš  
aus München

Hamburg  
2015

Gutachter der Dissertation

Prof. Dr. Adrian L. Cavalieri

PD Dr. Bernhard Schmidt

Gutachter der Disputation

Prof. Dr. Adrian L. Cavalieri

Prof. Dr. Wilfried Wurth

Datum der Disputation

04.11.2015

Vorsitzender des Prüfungsausschusses

Prof. Dr. Schmelcher

Vorsitzender des Promotionsausschusses

Prof. Dr. Jan Louis

Leiter des Fachbereichs Physik

Prof. Dr. Peter Hauschildt

Dekan der Fakultät für Mathematik,  
Informatik und Naturwissenschaften

Prof. Dr. Heinrich Graener

## Abstract

Over the last 20 years, enormous effort has been invested in the development and construction of free-electron laser (FEL) sources that emit light pulses tunable from the extreme ultraviolet (XUV) to the X-ray range. These efforts were driven by the predicted high brightness, femtosecond pulse duration and spatial coherence of the emitted radiation.

The large number of photons within an ultrashort time, along with the high spatial resolution available at X-ray FELs operating today, offers unique possibilities to decipher unexplored regimes in various disciplines of natural sciences. Yet, the precise measurement of the temporal profile, duration, spectral phase and arrival time of the X-ray pulses represents a major challenge.

In this work, the concept of streaking photoelectron spectroscopy was adapted to precisely measure the temporal properties of the FEL pulses. This concept has originally served to resolve the temporal properties of coherent XUV attosecond pulses generated as higher harmonics from ultrashort near-infrared laser pulses in rare gases. The method is based upon overlapping the XUV pulses with a synchronized long-wavelength laser field – the streaking field – in a noble gas target. The kinetic energy of photoelectrons, released from the ionization of the noble gas by the XUV pulse, is changed according to the instantaneous vector potential of the overlapping streaking field, resulting in a modified photoelectron spectrum that mimics the XUV pulses' temporal profile in momentum space. Measurement of the laser-field induced modifications to the photoelectron spectrum, with properly chosen laser field parameters, allows for the reconstruction of the temporal properties of the ionizing pulse.

This thesis reports the successful characterization of FEL X-ray pulses using single-cycle terahertz pulses as the streaking field. Using this scheme, we were able to measure the FEL pulse arrival time and temporal profile simultaneously on a single-shot basis. Precise knowledge of these pulse properties will give rise to time-resolved studies of light-matter interactions on an unprecedented ultrafast time scale with atomic resolution. In addition, it will facilitate better understanding and control of the FEL operation and thus advance new developments of even more powerful light sources for extended research opportunities.



## Zusammenfassung

Im Laufe der letzten 20 Jahre wurden große Anstrengungen in der Entwicklung und dem Aufbau von Freien-Elektronen-Laser (FEL) Quellen unternommen, die Lichtpulse in einem breiten Spektralbereich vom extremen Ultraviolett (XUV) bis zum Röntgenbereich emittieren. Diese Anstrengungen wurden durch die vorausgesagte hohe Brillanz, die Femtosekunden-Pulsdauer und räumliche Kohärenz der ausgesendeten Strahlung motiviert.

Die große Anzahl an Photonen innerhalb kürzester Zeit in Kombination mit der hohen räumlichen Auflösung der Röntgen-FELs, bieten einzigartige Möglichkeiten um unerforschte Gebiete in verschiedenen Disziplinen der Naturwissenschaften zu erkunden. Eine große Herausforderung stellt jedoch bis heute die präzise Messung des zeitlichen Profils, der spektralen Phase und der Ankunftszeit der Röntgenpulse dar.

In dieser Arbeit wurde das Verfahren der „Photoelektronen-Streaking-Spektroskopie“ weiterentwickelt, um die zeitlichen Eigenschaften der FEL-Pulse zu bestimmen. Diese Methode wurde ursprünglich für die zeitliche Charakterisierung von kohärenten XUV Attosekunden-Pulsen, welche als höhere Harmonische von ultrakurzen nah-infraroten Laserpulsen generiert werden, entwickelt. Dieses Konzept basiert auf der Überlagerung der ultrakurzen XUV Pulse mit einem synchronisierten langwelligen Laserfeld – dem Streaking-Feld – in einem Edelgas. Die kinetische Energie der Photoelektronen, die durch die Ionisation des Edelgases mittels der XUV-Pulse freigesetzt werden, wird entsprechend dem momentanen Vektorpotential des zeitlich überlappenden Streaking-Pulses geändert; mit der Folge, dass ebenfalls das Photoelektronenspektrum moduliert wird. Dementsprechend repräsentiert das Photoelektronenspektrum die zeitliche Struktur des zu charakterisierenden XUV-Pulses im Impulsraum. Daher, lassen Messung dieser Laser-induzierten Modulationen mit geeigneten Laserfeld-Parametern auf die zeitlichen Eigenschaften des ionisierenden Pulses rückschließen.

In dieser Arbeit wird die erfolgreiche Charakterisierung von FEL Röntgenpulsen mittels Terahertz-Pulsen, bestehend aus einem einzigen optischen Zyklus, als Streaking-Feld vorgestellt. Mit diesem Verfahren konnten wir die Ankunftszeit und die Pulsstruktur simultan und im Einzelschussmodus messen. Genaue Kenntnisse dieser Pulseigenschaften ebnet den Weg zur Erforschung der Wechselwirkungen zwischen Licht und Materie mit einer beispiellosen zeitlichen und räumlichen Auflösung. Außerdem wird dieses Wissen ein besseres Verständnis und eine bessere Kontrolle des FEL-Betriebs ermöglichen und damit Neuentwicklungen leistungsstärkerer Lichtquellen für erweiterte Forschungsmöglichkeiten vorantreiben.



## Contents

<b>1</b>	<b>Introduction</b>	<b>1</b>
<b>2</b>	<b>X-ray Free Electron Lasers</b>	<b>7</b>
2.1	Accelerator-based light sources	7
2.2	Undulator radiation	9
2.3	Principle of free-electron lasers	12
2.4	Radiation characteristics of SASE X-ray FELs	15
<b>3</b>	<b>Time resolved photoelectron spectroscopy as a temporal diagnostic tool</b>	<b>19</b>
3.1	Experimental challenges	19
3.2	High speed measurement technique: Photoelectron streaking spectroscopy	21
3.2.1	Semi-classical model	23
3.2.2	Streaking of Fourier limited pulses	27
3.2.3	Retrieval of spectral phase	29
3.3	Streaking spectroscopy at FELs	32
3.3.1	Laser-driven THz streaking spectroscopy	32
3.3.2	Transformation from energy to time	35
3.3.3	Influence of initial chirp in FEL pulses	36
3.3.4	Ponderomotive potential of the THz field	37
3.4	Resolution Limits	38
3.4.1	Resolution of the electron energy detector	38
3.4.2	Streaking strength and initial bandwidth	40
3.4.3	Gouy phase shift	42
<b>4</b>	<b>High field terahertz pulses</b>	<b>45</b>
4.1	Optical rectification – nonlinear optical phenomena	45
4.2	Materials for THz generation through optical rectification	48
4.2.1	Noncollinear velocity matching titled pulse front method in LN	49
4.2.2	Organic crystals for THz generation	56
4.3	Terahertz pulse detection – Electro-optic sampling	57
<b>5</b>	<b>Proof of principle of laser-based THz streaking at the FEL facility FLASH</b>	<b>63</b>
5.1	FLASH – soft X-ray facility	63
5.2	First experimental implementation & results	66
5.2.1	Experimental set-up	66
5.2.2	Energy to time conversion	69
5.2.3	Resolution of the measurements	72
5.2.4	Complete single-shot FEL temporal pulse characterization	73

5.2.5	First measurements with magnetic bottle spectrometer .....	78
5.3	Comparison & discussion on experimental parameters.....	80
5.3.1	Practical aspects of THz generation .....	80
5.3.2	THz field strength.....	83
5.3.3	Influence of the Gouy phase shift.....	83
5.4	Summary .....	86
<b>6</b>	<b>Characterization of the all-optical synchronization scheme at FLASH with time resolved photoelectron spectroscopy .....</b>	<b>87</b>
6.1	Timing at FELs .....	87
6.2	Conventional RF Synchronization.....	88
6.3	Optical synchronization at FLASH .....	89
6.3.1	Fiber link stabilization & optical cross-correlator.....	90
6.3.2	Temporal electron bunch stabilization .....	95
6.3.3	Optical locking of independent lasers at FELs .....	101
6.4	Characterization of the complete synchronization system .....	105
6.4.1	Experimental set-up & measurement.....	105
6.4.2	Jitter analysis.....	109
6.4.3	Optical versus RF synchronization .....	112
6.5	Summary .....	113
<b>7</b>	<b>X-ray pulse shaping at LCLS.....</b>	<b>117</b>
7.1	The Free-Electron Laser LCLS .....	117
7.1.1	Principle of longitudinal compression .....	118
7.1.2	Temporal shaping at X-ray FELS.....	120
7.2	Experimental implementation and results .....	121
7.2.1	Large dynamic range: THz streaking fields from LiNbO <sub>3</sub> .....	122
7.2.2	High Temporal Resolution: THz streaking fields from DSTMS .....	125
7.2.3	Complete X-ray pulse Characterization .....	134
7.3	Summary .....	135
<b>8</b>	<b>Conclusion &amp; Outlook.....</b>	<b>137</b>
	<b>Appendix A .....</b>	<b>143</b>
	<b>Appendix B .....</b>	<b>147</b>
	<b>Appendix C.....</b>	<b>151</b>
	<b>Appendix D.....</b>	<b>155</b>
	<b>Bibliography .....</b>	<b>157</b>

## List of figures

<b>Figure 1.1:</b> Photon beam brightness provided by accelerator-based light sources.....	3
<b>Figure 2.1:</b> Radiation pattern of a circulating relativistic charged particle.....	9
<b>Figure 2.2:</b> Schematic of a planar undulator with the oscillating electron beam.....	10
<b>Figure 2.3:</b> Electron-light wave interaction inside an undulator.....	13
<b>Figure 2.4:</b> Microbunching.....	15
<b>Figure 3.1:</b> Schematic of the attosecond streaking measurement geometry.....	22
<b>Figure 3.2:</b> Streaking of a Fourier limited XUV pulse.....	28
<b>Figure 3.3:</b> Streaking spectrogram .....	29
<b>Figure 3.4:</b> Streaking of a linearly chirped pulse.....	31
<b>Figure 3.5:</b> Schematic of single-shot, single cycle THz streaking measurement .....	34
<b>Figure 3.6:</b> Transformation from time to energy.....	36
<b>Figure 3.7:</b> TOF at synchrotrons at FELs.....	40
<b>Figure 3.8:</b> Auger decay.....	42
<b>Figure 4.1:</b> Schematic of THz pulse generation by optical rectification.....	47
<b>Figure 4.2:</b> Velocity matching with the tilted pulse front methode.....	52
<b>Figure 4.3:</b> THz generation in LN by tilted pulse front pumping.....	52
<b>Figure 4.4:</b> Pulse front tilt introduced by a grating.....	54
<b>Figure 4.5:</b> Change of the tilt angle .....	55
<b>Figure 4.6:</b> EO sampling .....	59
<b>Figure 5.1:</b> Schematic of the FLASH machine layout.....	64
<b>Figure 5.2:</b> Layout of the THz streaking experimental set-up used at FLASH.....	66
<b>Figure 5.3:</b> Electro optic sampling of the THz pulse used for the streaking experiments.....	67
<b>Figure 5.4:</b> Absolute THz electric field strength.....	70
<b>Figure 5.5:</b> Kinetic energy shift of the photoelectron peak.....	71
<b>Figure 5.6:</b> Field-free spectrum of He.....	72
<b>Figure 5.7:</b> Streaking spectrogram measured with a time-of-flight spectrometer.....	74
<b>Figure 5.8:</b> Two distinct single-shot streaked photoelectron spectra.....	75
<b>Figure 5.9:</b> Measurement accuracy.....	76
<b>Figure 5.10:</b> Arrival time jitter of the FEL pulse measured at FLASH.....	77
<b>Figure 5.11:</b> Spectrogram measured with a magnetic bottle.....	79
<b>Figure 5.12:</b> Comparison of the temporal waveform of the generated .....	82
<b>Figure 5.13:</b> Gouy pahse shift .....	85
<b>Figure 6.1:</b> Schematic overview of the laser-based synchronization.....	90
<b>Figure 6.2:</b> Schematic of the fiber link stabilization.....	92
<b>Figure 6.3:</b> Illustration of the optical cross-correlator (OXC) principle.....	94

<b>Figure 6.4:</b> Characterization of the fiber link. t.....	95
<b>Figure 6.5:</b> Electron bunch time structure at FLASH..	96
<b>Figure 6.6:</b> Schematic of the FLASH FEL with the longitudinal beam based feedback and the optical synchronization.....	97
<b>Figure 6.7:</b> Principle of the bunch arrival time measurement .....	98
<b>Figure 6.8:</b> Bunch arrival-time feedback for accelerator stabilization.....	100
<b>Figure 6.9:</b> Schematic of the two-color OXC.....	102
<b>Figure 6.10:</b> Characterization of the optical locking between the Ti:sapphire pump-probe laser and the optical reference laser at FLASH .....	103
<b>Figure 6.11:</b> Comparison between the electronic and optical synchronization between two laser sources.....	104
<b>Figure 6.12:</b> Experimental set-up for the relative timing measurement between FEL and external laser.....	106
<b>Figure 6.13:</b> Ne 2p photoelectron peak as a function of FEL and THz pulse delay .....	107
<b>Figure 6.14:</b> An averaged Ne 2p photoelectron streaking spectrogram.....	108
<b>Figure 6.15:</b> Total residual timing jitter characterized by THz streaking.....	108
<b>Figure 6.16:</b> Comparison of BAM and streaking data. ....	111
<b>Figure 6.17:</b> Comparison of THz streaking data with and without the optical synchronization system.....	113
<b>Figure 7.1:</b> Schematic layout of the LCLS FEL machine layout.....	118
<b>Figure 7.2:</b> Longitudinal electron bunch compression and temporal shaping.....	119
<b>Figure 7.3:</b> Averaged streaking curve measured at LCLS with LN .....	123
<b>Figure 7.4:</b> Double pulse separation measured with LN.....	124
<b>Figure 7.5:</b> Single-cycle THz pulse from DSTMS.....	126
<b>Figure 7.6:</b> Experimental set-up at LCLS with DSTMS generated THz streaking pulses.....	126
<b>Figure 7.7:</b> DSTMS streaking at LCLS in conjunction with the timing tool. ....	127
<b>Figure 7.8:</b> Double-slot foil at -26.800 $\mu\text{m}$ .....	130
<b>Figure 7.9:</b> Double-slot foil at -23700 $\mu\text{m}$ .....	131
<b>Figure 7.10:</b> Double-slot foil at -217400 $\mu\text{m}$ .....	132
<b>Figure 7.11:</b> Measurements and calculations of the double pulse separation .....	134
<b>Figure 7.12:</b> DSTMS THz streaking at LCLS for average spectral phase reconstruction. ....	135
<b>Figure 8.1:</b> Tandem streaking for self-calibrated measurements.....	141

## List of tables

<b>Table 1.1:</b> Operational and some future X-ray FEL facilities. ....	5
<b>Table 4.1:</b> Properties of commonly used materials for THz generation. ....	49
<b>Table 4.2:</b> Some material constants for ZnTe and GaP .....	61
<b>Table 5.1:</b> FLASH photon beam properties .....	65
<b>Table 5.2:</b> Calculated Rayleigh length and Gouy phase shift over the interaction length.....	85
<b>Table 7.1:</b> LCLS electron and X-ray beam parameters .....	118



## List of abbreviations

BAM	Bunch arrival time monitor
BC	Bunch compressor
BCM	Bunch compression monitor
BBF	Beam based feedback
COM	Center-of-mass
CTR	Coherent Transition radiation
cw	Continuous wave
DCF	Dispersion compensating fiber
DESY	Deutsches Elektron-Synchrotron
DM	Dichroic mirror
EDFA	Erbium-doped fiber amplifier
EOM	Electro-optic modulator
EOS	Electro-optic sampling
FEL	Free-electron laser
FLASH	Free-electron laser in Hamburg
FWHM	Full width half maximum
GaP	Gallium phosphide
LCLS	Linac Coherent Light Source
LLRF	low-level radio frequency
LN/LiNbO <sub>3</sub>	Lithium niobate
MO	Master oscillator
MLO	Master laser oscillator
MCP	Multi-channel plate
NIR	Near-infrared
OPA	Optical parametric amplifier
OXC	Optical cross-correlator
PBS	Polarizing beamsplitter
PPKTP	periodically-poled titanyl phosphate
RF	Radio-frequency
rms	Root mean square
SASE	Self-amplified spontaneous emission
SFG	Sum-frequency generation
SLAC	Stanford Linear Accelerator Center
THz	terahertz
Ti:sa	Titanium-doped sapphire
TOF	Time-of-flight
VUV	Vacuum ultra violet
XUV	Extreme ultraviolet
ZnTe	Zinc telluride



## 1 Introduction

Our knowledge of the structure of matter is steadily increasing in response to new developments of X-ray sources and the accompanied evolution of new scientific techniques. In 1895, Röntgen discovered X-rays while experimenting with cathode rays [1]. Laue, Friedrich and Knipping discovered that X-rays produce a diffraction pattern when transmitted through a crystal [2]. These findings confirmed the wave nature of X-rays as well as the lattice structure of crystals. Based on this work, W.H. Bragg and W.L. Bragg could explain the observed diffraction pattern as interference of the incident X-rays reflected from crystal lattice planes [3]. This was the starting point of X-ray diffraction. Since then the field of X-ray crystallography has evolved from resolving the structure of simple inorganic crystals like sodium chloride (NaCl) and diamond to very complex materials like proteins, viruses and the DNA [4,5].

The first technologies providing radiation from the ultraviolet to the X-ray spectral region were limited in terms of brightness. In the late 1960s the X-ray beam brightness increased tremendously with the advent of accelerator-based light sources [6]. Here the radiation, also known as synchrotron radiation, is generated by relativistic electrons oscillating in a magnetic field. The characteristics of the emitted radiation are strongly altered for accelerated charges moving at relativistic energies. Firstly, the frequency of the emitted radiation is strongly increased, i.e. shifted towards the X-ray range. Secondly, the emission is collimated into a narrow cone along the direction of the instantaneous motion of the electron. The first experiments performed at synchrotrons utilized the parasitic radiation from existing electron storage rings built for high energy physics. Later, electron storage-ring synchrotrons with the designated aim as radiation facilities were built, which are usually referred to as second generation light sources [7]. In the third generation of accelerator-based light source, a periodic arrangement of magnets with alternating polarity, known as undulator, is inserted into a straight section of a dedicated storage ring [8]. The emitted radiation is substantially increased and consists of narrow spectral lines as compared to the radiation delivered by the first and second generation of light sources. The

peak brightness - defined as the number of photons produced within a certain spectral bandwidth per unit time per unit area of the radiation source per solid angle of the radiation cone - of modern storage-ring synchrotrons approaches values which are about ten orders of magnitude higher than the laboratory X-ray sources available in the 1960's. The capability of these intense synchrotron X-ray sources is reflected in the number of discoveries in various fields of natural sciences and emergent technological applications in the last decades. In particular, biomolecular crystallography has profited from the better resolution resulting from the intense X-ray radiation. For instance, the structure of various proteins essential for biological processes and numerous viruses could be elucidated with the third generation light sources (see e.g. Ref. [9,10]).

Another light source which plays an important role in science ever since its first demonstration in 1960 is the laser [11]. In contrast to conventional light sources, lasers emit radiation with unique properties, namely, large spatial and temporal coherence, high spectral brightness and pulse durations from picosecond ( $10^{-12}$  s) to the femtosecond ( $10^{-15}$  s) region. Optical lasers cover a wide frequency range, from the visible to the far-infrared region which provide the possibility to study atomic and molecular processes on an ultrafast time scale at high intensities. However, an X-ray pulse with laser like characteristic would open new opportunities like time resolved structure determination. Several methods to generate short pulse and laser-like radiation in the X-ray region have been investigated, for example, plasma sources, inverse Compton scattering sources and high-harmonic generation. But currently the only efficient sources for radiation in the soft X-ray to the hard X-ray spectral region are free-electron lasers (FELs), the fourth generation of light sources.

Short-wavelength FELs deliver pulses with durations between hundreds of femtoseconds down to the sub-10 fs region with a tunable wavelength range from 45 nm (27 eV) to less than 0.1 nm (12 keV) and with  $10^{11}$ - $10^{13}$  photons per pulse. A comparison of beam brightness of FELs to other x-ray sources is shown in in **Figure 1.1**. The unprecedented peak brightness, ultra-short pulse duration and the short wavelengths of the FEL pulses offer completely new possibilities for high temporal and spatial resolution studies in various disciplines of natural sciences such as structural biology, femtochemistry, warm dense matter and material science.

In an FEL the high-power X-ray radiation is generated, by an intense, relativistic electron beam passing through the periodic magnetic field of a long undulator. A process of self-organization of the electrons, called microbunching, causes a density modulation in the electron bunch on the scale of the radiated wavelength  $\lambda$  [12]. The electrons in the individual microbunches emit in phase and the total radiation energy scales quadratically

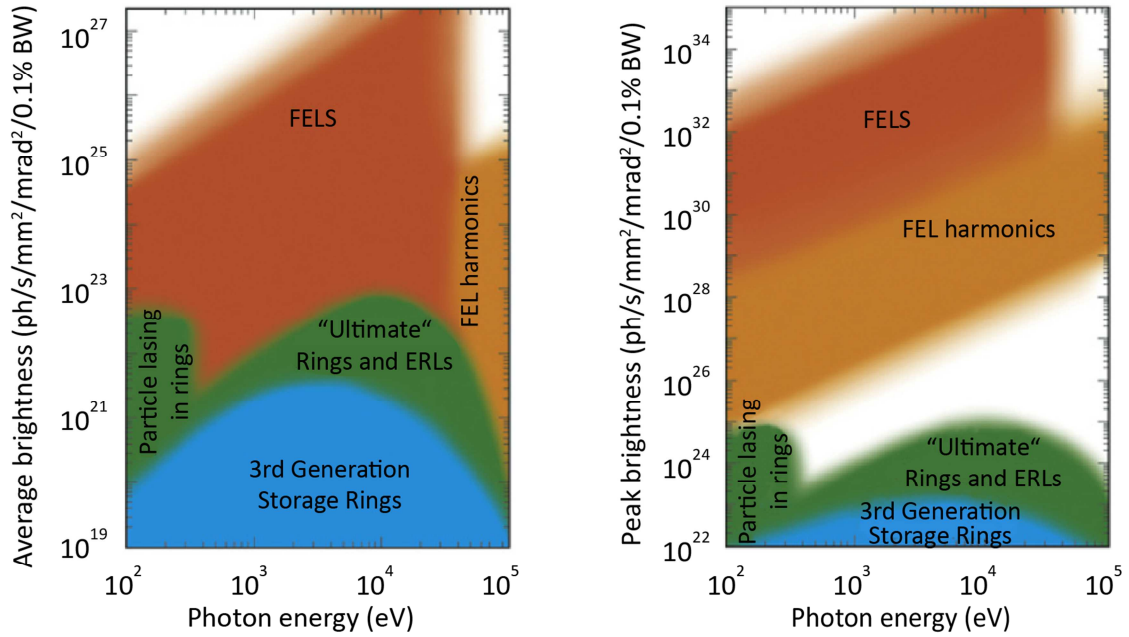


**Figure 1.1:** Photon beam brightness provided by accelerator-based light sources. Average and peak brightness of the third and fourth generation light sources are depicted. The brightness of X-ray FEL pulses is several orders of magnitude higher than any other light source (figure adapted from Ref. [13]).

with the number of electrons. This leads to an exponential amplification of the radiation. In contrast to that, in a synchrotron the  $N$  electrons comprising the bunch contribute independently to the radiated field and the emitted energy is  $N$  times the radiation energy of a single electron. Unlike for synchrotrons, the requirements on the driving electron beam of short wavelength FELs, where the amplification has to take place in a single pass of the electron beam through the undulator, are very demanding. For successful FEL operation they can only be met by a linear accelerator and not by a storage ring. While the principle of FELs was described by Madey already in 1971 [14], only recent advances in accelerator technologies enabled the successful demonstration of the first soft X-ray FEL in 2007 [15] and the first hard X-ray FEL in 2010 [16]. At present, the FELs running in the soft X-ray region are the Free-Electron Laser in Hamburg (FLASH) and Fermi@Elettra in Trieste [17]. The Linac Coherent Light Source (LCLS) in Stanford and the Spring-8 Angstrom Compact Free-Electron Laser (SACLA) in Hyogo are delivering pulses in the hard X-ray spectral region. **Table 1.1** summarizes several X-ray beam properties of the operational and some future FELs.

Currently, operational X-ray FELs are mainly based on the process of self-amplified spontaneous emission (SASE). The amplification process in the SASE FEL starts from shot noise in the electron beam and the emitted pulse consists of individual and independent,

temporally coherent intensity spikes with positions and peak heights changing from pulse to pulse. The duration of the emission spikes is characterized by the SASE coherence time and can range from several hundreds of attoseconds to several femtoseconds depending on the coherence length of the SASE process. Apart from SASE, variations of the electron beam parameters play an important role in the X-ray pulse characteristics. Generally the entire SASE pulse duration is estimated to be on the same order as the driving electron bunch, however fluctuations of the electron bunch parameters induce variations of the lasing fraction within the electron bunch from shot to shot. This can result in differences between the electron bunch profile and the emitted photon pulses. In imaging experiments of single biomolecules, which is one of the most outstanding X-ray FEL applications, meaningful diffraction data is only collected before the onset of radiation damage, which is expected to occur within the first few femtoseconds. Here, the X-ray pulse should terminate before significant structural changes can evolve, which are initiated by photo-ionization and the accompanied Auger decay of the atoms in the target [18,19]. For correct data evaluation precise knowledge of the FEL pulse duration and temporal profile on a single shot basis is required.

In time-resolved experiments, one pulse is used to initiate an event and a subsequent pulse is used to probe the system. To study the time evolution of the excited state, this measurement is repeated as the time delay between the pump and the probe pulses is varied continuously. X-ray FEL sources hold the promise for time-resolved studies of structural dynamics on an ultrafast time scale with atomic resolution. However, at SASE FELs the intrinsic timing jitter between the independent optical pump pulse and the X-ray probe pulse leads to shot-to-shot fluctuations in their relative arrival times and this sets the limit on the temporal resolution rather than the probe pulse duration. In order to account for the timing jitter, arrival time measurements of the probe pulse with respect to the pump pulse have to be performed on a single-shot basis.

In recent years, several methods have been proposed to control the FEL pulse shape and duration in order to extend the experimental capabilities of the FEL photon pulses. In the low charge mode at LCLS, it is possible to generate electron bunches with pulse durations below 10 fs [20]. Other methods, where attosecond photon pulse durations are expected, rely on the manipulation of the electron bunch with optical lasers (e.g. Refs.[21,22]). In addition, selectively spoiling the transverse emittance of the electron beam can result in X-ray pulse durations of few femtoseconds and hundreds of attoseconds [23]. In seeded FELs like FERMI, the amplification start-up mechanism is initiated by an external laser with temporal coherence and thus fully coherent FEL pulses with stable and controllable pulse parameters can be expected. To ensure reliable performance and further

optimization of these different methods, proper feedback on the generated photon pulse properties is fundamental.

Therefore, complete temporal characterization on a single shot basis is crucial to take full advantage of the novel FEL sources. It will help scientists to obtain deeper insights into light-matter interactions at ultrafast timescales and at very high X-ray intensities. Furthermore, precise knowledge of the temporal structure of the FEL pulses would aid in a better understanding of the operational principle of a FEL which would in turn facilitate future developments. To measure the temporal profile, duration and time-of-arrival of the FEL X-ray pulses, we have adapted a technique developed for attosecond metrology [24]. In this technique, called streaking, an X-ray pulse photo-ionizes a noble gas and the energy of the released photoelectrons is modified by an external laser field depending on their precise time of ejection. At FELs, we use single-cycle THz pulses generated by an independent optical laser to cope with the expected pulse durations as well as with the time-of-arrival jitter of the X-rays.

**Table 1.1:** Operational and some future X-ray FEL facilities. The Peak Brightness is defined as (photons/s/mm<sup>2</sup>/mrad<sup>2</sup>/0.1%-bandwidth), according to Ref. [25] The X-ray pulse durations are based on simulations.

FEL facility	$\lambda_{\min}$ (nm)	Peak brightness	X-ray pulse duration (fs)	Maximum Pulses/s	Expected operation
LCLS	0.12	$< 10^{33}$	$< 10$ -500	120	Operational
FLASH	4.45	$< 10^{30}$	10-100	$8 \times 10^3$	Operational
FERMI@Elettra	4	$< 10^{32}$	25-200	50	Operational
SACLA	0.1	$< 10^{34}$	$< 100$	60	Operational
XFEL	0.05	$< 10^{34}$	$< 100$	$27 \times 10^3$	2017
SwissFEL	0.1	$< 10^{33}$	2-13	100	2017
FLASH-II	4	$< 10^{33}$	10-200	$8 \times 10^3$	2015

In this thesis, the experimental realization of the temporal characterization of femtosecond X-ray FEL pulses using the streaking technique with single-cycle THz pulses is reported. *Chapter 2* is an introduction to the principals of FELs. In *chapter 3*, photoelectron streaking spectroscopy and the implementation of this method for X-ray pulse characterization measurements at FELs are presented. Optical laser-driven single-cycle terahertz radiation is a key element of our pulse characterization technique. Therefore, *chapter 4* deals with generation and detection schemes of THz radiation. *Chapter 5* reports on the first implementation of our measurement technique at FLASH. This is followed by a

discussion of the characterization of the all-optical synchronization scheme at FLASH in *chapter 6*. In *chapter 7* measurements performed at LCLS, with manipulated electron beams with the aim to shape the X-ray pulses are summarized. And finally, in *chapter 8* a conclusion of our findings and an outlook are given.

## 2 X-ray Free Electron Lasers

The fact that accelerated charges emit radiation was already well known from the beginning of particle accelerators used for high-energy physics. However, it was not expected that at relativistic velocities the properties of the radiation would be drastically altered. Visible radiation emitted by electrons in the bending magnet of a synchrotron was first observed in 1947 [26]. This experimental observation was followed a few years later by first calculations of the characteristics of this synchrotron radiation [27]. Since then these accelerator-based light sources evolved into powerful radiation sources in the X-ray spectral region for research throughout various fields of natural science.

In the following the fundamentals of accelerator based radiation sources are summarized with particular emphasis on the operation principals and radiation characteristics of high-gain FELs. A complete treatment of the theory of free-electron lasers and the full derivation of the results and equations presented in the following can be found in the review article of Ref. [28], in the textbooks of Ref. [12] and Ref. [29].

### 2.1 Accelerator-based light sources

The first known sources of synchrotron radiation were the bending magnets in existing storage rings. In these facilities relativistic electrons are moving on a quasi-circular orbit, with acceleration toward the center of the ring in the bending magnets where they emit synchrotron radiation tangentially to their orbit [30,31]. The total power emitted by a single electron with bending radius  $R$  in a magnetic field  $B$  can be calculated as [27]:

$$P_{syn} = \frac{e^4 \gamma^2 B^2}{6\pi\epsilon_0 c m_e^2} = \frac{e^2 c \gamma^4}{6\pi\epsilon_0 R^2}. \quad (2.1)$$

Here  $\epsilon_0$  is the vacuum permittivity,  $c$  the speed of light,  $e$  is the elementary charge,  $m_e$  is the electron rest mass and  $\gamma$  is the Lorentz factor:

$$\gamma = \frac{1}{\sqrt{1-\beta^2}} = \frac{W}{m_e c^2} \quad (2.2)$$

$$\beta \equiv \frac{v}{c}$$

where  $W$  is the total relativistic energy of the electron. The spatial distribution of the radiated power is illustrated in **Figure 2.1**. In the moving frame of reference of the electron the emitted light has the well-known  $\sin(2\theta)$  angular pattern of dipole radiation, i.e. the radiation intensity is distributed over a broad angular range with a peak orthogonal to the direction of acceleration and zero emission in the direction of acceleration. In the laboratory frame of reference the observed radiation pattern changes drastically at relativistic energies. As shown in **Figure 2.1b** most of the emitted power is relativistically contracted into a narrow cone in forward direction tangentially to the electron orbit. The transformation of the angles measured from the direction of motion between the two frames of reference is given by [32]

$$\tan \theta = \frac{\sin \theta'}{\gamma(\beta + \cos \theta')}, \quad (2.3)$$

where the primed angle is measured in the moving frame of reference. At highly relativistic velocities  $\beta$  approaches 1 and  $\gamma \gg 1$ . Hence, even for a broad angular distribution in the moving frame of reference of the electron ( $0 < \theta' < \pi/4$ ) the radiation in the laboratory frame will be confined into a narrow cone of half angle

$$\theta \approx \frac{1}{2\gamma} \quad (2.4)$$

in the direction of the instantaneous motion of the electron, seen as short radiation pulse by the observer. The emitted radiation is broadband and extends from zero to frequencies beyond the critical frequency  $\omega_c$  [27]

$$\omega_c = \frac{3c\gamma^3}{2R}. \quad (2.5)$$

Due to the relativistic length contraction and the relativistic Doppler effect the observed frequency spectrum can be even in the hard x-ray region.

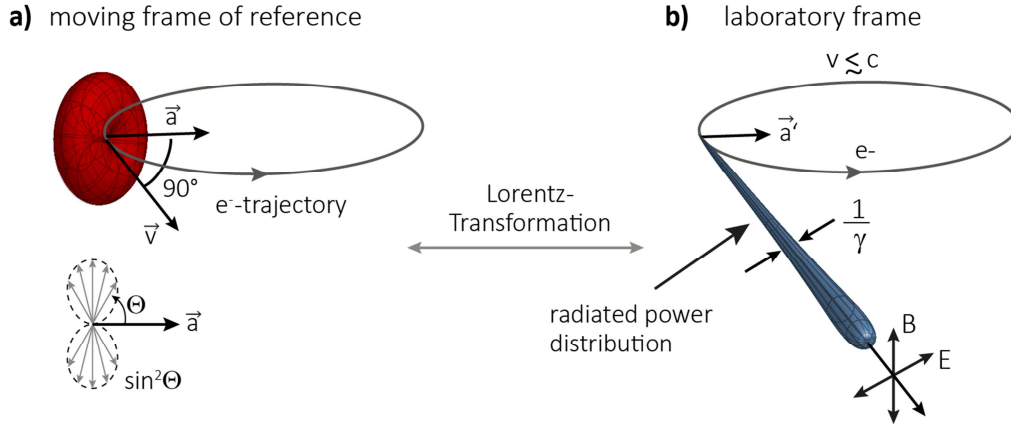


**Figure 2.1:** Radiation pattern of a circulating relativistic charged particle. The uniform magnetic field of a bending magnet forces the electron on a curved beam path. Due to this transverse acceleration the electron emits electromagnetic radiation. **a)** Radiation pattern of an accelerated electron and its three dimensional form in the reference frame moving with the electron. At large distance the radiation field has a broad angular distribution. The radiation power is zero along the acceleration, resulting in a donut like radiation pattern. **b)** Radiation pattern of a highly relativistic electron as it is seen by an observer in the laboratory frame of reference. The radiation is concentrated along a narrow cone tangent to the orbit of the electron.

## 2.2 Undulator radiation

In third generation accelerator-based light sources an undulator or wiggler, which is a device consisting of a periodic arrangement of dipole magnets of alternating polarity is inserted in to the beam path of the electron bunch [8]. Here, an electron bunch moving along the center of the insertion device (see **Figure 2.2**) in  $z$ -direction is deflected on a sinusoidal horizontal trajectory due to the Lorentz force. The corresponding electron acceleration causes the emission of electromagnetic waves in forward direction. A planar undulator produces a static magnetic field in the vertical direction ( $y$ -direction), whose strength varies along the  $z$ -direction [28] as:

$$B_y = -B_0 \sin\left(\frac{2\pi}{\lambda_u} z\right) \quad (2.6)$$

$\lambda_u$  is the undulator period and  $B_0$  is the peak magnetic field on the undulator axis. In the weak magnetic field of an undulator the electrons oscillate with a small deviation angle along the straight undulator axis ( $z$ -direction). This angle is smaller than the angular width of the natural radiation cone  $1/\gamma$ , as a result the individual radiation cones overlap and interfere. The generated radiation will be emitted into narrow spectral lines concentrated in a narrow spectral cone of  $1/(N\sqrt{\gamma})$  along the undulator axis, where  $N$  is the number of

magnetic periods. In comparison to bending-magnet radiation, the photon beam brightness<sup>1</sup> is increased by several orders of magnitude and the emission is quasi-monochromatic, due to concentration of radiation in narrow angular cone along the straight undulator axis in narrow spectral lines. The magnetic field of a wiggler is so strong, that the angular excursions of the electron are significantly greater than the natural emission cone. Hence, light emitted from different periods sums up independently, resulting in a broad radiation spectrum and cone. Due to the stronger acceleration the radiated power and the photon energies are higher.

The radiated frequency spectrum is determined by the relativistic electron energy and the undulator properties. The fundamental wavelength can be estimated with the following arguments. In the moving frame of reference of the electron the relativistic length contraction reduces the undulator period to  $\lambda_u^* = \lambda_u/\gamma$  and the electrons oscillation frequency increases to  $\omega^* = 2\pi c/\lambda_u^*$ . The frequency of the emitted radiation in the reference frame moving with the electron changes correspondingly to  $f^* = c\gamma/\lambda_u$ . For an observer in the fixed laboratory frame the wavelength is further blue shifted due to the Doppler effect.

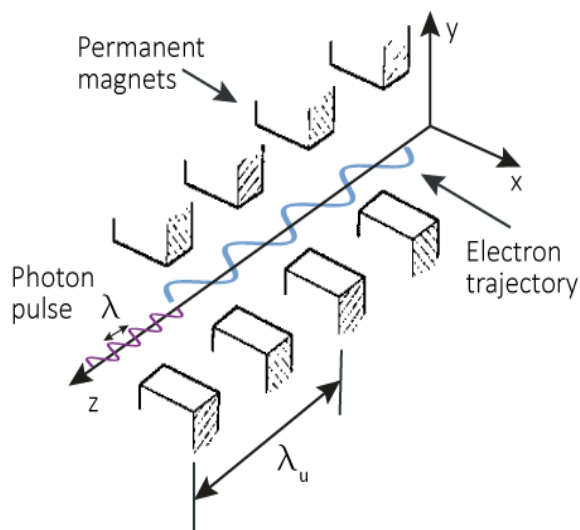


**Figure 2.2:** Schematic of a planar undulator with the oscillating electron beam. The magnetic field is generated by an arrangement of alternating north and south poles of permanent magnets. The resulting magnetic field points in the y-direction and varies sinusoidally in the z-direction. The undulator period  $\lambda_u$  is the distance between two equal poles. The electrons are deflected in the x-z plane. The emitted radiation is linearly polarized with the electric field vector in the same plane as the electron orbit (figure adapted from Ref.[32]).

<sup>1</sup> Number of photons produced per unit time per unit area of the radiation source per unit solid angle of the radiation cone per unit spectral bandwidth

The Doppler shift depends on the relative velocity and thus it depends on the observation angle  $\theta$  with respect to the direction of motion. The frequency of the radiation in the laboratory frame can be calculated with the appropriate Lorentz transformation and is given by [32]:

$$f = \frac{c}{\lambda_u (1 - \beta)}. \quad (2.7)$$

Here, an observer looking on axis of motion towards the moving electron bunch, where the shortest wavelengths are observed, is assumed. Recalling that:

$$\gamma^2 = \frac{1}{1 - \beta^2} = \frac{1}{(1 - \beta)(1 + \beta)} \quad (2.8)$$

and with  $\beta \rightarrow 1$ , as it is the case for highly relativistic electrons, this expression can be written as

$$1 - \beta \approx \frac{1}{2\gamma^2}. \quad (2.9)$$

Thus the radiation wavelength on the axis of motion in the laboratory frame transforms to:

$$\lambda_l \approx \frac{\lambda_u}{2\gamma^2}. \quad (2.10)$$

For highly relativistic electron energies the factor  $2\gamma^2$  can become so high that the emitted wavelength is several orders of magnitude smaller than the undulator period and the x-ray wavelength region can be reached.

A more precise calculation, taking into account that the sinusoidal trajectory of the electrons reduces their longitudinal velocity leads to somewhat longer wavelengths described by [33]

$$\lambda_l = \frac{\lambda_u}{2\gamma^2} \left( 1 + \frac{K^2}{2} + \gamma^2 \theta^2 \right) \quad \text{with} \quad (2.11)$$

$$K = \frac{eB_0 \lambda_u}{2\pi m_e c} = 0.934 \cdot B_0 [\text{T}] \cdot \lambda_u [\text{cm}]$$

$K$  is the dimensionless undulator parameter and is usually on the order of 1 for undulators ( $K \gg 1$  applies for wigglers),  $\theta$  is the observation angle measured from the direction of motion in the laboratory frame. Eq. 2.11 shows that the emitted wavelength can be tuned by changing the electron energy  $\gamma$  or the undulator parameter  $K$ .

The emission of the individual electrons is not correlated and the emitted radiation is incoherent with a total generated power directly proportional to the number of electrons ( $P_{X\text{-Ray}} \propto N_e$ ). This is different for FELs, where the main components are also an accelerator generating high-energy electrons and an undulator. But in FELs the radiated

power scales quadratically with the number of electrons ( $P_{X\text{-Ray}} \propto N_e^2$ ). This coherent emission of radiation is enabled through a density modulation in the electron bunch, the so called microbunching, which is on the scale of the emission wavelength  $\lambda$  [12]. This effect leads to an increase of the photon beam brightness by several orders of magnitude as compared to the third generation light sources as shown in **Figure 1.1** of the first chapter.

## 2.3 Principle of free-electron lasers

The following section provides a brief description of the light amplification process in the high-gain regime of a free-electron laser. Since the full mathematical treatment is rather complicated, only the basic equations which are necessary to understand the FEL mechanism will be given. The full derivations of the equations can be found for example in Ref. [28] and Ref. [33].

As an electromagnetic wave and a relativistic electron bunch co-propagate through the undulator, they can interact with each other and exchange energy. Energy transfer from the electrons to the electromagnetic wave can only occur, if the electrons have a velocity component parallel to the transverse electric field of the electromagnetic wave. This is accomplished in the undulator, where the moving electrons oscillate in the horizontal direction. The Lorentz force acting on an electron with the relativistic energy  $W = \gamma m_e c^2$  passing through a planar undulator is

$$\gamma m_e \dot{\mathbf{v}} = -e\mathbf{v} \times \mathbf{B}. \quad (2.12)$$

With a magnetic field as described in Eq.(2.6) the transverse component of the Lorentz force can be written as

$$\gamma m_e \frac{dv_x}{dt} = -ev_z B_y = -ev_z B_0 \sin(k_u z). \quad (2.13)$$

Here  $z$  is the position along the undulator axis and  $k_u = 2\pi/\lambda_u$ . Considering that  $\gamma$  is constant due to the absence of an electric field, integration of Eq. (14) gives the electron's transverse velocity

$$v_x(z) = \frac{Kc}{\gamma} \cos(k_u z). \quad (2.14)$$

Here  $K$  is the undulator parameter as defined in Eq.(2.11) As result of the sinusoidal trajectory the longitudinal velocity component varies along the undulator axis, and the average longitudinal velocity over one undulator period can be calculated to

$$\bar{v}_z = c \left( 1 - \frac{1}{2\gamma^2} \left( 1 + \frac{K^2}{2} \right) \right). \quad (2.15)$$

Thus, the electron bunch moving in forward direction with  $\bar{v}_z < c$  will be overtaken by the co-propagating electromagnetic wave moving along with the speed of light.

For a plane electromagnetic wave, defined by  $E_x(x,t) = E_0 \cos(k_l z - \omega_l t + \psi_0)$ , where  $k_l = \omega_l/c = 2\pi/\lambda_l$  and  $E_0$  and  $\psi_0$  initial amplitude and phase of the electric field the energy transfer between the electrons and the electromagnetic field is given by:

$$\frac{dW}{dt} = \mathbf{v} \cdot \mathbf{F} = -ev_x E_x. \quad (2.16)$$

Energy transfer from the electrons to the light wave ( $dW/dt < 0$ ) will take place when the x-component of the electron velocity and the electric field vector of the light wave point in the same direction. To achieve steady energy transfer over an extended interaction length it is necessary that electromagnetic wave slips forward by exactly one optical wavelength per undulator period. If this is fulfilled the electric field vector and the transverse electron velocity component will be periodically properly aligned, as illustrated in **Figure 2.3**. This can only be satisfied for certain resonance wavelengths, which can be derived using Eq. 2.20 and the equation of motion the electron in the undulator and it reads [28]:

$$\lambda_r = \frac{\lambda_u}{2\gamma_r^2} \left( 1 + \frac{K^2}{2} \right). \quad (2.17)$$

Comparison with Eq.2.11 shows that the wavelength, which meets the resonance condition is the same as generated in the undulator in forward direction. Thus, the spontaneously emitted radiation at the beginning of the undulator can serve as the input field to start the FEL process; this is usually referred to as self-amplified spontaneous emission (SASE).

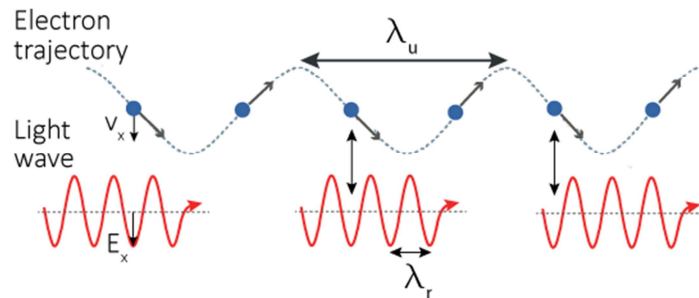


**Figure 2.3:** Electron-light wave interaction inside an undulator. Steady energy transfer is achieved when the relative phase between the electron transverse velocity and the transverse electric field of the light wave remain constant. This can be achieved if the difference of the propagation distance in one undulator period, known as the slippage length, between the light wave and the electron bunch is exactly the radiation wavelength  $\lambda$  (figure adapted from Ref. [34]).

As can be seen in **Figure 2.3**, depending on the initial phase to the electromagnetic wave some of the electrons in the bunch will lose energy others will gain energy, resulting in zero net energy transfer since the number of electrons which gain energy is the same as the number of electrons which supply energy to the radiation field with the wavelength  $\lambda_r$ . If this interaction is sustained over enough undulator periods the electron beam is modulated in energy at the wavelength  $\lambda_r$  of the co-propagating electromagnetic wave. As the beam propagates further in the undulator the energy modulation results in a spatial modulation of the electron beam density at the wavelength  $\lambda_r$  [35]. This effect is called microbunching and is illustrated in **Figure 2.4**. The electrons in the individual microbunches emit radiation in phase, which leads to a radiation enhancement in comparison to the incoherent emission. While the electron bunch passes through the undulator more and more electrons are radiating in phase and the emitted radiation adds up coherently, as a result the total emitted radiation power will be proportional to the square on the number of electrons  $P_{X-Ray} \propto N_e^2$ . The power of the emitted radiation in this high-gain regime grows exponentially with the travelled distance  $z$  in the undulator:

$$P_{X-Ray}(z) \propto \exp\left(\frac{z}{L_G}\right), \quad (2.18)$$

where  $L_G$  is the monoenergetic power gain length of FEL, which is defined as:

$$L_G = \frac{\lambda_u}{4\pi\sqrt{3}\rho}. \quad (2.19)$$

$\rho$  is the dimensionless Pierce parameter is on the order of  $10^{-3}$ - $10^{-4}$  for X-ray FELs. The exponential growth continues till the electron beam has been depleted so much that the resonance condition is no longer satisfied and the X-ray power and the electron density modulation achieve maximal saturation, as depicted in **Figure 2.4**.

The described FEL process, where the amplification takes part in a single pass of a bright electron beam through the undulator, is referred to as the high-gain regime. As it does not require an optical cavity for efficient amplification, it can be applied in the XUV and X-ray regime, where high-reflective optics are not available. Moreover, coherent sources in this wavelength range are difficult to realize and in the hard X-ray regime not available at all. Thus FELs in this wavelength range operate as SASE FELs, where the spontaneous radiation from the first part of the undulator is amplified [36,35].

Also Low-Gain FELs exist, where the undulator is placed inside a cavity, and the FEL radiation is amplified in several passes through the undulator [14], as successfully demonstrated in the visible and at longer wavelengths [37].

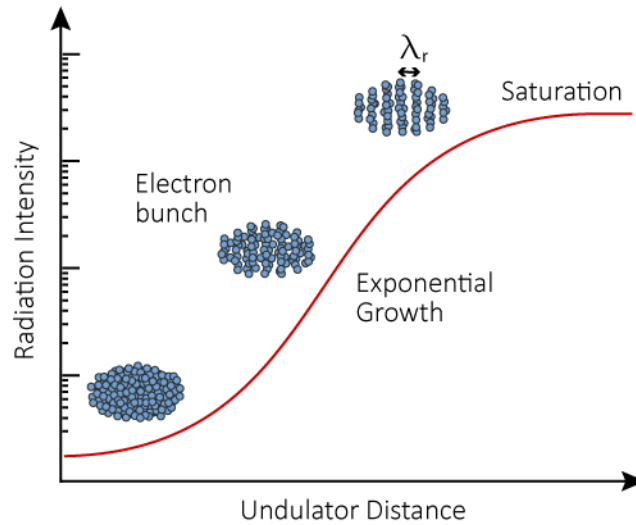


**Figure 2.4** : Growth of the radiation power and evolution of the microbunching within the electron bunch as a function of the undulator distance for a high-gain FEL. As the electron bunch, sketched as blue dots, moves through the undulator it emits radiation at the resonant wavelength  $\lambda_r$ . The interaction of the electron bunch with this electromagnetic wave leads to a periodic modulation of the electron energy and thus to a periodic modulation of the longitudinal electron density at the wavelength  $\lambda_r$ . This process of microbunching is illustrated at three different positions in the undulator. Electrons in the same microbunch emit coherently to each other, which results in an exponential growth of the radiation power along the undulator distance as illustrated above. Towards the end of the undulator, where the beam density modulation is about unity, the resonance condition is no more fulfilled and the FEL process reaches saturation (Figure adapted from [38]).

## 2.4 Radiation characteristics of SASE X-ray FELs

High-gain short-wavelength FELs generate intense radiation in a narrow band around the resonance wavelength. The emitted radiation is tunable over a broad spectral range with pulse durations from several hundred to a few femtoseconds with  $\sim 10^{11}$ - $10^{13}$  photons per pulse.

In a high-gain FEL a high degree of transverse coherence is reached for a sufficiently long undulator. This is due to optical guiding effects. Close to saturation the guided fundamental mode will usually dominate and the generated radiation will have almost full spatial coherence [28,39]. This property is important for a many experiments, especially for diffraction imaging experiment of single biomolecules, which is one of the most promising applications at FELs.

In a SASE FEL the amplification process originates from fluctuations in the electron beam current. Shot noise in the electron beam causes these fluctuations, which are random in time and space. This stochastic nature of the SASE start-up process significantly

influences the radiation characteristics, which are that of chaotic light and can be described by means of statistical optics [15]. The SASE FEL pulse is composed of individual intensity spikes each with the duration corresponding to the coherence time [41]

$$\tau_c = \frac{\sqrt{\pi}}{\sigma_\omega(z)} \approx \frac{1}{\rho\omega_r}, \quad (2.20)$$

with  $\sigma_\omega$  the root mean square (r.m.s) FEL spectral bandwidth. At the end of the exponential gain regime the bandwidth reduces to  $\sigma_\omega \approx \rho\omega_r$ , where  $\rho$  is the FEL parameter and  $\omega_r$  is the resonance frequency. The coherence time  $\tau_c$  is a measure for the temporal extent over which the electrons emit coherently, i.e. the emitted radiation fields with a defined phase relation and the fields can be added. In the hard X-ray range the coherence time is calculated to be only a few hundred attoseconds. At the XUV-FEL FLASH the coherence time is approximately 5 fs. The entire X-ray pulse duration is usually on the same order as the driving electron bunch. The average number of intensity spikes, or longitudinal modes, for a flattop pulse with the duration  $T_b$  can be estimated to

$$M \approx \frac{T_b}{\tau_c}. \quad (2.21)$$

The positions and the peak height of the spikes are random as they depend on the initial shot noise. Consequently the temporal structure of the pulse is changing from shot to shot. In the frequency-domain the single shot spectra of individual SASE pulses also show spiky substructure. The frequency spectrum with the bandwidth  $\sigma_\omega$  is composed of  $\sim M$  spikes with a width of  $\Delta\omega_s \sim 1/T_p$  for the individual spikes. The frequency spectrum is fluctuating from shot to shot, but the averaged spectrum is described by a smooth Gaussian distribution with a FWHM of  $\Delta\lambda/\lambda \sim 0.1\%$  [42].

The entire FEL pulse duration is usually estimated with the duration of the driving electron bunch. However, the amplification process strongly depends on beam parameters such as electron beam peak current, emittance and energy spread. Small variations of these parameters over the length of the electron bunch can lead to an uneven FEL lasing along the bunch. The fluctuations due to the beam parameter jitter can be larger than the SASE fluctuations and the X-ray pulse duration can deviate strongly from the electron bunch duration. These effects become stronger in the linear regime and weaken when the FEL runs is saturation.

The arrival-time of the FEL pulses with respect to synchronized, external laser pulses is also fluctuating from shot to shot, therefore influencing pump-probe experiments and hindering the use of FELs to their full potential. The main causes of this timing jitter are

electron energy beam fluctuations, which result in changes of the mean transit time of the electron beam in the bunch compressor. This issue is discussed in more detail in *chapter 6*.

In the next chapter a pulse characterization technique, that is able to determine the pulse duration and the underlying pulse structure of femtosecond FEL X-ray pulses in combination with their relative arrival time on a single-shot basis will be discussed.



### **3 Time resolved photoelectron spectroscopy as a temporal diagnostic tool**

The purpose of this chapter is to introduce the technique used for our temporal pulse characterization measurements at FELs. The introductory section provides a brief overview of the methods available up to now and summarizes their shortcomings. In Sec. 3.2 the basic concept of photoelectron streaking spectroscopy is discussed. The implementation of this measurement technique at FELs is addressed in Sec. 3.3. In the last section the limitations of this technique will be shortly discussed.

#### **3.1 Experimental challenges**

The field of X-ray science is steadily evolving as the performance of the corresponding light sources is improving. The current state-of-the-art X-ray light sources are FELs, which provide intense ultrashort X-ray pulses, thus, are laden with potential to probe dynamical processes on femtosecond time scales. To assure a correct interpretation of the acquired experimental data and to use the radiation pulses to their full potential, precise single-shot characterization of their duration, temporal profile, arrival time and eventually spectral phase is necessary. This is particularly important at the current SASE FELs, since the temporal intensity profile of the emitted radiation pulses is changing from shot to shot, as discussed in the previous chapter. These fluctuation induced artifacts in experimental data are most pronounced in experiments investigating nonlinear light-matter interaction in the X-ray regime, where precise knowledge of the pulse peak intensity is required. Moreover, to improve the understanding of FEL physics and to gain full control over the FEL properties, which would in-turn enable the development of novel and more advanced operation concepts, precise information about the radiation characteristics is invaluable.

Thus far, the temporal characterization of the FEL X-ray pulses on a single shot basis still represents a major challenge and a considerable effort is being invested in the

development of diagnostic tools for characterizing duration, temporal profile and time-of-arrival.

**Pulse duration and profile:** As a first approach, electron bunch duration measurements provide an estimate of the photon pulse duration. However, initial experiments performed at LCLS imply much shorter photon pulse durations than the electron pulses [19,43]. The FEL amplification can vary inside the electron bunch as it strongly depends on the time-dependent electron beam parameters, such as beam current, emittance and energy spread (the so-called slice parameters), and therefore the generated photon pulse duration and shape can differ from that of the electron bunch. Only complete and exact knowledge of the parameters of the driving electron bunch would allow for a precise determination of the resulting FEL pulse characteristics [44]. Yet, with current electron beam diagnostic tools these parameters cannot be accessed. Alternatively, the temporal profile of the FEL radiation pulse can be reconstructed with high accuracy by measuring the time-dependent energy-loss and energy-spread in the electron bunch caused by the FEL amplification process [45,46]. This technique, though, requires additional dedicated FEL infrastructure and fails to measure the X-ray pulse arrival time with respect to an external optical laser.

Cross-correlation measurements using multi-photon ionization processes in gases require averaging over many pulses. On the other hand, conventional photo-detectors and classical streak cameras are too slow for the characterization of the ultra-short FEL photon pulses.

The common cross-correlation techniques to measure ultra-short pulses, as used in the optical regime, are difficult or impossible to realize due to the small cross-sections of nonlinear processes in the XUV and X-ray range. Furthermore, novel techniques based on X-ray induced ultrafast optical transmission changes in solids rely on certain assumptions about the FEL pulse energy, pulse duration, pulse shape and spectrum to extract the FEL photon pulse duration from the measurements. However, these properties fluctuate at SASE FELs on a pulse-to-pulse basis, and comprehensive theoretical models of the material response to X-ray irradiation are required. Up to now, only pulse duration information could be provided but not the temporal pulse profile [47].

**Pulse arrival time:** The arrival time information is essential for pump-probe experiments conducted at these large-scale facilities. Due to the jitter and drifts in the arrival time, the delay between the two pulses from distinct sources cannot be controlled precisely (see *chapter 6*). Therefore, without additional information, the achievable time resolution is limited by the level of timing uncertainty between the FEL pulse and the optical pulse, rather than by their pulse durations.

As the largest contribution to the timing jitter can be attributed to the insufficient synchronization between the independent optical laser pulse and the electron bunch, simple time-of-arrival measurements of the electron bunch relative to the pump-probe arrival time laser pulse can mitigate this problem [48]. However, this method cannot address the shot-to-shot variation of the lasing portion within the electron bunch and cannot account for the additional timing jitter accumulated along the optical path between the electron bunch arrival-time measurement and the experimental end-station.

In contrast to beam based approaches, one can directly measure the relative arrival time of the FEL photon pulse and the optical pulse at the experimental end-station. In recent years, many different pulse arrival time monitoring techniques relying on the transient X-ray fluence-dependent effects in solids, have been developed and successfully implemented [49,50,51]. However, a disadvantage of these techniques is that the measurements are often highly invasive and cannot be performed in conjunction with the actual experiment.

Streaking photoelectron spectroscopy (also called laser dressed photoionization) represents an alternative. This technique was developed for temporal characterization of attosecond XUV pulses [24]. We adapted this technique and developed a time diagnostic tool to measure short-wavelength FEL pulses. Using independent laser-driven single-cycle terahertz pulses, we were able to simultaneously measure the pulse profile and the relative arrival-time of FEL photon pulses [52]. This technique is applicable over a broad range of photon energies produced at FELs and can be applied to pulses ranging from several femtoseconds to hundreds of femtoseconds. The set-up requires only a small fraction of the FEL power and can be used in parallel with an actual experiment. In the next section the theoretical background of this technique is presented.

### **3.2 High speed measurement technique: Photoelectron streaking spectroscopy**

The basic concept of a conventional streak camera is to convert the temporal profile of the photon pulse to an electron wavepacket by photoemission, which is subsequently deflected transversely by a fast voltage ramp. With this, the temporal information of the light pulse is mapped onto a spatial coordinate on the electron detection screen. The achievable temporal resolution with a conventional streak camera is limited to several hundred femtoseconds and hence not applicable to sub-100 fs photon pulses.

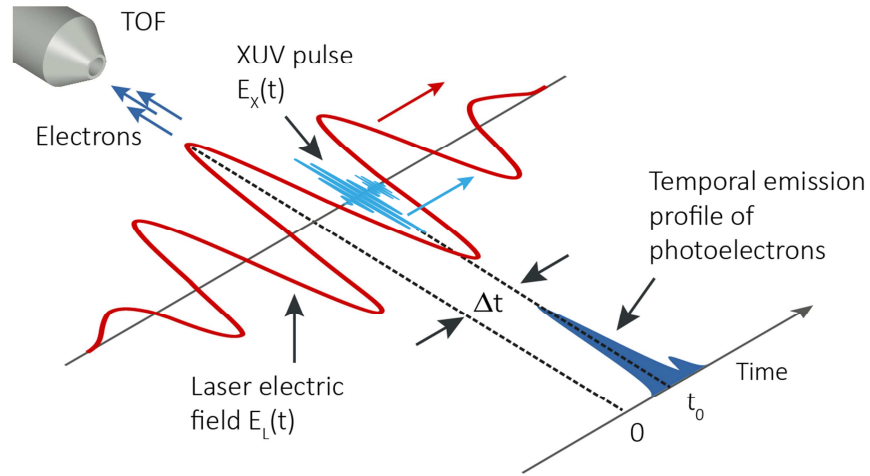


**Figure 3.1:** Schematic of the attosecond streaking measurement geometry. A short XUV pulse generates a photoelectron bunch by ionizing noble gas atoms in the presence of a strong, few-cycle phase-stable NIR laser pulse. The XUV pulse and a NIR streaking pulse are precisely synchronized to each other. The current profile of the generated photoelectrons is given by the temporal structure of the ionizing XUV pulse. After photoionization, the electrons are subject to the light electric field  $E_L(t)$  of the NIR pulse that introduces a momentum change in the final momentum distribution of the photoelectrons, depending on the instant of release  $t_0$  into the streaking laser field. The momentum change is detected with a time-of-flight (TOF) detector, which collects the electrons released along the direction of the streaking field polarization. The TOF is oriented such to be axially aligned with the linear polarization of the laser and the XUV pulse.

A similar concept is applied in the attosecond streak camera, which was proposed to measure the temporal properties of sub-fs XUV pulses with attosecond precision [53]. Here, the electromagnetic field of a strong near-infrared (NIR) laser pulse is used to project the temporal properties of the sub-fs XUV pulse onto the final momentum distribution of the photoelectron wavepacket created via ionization of a noble gas by the XUV pulse. In **Figure 3.1** a schematic of a photoelectron streaking spectroscopy experiment is shown. A linearly polarized XUV pulse is focused on to a noble gas target and temporally and spatially overlapped with an intense, linearly polarized light pulse. Photoelectrons emitted throughout the duration of the XUV pulse will be accelerated in the electric field of the intense optical laser pulse. The variation of the laser electric field during the photoemission results in different final momenta for electrons ejected at different times. The energy distribution of the ejected photoelectrons is observed in a narrow cone parallel to the laser electric field, from which the temporal profile of the ionizing pulse can be deduced. Usually the photoelectron spectrum is recorded with a time-of-flight (TOF) spectrometer, with the detector axis parallel to the linear polarization of both the pulses.

The emitted photoelectron wavepacket resembles the XUV pulse temporal properties: the number of emitted photoelectrons is mainly related to the instantaneous intensity of the XUV pulse (pulse envelope), while the initial momentum distribution of the electrons depends on the instantaneous frequency (spectral chirp) of the XUV pulse. However, the generated photoelectron bunch mimics the XUV pulse only when the following requirements are satisfied:

- The photoionization cross-section has to be constant within the entire spectral bandwidth of the ionizing XUV pulse, which, to a good extent, is satisfied in the absence of resonant processes.
- The photoelectric effect can be considered instantaneous.

In attosecond pulse metrology, a carrier-envelope-phase (CEP) stable few-cycle laser pulse at a central wavelength of 750 nm is used to generate attosecond XUV pulses through high-harmonic generation [54]. The produced XUV pulses are assumed to be fully coherent and identical from shot to shot. The same NIR pulse, which is used to generate the XUV pulses, provides the laser field, or the so called streaking field, consequently, the two pulses are perfectly synchronized. If the photoemission process is confined within one half-cycle of the laser field (1.25 fs for a carrier wavelength of 750 nm), the initial kinetic energy distribution of the photoelectrons released by the XUV pulse from the noble gas target will be broadened and shifted under the influence of the NIR laser streaking field. Due to the intrinsic synchronization, the relative delay between the XUV pulse and the streaking pulse can be controlled precisely and series of consecutive multi-shot measurements of the photoelectron spectra as a function of the XUV and streaking pulse delay can be recorded. The analysis of the acquired streaking spectrogram – a set of photoelectron spectra recorded as function of the ionizing XUV and NIR pulse delay – with a FROG<sup>2</sup>-type algorithm provides precise streaking field characteristics and complete information about the XUV temporal intensity profile and spectral phase, thus both pulses are fully characterized [55].

### 3.2.1 Semi-classical model

A semi-classical treatment of the photoionization process by the XUV in the presence of a strong laser field provides for an intuitive understanding of the streaking measurements. Due to the large difference between the XUV pulse frequency  $\omega_X$  and the optical laser pulse frequency  $\omega_L$ , the process of photoelectron streaking can be described in two subsequent

---

<sup>2</sup> Frequency-Resolved Optical Gating

steps: first an atom is ionized by absorption of an XUV photon, followed by acceleration of the ejected photoelectron in the laser field. The second step can be treated classically.

The XUV pulse with the central energy  $\hbar\omega_L$  ionizes some fraction of the atoms and photoelectrons with an initial kinetic energy of

$$W_i = m_e v_i^2 / 2 = \hbar\omega_x - E_b \quad (3.1)$$

are released, where  $E_b$  is the electron binding energy of the atom,  $\hbar$  the Planck constant,  $m_e$  the electron mass and  $v_i$  the initial velocity. Without the influence of the laser field – or streaking field - only the spectrum of the light pulse shifted by the ionization energy of the ionized material is observed and the width of the so called “field-free” photoelectron spectrum is given by the intrinsic bandwidth of the ionizing pulse. It should be noted that the experiment relies on the assumption that any possible influence of the laser streaking field on the initial state of the atoms can be neglected (ionization potential of the atoms unchanged).

For  $\hbar\omega_x \gg E_b$ , the electron rapidly moves away from the ion and therefore, the influence of the Coulomb potential of the ion on the electron motion can be neglected. Thus, the motion of the freed electron will be governed by the strong electric field of the NIR pulse [56]. The time-dependent velocity of a photoelectron released at time  $t_0$  into the NIR electric field  $E_L(t)$  can be calculated by integrating the classical equation of motion:

$$\begin{aligned} m_e \ddot{\mathbf{x}} &= -e\mathbf{E}_L(t) \\ \mathbf{v}(t) &= \mathbf{v}_i - \frac{e}{m_e} \int_{t_0}^t \mathbf{E}_L(t') dt' \\ &= \frac{e}{m_e} \mathbf{A}(t) + \mathbf{v}_i - \frac{e}{m_e} \mathbf{A}(t_0) \end{aligned} \quad (3.2)$$

where  $\mathbf{A}(t)$  is the vector potential of the electric field  $\mathbf{E}_L(t) = -d\mathbf{A}/dt$  in the Coulomb gauge,  $\mathbf{v}_i$  is the initial velocity without streaking field, and  $m_e$  and  $e$  are the electron mass and charge. The first term describes the oscillations of the electron in the laser field and goes to zero as the laser field approaches zero ( $t \rightarrow \infty$ ). The two last terms in Eq. 3.2 give the final drift velocity  $\mathbf{v}_f(t_0)$  measured after the laser pulse. The initial velocity is modified proportional to the vector potential of the laser field at the time of ionization. The momentum change after the end of the streaking pulse is given as:

$$\Delta\mathbf{p}(t_0) = -e\mathbf{A}(t_0). \quad (3.3)$$

If the electron is released before the laser pulse, the momentum change is zero, in agreement with the fact that free electrons do not absorb radiation. Here it is assumed, that

the electron does not experience any spatial variation of the field before the streaking pulse  $E_L$  has passed.

Let us assume a linearly polarized streaking field  $\mathbf{E}_L(t) = \mathbf{E}_0(t) \cos(\omega_L t + \varphi)$ , where  $E_0(t)$  is the envelope of the streaking pulse,  $\omega_L$  its angular frequency and  $\varphi$  the phase between the carrier and the envelope. Furthermore, let us choose the observation direction of the photoelectrons along the laser polarization. In this parallel observation geometry, the streaking effect directly couples to a change in kinetic energy of the ejected electrons. The final kinetic energy for an electron released at  $t_0$ , measured parallel to the electric field, can then be written as:

$$W_f(t_0) = W_i - \frac{e}{m_e} p_i A(t_0) + \frac{e^2}{m_e} \frac{A(t_0)^2}{2}, \quad (3.4)$$

where  $p_i$  is the initial moment of the electron. A derivation for arbitrary observation angles can be found in Appendix C. Within the slowly-varying envelope approximation, i.e.  $dE_0/dt \ll E_0 \omega_L$ , Eq. 3.4 can be further simplified to:

$$W_f(t_0) = W_i + 2U_p \sin^2(\omega_L t_0 + \varphi) + \sqrt{8W_i U_p} \sin(\omega_L t_0 + \varphi). \quad (3.5)$$

$U_p$  is the ponderomotive energy (cycle-averaged kinetic energy of a free electron oscillating in the electromagnetic field of the laser pulse) and it is given by:

$$U_p = \frac{e^2 E_0^2}{4m_e \omega_L^2}. \quad (3.6)$$

Provided that  $W_i \gg U_p$  (which is easily fulfilled in the streaking experiments presented in this thesis), the second term of Eq. 3.5 can be neglected, leading to a final kinetic energy modulation of

$$\Delta W(t_0) = W_f - W_i \approx \sqrt{8W_i U_p} \sin(\omega_L t_0 + \varphi) = e \sqrt{\frac{2W_i}{m_e}} A(t_0) \quad (3.7)$$

Thus, the influence of the streaking field results in a periodic modulation of the kinetic energy of the released photoelectrons as a function of relative delay between the ionizing XUV pulse and the streaking pulse (see Appendix C for more details).

The above formalism was derived for a point-like single particle. However, in reality, the released photoelectrons form a wavepacket, whose properties reflect the XUV pulse properties, as explained at the beginning of this chapter<sup>3</sup>. Therefore, a single particle description needs to be adapted to a distribution of electrons. The effect of the streaking

---

<sup>3</sup> In general, the released electron wavepacket may also contain information about the excitation dynamics in the system, but this is not subject of the presented thesis and will be ignored.

field on the initial time-momentum distribution  $n_e(p_i, t)$  of the emitted photoelectrons is given by [57,58]:

$$\sigma(p) = \int_{-\infty}^{\infty} n_e(p - eA(t), t) dt. \quad (3.8)$$

Thus, the width of the streaked photoelectron spectrum depends on the initial electron distribution, which in turn depends on the XUV pulse properties. The effect of the streaking field on an electron bunch with finite temporal duration will be explained in the next two sections.

A quantum-mechanical description of atomic XUV photoionization in a laser field can be found for example, in Ref. [53,56,59,60]. A comparison between the semi-classical and the quantum-mechanical treatment shows that both models are equivalent as long as the XUV pulse is significantly shorter than half the streaking field period. The semi-classical model, however, fails to account for interferences in the spectral domain that will occur as the XUV pulse duration (or the temporal extent of the photoelectron emission profile) becomes comparable to, or longer than the half-cycle period of the streaking field. These interferences appear between different parts of the electron wavepacket emitted at different times but receiving the same kinetic energy shift. As the XUV pulse duration increases, the streaking effect disappears and sidebands in the photoelectron spectrum start to develop and eventually well-separated sidebands will occur for long enough XUV pulses [61]. The sidebands are separated from the main photoelectron peak by multiples of the streaking field photon energy  $\hbar\omega_L$ . The sidebands can be used as a cross-correlation between XUV pulses and the envelope of the streaking pulse [62]. The sidebands have also been used for pulse duration and time-of-arrival measurements of X-ray FEL pulses [43,63]. However, this method does not allow for determination of the pulse duration on a single shot basis. In addition, in time-of-arrival measurements it is not possible to determine which pulse, NIR or FEL, arrives first.

For the rest of this chapter, it is assumed that the ionizing pulse and therefore, the duration of the emitted electron wavepacket is shorter than the half-cycle oscillation of the laser field, i.e. the photoemission process in the presence of an external laser field is well described by the semi-classical picture. Furthermore, in the work presented in this thesis the photoelectron spectra are always measured in a direction parallel to the streaking field polarization.

### 3.2.2 Streaking of Fourier limited pulses

In **Figure 3.2** the effect of the streaking field on an electron bunch released by a Fourier limited (also known as bandwidth-limited) XUV pulse is depicted for two different delays between the XUV and the NIR pulse. The temporal-emission profile of the photoelectrons mimics the ionizing XUV pulse, as depicted on the horizontal axis. The photoelectron energy spectrum is observed along the polarization of the streaking field and is shown on the vertical axis. Photoelectrons emitted at different instants accumulate different momentum changes, as indicated with the vertical arrows. In the upper panel the XUV pulse is overlapped with an extremum of the laser vector potential, resulting in maximal momentum shift of the photoelectron spectrum.

In the lower part of **Figure 3.2** the XUV pulse is synchronized with a zero crossing of the vector potential of the streaking pulse. Due to the finite temporal width of the electron wavepacket, electrons ejected before the zero-crossing of the vector potential are decelerated, while electrons ejected after the zero-crossing are accelerated. Consequently, the width of the final momentum distribution is broader as compared to the field free spectrum, but not shifted. As a result, the temporal photoemission profile, which represents a replica of the temporal structure of the ionizing pulse, is mapped onto a corresponding final velocity distribution of the generated photoelectrons. Probing the electron wavepacket at a consecutive zero transition, results in an identical broadening of the photoelectron energy spectrum.

In general, the width of the final electron energy distribution depends on following factors: (1) the slope of the streaking field (or streaking strength), (2) the variation of the streaking field strength due to the duration of the ionizing pulse, and (3) the bandwidth and spectral chirp of the ionizing pulse [53]. Accordingly, if the time-dependent streaking field is defined, the temporal duration and chirp (streaking with chirped pulses will be considered in the next section) of the ionizing pulse can be determined by comparing the spectra with and without streaking field. For Fourier-limited pulses the temporal profile can be retrieved unambiguously from a single streaked spectrum.

According to Eq.(3. the momentum change of the electrons is directly proportional to the laser vector potential at their time of release. Therefore, for perfectly synchronized and reproducible pulses a set of consecutive measurements of the photoelectron spectra over the full range of delays between the streaking pulse and the XUV pulse will trace out the vector potential of the streaking laser field [64,65], which is required for the retrieval of the ionizing XUV pulse profile from the streaked spectra. Here, it is also assumed that the ionizing XUV pulse is significantly shorter than the laser field half-cycle.

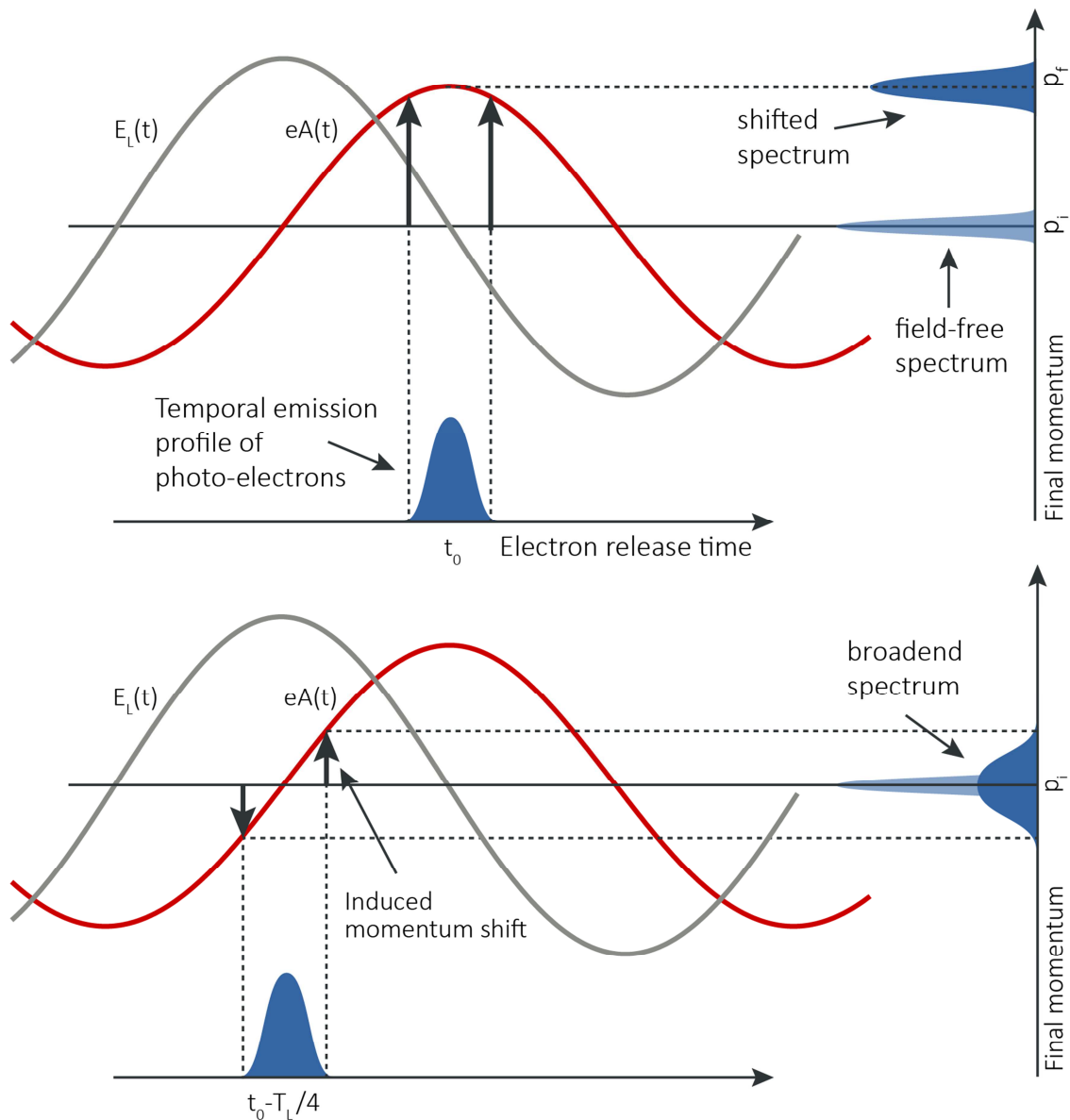


**Figure 3.2:** Streaking of a Fourier limited XUV pulse. The photoelectrons, released during the ionization of a noble gas by the XUV pulse form an electron bunch with a temporal emission profile that mimics the temporal characteristics of the ionizing XUV pulse. The grey and the red curves represent the electric field and corresponding vector potential of an NIR laser pulse that is temporally and spatially overlapped with the XUV pulse. In the upper panel the photoemission coincides with a maximum of the laser field’s vector potential. The final momentum distribution of the photoelectrons is plotted on the vertical axis. Compared to the field free case, the photoelectron spectrum is shifted to higher energies and slightly broadened (due to the curvature of the vector potential). When the photoemission is probed at a zero-crossing of the vector potential, as shown in the lower panel, the initial momentum distribution is symmetrically broadened around the initial central energy, resulting in the largest broadening of the photoelectron spectrum.

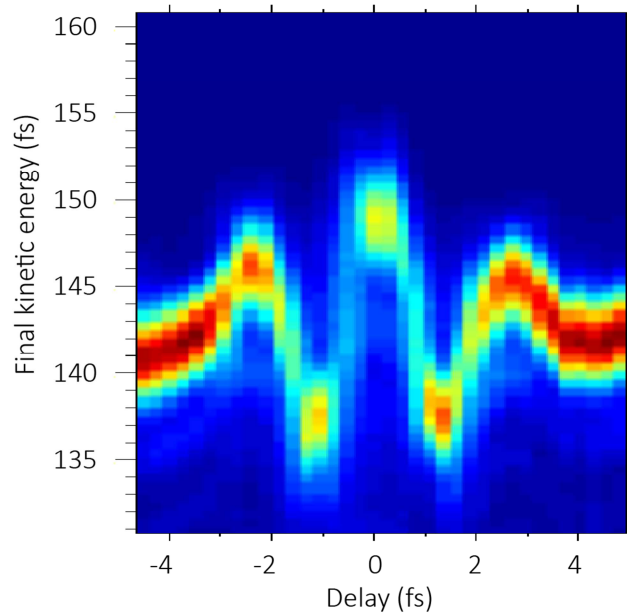


**Figure 3.3:** Plotting the photoelectron spectra as a function of the delay between the NIR laser pulse and the ionizing attosecond XUV pulse results in a streaking spectrogram as shown in the picture. The streaking measurement was recorded from Ne 2p. This figure shows a measurement with  $\sim 4$  fs long NIR pulse with a carrier wavelength of  $\sim 750$  nm and with XUV pulses with pulse duration of  $\sim 500$  attoseconds. The centroids of the streaked photoelectron spectra follow the evolution of the NIR laser vector potential.

In **Figure 3.3** a measurement of a streaking spectrogram is shown. A streaking trace from Ne 2p photoelectrons produced with coherent XUV pulses (with a bandwidth of 3.7eV), generated through higher harmonics from a  $\sim 4$  fs long NIR pulse with a carrier wavelength  $\lambda_L=750$  nm is presented. The streaking field is provided by the same NIR laser pulse; consequently the two pulses are precisely synchronized. The shift in kinetic energy as a function of delay, reveals the vector potential of the streaking laser field. Subsequently, the streaking field can be used to retrieve the temporal properties of the ionizing XUV pulse.

### 3.2.3 Retrieval of spectral phase

If the ionizing pulse is spectrally chirped, then the same time-frequency dependence is imprinted onto the released photoelectron distribution. This results in a different behavior of the streaked photoelectron spectra as compared to the streaking with a Fourier-limited XUV pulse. **Figure 3.4** illustrates the case of a linearly chirped XUV pulse. Here, the electrons that are released by the leading edge of a positively chirped XUV pulse are lower in energy than the electrons released by the trailing edge, as depicted by the colors in the figure. If this

photoemission occurs at a positive slope of the vector potential, the leading low-energy electrons will be further decelerated while the more energetic electrons at the trailing edge will be further accelerated, as indicated in the figure. This results in a broader streaked spectrum than the photoelectron spectrum generated by a transform-limited pulse of the same pulse duration. On the contrary, if the positively chirped XUV pulse is overlapped with a negative slope of the vector potential, the observed streaking spectrum will be narrower, as shown in the lower panel of **Figure 3.4**. Consequently, the photoelectron spectrum will be broadened and narrowed, when compared at consecutive zero-crossings of the streaking field, as the width of the streaked spectrum depends on the sign of the slope of the vector potential. Thus, for a linearly chirped XUV pulse a minimum of two measurements at opposite slopes of the vector potential are required to infer the temporal duration and the shape of the ionizing pulse [66,67]. Likewise, higher orders of chirp would lead to different modifications in the streaked spectrum.

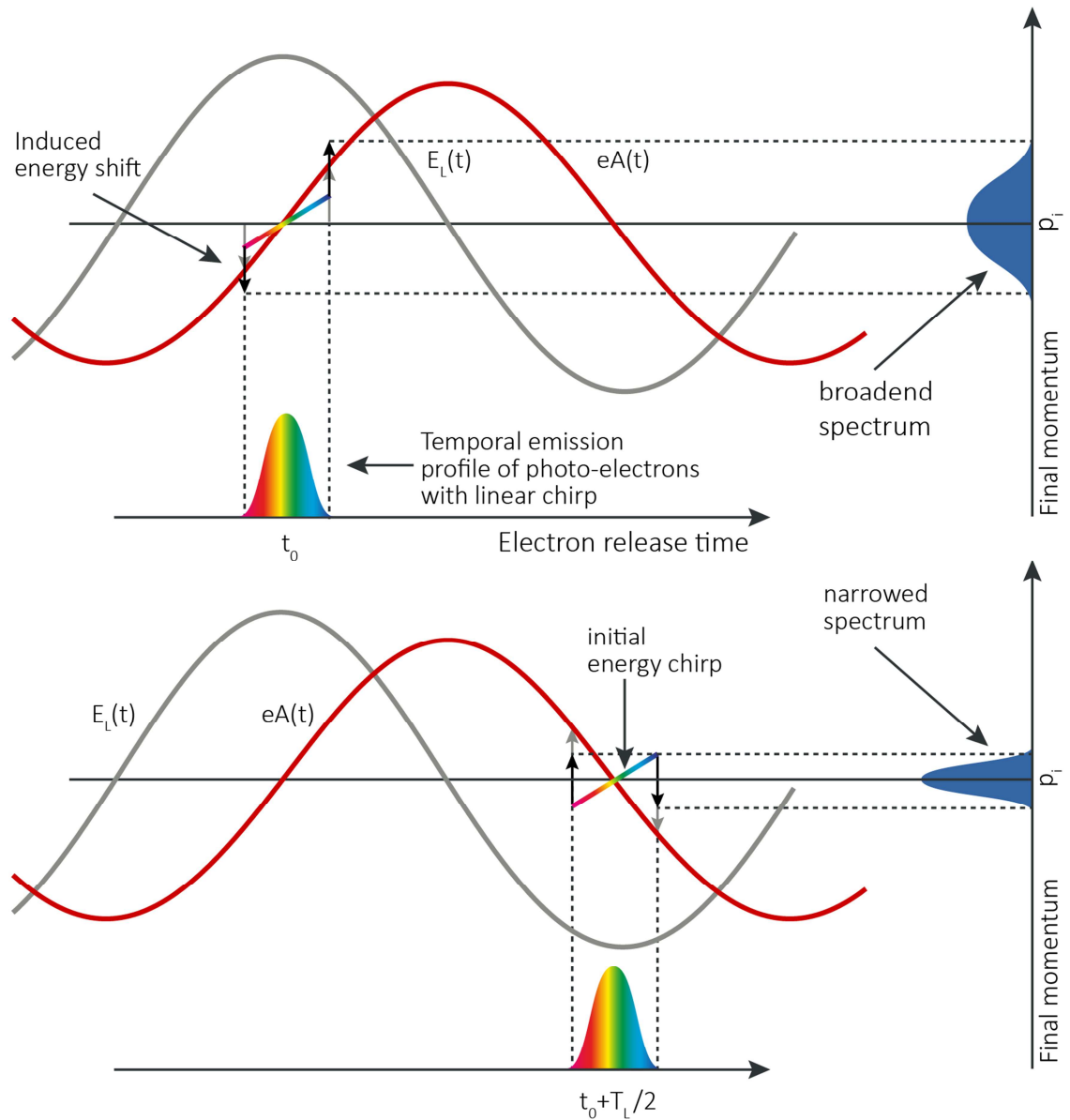


**Figure 3.4:** Streaking of a linearly chirped pulse. If the ionizing XUV pulse is spectrally chirped (time-frequency dependence), then the photoelectron bunch, released by this pulse, will carry this information in its initial momentum distribution. For instance, for a positively chirped pulse (as indicated by the colors in the figure) the electrons ionized by the preceding red-shifted photons will carry less energy than the electrons ionized by the trailing blue-shifted part of the pulse. If this electron bunch is probed at a zero-crossing of the vector potential, which is parallel to the initial chirp of the ionizing XUV pulse, the photoelectron spectrum will be broadened, as the red-shifted earlier electrons are shifted down in energy, while later blue-shifted photoelectrons gain energy. In the lower panel the bunch is probed at a zero-crossing of the vector potential with opposite sign, resulting in a narrower photoelectron spectrum.

### 3.3 Streaking spectroscopy at FELs

As discussed in the previous section, in attosecond metrology the NIR streaking field and the coherent XUV pulses are intrinsically synchronized and reproducibility of the pulses are expected. Consequently, as the parameters are constant, a multi-shot measurement over the full range of delays between the XUV pulse and the NIR pulse can be recorded. From this set of measurements the streaking field parameters and the XUV pulse properties can be retrieved.

In contrast, at SASE FELs the temporal profile and the arrival time of the X-ray pulse is changing from shot to shot. Therefore, ideally the pulse measurements should be performed on single-shot basis. In addition, SASE FEL pulses are expected to be as long as  $\sim 100$  fs. Since the duration of the ionizing FEL pulse has to be shorter than a half-cycle of the streaking field period, longer streaking field in the THz regime (1 THz equals to 500 fs half-cycle duration) are required.

At FLASH it is possible to send the FEL-driving electron bunch through an additional dedicated undulator to generate multi-cycle, phase-stable THz pulses. In a previous work, this THz source was used as the streaking field for the temporal characterization of the XUV FEL pulses [68]. As in attosecond metrology, the streaking THz pulse and the ionizing FEL pulse are intrinsically synchronized, which allows the streaking field parameters to be accessed by “traditional” attosecond methods. However, this technique does not provide any timing information for pump probe experiments. Furthermore, as the electron bunch generates the streaking field, the THz characteristics change as the electron beam is tuned, limiting the utility of this technique to FEL studies where beam parameters are varied systematically. For example, when the accelerator is tuned for the shortest FEL pulses, using very low charge and highly compressed bunches, the beam-based generated THz might be not strong enough for streaking.

#### 3.3.1 Laser-driven THz streaking spectroscopy

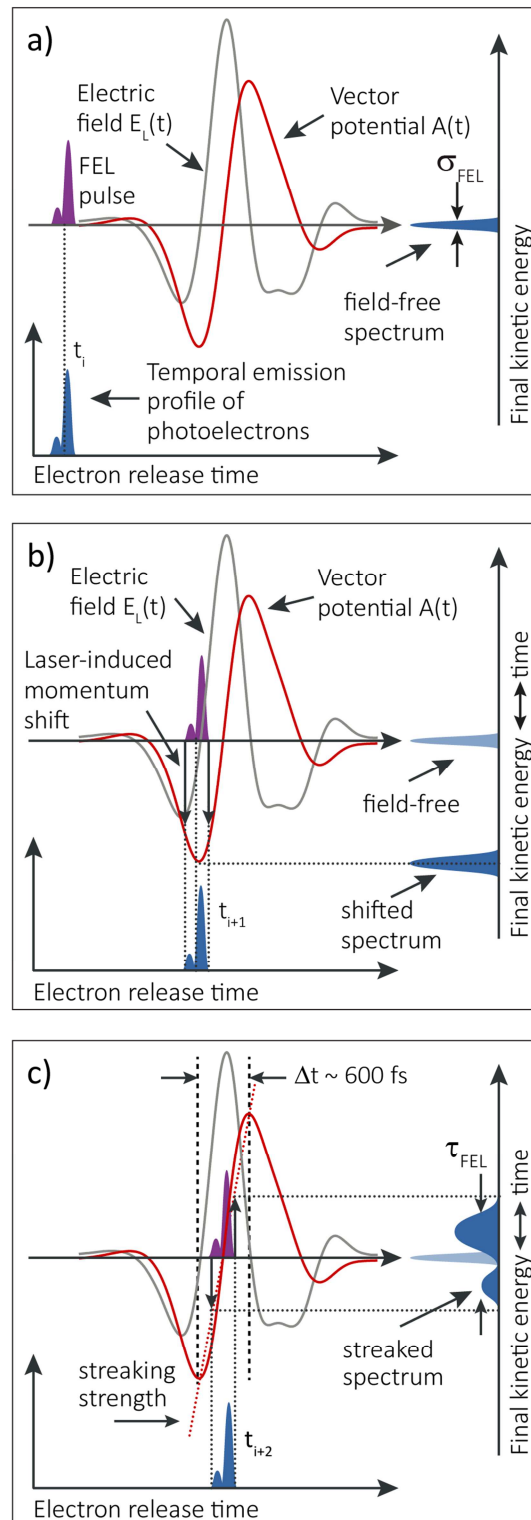
Using an independent laser-driven THz source for pulse characterization at FELs overcomes the limitations of streaking with accelerator-based THz sources, while maintaining the capability to characterize 100 fs long pulses. In addition, as laser-driven THz fields are locked to the external laser, the streaking measurement provides the capability to determine simultaneously the FEL pulse arrival time and its pulse profile on a time base that is synchronized to the pump-probe experiment environment.

To generate the THz pulses, the method of choice is optical rectification of femtosecond Ti:sapphire laser pulses in a LiNbO<sub>3</sub> crystal (see Chapter 4) [69]. With this technique high-field, phase-stable single-cycle THz pulses with pulse durations of ~2 ps are generated. In **Figure 3.5** the grey and the red curves represent the electric field and the corresponding vector potential of a single-cycle THz pulse (real measurement). The THz vector potential half-cycle length is about ~600 fs, indicated with  $\Delta t$  in the aforesaid figure. This is significantly longer than the maximum expected FEL pulse duration and timing jitter. Consequently, once the temporal overlap between the X-ray pulse and the THz pulse is established, all the X-ray pulses will arrive at a unique position on the monotonically rising streaking field ramp.

**Figure 3.5** explains the concept of single-cycle THz streaking measurements. The overlap of the ionizing FEL pulse and the THz streaking field at three different delay times is shown. In the first panel the two pulses are not overlapped, consequently the photoelectron spectrum remains unperturbed and only the FEL pulse spectrum shifted by the ionizing potential of the target gas is measured. In the second panel the FEL pulse is overlapped with an extremum of the vector potential, resulting in a maximally downshifted photoelectron spectrum with minimized spectral broadening. Consequently, the temporal structure of the pulse is not observed in the measured spectrum. In the last panel the ionizing FEL pulse coincides with a zero crossing of the THz vector potential  $A(t)$ . The ejected electrons acquire a momentum shift of opposite sign, resulting in a maximally broadened photoelectron around the field-free central energy. At this temporal overlap, the arrival time as well as the temporal profile and duration of the FEL pulse can be accessed with highest resolution.

If the streaked photoelectron spectrum is significantly broader than the initial bandwidth of the ionizing FEL pulse, the temporal profile of the FEL pulse can be recovered directly from the measured spectrum. In this case, also referred to as the strong streaking regime, the energy gradient that is imprinted onto the electron wavepacket by the streaking field is much larger than the initial energy variation caused by an ionizing chirped FEL pulse. In the measurements presented in this work, the broadening of the electron spectra due to streaking is much broader than the initial bandwidth of the ionizing FEL pulse and potential frequency chirp of the FEL pulse can safely be neglected. Here, the degree of spectral broadening is assumed to depend only on the duration of the FEL pulse as well as on the gradient of the THz streaking field. Thus, a broader streaked spectrum can be observed by either increasing the X-ray pulse duration or with stronger THz fields with steeper gradients.

**Figure 3.5:** Schematic of single-shot, single cycle THz streaking measurement. In a)-c) three different delay-instances between the ionizing FEL pulse and the THz streaking pulse are depicted. The grey and the red curves represent the electric field and the corresponding vector potential of a single-cycle THz pulse. On the lower horizontal axis the temporal emission profile of the photoelectrons released from a rare gas by the FEL pulse is shown. The photoelectron profile, shown in blue, mimics the temporal characteristics of the ionizing pulse. On the vertical axis the corresponding kinetic energy distribution of the photoelectron emission is depicted. In **a)** the two pulses do not overlap in time and the photoelectron spectrum is unaffected. In this case, the measured photoelectron spectrum reveals the intrinsic bandwidth  $\sigma_{\text{FEL}}$  of the FEL pulse. Panel **b)** shows the overlap with a minimum of the streaking pulse vector potential. The influence of the streaking field results in a maximal downshift of the photoelectron spectrum and only in a small broadening due to the curvature of the vector potential. Thus, the electron release time is translated in kinetic energy, but the FEL pulse structure cannot be observed. In **c)** emission around the zero-crossing of the vector potential is depicted. Due to the finite duration of the emission profile, the initial kinetic energy distribution gets broadened, as the electrons obtain energy shifts in opposite directions, however, the center of the distribution is not shifted. As a result, the underlying temporal structure of the FEL ionizing pulse is mapped into an energy distribution of the photoelectron wavepacket. The temporal dynamic range of the measurement is given by the length of the THz vector potential half-cycle, indicated with  $\Delta t$ .



### 3.3.2 Transformation from energy to time

In order to perform a calibrated transformation from the streaked photoelectron spectra to the time domain, the streaking field characteristics, including the THz vector potential shape and the THz electric field strength, must be precisely known. Due to the temporal jitter at FELs, the vector potential cannot be determined precisely from the streaking spectrogram. However, here a transformation map can be obtained from the THz electric field, measured independently by electro-optic-sampling (a time-domain measurement of the THz pulse; will be explained in chapter 4). The streaking measurement itself provides access to the THz electric field strength. Overlap with an extrema of the streaking pulse results in maximal kinetic energy shift as depicted in **Figure 3.5b**. A closer look at Eq. (3.7) indicates that the maximal kinetic energy shift due to streaking scales linearly with the electric field strength  $E_0$ . The maximal kinetic energy shift reads as:

$$\Delta W_{\max} = \frac{e\lambda_L}{\sqrt{2m_e}\pi c} \sqrt{W_i} E_0. \quad (3.9)$$

Thus, the maximally shifted single-shot ( $\Delta W_{\max}$ ) measurement in a streaking spectrogram recorded over the full range of delays, reveals the electric field strength. With the maximal measured single-shot kinetic energy shift and the independently characterized THz electric field shape (through EO-sampling), a unique mapping is established between the streaked kinetic energy and time by using Eq(3.7). With this transformation map the temporal profile of the FEL pulse can be retrieved unambiguously from a single streaked spectrum. The illustration in **Figure 3.6** demonstrates the mapping from the measured photoelectron spectrum to FEL intensity pulse profile with the constructed streaking map.

As already mentioned, not only the temporal profile can be extracted from the streaking measurement, but also the arrival time of the FEL pulses with respect to the pump laser pulse that is used to generate the THz pulse. For the measurements presented in this thesis, usually the center-of-mass of the streaked photoelectron spectrum is transformed to time to give the FEL pulse arrival time with respect to the pump-probe laser. However, as the FEL pulse profile is also measured, this can also be chosen according to the needs of the experiment.

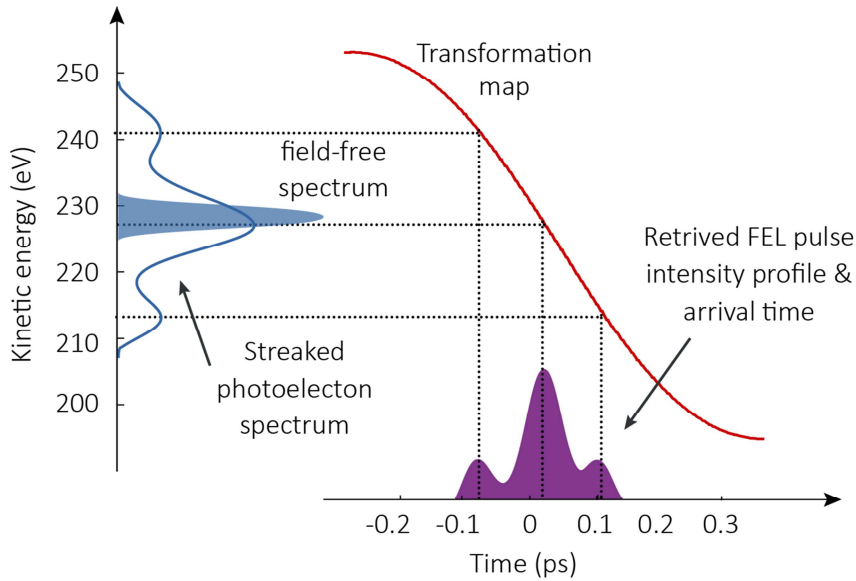


**Figure 3.6:** Illustration of the mapping from the measured photoelectron spectrum to the FEL pulse temporal profile. When the streaked photoelectron spectrum is significantly broader than the initial spectral bandwidth of the FEL photon pulse, the temporal profile of the ionizing FEL pulse can be recovered directly.

### 3.3.3 Influence of initial chirp in FEL pulses

Till now, only the strong streaking regime was considered, assuming that the initial energy distribution in the released electron wavepacket is small compared to the energy shift introduced by the streaking field. In this case, the FEL temporal profile can be inferred directly from a single-shot measurement at a zero-crossing of the THz vector potential. However, for FEL pulses with a broad initial bandwidth and large initial energy variation across the pulse, it may not be possible to neglect the initial chirp in the measurements.

As described previously, for linearly chirped pulses at least two measurements of the streaked photoelectron spectrum at opposite slopes of the vector potential are required to infer the temporal duration and shape of the ionizing pulse [66]. At FELs, different experimental approaches can be taken. To achieve this on a single shot basis, both signs of the slope have to be recorded simultaneously. For this two time-of-flight detectors, both mounted in the plane of the streaking field polarization but in opposite directions could be used to record two spectra with opposite slope. The change of sign could also be realized by a phase-shifted streaking pulse, which could be obtained by taking advantage of the Gouy phase shift, which occurs when a Gaussian beam travels through a focus [70]. A Gaussian beam passing through a focus acquires an additional  $\pi$  phase shift with respect to a plane

wave. Information about the average chirp of the pulses could be obtained by flipping the phase of the THz pulse itself. This can be realized easily for certain THz generation methods.

### 3.3.4 Ponderomotive potential of the THz field

The ponderomotive potential is the cycle-averaged quiver energy of a free electron in an oscillating electric field with frequency  $\omega_L$ . It is given by:

$$U_p = \frac{1}{2} m_e \langle \dot{r}^2 \rangle = \frac{e^2 E_0^2}{4m_e \omega_L^2}, \quad (3.10)$$

or, rewritten in practical units as:

$$U_p \text{ (in eV)} = 9.3 \times 10^{-14} I \lambda^2, \quad (3.11)$$

where  $I$  is the intensity in ( $\text{W}/\text{cm}^2$ ) and  $\lambda$  is the wavelength of the laser field in  $\mu\text{m}$ . As can be seen from the equations, the ponderomotive potential has a quadratic dependence on the wavelength. Therefore, very high values of  $U_p$  can be achieved with long wavelength pulses.

According to Eq. (3.7) the kinetic energy shift increases with increasing initial kinetic energy and increasing ponderomotive potential. Therefore, a change of the streaking wavelength from the NIR ( $\sim 800$  nm) to the THz ( $\sim 300$   $\mu\text{m}$ ) comes along with reduced streaking pulse intensity by several orders of magnitude for the same kinetic energy shift. Thus, already at moderate THz pulse intensities a substantial kinetic energy shift is achieved. It should be also mentioned that the classical treatment, described in Sec. 3.2.1 requires  $\hbar \omega \ll U_p$ . In this case the non-perturbative regime is reached and the electric field of the pulse can be treated classically as static electric field, while for  $\hbar \omega \gg U_p$  the multiphoton picture is appropriate.

Furthermore, at THz wavelengths no laser induced ionization is expected, as the ionization potential of the target gas is much higher than the THz photon energy, which is typically on the order of a few meV. In contrast, in attosecond streaking, where streaking wavelengths of  $\sim 800$  nm are used, the maximal kinetic energy shift (and thus the maximal temporal resolution) might be limited by the onset of laser induced ionization. Here, above-threshold-ionization (ATI) by the streaking laser field can generate background electrons, which limits the usable intensity.

### 3.4 Resolution Limits

The temporal resolution in THz streaking of X-ray pulses depends on several parameters. The two most important ones are the energy resolution of the photoelectron spectrometer and the streaking strength, which gives the degree of broadening. In addition, the initial FEL pulse bandwidth and the evolution of the THz pulse in the interaction region are limiting the achievable temporal resolution as well. Moreover, shot-to-shot phase and intensity fluctuation of the streaking pulse, as well as energy jitter in the FEL pulse degrade the temporal resolution of the measurement. In the next sections I will discuss individual influences of some of these factors.

#### 3.4.1 Resolution of the electron energy detector

The energy of the photoelectrons is detected with a time-of-flight (TOF) spectrometer. Electrons that enter the TOF pass a magnetically shielded drift tube followed by a post-acceleration stage before they reach the electron detector. The energy of the photoelectron is determined by measuring the time  $t$  required by the electron to travel from the interaction region to the detector placed at a known distance  $L$  (= drift tube). The kinetic energy of the electron is given by:

$$E_{kin} = \frac{1}{2} m_e \frac{L^2}{t^2}. \quad (3.12)$$

A measure of the energy resolution  $\Delta E$  is described by:

$$\Delta E_{kin} = \frac{2\sqrt{2}}{\sqrt{m_e}} \frac{\Delta t}{L} E_{kin}^{3/2}, \quad (3.13)$$

where  $\Delta t$  is the smallest interval that can be resolved by the electronic detection system. The post acceleration ensures a flat response of the electron detector (multi-channel plate, MCP) regardless of the initial electrons' kinetic energy. The acceptance angle of the TOF spectrometer is defined by its geometry (length of the drift tube and MCP diameter). In order to enhance the sensitivity, the TOF is equipped with an electrostatic lens at the entrance of the drift tube, which increases the effective acceptance angle for electrons within a specific kinetic energy range. This is especially important for measurements at FELs, as the full spectral distribution of the kinetic energy of the photoelectrons is collected in a single shot. This has a drawback though, because a larger acceptance angle is usually accompanied by a decrease of the energy resolution. This degradation is due to variations in

the electron flight length for electrons of same energy, but with different direction of movement.

From Eq. 3.13 one can see that the resolution of the detector decreases as a function of increasing electron kinetic energy. The equation also reveals that the energy resolution of the TOF is limited by the length of the drift tube and the temporal resolution of the detection electronics. The latter one includes the response time of the MCP electron detector and the resolution of the analog-to-digital (ADC) converter [71]. To improve the energy resolution, retardation potentials can be applied to increase the flight time of the electrons, before they enter the drift tube.

So far, at FELs, the relative energy resolution of electron TOF spectrometers could not be improved beyond  $\sim 1\%$ . The problem arises from the fact that a full spectral distribution of the photoelectron spectrum must be collected within one FEL shot. For this multi-electron acquisition, the energy resolution is severely degraded by the MCP detector signal width. This issue is illustrated in **Figure 3.7**. In the first panel, the signal resulting from a single electron response is illustrated. The signal is amplified and a pulse with a characteristic duration determined by the capacitive properties of the MCP amplifier is produced. For the detector used in the measurements presented in this thesis the signal is  $\sim 1.5$  ns in duration. The rising edge of this signal can be determined with high accuracy, depending mostly on the temporal resolution of the ADC that samples the pulse. In panel b) the MCP response for multiple distinct single-electron events are depicted. This situation is typical in the case of experiments at synchrotrons, where, on average, less than one electron per X-ray shot is detected. The accumulated arrival time distribution of the single photoelectron events gives the photoelectron spectrum. The time resolution is mostly determined by the rise time of the MCP signal and the resolution of the digitizer. In contrast, in our measurements at FELs, the entire photoelectron spectrum must be recorded in one FEL shot, thus many electrons per pulse are detected. The sum of the individual electron signals is collected and the detector acts as a current amplifier, rather than a discriminator for counting single-electron events. The measured photoelectron spectrum is a convolution of the actual signal and the width of the single-electron signal. Therefore, to increase the resolution of single-shot TOF measurements, the pulse width of a single-electron event must be reduced. To achieve this, MCP amplifiers with a smaller diameter can be used; however, this would reduce the collection efficiency.

Here, it should be also noted that geometrical factors influence the energy resolution of the TOF. In order to achieve high resolution, the size of the interaction region should be significantly smaller than the TOF spectrometer length and the detector acceptance angle should be small as well. Typically an increase of the collection efficiency (thus an increase of

the acceptance angle) leads to a decrease of the energy resolution and vice versa. The degradation of the energy resolution is due to variation in the electron flight length.

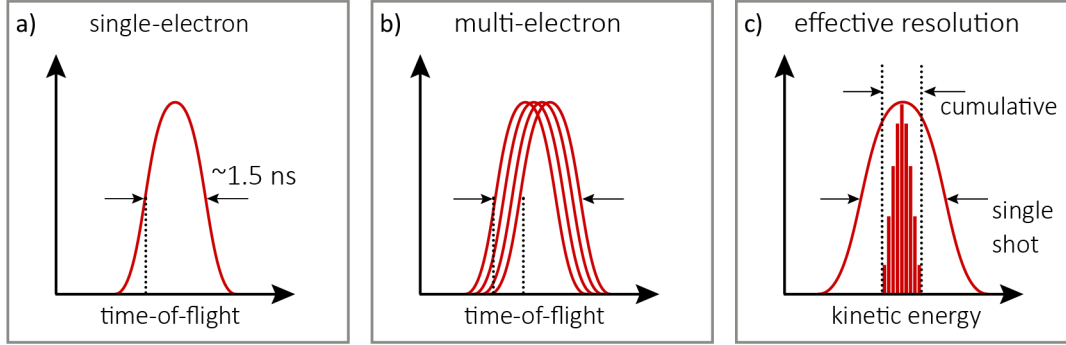


**Figure 3.7:** In **a)** the single-electron response of the detector is depicted. In **b)** multiple electron events are depicted. In **c)** the effective resolution of the single-shot multi-electron detection and the cumulative single-electron detection are shown. At FELs the recorded flight time spectrum consists of a convolution of the actual signal with the duration of the MCP signal of a single-electron. Here, the achievable resolution is limited by the duration of the MCP signal of a single electron event; while for the single electron hit, the resolution is usually limited by the resolution of the digitizer and the rise time of the MCP signal.

### 3.4.2 Streaking strength and initial bandwidth

The streaking strength determines the degree of broadening of the photoelectron spectra and thus directly influences the achievable temporal resolution, as in the streaking measurement, differences in the initial and the streaked photoelectron spectral bandwidth are observed. To be able to retrieve the temporal properties of the ionizing pulse a detectable change in the streaked photoelectron bandwidth has to be accomplished. The temporal information of the X-ray pulse can be retrieved with highest resolution, if the photoelectrons are released at the zero crossing of the streaking pulse vector potential. At this position, the temporal resolution is determined by the maximal streaking speed/strength which is given by:

$$s = \frac{\partial(\Delta W)}{\partial t}. \quad (3.14)$$

The average streaking speed is given by the ratio of the peak-to-peak amplitude of the kinetic energy shift to the rise time of the streaking vector potential:

$$s_{avg} = \frac{\Delta W_{max-min}}{\Delta t_{rise}}. \quad (3.15)$$

With this, the temporal resolution of the streaking measurement can be expressed as:

$$\tau_{res} = \frac{\sigma_{filedfree}}{S}, \quad (3.16)$$

where  $\sigma_{filedfree}$  is the width of the photoelectron spectrum without streaking field. Clearly, the temporal resolution can be increased by stronger and steeper streaking fields. This value only represents an upper limit for the temporal resolution. For the real temporal resolution, also the other factors have to be taken into account. As the duration  $\tau_x$  of the X-ray pulse decreases, its bandwidth  $\Delta\omega_x$  increases as  $\propto 1/\tau_x$  and the contribution to the broadening of the streaked photoelectron bandwidth  $\Delta W$  decreases as  $\propto \tau_x$ , resulting in imperceptible changes of the spectral width compared to the initial width [53]. Thus, a narrower initial bandwidth leads to higher temporal resolution under otherwise same experimental conditions. Here, the streaking strength can be increased by stronger and steeper streaking fields.

At X-ray FELs radiation pulses can reach spectral bandwidths up to several eV, which as we have seen before has negative influence on the temporal resolution eV. One way to increase the temporal resolution, when measuring spectrally broad pulses is to use Auger electrons instead of direct photoelectrons for streaking [72]. The Auger process is depicted schematically in **Figure 3.8**. The kinetic energy of Auger electrons is only determined by the involved atomic orbitals and is not affected by the ionizing photon energy  $\hbar\omega_x$ . Their natural linewidth is related to the lifetime of the observed core hole by the uncertainty principle. Typical widths are in the range of  $\sim 100$  meV [73]. In contrast, the linewidth of the direct photoelectrons are given by the bandwidth of the ionizing X-ray pulse. Therefore, using Auger lines for THz streaking might improve the resolution of the measurement, especially at higher photon energies, as the initial field-free width is narrower. However, in this case the resolution is ultimately limited by the lifetime of the core hole. For ionizing X-ray pulses with duration  $\tau_x$  that is shorter than the lifetime of the created core hole state  $\tau_h$ , the temporal evolution of the emission profile for photoelectrons and Auger electrons is different. Photoelectrons are only emitted while the X-ray pulse is present and the emission profile follows the temporal profile of the exciting pulse (here a constant transition cross section within the bandwidth of the X-ray pulse is assumed). While the Auger electrons are a result of a spontaneous relaxation process, the emission profile is a convolution of the X-ray pulse profile with an exponential decay corresponding to the Auger lifetime. In addition, the spectral phase cannot be measured, as the Auger electrons are not sensitive to the ionizing photon energy. It should be also mentioned, that the cross section for single Auger lines is much lower than for photo-lines.

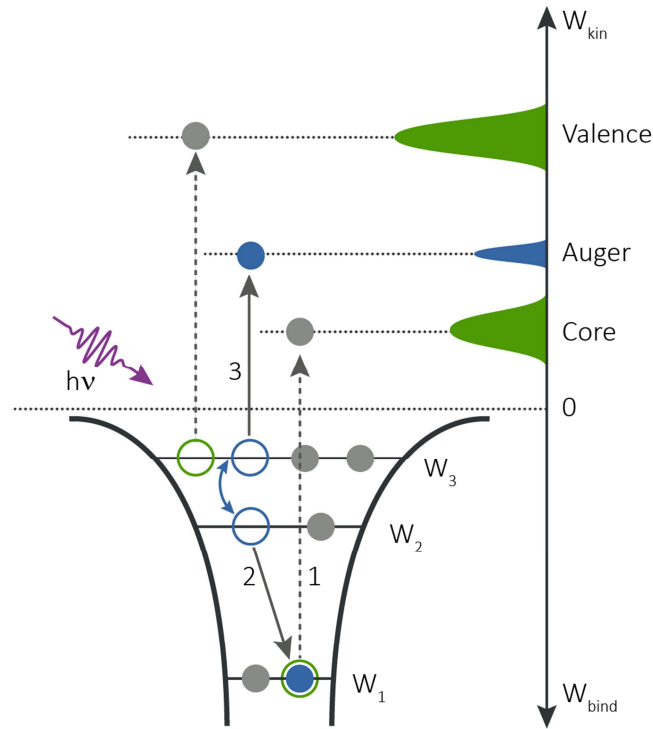


**Figure 3.8.** A schematic depicting the relaxation of the core hole through Auger electron emission. An incident X-ray pulse creates a core hole through the ejection of an electron from state  $W_1$  to vacuum state (referenced as zero). The core hole, created by core-level ionization, can decay by emission of a characteristic X-ray photon or non-radiantly by emission of an Auger electron. The Auger process occurs as follows: an electron from state  $W_2$  subsequently fills the core hole  $W_1$ , the excess energy between these two states is transferred to another electron, which is ejected from state  $W_3$  into the vacuum state. The ejected secondary electrons are called Auger electrons. Unlike the kinetic energies of the core and valence electrons, the kinetic energy of the observed Auger electrons ( here:  $W_{kin} = W_1 - W_2 - W_3$  ) is independent of the energy of the incident X-ray pulse (figure reproduced from Ref.[74]).

### 3.4.3 Gouy phase shift

A Gaussian beam passing through its focus experiences an additional phase shift of  $\pi$  with respect to a plane wave. This phenomenon is referred to as the Gouy phase shift and it can be written as [70]:

$$\phi(z) = -\arctan\left(\frac{z}{z_R(\lambda)}\right), \quad (3.17)$$

where the beam is travelling in the  $+z$  direction and  $z_R$  is the Rayleigh length, given by:

$$z_R = \frac{\pi w_0^2}{\lambda_0}, \quad (3.18)$$

where  $w_0$  is the beam waist of the focal spot and  $\lambda_0$  is the central wavelength of the pulse. The phase shift is  $\pi$  in the transition from  $-\infty$  to  $\infty$ , while from  $-z_R$  to  $z_R$  the pulse experiences a phase shift of  $\pi/2$ .

Consequently, during propagation of the X-ray pulse and the streaking pulse through the focus, the streaking pulse phase with respect to the ionizing pulse is changing. The width of the streaked photoelectron spectrum is a convolution of the XUV pulse duration and the Gouy phase shift. In order to minimize the influence of the Gouy phase shift, loose THz focusing is desirable. However, for high THz electric field strengths, tight focusing is required. Therefore, it is necessary to minimize the interaction length between the THz and the FEL pulses, which is defined by the noble gas target density. For this reason, the gas target length must be much smaller than the Rayleigh range of the streaking pulse. Another possibility is to restrict the TOF acceptance angle, which would reduce the contribution from photoelectrons emitted at different points within the interaction region (along the beam propagation axis) and thus with different streaking phases.



## **4 High field terahertz pulses**

The part of the electromagnetic spectrum from 0.1 to 10 THz, which corresponds to wavelengths in the range from 3 mm to 30  $\mu\text{m}$ , is usually referred to as the terahertz (THz) radiation. This part of the electromagnetic spectrum was termed the THz gap in the past, because of lack of sources, particularly high intensity ones in this range. In recent years, the generation of high-intensity THz pulses has been made possible through amplified femtosecond laser systems. The most widely used techniques for THz pulse generation utilizing ultrashort pulses are photoconductive antennas [75], four-wave-mixing in a laser induced plasma [76,77] and optical rectification [78,69]. The single-cycle THz transients produced from photoconductive antennas have small pulse energies and the highest reported energy up to now was only 0.8  $\mu\text{J}$  [79]. Furthermore, the involved high-voltage switching imposes practical challenges and sets limitations on the achievable signal/noise. In addition, the conversion efficiency of THz generation in laser induced plasma in air is pretty low even though it promises broadband pulses [80]. Up to date, the most efficient and the best accessible table-top technique for the generation of high intensity single-cycle THz pulses is optical rectification of femtosecond laser pulses, usually in the near-infrared (NIR) spectral range (e.g. Ti:sapphire laser system). For THz streaking spectroscopy at FELs this is the most suitable and practical source. Therefore, this technique will be described in the next sections. This is followed by a discussion of electro-optic sampling, which is used for the temporal characterization of THz pulses.

### **4.1 Optical rectification – nonlinear optical phenomena**

In a second-order nonlinear medium THz radiation can be generated by optical rectification of a femtosecond near-infrared (NIR) laser pulse. The generation process can be seen as difference-frequency mixing of the spectral components contained within the spectral bandwidth of the driving optical pulse. The electric field waveform associated with the generated THz pulse in turn can be detected with the inverse process of the mixing. The

detection scheme is usually referred to as electro-optic sampling and this technique is elaborated in Sec. 4.3. In the following chapter the theoretical background of these processes will be described.

Non-linear optical phenomena are governed by the non-linear dependence of the induced polarization  $\mathbf{P}$  on the applied electric field  $\mathbf{E}$  in the Maxwell Equations. The wave equation for linear and nonlinear medium is derived in Appendix A.

The polarization  $\mathbf{P}$  in a dielectric medium is the macroscopic sum of the dipole moments per unit volume induced by the applied electric field  $\mathbf{E}$ . In linear optics the induced polarization is proportional to the applied electric field strength and it can be described by:

$$\mathbf{P}(t) = \varepsilon_0 \chi^{(1)} \mathbf{E}(t) \quad (4.1)$$

where  $\varepsilon_0$  is the electric permittivity of free space and  $\chi^{(1)}$  is the linear susceptibility of the medium. This describes linear-optical effects. For high pulse intensities, when the electric field strength of the optical pulse is comparable to the interatomic or crystal field strengths ( $10^5$ - $10^8$  V/m), the induced polarization in a material will in general be a nonlinear function of the applied electric field. Therefore the induced polarization  $\mathbf{P}$  in a material is expanded into a power series of the electric field  $\mathbf{E}$ :

$$\begin{aligned} \mathbf{P} &= \varepsilon_0 \left[ \chi^{(1)} \mathbf{E} + \chi^{(2)} \mathbf{E}^2 + \chi^{(3)} \mathbf{E}^3 + \dots \right] \\ &\equiv \mathbf{P}^{(1)} + \mathbf{P}^{(2)} + \mathbf{P}^{(3)} + \dots \end{aligned} \quad (4.2)$$

$\chi^{(2)}$ ,  $\chi^{(3)}$ , ...  $\chi^{(n)}$  are the nonlinear susceptibility tensors of the rank  $n+1$ . In general, the higher order susceptibilities are progressively smaller and for the sake of clarity, the terms  $\chi^{(3)}$  and higher orders are neglected in this thesis as only the second-order nonlinearity is relevant for THz generation and detection.

When an optical pulse  $\mathbf{E}(t) = E(t) \exp(-i\omega_0 t)$ , with slowly varying envelope  $E(t)$  and a central frequency  $\omega_0$ , propagates through a crystal for which the second-order susceptibility  $\chi^{(2)}$  is nonzero, the induced polarization  $\mathbf{P}^{(2)}$  is:

$$\begin{aligned} \mathbf{P}^{(2)} &= \varepsilon_0 \chi^{(2)} \mathbf{E}^2 \\ &= \varepsilon_0 \chi^{(2)} (E(t)e^{-i\omega_0 t} + E^*(t)e^{i\omega_0 t})^2 \\ &= 2\varepsilon_0 \chi^{(2)} E(t)E^*(t) + (\varepsilon_0 \chi^{(2)} E^2(t)e^{-2i\omega t} + c.c.). \end{aligned} \quad (4.3)$$

The first term at zero frequency is responsible for the generation of a d.c field in the crystal. This process is known as optical rectification. The term at double the input frequency can lead to the generation of electromagnetic radiation at the second-harmonic frequency of the input field.

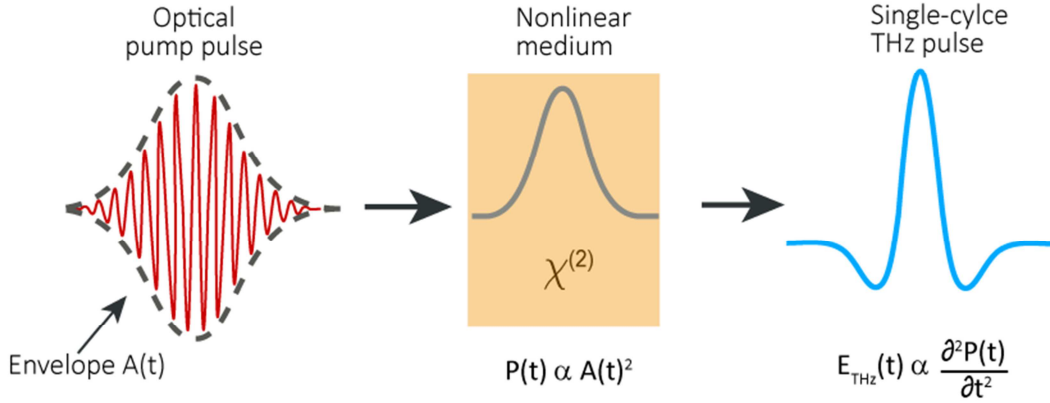


**Figure 4.1:** Schematic of THz pulse generation by optical rectification of a femtosecond optical pulse. The NIR pump pulse induces a second order polarization in the nonlinear crystal, which time dependence is proportional to the input pulse envelope. The induced polarization is the source of the THz radiation. The generated THz pulse is proportional to the second derivative of the induced polarization.

An intuitive explanation for optical rectification or difference mixing could be obtained by considering the optical pulse as a sum of monochromatic waves with frequencies in the spectral band around  $\omega_0$ . Upon propagation through a nonlinear medium, the different components are mixed pairwise producing radiation with the difference frequency. The process of difference frequency mixing generating the THz generation at frequency  $\Omega$  can be described by the equation:

$$P_{\text{THz}}(\Omega) = \epsilon_0 \chi^{(2)} E_{\text{opt},1}(\omega) E_{\text{opt},2}^*(\omega + \Omega), \quad (4.4)$$

where  $E_{\text{opt},1}$  and  $E_{\text{opt},2}$  are the components of the optical driving pulse with frequency  $\omega$  and  $\omega + \Omega$ . Since the generated radiation is a result of difference frequency mixing among the different Fourier components contained in the Fourier spectrum of the ultrashort optical pulse, the frequency of the THz ranges from 0 to the bandwidth of the laser pulse. However, there is an upper frequency limit for the bandwidth set by transverse optical phonon of the nonlinear crystal, where the absorption of THz radiation by this phonon, which usually lies in the range from 5 THz to 11 THz, plays a significant role [81,82]. Usually a high  $\chi^{(2)}$  is due to the polarization due to the excitation of this phonon-polariton by the optical pulse; however the same phonon frequency dictates the bandwidth of the emitted THz radiation [83]. Many nonlinear semiconducting crystals have been shown to produce terahertz radiation, these include the zinc blende crystals zinc telluride (ZnTe) [84], gallium phosphide (GaP) [85], and the ferroelectric lithium niobate  $\text{LiNbO}_3$  (LN) [69].

A schematic of the THz generation through  $\chi^{(2)}$  process is shown in **Figure 4.1**. Here,  $P^{(2)}$  is proportional to the intensity of the pump field (which is strictly positive), and this  $P^{(2)}$  is the source term for  $E_{\text{THz}}$  generation as given by

$$E_{\text{THz}} \propto \frac{\partial^2 P^{(2)}}{\partial t^2}. \quad (4.5)$$

## 4.2 Materials for THz generation through optical rectification

Crystallographic symmetry determines whether or not a crystal has a non-zero  $\chi^{(2)}$ . Crystals without inversion symmetry are relevant for optical rectification or difference frequency generation since centrosymmetric crystals have a vanishing  $\chi^{(2)}$  tensor. Further, several other requirements have to be met for efficient THz generation. In most cases a single crystal has to be used, since for many polycrystalline materials the random grain orientation might result in an averaging effect resulting in a reduced efficiency. Also, a high damage threshold for the material of choice is necessary, since high pump pulse intensities have to be used. And finally, the other important factors which must be taken into consideration are the effective nonlinear coefficient  $d_{\text{eff}}$ , THz absorption and phase matching between the optical pump pulse and the THz radiation. The efficiency of THz generation can be described with the following equation [86]:

$$\eta_{\text{THz}} = \frac{2\Omega^2 d_{\text{eff}} L^2 I}{\epsilon_0 n_{\text{NIR}}^2 n_{\text{THz}} c^3} \exp[-\alpha_{\text{THz}} L/2] \frac{\sinh^2 [\alpha_{\text{THz}} (L/4)]}{[\alpha_{\text{THz}} (L/4)]^2} \quad (4.6)$$

where  $\Omega$  is the angular frequency of the generated THz,  $L$  is the length of the nonlinear crystal,  $I$  the intensity of the optical pump pulse,  $\epsilon_0$  the vacuum permittivity,  $\alpha_{\text{THz}}$  is the THz absorption coefficient in the crystal and  $n_{\text{NIR}}$  and  $n_{\text{THz}}$  are the refractive indices of the NIR and THz, respectively. Pump depletion or absorption is not taken into account in Eq.4.6. The nonlinear susceptibility tensor  $\chi^{(2)}$  can be simplified and represented by a 3 x 6 d-matrix when permutability of the elements  $\chi_{ijk}^{(2)}$  is assumed. The elements of the d-matrix are [87]:

$$d_{ijk} = \frac{1}{2} \chi_{ijk}^{(2)} \quad (4.7)$$

Crystallographic symmetry determines the nonvanishing and independent components of the d-matrix. Usually the highest nonvanishing component is referred as  $d_{\text{eff}}$ .

In order to compare different crystals for optical rectification Eq.4.6 is used to define a figure of merit (FOM) as [86]:

$$\text{FOM}_{\text{NA}} = \frac{d_{\text{eff}}^2 L^2}{n_{\text{NIR}}^2 n_{\text{THz}}}, \quad (4.8)$$

$$\text{FOM}_{\text{A}} = \frac{4d_{\text{eff}}^2}{n_{\text{NIR}}^2 n_{\text{THz}} \alpha_{\text{THz}}^2}. \quad (4.9)$$

Eq. 4.8 describes the case for negligible THz absorption in the material, while equation (5.8) is valid when significant absorption is present. The values for some crystals are summarized in **Table 4.1**. As can be seen, LN and organic crystals like DSTMS present the best suitable choices for achieving high field single cycle THz transients as indicated by the high FOM. Since the vast majority of the work conducted in this thesis utilizes LN as the terahertz generation medium, only the generation process in LN is described in detail. However few experiments were performed with THz generated from DSTMS.

It should be mentioned that for ZnTe collinear velocity matching inside the material (see Table 4.1) is well fulfilled for Ti:sapphire wavelengths. The overall efficiency, though, is limited by the applicable NIR pump intensity [88], due to two-photon absorption, enabled due to the low band-gap in ZnTe [89].

**Table 4.1:** Properties of commonly used materials for THz generation with optical rectification. Values are taken from Ref. [86], except for DSTMS. For ZnTe, GaP and Ln  $n_{\text{THz}}$  and  $\alpha_{\text{THz}}$  are given for 1THz.

Material	$d_{\text{eff}}$ (pm/V)	$n_{800\text{nm}}^{\text{gr}}$	$n_{\text{THz}}$	$n_{1.55\mu\text{m}}^{\text{gr}}$	$\alpha_{\text{THz}}$ (cm <sup>-1</sup> )	FOM (pm <sup>2</sup> cm <sup>2</sup> V <sup>-1</sup> )
ZnTe	68.6	3.13	3.17	2.81	1.3	7.27
GaP	24.8	3.67	3.34	3.16	0.2	0.72
sLiNbO <sub>3</sub>	168	2.25	4.96	2.18	17	18.2
DSTMS	210 (1.9μm) [90]	3.2 [90]	2.25 (2THz) [91]	2.07 [90]	35 [91]	15

#### 4.2.1 Noncollinear velocity matching titled pulse front method in LN

In order to enhance the efficiency of any nonlinear optical frequency conversion process, phase-matching condition between the involved frequency components has to be fulfilled. For optical rectification the phase matching condition is given by [92]:

$$\Delta k(\Omega) = k(\Omega) + k(\omega) - k(\omega + \Omega) = 0 \quad (4.10)$$

where  $\omega$  is the optical near-infrared (NIR) frequency,  $\Omega$  is the THz frequency and  $\Delta k$  the wave-vector mismatch. Under the condition  $\Omega \ll \omega$  equation (4.6) can be written as:

$$\Delta k(\Omega) \approx k(\Omega) - \left. \frac{\partial k}{\partial \omega} \right|_{\omega_0} \cdot \Omega = (n(\Omega) - n_g(\omega_0)) \cdot \frac{\Omega}{c} \quad (4.11)$$

Here  $\omega_0$  is the mean pump frequency,  $c$  the speed of light in vacuum,  $n(\Omega)$  the refractive index of the material for the generated THz and  $n_g = n(\omega_0) + \omega_0 dn/d\omega$  is the group index of the optical pump light. Thus, phase matching is achieved if the refractive index of the material in the THz region is equal to the group index of the optical pump pulse.

$$n_{NIR}^g = n_{THz} \quad (4.12)$$

Consequently, the phase-matching condition can be reformulated as matching the THz phase velocity of a certain frequency to the group velocity (envelope) of the optical pump pulse:

$$v_{NIR}^g = v_{THz}^{ph} \quad (4.13)$$

An intuitive understanding suggests that when the pump and the generated radiation travel with the same speed and in the same direction, the three waves participating in the difference-frequency generation process will remain in phase and maximal energy conversion efficiency will be reached.

In non-dispersive materials, where the refractive index does not depend on the frequency, the generated THz amplitude would grow linearly for every frequency component with increasing crystal thickness, and the bandwidth of the THz wave would only depend on the bandwidth of the optical pump pulse. However, all nonlinear crystals are dispersive in both the optical and the THz spectral band, especially close to the frequencies of the phonon-polariton spectrum, therefore phase-matching can only be reached for a certain THz frequency range.

Even though LN offers very high possible efficiency (Table 4.2), there is a big difference between  $n_{THz}$  and  $n_{NIR}^g$ , consequently collinear phase matching is not possible. Therefore, a different velocity matching technique has to be used. In the case where the THz refractive index is larger than the NIR group index, noncollinear velocity matching can be realized by tilting the pump pulse intensity front as suggested by Hebling et al [93]. The principal of this technique is shown in **Figure 4.2**. Here, a tilted NIR pulse front generates THz radiation (in phonon-polariton form in the crystal), which according to Huygen's principle travels perpendicular to this front with a phase velocity  $v_{THz}^{ph}$  [93]. The angle between the THz propagation direction and the pump pulse propagation direction is equal to the tilt angle,  $\gamma$ , of the intensity front of the NIR. The projection of the group velocity of the NIR pump pulse

on to the propagation direction of the THz radiation has to be equal for the velocity phase matching condition to be met. Here the velocity matching condition changes to:

$$v_{NIR}^g \cdot \cos \gamma = v_{THz}^{ph} \quad (4.14)$$

which requires the following relation between refractive indices and the tilt angle to be satisfied.

$$\cos \gamma = \frac{n_{NIR}^g}{n_{THz}^{ph}} \quad (4.15)$$

The latter equation can be fulfilled in materials where the dielectric constant in the THz region is larger than in the visible by properly choosing the tilt angle  $\gamma$  of the intensity front of the NIR radiation.

In the case of the LN, the required pump pulse front tilt inside the crystal is around 63°-65° for pump pulses with a central wavelength of 800 nm. In **Figure 4.3** an experimental setup for tiled pulse front THz-generation is shown schematically. Since a large tilt angle is needed, a diffraction grating (2000 lines/mm) is used to introduce the necessary angular dispersion. In appendix B the equivalence of angular dispersion and intensity pulse front tilt is described in detail. The lens telescope (2:1 focal length ratio) is used to image the pump spot at the grating into the crystal. Due to the angular dispersion, the different spectral components propagate in different directions and are therefore spatially separated, which in turn results in a pulse duration lengthening. The imaging system compensates for this spatial separation of the different frequencies and at the image plane the original pulse duration, before diffraction, is reconstructed. A half-wave plate rotates the pump laser polarization from *p*-polarization to *s*-polarization in order to be parallel to the optical axis of the LN ( $d_{33}$  is the component with the highest value of the electro-optic tensor in LN). The exit surface of the LN generation crystal is at the tilt angle  $\gamma$  for normal incidence of the THz. The tilt angle of the pump pulse is influenced by three factors:

- The tilt introduced by the grating.
- The change of the tilt angle by the imaging system.
- The change of the tilt angle upon entrance into the crystal to the final tilt  $\gamma$ .

In the following, these three effects will be described.

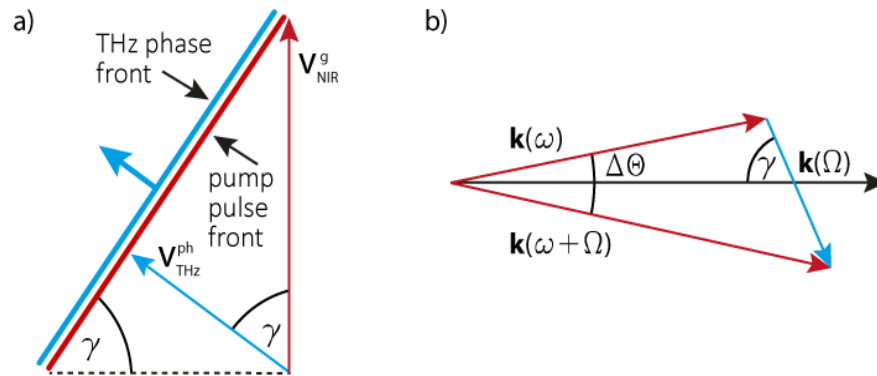


**Figure 4.2:** Velocity matching with tilted pulse front: **a)** The tilted intensity front of the NIR pulse propagates in the direction of the red arrow inside the LN crystal and generates a plane THz (phonon-polariton wave inside the crystal) wave. The THz propagation direction is perpendicular to the tilted intensity front, according to Huygen’s principle. Thus, the angle  $\gamma$  between the THz propagation direction and the propagation direction of the pump is equal to the tilt angle of the NIR pulse front. **b)** Wave-vector diagram for phase matching. The introduced pulse front tilt is equal to angular dispersion. Here, the propagation direction is frequency dependent. Two frequency components contained within the wide spectral bandwidth of an optical femtosecond pulse, generate the THz wave at the frequency  $\Omega$ .

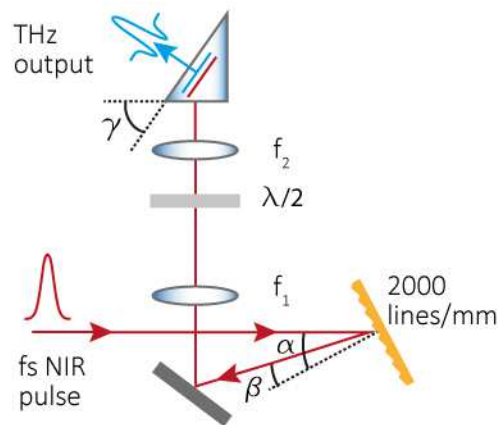


**Figure 4.3:** THz generation in LN by tilted pulse front pumping. A near-infrared laser pulse is diffracted from a 2000 lines/mm grating, which results in pulse front tilt. The laser is horizontally polarized for which the efficiency of the grating is high. The laser spot on the grating is imaged with a 2:1 telescope on to the generation crystal, which is cut at the angle  $\gamma$  as indicated in the figure. The telescope is reconstructing the short pulse duration in the image plane, which is close to the LN crystal entrance surface. Before the pulse enters the LN crystal, its polarization is rotated by  $90^\circ$  with a half-wave plate, to be parallel to the optical axis. The optical axis of the generation crystal is perpendicular to the plane of the figure. The THz radiation is emitted perpendicular to the LN-crystal surface. The direction of the tilt of the pulse is flipped in the image plane to the 4f configuration of the imaging system.

### Pulse front tilt introduced by the grating

It is well known that a femtosecond optical pulse experiences a time delay across the beam when a tilt is introduced in the intensity pulse front relative to its phase front. This tilt of the phase front is achieved when propagating through a diffraction grating or a dispersive prism [94]. The formation of the pulse front tilt upon diffraction from a grating is shown in **Figure 4.4**. A monochromatic beam with input diameter  $D_i$  and wavelength  $\lambda$  impinges on the grating at an angle  $\alpha$  and is diffracted at an angle  $\beta$ . The diffraction of the beam is described with the grating equation:

$$\sin \alpha + \sin \beta = m\lambda/d \quad (4.16)$$

here  $d$  is the groove spacing of the grating, and  $m$  the diffraction order. In **Figure 4.4** the two sides of the beam (marked with 1 and 2) are subject to different path lengths, the ray marked with 2 will travel the distance of  $a + b$  (in green and blue) more than ray 1, resulting in a time delay. The path difference  $\Delta$  can be calculated with:

$$\begin{aligned} a &= \sin \alpha \cdot G \\ b &= \sin \beta \cdot G \\ G &= \frac{D_i}{\cos \alpha} \end{aligned} \quad (4.17)$$

$D$  is the width of the beam after diffraction is given by  $D = \cos \beta \cdot D_i / \cos \alpha$ . With these variables the intensity front tilt relative to the phase front, which is perpendicular to the wavevector, can be calculated from:

$$\begin{aligned} \tan \gamma'' &= \frac{a+b}{D} \\ &= \frac{\sin \alpha + \sin \beta}{\cos \beta} \\ &= \frac{m \cdot \lambda}{d \cdot \cos \beta} \end{aligned} \quad (4.18)$$

In the last step the grating equation was used. The introduced angular dispersion is obtained by differentiating the grating equation with respect to  $\lambda$  (holding the incident angle  $\alpha$  fixed):

$$\frac{d\beta}{d\lambda} = \frac{m}{d \cdot \cos \beta} \quad (4.19)$$

Comparing the last two equations shows the relation between angular dispersion and pulse front tilt:

$$\tan \gamma'' = \lambda \frac{d\beta}{d\lambda} \quad (4.20)$$

The introduced pulse front tilt depends only on the wavelength and the angular dispersion, not on any grating specific properties. Thus Eq. 4.16 might also apply for other spectral devices, which introduce angular dispersion. In Fact, angular dispersion always results in pulse front tilt, no matter how it is created [95]. Since a femtosecond pulse contains a broad spectral range, the above consideration can be generalized by summing over its components.

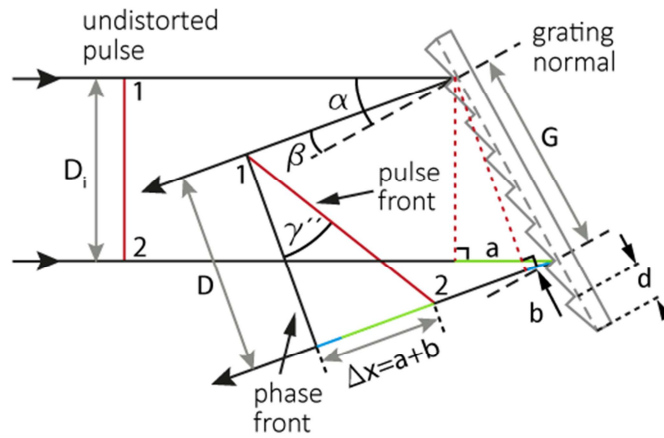


**Figure 4.4:** Pulse front tilt introduced by a grating. The phase and the intensity fronts are parallel to each other on the input. Upon diffraction, the side of the beam marked with 2 propagates an additional path  $a+b$ , this results in a tilt angle  $\gamma''$  between the intensity and phase front of the pulse at the output. The path difference and hence the pulse front tilt is determined by the grating orientation and the diffraction angle  $\beta$ .

### Change of the pulse front tilt by the imaging system

The grating introduced angular dispersion gives rise to group-velocity dispersion and consequently, the pulse duration is stretched temporally. Therefore the pump intensity decreases as the pulse moves away from the grating [95]. Upon diffraction off the grating, the spectrum of the femtosecond pulse is spatially dispersed. Thus an imaging system is used to overlap the different wavelengths spatially in the image plane, which is set to be close to the entrance surface of the generation crystal to reconstruct the short pulse duration before diffraction. Furthermore, the tilt angle can be modified by a proper choice of the demagnification factor  $M$  of the lens system in order to achieve the desired pulse front tilt in the image plane. Demagnification changes the pump beam diameter, while the delay  $a+b$  remains unchanged and thus the tilt angle in the image plane is modified according to:

$$\tan \gamma' = \frac{M(a+b)}{D} = \tan \gamma'' \cdot M \quad (4.21)$$

In the THz setup used in the experiments presented in this work a 2:1 telescope ( $f_1=150\text{mm}$ ,  $f_2=75\text{mm}$ ) was used. The increase of the tilt angle introduced by a demagnification of 2 of the lenses is depicted in **Figure 4.4a**. In addition due to the 4f configuration of the imaging system the tilt in the image plane is reversed.

### Change of the pulse front tilt at the free-space/generation crystal interface

Finally, the tilt angle of the pump pulse is changed again upon entry into the crystal because of the change in the refractive index. The higher group index  $n_{NIR}^g$  of the crystal leads to a shortening along the  $\Delta x$  direction, since the velocity of light is decreased in the medium, and the final tilt angle  $\gamma$  is changed according to:

$$\tan \gamma = \frac{M(a+b)}{n_{NIR}^g D} = \frac{\tan \gamma'}{n_{NIR}^g} \quad (4.22)$$

Using Eq. 4.18 and 4.17 the final tilt can be written as:

$$\tan \gamma = \frac{Mm\lambda}{n_{NIR}^g d \cos \beta} \quad (4.23)$$

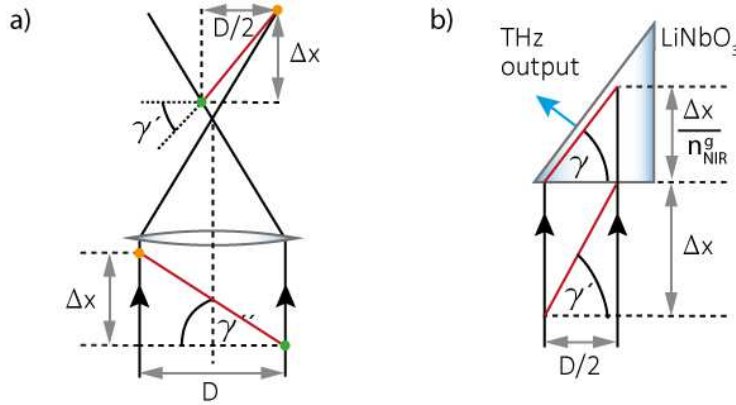


**Figure 4.5:** Change of the tilt angle **a)** Imaging system: The pulse front tilt angle is increased due the demagnification (2 in this case) of the beam in the transverse direction by the imaging system. **b)** Entrance into LN: When the pump beam enters the crystal, the tilt angle is decreased, owing to the higher group index  $n_{NIR}^g$  of the crystal material.

## Experimental implementation

Besides the tilt angle  $\gamma$  of the pump intensity front inside the crystal other requirements must be fulfilled for optimal conversion efficiency and optimal THz beam characteristics. The pump-pulse duration (which varies due to the introduced dispersion) should be minimal across the tilted pulse front and the pulse front should be planar [96]. The first condition entails that the tilt angle  $\theta$  of the grating image inside the crystal coincides with the tilted pulse front  $\gamma$  over the complete pump beam cross section. The tilt angle  $\theta$  of the grating image inside the crystal is described by [97] :

$$\tan \theta = n_{NR} M_2 \tan \beta, \quad (4.24)$$

where  $M_2$  is the horizontal magnification factor of the imaging system for the grating image. Further, the LN crystal should be cut at the same angle  $\gamma$ , so that the generated THz radiation is coming out perpendicular to the output face, and hereby reducing Fresnel losses. For efficient THz generation typical parameters are:  $\gamma = 63^\circ$ ,  $m=1$ ,  $M = 2$ ,  $\lambda = 800$  nm and a grating with a line spacing of  $d=500$  nm (2000 l/mm), which are the same parameters as used in the tilted pulse font set-up for THz generation in this thesis. For this values the grating orientation and diffraction angle are  $\alpha = 66^\circ$  and  $\beta = 44^\circ$ . This configuration is advantageous, as it is close to the Littrow configuration where diffracted beam goes along the same path as the incident beam and the grating efficiency is usually maximal at this configuration geometry [98].

It should also be mentioned that LN has a large bandgap, permitting only three-photon absorption at a pump wavelength of 800 nm. This allows high pump intensities, which is essential for the generation of high-energy THz pulses.

### 4.2.2 Organic crystals for THz generation

Owing to their high second-order nonlinear susceptibility (Table 4.1), organic crystals have gained tremendous interest as THz generators. Recently high field THz generation in several organic crystal like OH1 (2-(3-(4-Hydroxystyryl)-5,5-dimethylcyclohex-2-edylidene) malonitrile), DSTMS (4-N,N-dimethylamino-4'-N'-methyl-stilbazolium 2,4,6-trimethylbenzenesulfonate) and DAST (4-N,N-dimethylamino-4'-N'-methyl-stilbazolium tosylate) have been demonstrated [90,99]. The velocity phase matching condition is met in collinear propagating geometry and therefore a titled pulse front scheme is not necessary. However, the phase matching condition is best met when the pump beam wavelength is in the range from 1400 nm to 1700 nm (rather than the usual 800 nm wavelength which is obtained

from Ti-sapphire laser systems) [91]. The absorption of the pump light in the DSTMS crystal is reduced in this wavelength region, leading to increased damage threshold which enables higher pump fluences and hence higher conversion efficiency. However, this requires conversion of Ti:sapphire NIR pulses to the longer wavelengths through an Optical Parametric Amplifier (OPA). Therefore, this method of THz generation is beneficial only with amplifier systems delivering at least 5 mJ pulses, since efficiency of the OPA can be safely assumed to be ~25% [100,101]. In addition, the growth of single crystals of these organic materials is still in a nascent stage and the process is expensive. For this reason, the field of THz generation from organic crystals is still in a developmental stage.

The single-cycle THz pulses emitted from organic crystals have a frequency spectrum centered at higher frequencies than LN. For comparison, THz from LN is in the spectral range from 0.1 to 1.5 THz, while DSTMS is in the range from 1-4 THz. The presence of higher frequencies implies a steeper ramp for streaking measurements resulting in an improved time resolution, hence opening new avenues for photoelectron streaking at FELs. For these reasons, depending on the requirements of time resolution, both LN and DSTMS were used for different experiments presented in this thesis.

### **4.3 Terahertz pulse detection – Electro-optic sampling**

Characterization of the generated THz pulses requires a detection scheme with a response that matches their broad bandwidth. The most well established method for this purpose is free-space electro-optical sampling (EOS) [102]. EOS relies on the linear electro-optical effect, also known as Pockels-effect [103]. Here, refractive index changes are induced in a material by an applied electric field, resulting in phase retardation of probe light transiting through the medium. This results in a change of the polarization state of a probe beam co-propagating with the THz in a crystal. Since the effect is linear to the applied field, it is a direct measure of the THz electric field strength. A brief description of this technique utilized in characterizing THz pulses generated by optical rectification is described in this section. An explanation on the relation between the induced refractive index changes by the THz field transient  $E_{\text{THz}}$  is described in detail in Ref. [104], however here I just state the relations without going into details. Further, Einstein convention of summing over repeated indices (corresponding to x,y,z directions) is used in representing the tensor products.

The essence of EO sampling is captured through a simplistic assumption of an anisotropic medium with two principle optical directions (the third axis neglected for clarity). The induced polarization  $\mathbf{P}$  depends on the direction of polarization and

propagation of the electric field  $\mathbf{E}$  with respect to the principle axes. In this case, the electric displacement vector  $\mathbf{D}$  is not necessarily parallel to the electric field  $\mathbf{E}$  and is given by:

$$D_i = \varepsilon_0 \varepsilon_{ij} E_j \quad (4.25)$$

where the dielectric permittivity  $\varepsilon_{ij} = 1 + \chi_{ij}$  is a two dimensional tensor and  $\varepsilon_0$  the dielectric constant. When the diagonalized susceptibility  $\chi_{ij}$  has unequal eigenvalues, it indicates that the material exhibits birefringence due to different refractive indices along the different axis of anisotropy. The polarization parallel and perpendicular to the axis of anisotropy are termed as extraordinary and ordinary polarization.

A precise description of the  $\chi_{ijk}^{(2)}$  nonlinearity in any crystal could be formulated by considering a second rank tensor theory in three dimensions. Here, the polarization is created by the THz field through the  $\chi_{ijk}^{(2)}$  nonlinearity as:

$$P_{i,THz}^{(2)}(\omega_2) = 2\chi_{ijk}^{(2)}(\Omega = \omega_1 - \omega_2; \omega_1, -\omega_2) E_j(\omega_1) E_k^*(\Omega) . \quad (4.26)$$

Eq. 4.26 is the analog of the  $\chi_{ijk}^{(2)}$  nonlinearity which is responsible for difference frequency mixing and THz generation through optical rectification as elucidated in THz generation chapter. The difference being that here  $P_{THz}^{(2)}$  is generated through  $E_{THz}$  while in the former case,  $E_{THz}$  was generated through a source  $P^{(2)}$  generated from NIR pump beam. The EOS technique is simply the inverse of THz generation process made possible by the same  $\chi_{ijk}^{(2)}$  nonlinearity. Under the assumption that the THz field is slowly varying, i.e  $\Omega=0$ , the THz field induced refractive-index changes in an electro-optic material at visible-near-IR (NIR), could therefore be written as [104]:

$$n^2 = (n_0 + \Delta n)^2 = \varepsilon = 1 + \chi + \chi^{(2)} E = n_0^2 + \chi_{ik}^{(2)} E_{k,THz} \quad (4.27)$$

When the induced refractive index changes are small (i.e when  $\Delta n_0^2$  could be neglected), the induced refractive index changes are linearly proportional to  $E_{THz}$  Eq. 4.27. EOS technique thus provides for an amplitude and phase sensitive detection of the THz field in time domain by delaying the THz pulse with respect to the NIR pulse. This change in refractive index is measured through the polarization change or the induced birefringence. A schematic of EOS technique through balanced detection scheme is shown in **Figure 3.1**. The linearly polarized NIR probe pulse, which is used as the electro-optic sampling beam, is delayed with respect to the THz pulse with an optical delay stage. Without the THz field, the axis of a  $\lambda/4$  waveplate is set to  $45^\circ$  with the axis of polarization of the incident wave, resulting in a circularly polarized beam. The circularly polarized light when passing through the Wollaston prism is split into two purely s and p-polarized components. The difference signal of these two polarization states are recorded with two diodes  $I_A$  and  $I_B$ . Ideally, for a circular polarized light, the difference signal is zero. The THz field induced polarization change of the

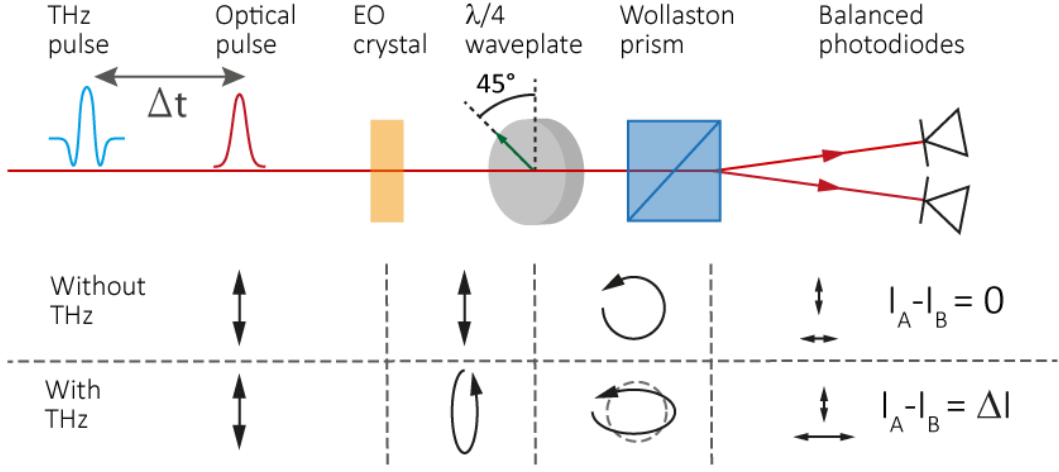


**Figure 4.6:** A linearly polarized optical sampling pulse and the THz pulse are overlapped in a EO crystal like ZnTe or GaP. The THz induced polarization of the optical pulse is measured through balanced detection scheme involving a  $\lambda/4$  waveplate and Wollaston prism. The table below indicates the polarization state of the optical pulse after every optical component with and without the THz field. Without the presence of THz field, the axis of the  $\lambda/4$  waveplate is set  $45^\circ$  with the axis of polarization of the incident wave, resulting in a circularly polarized beam. The circularly polarized light when passing through the Wollaston prism is split into two purely  $s$  and  $p$ -polarized components and the difference signal of these are recorded with two diodes. Ideally, for a circular polarized light, the difference signal is zero. The THz field induced polarization change of the NIR pulse is measured as a deviation in the ellipticity from this circular polarization state.

NIR beam is measured as a deviation in the ellipticity from this circular polarization state. This scheme is referred to as balanced detection and has the advantage that it is insensitive to laser noise. Unlike single shot measurements, the described EOS technique relies on averaging over several shots. Hence the noise level is determined by the stability and the repetition rate of the optical laser.

For the sake of completeness, I briefly summarize the mathematical dependences of induced birefringence; however the readers are referred to Ref. 104 for detailed derivations. Eq. 4.25 could be rewritten as:

$$E_i = \epsilon_0 \eta_{ij} D_j \quad (4.28)$$

where  $\eta_{ij}$  is related to the electro-optic coefficient tensor  $r_{ijk}$  by:

$$\eta_{ij} = r_{ijk} E_{k,THz}(\Omega) \quad (4.29)$$

As  $\eta_{ij}$  is a real symmetric tensor, 6 independent variables are enough for representing  $\eta_{ij}$  and hence 18 for  $r_{ijk}$ . The  $E_{THz}$  induced change in refractive index could then be derived to depend on the electro-optic coefficient as:

$$\frac{1}{\Delta n_h^2} = r_{hk} E_{k,THz} \quad (4.30)$$

where  $h$  runs from 1 to 6 and the phase retardation or the induced birefringence  $\Gamma$  is related to  $E_{THz}$  as:

$$\Gamma \propto r_{hk} E_{k,THz} L n_{NIR} \frac{1}{\lambda} \quad (4.31)$$

where  $r_{hk}$  is the linear electro-optic coefficient, whose values are material dependent and  $L$  is the thickness of the crystal. The phase retardation also depends on the orientation of the crystal and the direction of polarization of the THz and the probe beam radiation [105]. ZnTe and GaP crystal are most commonly used for EOS. Due to crystal symmetry, the only nonzero component in the electro-optic coefficient tensor is  $r_{41}$ . The linear electro-optic coefficients and other important parameters for ZnTe and GaP are listed in **Table 4.2**. Usually, any crystal producing THz radiation through optical rectification could be used for characterizing a THz field of similar frequency range through the EO sampling technique since the condition of velocity phase matching is satisfied. The resolution of this technique is limited by the absorption of the THz radiation in the EO crystal, which is set by the frequency of the transverse-optical lattice vibrations, which for instance occur at 5.3 THz for ZnTe and 11 THz for GaP [81]. Hence, different crystals are necessary for characterizing THz radiation with different bandwidths. For best time resolution and, thus, for a broad frequency bandwidth detection, the sampling pulse duration must be shorter than the inverse bandwidth of the THz pulse. Furthermore, since the birefringence depends on  $E_{THz}$  an absolute value for the THz field can be determined using EOS technique. From the modulation of the balanced photodiode signals  $I_A$  and  $I_B$  in the EO detection, the THz peak field can be calculated as [84]:

$$\frac{I_A - I_B}{I_A + I_B} = \sin \Gamma = \frac{2\pi}{\lambda} n_{NIR}^3 n_{THz} r_{41} E_{THz} L t, \quad (4.32)$$

where  $t$  is the Fresnel coefficient, which is required to take into account the optical losses at the crystal-air interface.

Several factors could lead to artifacts including pulse broadening and distortions in the measured pulse. One problem that is commonly encountered is called over-rotation. When dealing with strong  $E_{THz}$  fields, like the ones presented in this thesis, the measured trace has an awkward shape when the induced birefringence exceeds  $2\pi$ . This could be alleviated by choosing thin crystals with small electro-optic coefficient. However, for thinner crystals, a second replica of the THz field is observed in the EOS trace due to the interaction of the  $E_{THz}$  with the NIR probe reflected from the back side of the crystal. Furthermore, frequency dependence of the electro-optic coefficient contributes to pulse broadening and

distortions. The effects of over-rotation and replicas can be alleviated by using a piece of EO crystal with a thin active layer, (0.2 mm) glued in front of a 1 mm piece of inactive cut of the same crystal to enable a longer scan without observing replica artefacts.

**Table 4.2:** Some material constants for ZnTe and GaP according to Ref [106] .

<b>Material</b>	<b>Crystal structure</b>	<b>Electrooptic coefficient (pm/V)</b>	<b>Surface orientation</b>	<b>LowestTO-phonon (THz)</b>
ZnTe	Zincblende	$r_{41}=3.90$	110	5.3
GaP	Zincblende	$r_{41}=0.97$	110	11



## 5 Proof of principle of laser-based THz streaking at the FEL facility FLASH

The Free Electron Laser in Hamburg (FLASH) is the first vacuum-ultraviolet and soft X-ray FEL facility and is available for user experiments since 2005. Since then a great number of experiments in various disciplines of natural sciences have been successfully performed. However, complete temporal characterization of the delivered X-ray pulses that differ from shot-to-shot, was lacking. The THz streaking technique described in Chapter 3 was successfully applied to measure the FEL photon pulses in the time domain at FLASH. The measurements, results and figures presented here have been published in Ref [52].

This chapter starts with a short overview of the FLASH facility. In Sec. 5.2 the experimental implementation and results will be described. Some important aspects of the measurements will be discussed in Sec. 5.3.

### 5.1 FLASH – soft X-ray facility

The stringent constraints on the electron beam quality, namely high peak current, low emittance, small energy spread and short bunch lengths, which are required to achieve FEL amplification can only be provided by a linear accelerator. The FLASH facility is equipped with a linear accelerator, which operates as a single pass high gain SASE FEL. The machine layout of the FLASH facility is shown in **Figure 5.1**. The electron bunches are produced by a laser-driven photocathode which is mounted in a radio-frequency (RF) cavity (electron gun). Typically the bunch charge is on the order of 0.1 nC to 5 nC. The high peak current required for FEL emission cannot be produced immediately in the laser gun as Coulomb forces would lead to a significant deterioration of the electron bunches. However at relativistic energies the repulsive forces between the electrons in the bunch are largely canceled by attractive magnetic forces. Thus, the electron bunches with a modest current of  $\sim 30$  A (generated by 10 ps UV-laser pulses) are quickly accelerated to relativistic energies. With 7 accelerating modules, each consisting of eight superconducting cavity arrays with a

resonance frequency of 1.3 GHz, the bunches are accelerated up to 1.25 GeV. To reach the high peak current for the FEL amplification process the initially long electron bunches are compressed longitudinally in two magnetic chicane bunch compressors to achieve a peak current of several kA. The VUV- and soft X-ray FEL radiation is produced in a 27 m long fixed-gap planar undulator via SASE. The undulator consists of six undulator segments with an undulator period  $\lambda_u$  of 27.3 mm and an on-axis peak magnetic field of 0.47 T. In between the undulator segments, quadrupoles for beam focusing are installed to assure overlap between the electron beam and the photon beam. To ensure stable operation of the FEL process various electron and photon diagnostic and control tools are installed. The complete machine is approximately 315 m long.

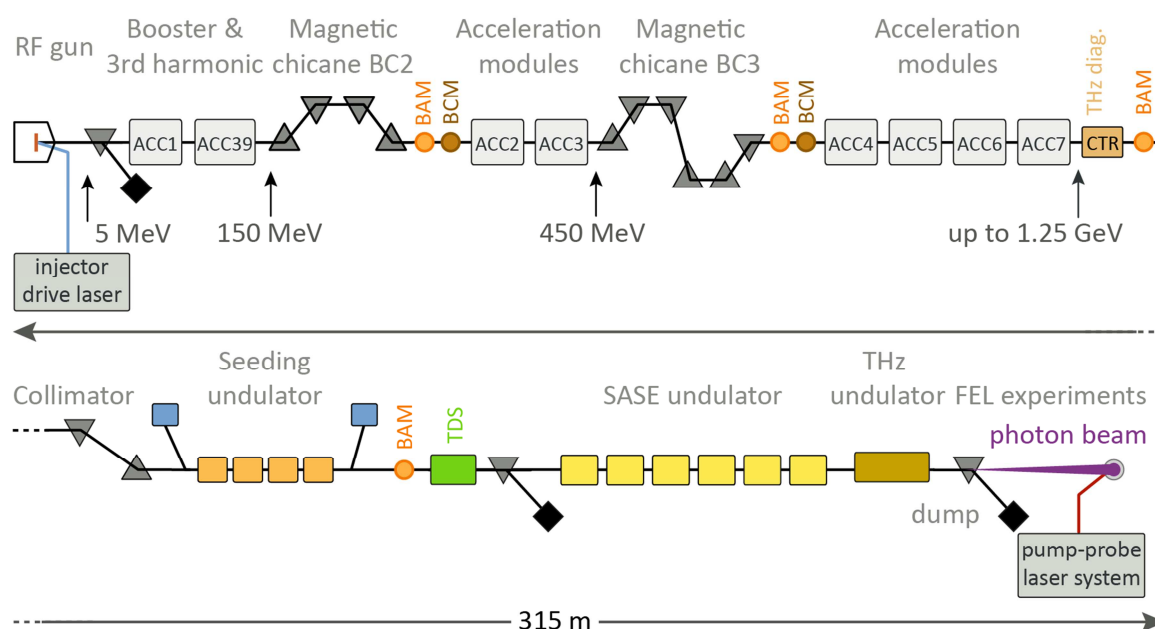


**Figure 5.1:** Schematic of the FLASH machine layout. The laser-driven photo-injector gun produces electron bunches, which are subsequently accelerated to energies up to 1,2 GeV in seven superconducting accelerating structures (ACC). At intermediate energies of 150 MeV and 450 MeV the electron bunches are compressed longitudinally in two magnetic chicanes BC1 and BC2. In a 27 m long fixed-gap undulator modules the FEL SASE pulses are generated. The FEL photon beam is transported over a distance of 60 m to the experimental hall. The complete machine is roughly 315 m long. Some electron beam diagnostic tools are indicated schematically in the sketch. The second undulator FLASH2, which is currently under construction, is not shown (Courtesy Sebastian Schulz).

The advantage of superconducting cavities is their very low surface resistance resulting in RF power dissipation of several orders of magnitude lower than in normal copper cavities. Although in principal superconducting cavities allow for continuous wave operation at a reduced field gradient, a pulsed operation mode was chosen at FLASH [107]. In this scheme the resonator cavities are loaded with RF pulses with a flat top of 800  $\mu$ s at 10 Hz. This facilitates the acceleration of macro bunches at 10 Hz, consisting of up to 800 bunches with an intra-bunch repetition rate of 1 MHz. The cavities are operated in pulsed mode to keep the cryogenic load at a reasonable value [108]. A detailed description can be found in Ref. [33,15].

**Table 5.1** summarizes some FEL pulse parameters for FLASH in 2012. The values for the pulse duration are estimates. However, precise information of the pulse duration and temporal structure are necessary in order to determine the peak power of the optical pulse. Consequently, parameters derived through the pulse duration like peak power and peak brilliance are only estimates. Furthermore, due to the stochastic nature of the SASE process most of the FEL pulse properties, including spectral distribution, intensity and temporal profile, fluctuate from shot to shot. Pulse parameters, which are critical for the correct interpretation of experiments, need to be characterized on a single shot basis.

Up to now, for user experiments no precise information of the temporal characteristics of the delivered FEL photon pulses, including pulse structure and arrival time is available on a single-shot basis. One method to characterize the FEL pulses is photoelectron streaking spectroscopy. This pulse characterization technique could be implemented in parallel with the user experiments since it is non-evasive and does not require high pulse energies.

**Table 5.1:** FLASH photon beam properties<sup>[109]</sup>

Parameter	Value
Wavelength range fundamental	4.2 - 45 nm
Average single pulse energy	10 – 500 $\mu$ J
Pulse duration (FWHM)	< 50 – 200 fs (estimated)
Peak power	1 – 3 GW
Peak brilliance	$10^{29}$ - $10^{31}$ photons/s/mrad <sup>2</sup> /mm <sup>2</sup> /0.1%bw
Spectral width (FWHM)	0.7 – 2 %

## 5.2 First experimental implementation & results

### 5.2.1 Experimental set-up

The experimental layout of the streaking set-up at FLASH is shown in **Figure 5.2**. A  $\sim 3$  mJ,  $\sim 50$  fs Ti:sapphire near-infrared (NIR) laser pulse is split into two parts by a dielectric beam splitter (99% reflection and 1% transmission). The reflected part is used for THz generation, while the transmitted is used for EOS characterization of the THz pulses. The THz is generated by optical rectification in LiNbO<sub>3</sub> using the tilted pulse front technique. In the THz generation set-up, a diffraction grating with a density of 2000 grooves/mm, a 2:1 telescope and a stoichiometric lithium niobate (sLN) crystal doped with 0.6 mol % MgO were used as described in chapter 4.

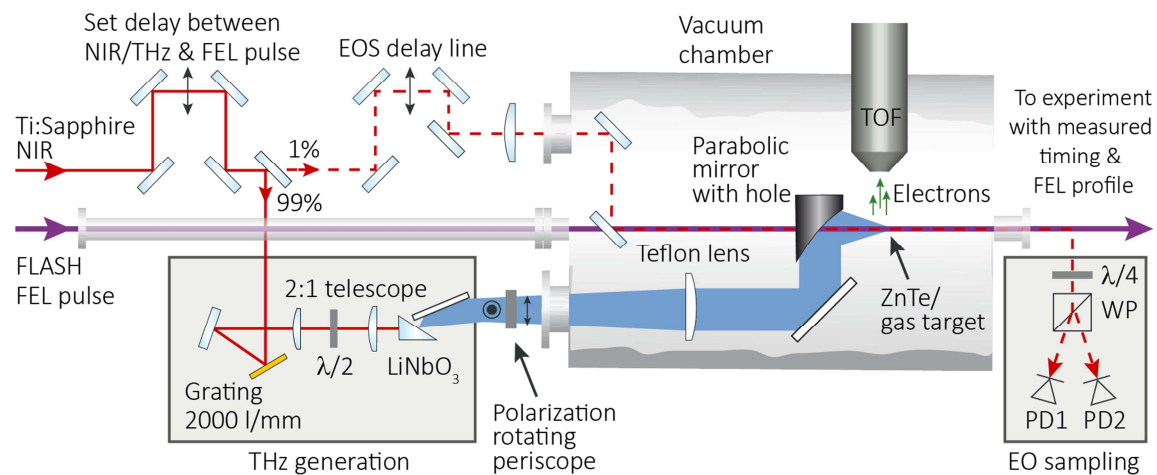


**Figure 5.2:** Layout of the THz streaking experimental set-up used at FLASH: The NIR laser pulse is split into two parts. Most of the pulse energy is used for the tilted pulse-front THz generation in LiNbO<sub>3</sub>, in set-up geometry as shown. The remaining 1% pulse energy is used as a probe for electro-optic sampling (EOS) of the THz pulses in a 500  $\mu\text{m}$  thick zinc telluride (ZnTe) crystal. The NIR probe pulse and the FEL pulse pass through a 2 mm hole in the parabolic mirror and are collinearly overlapped with the THz beam and focused into the interaction region, which is fixed by the position of the time-of-flight (TOF) spectrometer. For the EO-sampling a ZnTe crystal is placed in the exact interaction region. The crystal is also used as an observation screen for monitoring the spatial overlap of the FEL and the NIR probe pulses. For the streaking measurement a gas nozzle providing neon or helium is placed in the interaction region. The FEL pulses eject a burst of photoelectrons from the atomic gas system and the kinetic energy of the photoelectrons is modified by the THz pulse. Recording the photoelectron spectrum with the TOF spectrometer consequently enables characterization of the FEL pulse.

The THz pulse energy directly after the sLN crystal was  $\sim 4 \mu\text{J}$ , measured with a calibrated pyroelectric detector from Microtech Instruments. The polarization of the outgoing THz pulse was rotated by 90 degrees, using a periscope, in order to be horizontal and parallel to the axis of the time-of-flight detector that was used to collect the photoelectrons. The THz beam was coupled into the vacuum chamber through a 7 mm thick polymer window. A 275 mm focal length Teflon lens was used to collimate the THz radiation and a 3-inch effective focal length, 90-degree off-axis parabolic mirror, was used to focus the THz in the interaction region, which is precisely defined by the position of the TOF spectrometer entrance aperture and the gas target position. The NIR probe beam and the FEL beam were passed through a 2mm hole in the parabolic mirror and collinearly overlapped with the THz beam. All three beams were adjusted to be spatially and temporally overlapped. For the coarse alignment of the THz beam and the NIR probe beam a MCT detector was placed at the interaction region, while fine alignment was achieved by the EOS measurement. The spatial overlap of the NIR and the XUV was adjusted by observing the fluorescence from a ZnTe (or Ce:YAG) crystal induced by the NIR and XUV pulses.

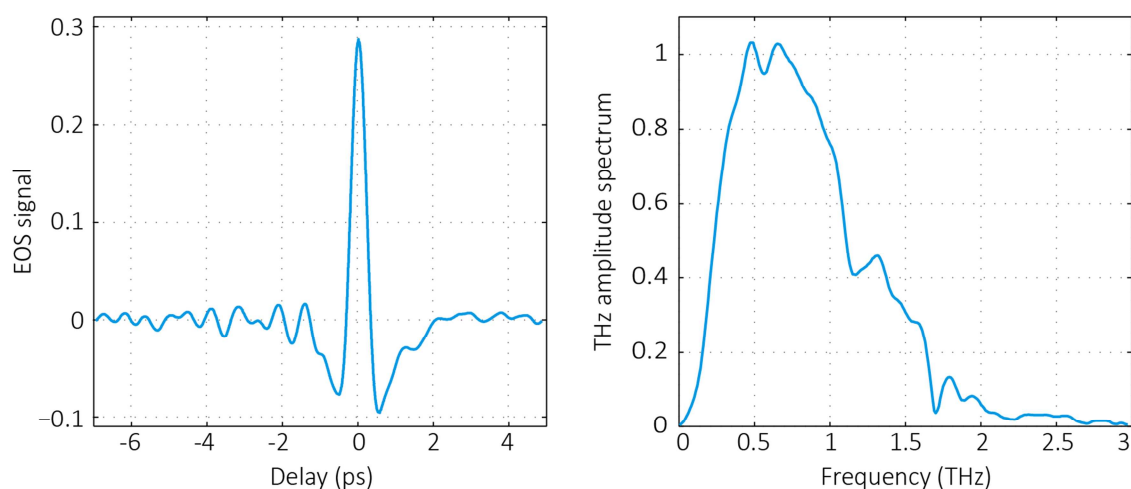


**Figure 5.3:** Electro optic sampling of the THz pulse used for the streaking experiments. The measurement was performed in a  $500 \mu\text{m}$  ZnTe crystal using balanced electro-optic detection. The single-cycle pulse is  $\sim 2$  ps in duration with a carrier frequency of  $\sim 0.6$  THz. Due to the low repetition rate of the pump-probe laser at FLASH (10 Hz) the EOS measurement suffers from a high noise level. Therefore, a high frequency filter was applied to the measured data. The oscillations for negative times arises from absorption and reemission of the THz by water vapor (corresponding to 1.7 THz), as during the beam time the EO sampling could only be performed in air. The THz amplitude spectrum, displayed on the right panel, is calculated by a numerical Fast Fourier Transformation (FFT) from the measured THz waveform.

The temporal shape of the THz pulse at the interaction region was characterized by EOS in a 500  $\mu\text{m}$  thick ZnTe crystal, which was mounted on a manipulator arm. The measured THz waveform is shown in **Figure 5.3**, it consists of a  $\sim 2$  ps long single-cycle, with a central frequency at  $\sim 0.6$  THz. The oscillations at negative time delays in the measured THz electric field originate from THz absorption and re-radiation by water vapor, as the EO measurement was performed in atmospheric ambience.

For the streaking measurement a 100  $\mu\text{m}$  gas nozzle, mounted on a xyz-manipulator, providing the gas target for the photoemission could be placed in the interaction region. Gas streaming with a continuous flow rate was introduced into the experimental chamber and the background pressure was adjusted to be  $\sim 3 \times 10^{-6}$  mbar (for helium). This value was chosen based on the signal level of the measured TOF trace and was kept constant during the streaking measurement. If the electron number that built up the signal is too low, the measured signal will be dominated by statistical fluctuations of the discrete electron counts. On the other hand, space charge effects could deteriorate the measurement if the number of electrons is too high. Typically, the number of electrons in the TOF traces is about 50-500 electrons. Furthermore, the background pressure in the experimental chamber is determined by the vacuum conditions for the MCP detector and the entire FEL beamline.

The distance between the tip of the gas nozzle and the XUV beam should be minimized to reduce the interaction length between the gas and the XUV, which in turn decreases the influence of the Gouy phase shift. This shift, results in a phase change between the THz streaking wave and the envelope of the XUV pulse while passing the interaction region, leading to additional broadening of the acquired spectra (in Section 5.3.3 this effect is explained in more detail). It should be noted that the nozzle tip cannot be moved arbitrarily close to the THz beam, as this could lead to a locally enhanced THz-field.

Field free 2p (21.6 eV, the splitting of 0.1 eV due to spin-orbit coupling can be neglected) and 2s (48.5 eV) photoemission peaks from neon (Ne) were used to calibrate the TOF spectrometer. Helium was used (24.6 eV) in the pulse characterization measurements, due to its isolated photoemission line, leading to a clean streaked photoelectron spectrum. This avoids the possibility of photoelectrons from different binding energies to overlap with each other when they are streaked. Soft X-ray FEL pulses with approximately 10  $\mu\text{J}$  pulse energy at 4.8 nm (258 eV photon energy) with an independently measured bandwidth of  $\sim 2.5$  eV full-width-maximum (FWHM) [110] were used to generate the He 1s electrons with an initial kinetic energy of  $\sim 233$  eV.

The THz pulses were polarized along the direction of detection (which is horizontal), such that the streaking effect directly coupled to the observed photoelectron kinetic energy.

The FEL pulses are also polarized along the observation direction; this is beneficial as the photoelectron emission probability along the direction of the FEL polarization is increased.

Coarse temporal overlap between the NIR probe pulse (thus THz pulse) and the FEL pulse was achieved with a fast photodiode. Precise temporal overlap was then established by monitoring the changes in the photoelectron spectrum induced by the THz streaking field, as a function of time delay between the THz pulse and the FEL. The NIR pulse generating the THz streaking pulse and the FEL pulse were synchronized electronically to a common radiofrequency (RF) distribution network at the accelerator facility to with  $\sim 100$  fs r.m.s. precision, which is significantly shorter than the streaking field half cycle of  $\sim 600$  fs. As a result, once the timing between the FEL pulse and the THz pulse is established, all single-shot acquisitions occur on a uniquely defined, nearly linear portion of the streaking ramp. The recorded data gives access to the temporal shape and arrival time of the FEL pulses on a single-shot basis.

### 5.2.2 Energy to time conversion

The possibility to characterize the THz pulse independently (by EOS) of the streaking measurement is one of the most important aspects of our technique, as knowledge of the precise streaking pulse properties is a strict requirement for a unique calibration of the streaked spectra from kinetic energy to time.

For the measurements presented here, we can assume a constant transverse streaking beam intensity over the focus of the ionizing FEL pulse, since the THz focal spot size is on the order of  $\sim 1$  mm and is much larger than the NIR and the XUV pulse focal spot size ( $\sim 50$   $\mu\text{m}$ ). However, owing to the broadband nature of the single-cycle THz pulse and the frequency-dependent focusing, it is expected that the spectral content varies across the transversal beam profile, resulting in different field strengths and temporal shapes of the THz streaking pulse across the transverse dimension of the THz focus. Sampling a different spot in the transverse dimension may result in a discrepancy between the EO detected and the actual streaking field. Therefore, it is of crucial importance to establish precise overlap between the NIR and the XUV and to maintain during the experiment. Along the longitudinal dimension differences can arise from a phase shift acquired by the THz beam while propagating through the focus, i.e. the Gouy phase shift.

The electric field strength can be determined from the peak modulation of the EO signal. Using our experimental parameters a peak electric field of  $\sim 12$  kV/cm is calculated. Yet, several factors may lead to an underestimation of the field strength. The measured THz signal is a function of the angle between the THz polarization and the crystal (100) axis as

well as between the THz polarization and the probe beam polarization, where both have to be optimized to determine the maximum signal [111].

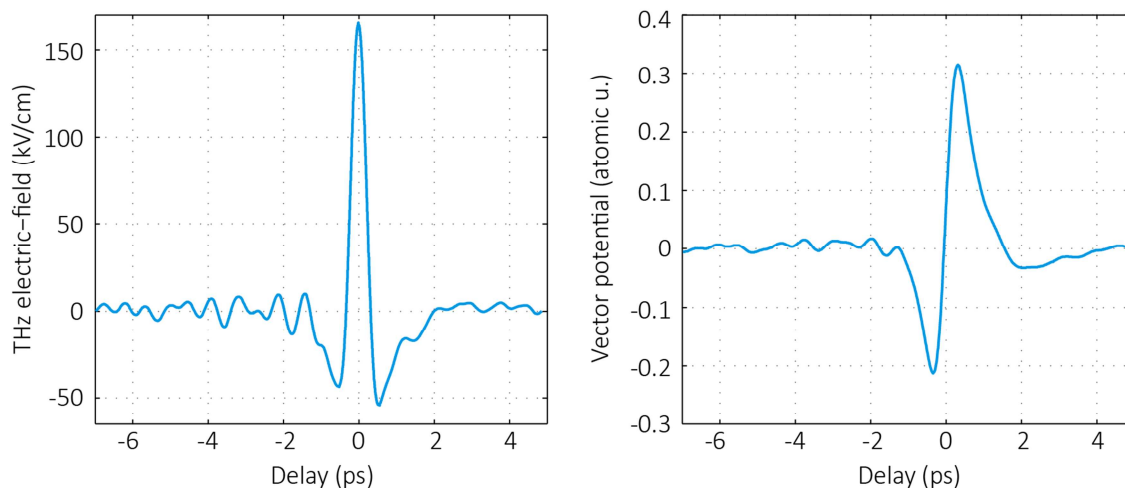


**Figure 5.4:** The absolute THz electric field strength is 165 kV/cm and was calculated using the experimentally observed maximum shift of the single-shot spectra. Numerical cumulative integral of the EO sampled scaled electric field of the THz pulses yields the THz vector potential here displayed in atomic units.

During the beam time the crystal was positioned in a fixed, non-rotatable mount. Thus the crystal orientation could not be optimized, resulting in an underestimation of the THz field strength. Furthermore, impurities and defects in the EO crystal also lead to a reduced effective electro-optic coefficient and only an imperfect crystal was available for the measurements. Therefore the absolute electric field strength is determined independently by the single-shot photoelectron spectra that experience the maximal kinetic energy shift in the streaking spectrogram. In the measurement presented here (see **Figure 5.7**) the maximal up-shifted and down-shifted photoelectron spectra were found at 257 eV (+23 eV) and 197 eV (-37 eV). For this energy shift a peak THz electric field strength of 165 kV/cm is derived. In **Figure 5.4** the scaled THz electric field is depicted on the left panel and the corresponding vector potential, which is calculated numerically by cumulative integration, is plotted on the right.

With this vector potential the kinetic energy shift of the He 1s photoelectron peak is calculated over the full range of delays. The resulting streaking map, which gives the transformation from photoelectron spectrum to real temporal profile of the ionizing FEL pulse, is displayed in **Figure 5.5**. Direct transformation from photoelectron spectrum to temporal profile is possible, when the streaked photoelectron spectrum is considerably broader than the FEL bandwidth, as discussed in Chapter 3. The variable transformation from energy

to time requires a rescaling of the signal intensity, as the number of electrons in the time interval has to be the same as the number in the corresponding energy interval:

$$\int_{E_1}^{E_2} S_E(W) dE = \int_{t(W_1)}^{t(W_2)} S_t(t) dt \Rightarrow S_t(t) = S_E(W) \left| \frac{dW}{dt} \right|. \quad (5.1)$$

Thus each mapped pulse profile has to be multiplied with the scaling factor  $|dW/dt|$ . The rescaling factor is important, as we are interested in the shape of the FEL pulse.

Alternatively the peak field strength can be estimated from the pulse energy and the focal spot size according to:

$$E = \sqrt{\frac{2I}{c\epsilon_0}} \quad \text{with} \quad I = \frac{E_{pulse}}{A\tau}. \quad (5.2)$$

For  $\sim 2 \mu\text{J}$  pulse energy, a pulse duration of  $\sim 2$  ps and a beam diameter of  $\sim 2$  mm the corresponding field strength is  $\sim 155$  kV/cm, which is in good agreement with the field strength estimated from the shift. The spot size was not measured during the beam time, but is estimated from measurements that were performed in the laboratory with similar collimating and focusing optics.

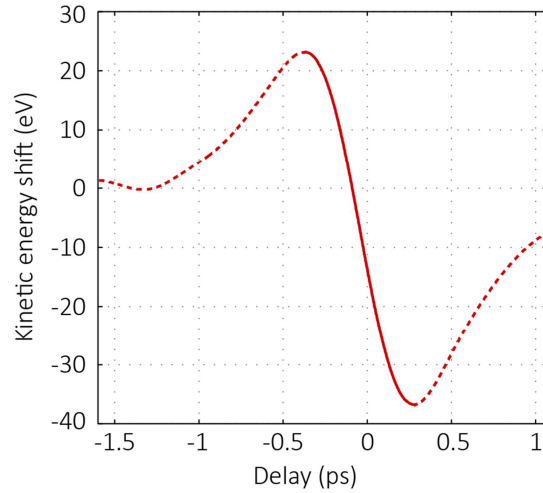


**Figure 5.5:** The graph shows the kinetic energy shift of the photoelectron peak calculated from the THz vector potential. The maximum shift is +23 eV/-37 eV corresponding to the maximally up- and downshift in the single-shot spectra. The asymmetry in the kinetic energy shift is a result of the asymmetry in the THz pulse shape. The red continuous line is the streaking map that provides the transformation from measured photoelectron kinetic energy to time.

### 5.2.3 Resolution of the measurements

As mentioned before, the streaking strength, or degree of broadening, in combination with the energy resolution of the photoelectron spectrometer mainly define the achievable temporal resolution in the streaking measurement.

The energy resolution of the photoelectron spectrometer can be determined by comparing the bandwidth of the average field-free photoelectron spectrum of the He 1s line to an independent measurement of the average FEL photon bandwidth. The unstreaked, field-free photoelectron spectrum is nearly Gaussian, as depicted in **Figure 5.6**, with a measured bandwidth of 7.2 eV FWHM, which is a convolution of the energy resolution and the FEL bandwidth. The independently measured FEL bandwidth is about 2.5 eV and with  $\sigma_{Res} = \sqrt{\sigma_{Measured}^2 - \sigma_{Bandwidth}^2}$  the photoelectron spectrometer energy resolution is found to be 6.8 eV.

The average THz streaking strength was  $s_{avg} \approx 60 \text{ eV}/600 \text{ fs} = 0.1 \text{ eV fs}^{-1}$ . Measurements that fall near the zero-crossing are transformed with the highest resolution, as the gradient of the streaking map at this point is steeper than the average of 0.1 eV/fs. The bandwidth of the field-free spectrum in conjunction with the THz streaking map is used to determine the minimum separation between two distinguishable features in the FEL pulse temporal profile. In these measurements the minimum separation is  $\sim 40 \text{ fs}$ .

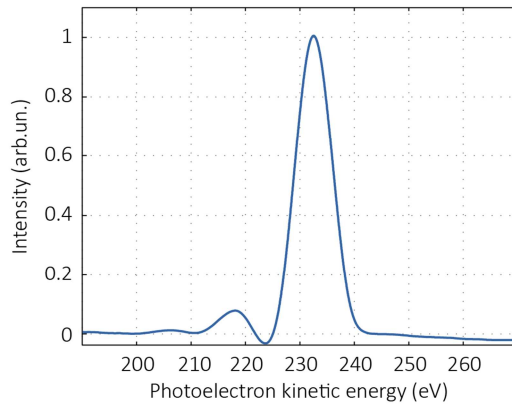


**Figure 5.6:** Average of 100 field-free photoelectron spectra of the He 1s, which were collected at negative time delays. The width of the field-free spectrum is about 7.2 eV. The measured photoelectron spectrum is a convolution of the bandwidth of the FEL pulse and the spectrometer resolution.

#### 5.2.4 Complete single-shot FEL temporal pulse characterization

In **Figure 5.7** a single shot and the corresponding averaged streaking spectrogram are shown. The delay between the THz and the soft X-ray pulses was scanned in 100 fs steps. Approximately 400 single-shot spectra were averaged at each time delay to generate the averaged spectrogram. For large delays, where the THz field is weak the He 1s photoemission peak is nearly unaffected and located near its field-free energy. Close to temporal overlap the kinetic energy of the photoelectrons is shifted and broadened depending on the THz streaking field phase. In the averaged spectrogram the single valued streaking ramp is indicated. As the streaking ramp of  $\sim 600$  fs is significantly longer than the maximum expected FEL pulse duration and timing jitter, once the streaking THz pulse and the FEL are temporally overlapped, all single-shot acquisitions will occur on a unequivocally defined position on the streaking ramp.

**Pulse structure:** In **Figure 5.8** characteristic streaking single-shot measurements are shown, taken from the scan depicted in **Figure 5.7**. On the left two different streaked single-shot spectra are depicted. The statistical error in the single-shot spectrum is calculated according to the number of electrons collected within the energy resolution window of the detector. As the photoelectron spectrum is heavily oversampled, boxcar integration is performed across the spectrum, resulting in a smooth error envelope that bounds the measured spectrum.

To determine the temporal FEL pulse profile, first the measured spectra were Fourier filtered to remove the high frequency noise. In the second step the energy resolution of the TOF spectrometer is deconvolved from the measured streaked photoelectron spectra, the resulting spectrum is shown in blue in **Figure 5.8**. The corresponding transformation of the measured and the deconvolved photoelectron spectra to time is shown in the panels on the right. In the temporal profile plots, positive time corresponds to the leading edge of the soft X-ray FEL pulse. The two mapped FEL pulses have a quite different structure. The pulse plotted in **b)** exhibits a dominant central feature with a width of  $53 \pm 5$  fs at FWHM and has weaker satellite features at approximately 100 fs from the main peak. While the other depicted FEL pulse consists of nearly equal peaks with individual durations of  $40 \pm 5$  fs separated by  $\sim 85$  fs. The accuracy of the measurement is determined from the upper and lower statistical error bounds on the streaked photoelectron spectrum. For this the number of the photoelectrons within the energy resolution window of the TOF spectrometer in the single-shot photoelectron spectrum is determined by boxcar integration, centered at each collected data point. As the spectra are heavily oversampled an error envelope is generated rather than discrete points with individual error bars.

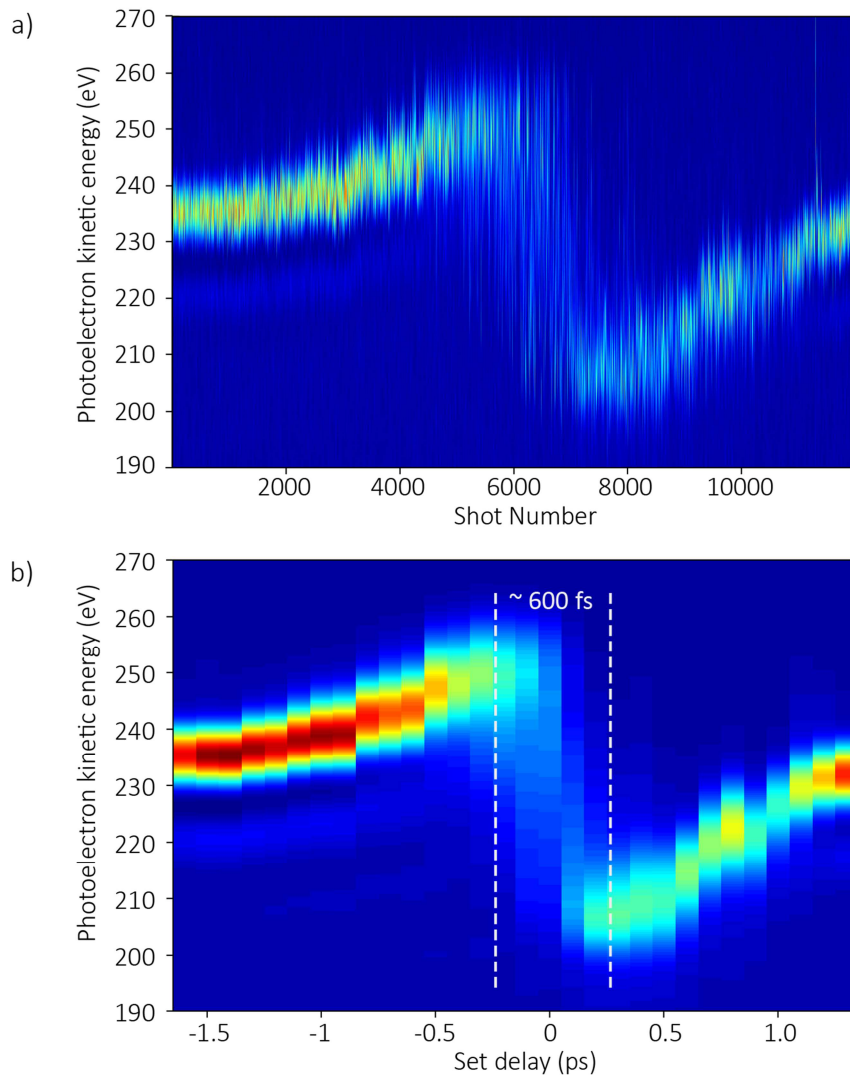


**Figure 5.7:** Streaking spectrogram measured with a time-of-flight spectrometer. Photoelectron spectra of He 1s as function of set delay between the THz streaking pulse and the ionizing FEL pulse at a wavelength of 4.8 nm (258 eV) are shown. Coarse synchronization between the FEL pulse and THz pulse was maintained electronically to  $\sim 100$  fs rms. **a)** Intensity plot for photoelectron spectra of  $\sim 12000$  consecutive shots, which were recorded as the time delay between the two pulses was changed in 100 fs steps. Far from temporal overlap the photoemission peak is not significantly shifted or broadened. Near time-zero where the streaking is strongest, the photoelectron spectra are shifted and broadened, allowing for temporal characterization. The timing jitter between the FEL and the THz pulse, or equivalently the NIR pump pulse that is used to generate the THz, manifests itself in a shifting photoemission peak from shot-to-shot, although the delay is changed continuously. **b)** Corresponding averaged streaking spectrogram. Each time slice is an average of  $\sim 400$  single-shot measurements. The streaking ramp of  $\sim 600$  fs is longer than the maximum expected FEL pulse duration and timing jitter.

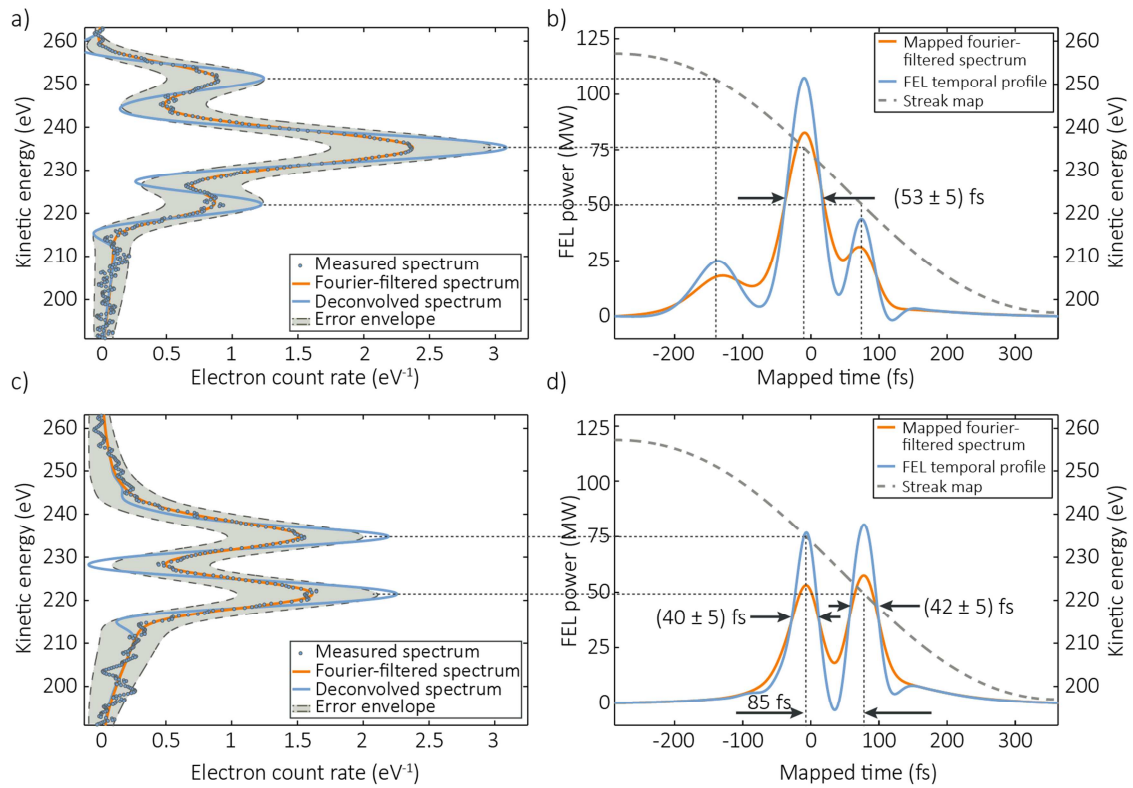


**Figure 5.8:** **a),c)** Two distinct single-shot streaked photoelectron spectra. The shaded error envelopes are calculated by boxcar integration, based on the number of electrons collected within the 6.8 eV FWHM resolution window of the time-of-flight spectrometer. The blue dots are raw data points in the measured streaked spectra. Orange curves show the spectra after Fourier filtering to remove high-frequency noise. Blue curves are filtered, streaked spectra following deconvolution of the photoelectron spectrometer resolution. **b),d)** Retrieved FEL pulse profiles on the pump-probe laser time base using the single-valued streaking ramp. Scales on the right correspond to the streaking map; scales on the left correspond to the FEL power that is obtained by assuming pulse energy of 10  $\mu$ J for the single-shot measurement shown in **a**. A  $53 \pm 5$  fs FWHM substructure is observed in the first single-shot measurement and a  $\sim 40 \pm 5$  fs FWHM substructure in the second.

The spectrometer energy resolution is deconvolved from the upper and lower bounds of the error envelopes. Mapping the deconvolved error envelopes to time provides an upper and lower bound for the pulse temporal profile. As displayed in **Figure 5.9** for the central feature of **Figure 5.8b** the upper bound was found to be 59 fs and the lower 48 fs FWHM. Based on this analysis we concluded that the temporal profile was measured with an accuracy of  $\pm 5$  fs. For the measurements a single-shot pulse energy measurement was not available, thus the average pulse energy of 10  $\mu$ J was used to calculate the FEL pulse power profile.

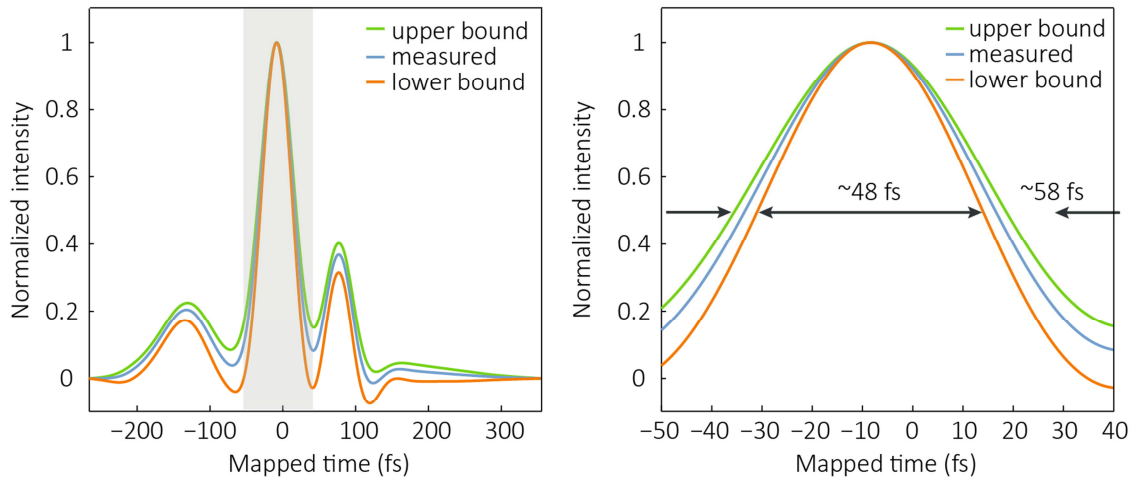


**Figure 5.9:** The spectrometer energy resolution is deconvolved from the measured spectrum and from the upper and lower bounds of the error-envelope that was determined statistically. Following deconvolution the spectra are mapped to time, the resulting curves are plotted in the left panel. The mapped upper and lower bound provide and measure for the accuracy of the pulse time profile measurement. On the right side a close-up of the central peak is shown. The measured peak has a width of 53 fs, the upper bound is 58 fs and the lower bound is 48 fs wide at FWHM. From this the measurement accuracy is found to be  $\pm 5$  fs FWHM.

Comparison of the two individual pulses demonstrates the importance of measuring the delivered FEL pulses on a single shot basis. While the pulse energy is comparable, the peak power for the two pulses is different. However, to calculate the peak power the exact pulse profile has to be known. The peak power is a crucial parameter in experiments that exhibit nonlinear dependences on the photon flux and a precise knowledge is required to interpret dynamics that occur on a time scale that is faster than the total FEL pulse duration. In imaging experiments, where radiation damage can occur within the first few femtoseconds of FEL exposure, precise information of the temporal profile is important.

The structure in the FEL pulse profile does not arise from the individual longitudinal FEL modes, which would have a duration of  $\sim 5$  fs at the FEL operation parameters. In fact, the structure is a result of the uneven FEL amplification over the length of the electron bunch, which originates from small changes in the electron beam parameters, such as charge, bunch length, emittance or energy spread.

**Arrival time:** The streaking measurement shown in **Figure 5.7** provides simultaneously the arrival time information of the FEL photon pulse on a time base that is synchronized to the pump-probe laser that generates the THz. To determine the arrival time, the center-of-mass of the retrieved FEL pulse profile of  $\sim 450$  consecutive FEL pulses, measured close to time

zero in the delay scan, is calculated and displayed in **Figure 5.10**. The Gaussian fit to the distribution has a width 87 fs r.m.s., which is a measure of the short-term timing jitter between the FEL and the pump-probe laser. This value is consistent with the expected performance of the electronic laser synchronization [112].

The accuracy of the relative arrival time information is mainly influenced by the stability of the THz streaking field and fluctuations in the mean FEL photon energy. Variations of the electric field strength directly translate to a change of the gradient of the THz vector potential and thus to a variation of the streaking strength from shot-to-shot. The stability of the THz pulse is a function of the driving optical laser. During these experiments the optical laser pulse energy was stable to within 1% r.m.s. For THz generation in saturation, the THz field scales with the square root of the driving laser pulse energy. Accordingly, the THz field is stable to within 0.5% r.m.s. These fluctuations can be neglected when considering the stability of the transformed time base. If better accuracy is required, the pump laser intensity of each single pulse could be recorded to scale the THz field strength. The fluctuation in the mean FEL photon energy leads to a photoelectron kinetic energy offset and corresponding temporal offset. During our measurements the FEL photon energy fluctuated from shot-to-shot at a level of 1 eV r.m.s., which translates to a time-of-arrival uncertainty of  $\sim 6$  fs r.m.s. These fluctuations are the predominate source of uncertainty in the time base of the retrieved FEL pulse profile.

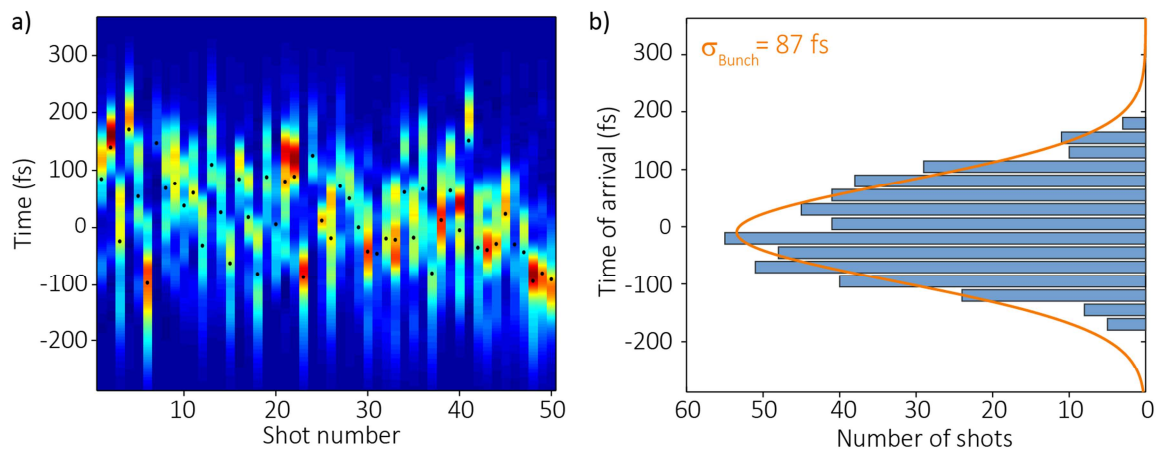


**Figure 5.10:** Arrival time jitter of the FEL pulse measured at FLASH. **a)** False color plot of 50 consecutive single-shot measurements recorded close to time zero. The center of mass of the individual photoelectron spectra (black dots) is used to determine the arrival time of each pulse. **b)** Distribution of arrival times collected over  $\sim 450$  consecutive shots with a Gaussian fit. The corresponding width of the fit is  $\sim 87$  fs r.m.s., which is a measure of the short-term timing jitter between the pump-probe laser, which is generating the THz, and the FEL.

This uncertainty could be reduced considerably by recording the FEL photon spectrum on a single-shot basis. To achieve this, for example, the photoelectron spectrum perpendicular to the streaking field polarization could be measured directly at the interaction region using a second TOF. The photoelectron distribution in this direction represents the field-free spectrum, since the kinetic energy shift is negligible in this direction ( $U_p \ll W_0$ , see Appendix C). Furthermore, using Auger electrons instead of photoelectrons eliminates this source of uncertainty, as the kinetic energy and spectral width of the Auger lines are entirely independent of the spectral properties of the ionizing pulse. It should be noted that the FEL photon energy fluctuation has only a minimal influence on the retrieved pulse profile, as the streaking map transformation is almost linear at the zero crossing and a small offset in the kinetic energy does not affect the spectral broadening.

### 5.2.5 First measurements with magnetic bottle spectrometer

The energy resolution and the detection efficiency of the electron detector are crucial in the THz streaking experiments. Without a sufficient number of detected electrons, the signal could suffer from statistical fluctuations of the discrete signal generated by single electrons, which is not favorable for single shot measurements. On the other hand, the ionizing FEL pulse energy and the target gas density have to be reduced to a level where space charge effects, which would lead to broadening of the photoelectron spectrum, are negligible. Therefore, in the first recorded THz streaking measurements which were taken during the pulse characterization beam time at FLASH in 2011, a magnetic bottle electron spectrometer was used. Similar to a normal TOF spectrometer the bottle measures the flight time of the electrons over a known distance from which the electron energy can be inferred. However, in a magnetic bottle a strong inhomogeneous magnetic field is applied in the interaction volume and a weak homogeneous magnetic field is applied in the drift tube. The ejected photoelectrons are collected by the strong field and guided through the drift tube towards the MCP by the homogeneous magnetic field, resulting in substantially increased electron collection efficiency.

**Figure 5.11** shows a streaking spectrogram collected with the magnetic bottle. The upper panel shows an intensity plot of consecutive single-shot photoelectron spectra, recorded as the relative delay between the FEL pulse and the THz streaking pulse was continuously varied. The measurement was performed in Ne with 90 eV FEL photon energy. Coarse synchronization between the FEL and the streaking pulse was maintained electronically. In the lower panel the time averaged spectrogram is plotted. As expected when temporal overlap between the two pulses is approached, the photoemission spectrum

is shifted and broadened, indicating that the spectra are streaked. From the furthest kinetic energy shift of  $\sim 6\text{eV}$ , the THz electric field strength was estimated to be  $\sim 50\text{ kV/cm}$ . The observed “splitting” of the streaked photolines arises from the near  $4\pi$  collection efficiency of the detector. Due to the inhomogeneous magnetic field, photoelectrons that are emitted away from the detector are flipped around and guided to the MCP, where they are measured with an opposite phase of the THz streaking field than the electrons that are emitted in the direction of the detector axis. This effect results in the observed double streaking feature. To test this, an aluminum foil was inserted at the backside of the photoemission target, which grounded the electrons emitted away from the detector and the double streaking feature disappeared. As it is important for the streaking measurements to distinguish between the backscattered and the forward emitted electrons, the magnetic bottle was replaced with an electron time-of-flight spectrometer for the rest of the measurements presented here. Note, after this measurement the THz was optimized, resulting in a higher streaking field for the other measurements presented in this chapter.

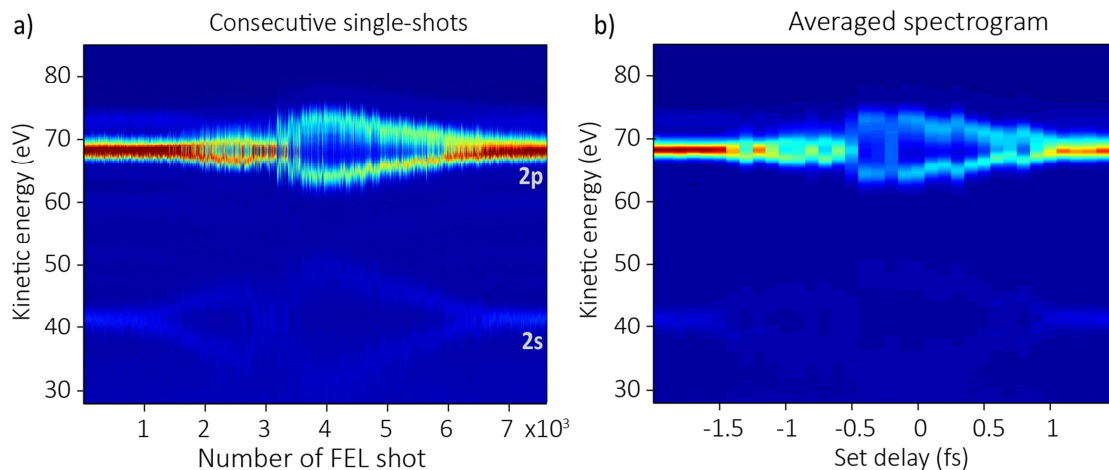


**Figure 5.11:** Spectrogram measured with a magnetic bottle. Neon photoelectron spectra as a function of relative delay between the THz streaking pulse and the ionizing 90 eV soft X-ray FEL pulse are depicted. **a)** Intensity plot of single-shot neon photoelectron spectra, shown in the order they were collected as the delay between the ionizing FEL pulse and the THz streaking pulse was varied continuously. Both, the Ne 2s and 2p lines are visible. For the Ne 2p the maximal up-shift in energy is  $\sim 6\text{ eV}$  and the maximal down-shift is about 5 eV, corresponds to a THz streaking field of  $\sim 50\text{ kV/cm}$ . **b)** Time averaged streaking spectrogram. Each delay bin is averaged over  $\sim 200$  single-shots and is 100 fs wide. The observed double streaking curve arises from the  $4\pi$  collection efficiency of the electron detector. Here, in the m the THz vector potential with opposite phase is traced out.

### 5.3 Comparison & discussion on experimental parameters

Successful operation of the streaking technique for characterizing FEL pulses strongly depends on the THz pulse properties including transversal beam profile, energy stability, field strength, temporal shape of the waveform and the THz evolution in the interaction region. Some of these aspects will be discussed in the following text.

#### 5.3.1 Practical aspects of THz generation

As described in Chapter 4 the used titled pulse front set-up consist of a femtosecond pump laser, an optical grating, an imaging telescope and the LiNbO<sub>3</sub> crystal. In order to align and optimize the THz generation setup, most of the components are mounted on translation and/or rotation stages. The alignment of the generation setup is a lengthy procedure as all the parameters are coupled to each other. The setup conditions, the crystal properties and NIR pulse properties will affect the properties of the generated THz radiation. In particular, the temporal shape of the THz pulses is strongly dependent on to the tilt angle of the pulse front, the input amplitude, and the temporal and spatial properties of the NIR pump pulse. In addition, the transport and the focusing of the THz radiation will also influence the temporal shape. Moreover, the generated THz pulse will show spatial chirp due to the way it is generated and also temporal chirp is not excluded [113].

Problems may arise from the fact, that only optimizing for energy by observing the THz output with a pyro-detector may not result in the optimum THz properties. For example, different combination of the telescope position, (the telescope images the pump laser on the grating into the crystal and compensates for the spatial separation of the different frequencies) and the LN crystal positions can be found with similar THz conversion efficiencies, but with different THz pulse properties. In order to compare different setup settings EOS measurements have to be performed. However, already small changes in the THz setup may result in big differences in the spatial beam properties of the generated THz radiation, which in turn changes the focusing of the THz.

The exact NIR pump pulse properties also influence the actual alignment of the generation setup. Ideally a transform limited pulse should be used. Usually, small temporal chirp in the pump beam does not influence the conversion efficiency, as the grating angle or the imaging optics position can be slightly changed to compensate for the chirp. However, it might influence the properties of the pulse produced.

The pump-probe laser at FLASH has to be transported several meters to the actual experiment, where the streaking measurement is performed. In order to avoid self-phase

modulation the NIR pulse is not entirely compressed after the amplifier in the laser hutch. Only, after the beam transport to the experimental end-station, the NIR pulses are passed once through a pair of parallel transmission gratings to compress the pulse temporally. In this single pass geometry, the output beam acquires spatial chirp. In Ref. 114 it could be demonstrated that simultaneous spatial and temporal chirp (= dispersive medium) yields pulse front tilt. This changes the alignment conditions of the pulse front tilt set-up and phase matching conditions may not be optimal.

### **THz pulse shape for different pump pulse conditions**

In **Figure 5.12** in the left panel there different EO-sampling measurements are depicted. The THz streaking pulse that was used for the measurements presented here is shown in blue color. The orange and the green dashed EO traces have been recorded at a different beamtimes at FLASH. Although, the THz radiation was generated with the same THz generation setup and the same pump-probe laser at FLASH, the resulting temporal shape of the three pulses is quite different. Firstly, the main peak in the green waveform is substantially longer than the peak of the two other EO traces. This leads to an increase of the rise time of the streaking ramp and consequently to a reduction of the temporal resolution. Secondly, the blue trace shows one main positive peak and two much smaller peaks in the negative direction, while for the other two curves the ratio of the positive amplitude and the negative amplitudes increases. For the THz waveform plotted in green, the peak in the positive direction and the peak in the negative are almost equal. The difference in these curves could not be explained by the Gouy phase shift. The differences might result from different NIR pulse properties, including linear and higher orders of chirp. On the right panel, a Ne streaking spectrogram recorded with  $\sim 258$  eV FEL pulses and the green transient as the streaking pulse is shown. For this measurement the THz beam was transported and focused into the interaction region with a telescope consisting of a 300 mm collimating Teflon lens and a 150 mm focal length off axis parabolic mirror, resulting in half of the streaking power as compared to the streaking measurements presented in the main part of this chapter (however The THz energy was the same). The rise time of the streaking ramp is much slower than the rise time of the spectrogram in Figure 5.7, were the blue curve was used as the streaking pulse. Furthermore, the photoelectron spectra are mainly shifted to lower energies, while the shift to higher kinetic energies is much lower. The streaked spectra at the zero crossing that are used to analyze the temporal properties of the FEL pulse are barely broadened due to the low streaking strength.

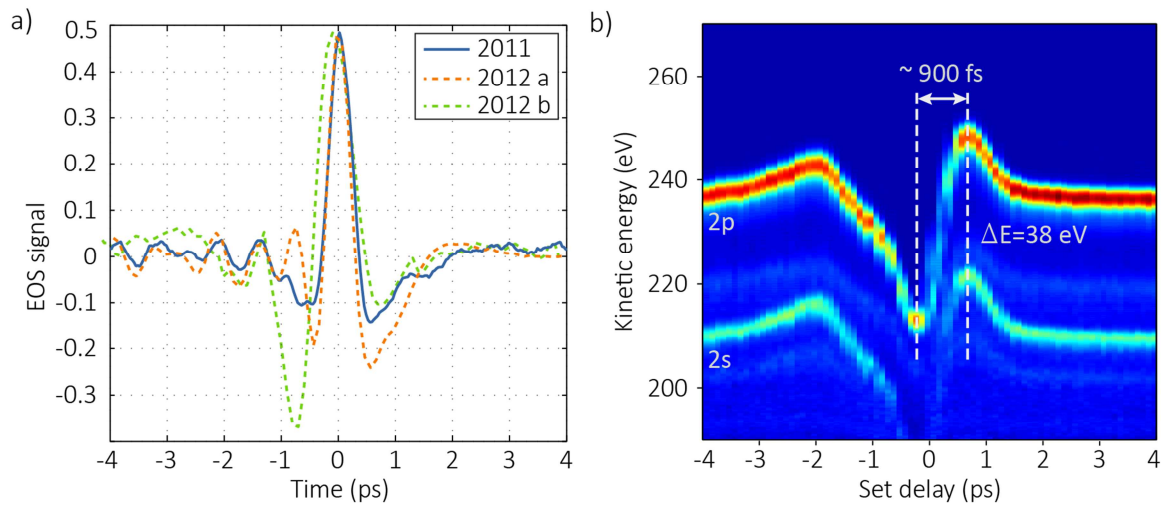


**Figure 5.12:** Comparison of the temporal waveform of the generated THz. **a)** Three different EO-sampling measurements are depicted. For better comparison the maximal EO-signal was scaled. The blue curve corresponds to the THz streaking pulse that was used for the measurements presented in this chapter. The orange and the green dashed EO traces have been recorded at different beamtimes at FLASH, though the same THz generation setup and similar NIR pump pulse properties were used. Clearly, the depicted electric field transients are quite different. Firstly, the main peak in the green waveform is substantially longer than the peak of the two other EO traces. This is important, as the duration of this peak (at its zero crossing) corresponds to the rise time of the streaking ramp. Secondly, the blue trace shows one main positive peak and two much smaller peaks in the negative direction, while for the other two curves the ratio of the positive amplitude and the negative amplitudes is more similar. The curve in green is almost symmetric. In **b)** a Ne streaking spectrogram recorded with  $\sim 258$  eV FEL pulses and the green transient as the streaking pulse is depicted. For this measurement the THz beam was transported and focused into the interaction region with a telescope consisting of a 300 mm collimating Teflon lens and a 150 mm focal length off axis parabolic mirror, resulting in half of the streaking power as compared to the streaking measurements presented in the main part of this chapter (THz pulse energy was roughly the same in both measurements). The rise time of the streaking ramp is  $\sim 900$  fs.

### Streaking versus EOS for streaking pulse parameter recovery

In the measurements presented here, we constructed the transformation map from energy to time from the THz pulse characterized with EOS. However, wavelength-dependent absorption and dispersion in the ZnTe detection crystal may result in distortions of the measured electric THz waveform. In addition, impurities and saturation effects in the detection crystal may also lead to significant deterioration of the detectable field strength. In the streaking measurement, instead, a flat and dispersion free response is expected, and the averaged streaking spectrogram should provide a more precise transformation map. However, the presented measurements were hampered by the large temporal jitter

between the FEL and the THz pulses. If the arrival time jitter is much smaller than the rise time of the streaking ramp it is expected that the precise shape of the THz vector potential can be determined from the spectrogram itself.

Moreover, the frequency components of the broadband pulse are focused to focal plane, which means that the strength of the THz electric field is distributed over a certain volume. It might be that the sampled volume is different in the EO measurement and the streaking measurement, which could lead to different estimations of the absolute electric field strength and may explain the discrepancy in the field-strength in the EO-measurement and streaking measurement.

### **5.3.2 THz field strength**

The temporal resolution of the measurement would be improved by scaling up the THz field strength, which leads to an increase of the streaking strength. Due to its large bandgap and high damage threshold of LN the THz output energy can be increased by scaling up the NIR pump pulse energy. However, higher pump pulse energies are accompanied with redshift and spectral narrowing of the generated THz frequency spectrum [69]. To increase the high frequency components of the generated radiation the propagation distance of the beams inside the crystal should be minimized. This could be achieved with an elliptical pump laser spot that is stretched in the vertical axis with cylindrical lenses [115]. Enhancement of the THz energy can also be reached by cooling the LiNbO<sub>3</sub> crystal, which reduces the THz absorption significantly. Especially the absorption of higher frequency components is suppressed, which may result in a better focusability and shorter THz pulse durations (decreased rise time), which consequently results in an improved THz streaking strength [116]. It has been demonstrated, that by cooling the LN crystal down to 10 K the THz frequency could be tuned to more than 4 THz [117].

Higher and steeper streaking fields can also be achieved with organic crystals like OH1, DAST and DSTMS [118]. They exhibit large nonlinear optical coefficients and high THz generation efficiencies could be demonstrated [119]. Measurements that have been performed with DSTMS generated THz will be presented in chapter 7.

### **5.3.3 Influence of the Gouy phase shift**

As the THz and the X-ray pulse propagate through the interaction zone, the phase of the THz electric field changes. This is a consequence of the Gouy phase shift [120,121]. Since a short focal length (76.2mm) parabolic mirror was used to focus the THz beam, the Gouy phase shift happens over a distance of just few mm. On the other hand, the X-rays are focused with

much longer focal length optics, leading to an extended region of high intensity where photoionization can occur. Typically, the gas target is also spread out, so that photoelectrons can originate over a length of several mm. Thus, photoelectrons created at different positions within the interaction zone will see a varying phase of the THz electric field. Consequently, the Gouy effect leads to an effective dephasing of the streaking field and the X-ray pulse. This gives rise to an additional broadening of the streaked photoelectron spectra, and consequently leads to an overestimation of the pulse duration of the ionizing pulse and ultimately to a degradation of the temporal resolution of the measurement.

In order to evaluate the influence of THz Gouy phase shift, both the interaction length (basically given by the gas volume) and the evolution of the THz phase along this interaction length need to be determined. **Figure 5.13** illustrates this problem schematically; here the evolution of the beam waist of THz beam and a X-ray beam propagating in z-direction are shown. Unfortunately, during these measurements the size of the gas target was not measured. However, during another measurement campaign, where the same gas nozzle and settings were used, the gas diameter was estimated. For this, the gas nozzle was scanned in the transverse direction and the photoelectron yield at each position was measured, resulting in a FWHM of the gas density distribution of  $\sim 500 \mu\text{m}$ .

The phase shift  $\Delta\phi$  within the interaction length can be calculated with Eq. 3.17. For pulses with a central frequency of 0.6 THz and different beam diameters the phase shift due to the Gouy effect is listed in **Table 5.2**. The phase change of the pulse is equivalent to a time shift of the THz and X-ray pulse overlap and thus to a temporal shift of the X-ray pulse on the streaking ramp. A phase change of  $\Delta\phi$  along the interaction region leads to a time shift of

$$\Delta t = \frac{\Delta\phi}{360^\circ} T, \quad (5.3)$$

where T is the duration for one oscillation period. In the experiment the THz beam diameter is estimated to be 2 mm which would lead to a time smearing of 15 fs.

However, this approach might not be good enough for the broadband single-cycle THz pulses. For the different spectral components the Gouy phase shift will evolve on a different spatial scale, due to the wavelength dependence of the Rayleigh length and beam waist. In particular, the blue colors will experience a steeper shift than red colors. Therefore, the phase variation is not properly described by  $\phi = -\arctan(z/z_R)$  in the focal region. Here, the precise evolution of the phase depends on the spatial profile of the beam and the focusing geometry [122]. Between symmetric locations far away in front and behind the focus an overall shift of  $\pi$  is expected. An overall phase shift of  $\pi$  is expected for waveforms observed at well distant positions in front and behind the focus. In the focal region all

possible electric field shapes can evolve. To characterize the phase variation precisely, it is essential to measure the pulse at well-defined positions through the focus. Therefore, it might be more reasonable to measure the evolution of the THz electric field shape directly with electro-optic sampling to evaluate the time smearing in the streaking measurement caused by the Gouy phase shift.

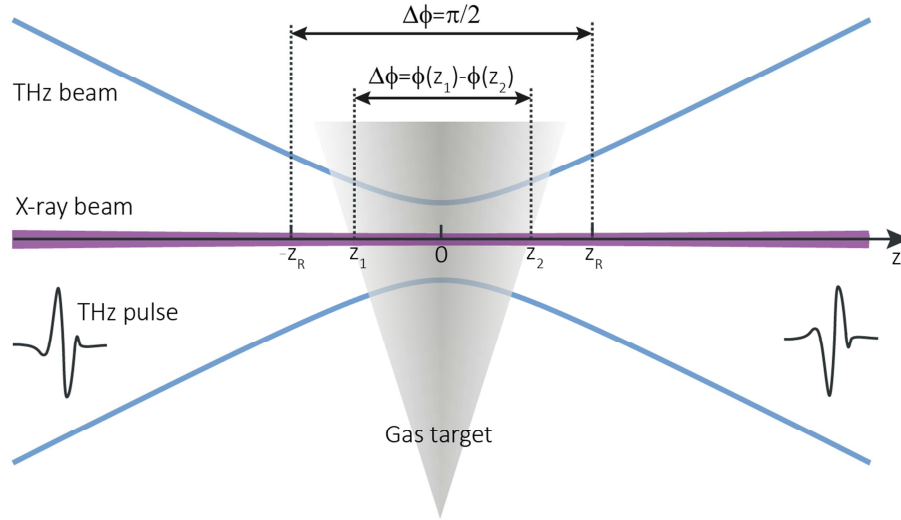


**Figure 5.13:** A Gaussian beam propagating in the  $z$  direction is depicted,  $z_r$  is the Rayleigh length and  $z=0$  is the position of the beam waist. To evaluate the spectral broadening due to the Gouy phase evolution the gas density distribution, which defines the interaction length, and the change of the streaking phase  $\Delta\phi$  of the THz streaking pulse within this interaction length (from  $z_1$  to  $z_2$ ) should be determined.

**Table 5.2:** Calculated Rayleigh length and Gouy phase shift over the interaction length of  $500\ \mu\text{m}$  for THz pulses with a central frequency of 0.6 THz for different values of the focus spot size.

Diameter at focus (mm)	$z_R$ (mm)	$\Delta\phi$ ( $500\mu\text{m}$ )
3	14	$2^\circ$
2	6.3	$4.5^\circ$
1.5	3.5	$8.2^\circ$

## 5.4 Summary

We have successfully demonstrated the first laser-based THz streaking at FLASH for single-shot temporal characterization of the delivered FEL photon pulses. The temporal profile of individual FEL pulses was characterized with 5 fs full-width at half-maximum accuracy. Simultaneously, their arrival time with respect to the FLASH pump-probe laser was measured with an accuracy of 6 fs r.m.s. During our measurements, the FEL was operating in the exponential gain regime, where it is very sensitive to electron beam parameters and thus pulse-to-pulse fluctuations are more severe. In the saturation regime, shot-to-shot fluctuations in the temporal pulse profile are expected to be less pronounced. Furthermore, in this regime FEL pulses with higher flux are generated. Thus, THz streaking measurements in this regime are expected to be even more reliable.

The method is realized with standard laser technology and the apparatus does not require any dedicated accelerator structure. It is applicable as a temporal diagnostic tool for machine studies and FEL optimization for special lasing parameters and pulse shapes, as it is completely independent from all other FEL parameters.

As the measurement is made in transmission geometry and barely affects the FEL pulse, it can be performed simultaneously with time-resolved experiments. Here, the precise FEL pulse arrival time data can be used for post-processing the acquired data, improving the time resolution in pump-probe experiments to a level limited only by the FEL and optical pump-pulse durations. Furthermore, the data can be post-processed according to the true single-shot FEL pulse intensity profile, which is particularly important for single-molecule imaging and nonlinear extreme-time scale X-ray science.

In the future, with increased THz streaking strength and increased energy resolution of the photoelectron spectrometer, the resolution of the THz streaking measurements may be improved to resolve the fundamental FEL pulse substructure separated by only several femtoseconds.

## **6 Characterization of the all-optical synchronization scheme at FLASH with time resolved photoelectron spectroscopy**

In this chapter THz streaking measurements carried out with the purpose to characterize the performance of the optical synchronization system at FLASH FEL facility will be presented. In general, a measure of the facility-wide level of synchronization is the timing stability that can be maintained between the FEL X-ray pulses and independent optical laser pulses. With the all-optical synchronization system at FLASH a facility-wide timing to better than 30 fs r.m.s. for 90 fs FWHM FEL photon pulses is demonstrated. The measurements, results and figures presented in this chapter are adapted from our publication Ref. [123].

In the first section of this chapter, a short description of the timing sensitive devices in a FEL facility is given. In the following Sec. 6.2 and 6.3, a brief introduction to the synchronization system at FLASH is given, with a particular focus on the optical synchronization. Furthermore, a description of the longitudinal electron beam stabilization within the optical synchronization system is discussed in Sec. 6.3. The presented measurements related to the optical synchronization system were realized by S. Schulz and co-workers [124]. The electron bunch arrival time measurements were carried out by M. K. Czwalińska [125]. Finally, in Sec. 6.4 the THz streaking measurements are presented and the results are discussed.

### **6.1 Timing at FELs**

The femtosecond duration of X-ray FEL pulses offers new possibilities to study light-matter interactions. Most commonly, an optical laser pulse is used to excite the system and the evolution of the system is probed with a subsequent FEL pulse. However, the measurement resolution is typically limited by the level of synchronization that can be achieved between the two independent sources. The timing stability between the FEL photon pulse and the optical laser pulse is determined by:

- The stability of the common accelerator reference signal.
- The level of synchronization that can be achieved between the optical pump laser and the accelerator reference signal.
- The stability of the FEL photon pulse arrival time at the experiment, again with respect to the same reference. This stability is mainly determined by the fluctuations of the arrival time of the FEL driving electron bunch at the undulator.

Electron bunch timing jitter is accumulated at various locations along the accelerator. The main contribution can be attributed to the electron source and the amplitude and phase stability of the accelerating cavities. In the electron source the arrival time jitter is the result of a combination of the laser pulse arrival time on the photo cathode and the phase of the radio-frequency (RF) cavity [126]. Fluctuations in the amplitude and phase of the accelerating fields cause variations in the mean electron bunch energy. In the bunch compressor, which is required to generate the high peak currents necessary for the high gain FEL process, these variations lead to transit time fluctuations of the electron bunch through the magnetic chicane affecting the arrival time of the electron bunch most significantly, with respect to the accelerator reference.

The bunch compression, a critical parameter in the FEL process, also strongly depends on the electron beam phase in the cavities. RF phase fluctuations or arrival time jitter of the electron beam at the chicane location cause peak current fluctuations. The fluctuations lead to variations of the FEL photon pulse parameters including intensity and temporal profile with increasing severity as shorter pulses are delivered, as here stronger compression is required. Thus, the amplitude and the phase of the RF fields in the cavities prior the compression should be precisely controlled to generate stable electron bunches.

## 6.2 Conventional RF Synchronization

In the conventional electronic synchronization scheme the timing signal is provided by a master RF oscillator (MO), which is distributed across the facility via coaxial cables. The MO is operated at the frequency of the accelerating fields (1.3 GHz at FLASH). The timing of the different sub-systems is determined by measuring the phase relation between the reference signal from the MO and the RF signal from the device under consideration.

To this end with the conventional RF based synchronization scheme, it has not been possible to synchronize FEL pulses to independent optical laser pulses to better than 100 fs r.m.s. One approach to improve the level of synchronization is to use an all-optical

scheme, where highly stable laser pulse trains are distributed via length-stabilized optical fibers across the accelerator facility [127]. This scheme will be discussed in the following.

### 6.3 Optical synchronization at FLASH

In the optical synchronization scheme, shown schematically in **Figure 3.1**, the timing reference is derived from a femtosecond mode-locked master laser oscillator (MLO). The timing information is contained in the precise repetition rate of the optical pulse train, which is distributed to the different sub-systems along the facility through actively length-stabilized optical fibers (Sec. 6.3.1). Apart from the capability to stabilize the transport of the timing signal, a major advantage of the optical synchronization scheme is given by the possibility for temporal diagnostics based on mixing optical signals which is more precise than mixing electronic signals. The applications of the optical reference at the end-stations can be divided into three different categories:

- External lasers can be locked to the MLO by optical cross-correlation techniques. This synchronization scheme offers the possibility of sub-5 fs timing stability between the MLO and different external lasers such as the pump-probe laser, the seed laser, the photoinjector laser and laser-based electron beam diagnostic systems .
- From the optical pulse train highly phase-stable RF signals can be extracted, which are needed for the control of the accelerating fields and for RF-based synchronization of other devices, by means of the conventional way of phase detection. This can be realized with different methods. In the frequency domain an infinite pulse train operating at a repetition rate  $f_0$  translates to a frequency comb with components at  $nf_0, n \in \mathbb{N}$ . The most conventional way to extract RF signals is to detect the optical pulse train with a large bandwidth photodetector and to separate a suitable harmonic with a band-pass filter. The phase of this signal can then be compared to the phase of the RF signal of the device to be synchronized.
- The optical pulse train from the MLO can be used directly in diagnostic tools, like for the bunch arrival time monitors (BAM) installed along the accelerator, to measure the arrival time of the electron bunches with femtosecond resolution. At FLASH several BAMs are installed at specific locations, most importantly after the magnetic chicanes for electron bunch compression and at the end of the final accelerating stage. The arrival time information can be used for post-processing, i.e. time-sorting in pump-probe experiments. Moreover, the measured arrival time information can be implemented in the RF cavity feedback system at FLASH to stabilize the electron bunch arrival time at the entrance of the undulator.

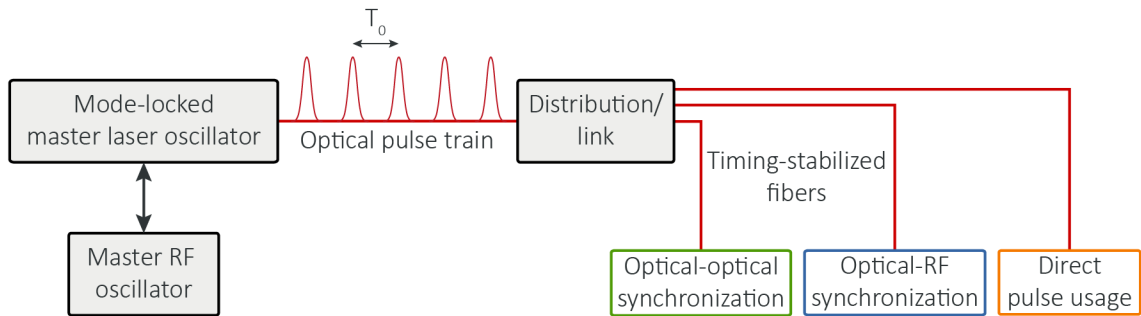


**Figure 6.1:** Schematic overview of the laser-based synchronization. The timing reference, a low noise optical pulse train, is provided by a mode-locked femtosecond laser (master laser oscillator). The pulse train, which contains the timing information as its precise repetition rate, is distributed across the accelerator facility through actively length-stabilized optical fiber links. At distant locations external laser systems, like the pump-probe laser and the gun laser, can be synchronized with the reference pulse train by optical cross-correlation methods. Furthermore, RF-signals can be generated at harmonics of the fundamental repetition rate of the provided reference pulse train for the synchronization of RF subsystems (like the accelerating modules). The delivered optical pulse train can also be used directly at remote locations for diagnostic tools. The MLO is locked to the master RF oscillator because of its better long-term stability.

### 6.3.1 Fiber link stabilization & optical cross-correlator

The **master laser oscillator** is realized using a femtosecond mode-locked erbium-doped soliton fiber laser (EDFA) at a repetition rate of 216 MHz, which is the sixth sub-harmonic of the RF used for the acceleration in the cavities. The timing information is encoded in the highly accurate repetition rate of the pulse train of this mode-locked laser. The laser is operating at a central wavelength of 1560 nm. At this wavelength many fiber-optic components, developed for the telecommunication industry, are already available. In particular, at this wavelength dispersion compensating optical fibers exist, which is crucial for the fiber link stabilization scheme and the nonlinear optical methods applied in the synchronization system. Mode-locked lasers exhibit an excellent short-term stability [128]. However, thermal and acoustic expansion and contraction of the laser cavity influence the long-term stability considerably. Therefore, in order to maintain medium-term stability and to avoid long-term drifts, the MLO has to be synchronized to the master RF oscillator [129]. In order to synchronize the MLO to the master RF oscillator conventional RF phase-locking techniques are applied, for example described in Ref. [126].

The optical reference signal from the MLO is distributed on a fiber optic network. The various devices at the remote end stations, including the bunch arrival time monitor and the experimental pump-probe laser system, have an individual point-to-point connection to the

MLO. Since the optical fibers in the accelerator are subject to temperature and humidity changes, as well as mechanical vibrations, they are length stabilized and therefore transit-time stabilized using single-color optical cross-correlators (OXC) [130].

The **fiber link stabilization** and distribution scheme is shown in **Figure 6.2**. Pulses from the MLO are split with a polarizing beam splitter. Part of the reference pulse train is sent directly to an OXC and the other part is coupled into the fiber link. At the end of the fiber, a part of the laser power of the pulses sent down the fiber is reflected back through the same fiber by a Faraday rotating mirror, while the rest of the laser power is used for the synchronization. The Faraday rotator changes the polarization state of the returning pulses by 90°. Consequently, the polarization of the backward travelling pulses is orthogonal to that of the forward travelling pulses, which allows the pulses to be separated, when they arrive back at the first beam splitter. These back reflected pulses are combined with the pulses directly from the MLO and their relative timing is detected in an OXC. The detected changes in the round-trip transit time for pulses sent through the fiber, measured by the OXC, are used as feedback for the stabilization of the fiber length and consequently of the pulse transit time. Here, a fast piezo-based fiber-stretcher and a motorized optical delay stage are incorporated in the fiber link to apply the required optical path length changes. The piezo-based actuator has a range of  $\pm 4$  ps, and when its maximum range is reached, the motorized optical delay line is moved, such that the operation point of the stretcher is centered again.

To compensate for the power losses and to increase the pulse energy in the cross-correlator, two erbium-doped fiber amplifiers are installed in the fiber-link network, as depicted in **Figure 6.2**. Furthermore, as for the applied optical techniques short laser pulses are required a chromatic dispersion compensating fiber is incorporated in the link to account for pulse broadening in the fiber-link and in the OXC.

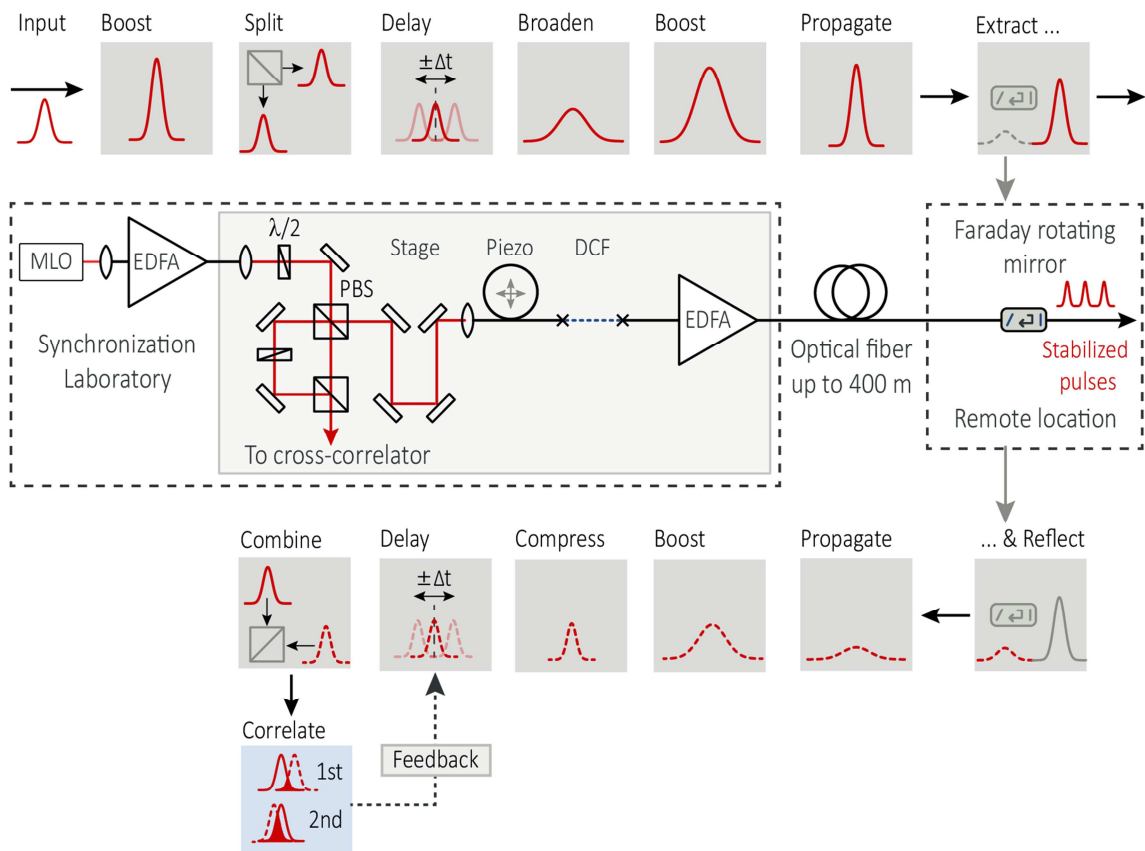


**Figure 6.2:** Schematic of the fiber link stabilization. The pulses from the MLO are initially amplified in an EDFA. Then, the pulse is split with a polarizing beamsplitter (PBS). One component is sent to the OXC, while the other component is propagated down the fiber optic cable that runs along the accelerator tunnel to the remote end station. At the end of the fiber link, a fraction of the pulse energy is reflected back down the same fiber and its polarization state is rotated by 90° by a Faraday rotating mirror, while the rest of the pulse energy can be used for the synchronization of the corresponding device. The timing between the back-reflected pulse and the reference pulse that did not travel through the fiber is then measured in the OXC. The detected changes in relative timing can be used as feedback to adjust the length of the link using a fast piezo-based fiber-stretcher (Piezo) and a motorized optical delay line (Stage). To account for pulse broadening in the fiber link, a dispersion compensating fiber (DCF) is installed.

A fundamental limit on the bandwidth of this feedback is given by the fiber length, because one of the pulses has to travel down the link and back before it is mixed with a pulse coming directly from the MLO. Therefore, only changes occurring on a time scale longer than the link transit time ( $\sim 3.8 \mu\text{s}$  for a 400 m long link) can be detected and compensated. Timing changes in the link mainly arise from thermal expansion/contraction

of the fiber, temperature- or humidity-induced changes of the refractive index and mechanical vibrations, which are all typically longer than a millisecond. They can all be compensated by the stabilization based on the OXC. In practice, the maximum speed of the piezo-based fiber stretcher sets also a limit to the feedback bandwidth.

An **optical cross-correlator** is used to measure the changes in the round-trip transit time. In **Figure 6.3** the measurement principal of an OXC is shown. In the first stage, the two input pulses, with arbitrary temporal delay are mixed by sum-frequency generation (SFG) in a nonlinear crystal. The intensity of the SFG signal depends on the precise temporal overlap and on the individual intensities of the optical pulses  $I_{Pulse1}(t)$  and  $I_{Pulse2}(t)$  and is given by:

$$I_1^{SFG}(\tau) = \int_{-\infty}^{\infty} I_{Pulse1}(t) I_{Pulse2}(t - \tau) dt . \quad (6.1)$$

However, in this first stage of the OXC the temporal order of the pulses cannot be determined, as the SFG signal is symmetric as a function of relative delay  $\tau$ . Furthermore, as the SFG signal also depends on the input pulse amplitudes, pulse intensity fluctuations cannot be distinguished from changes of the relative timing. Thus, in order to identify which pulse arrives first and to balance the OXC (in order to decouple amplitude and time fluctuations), a second measurement is performed. For this, one of the two pulses is delayed with respect to the other by a fixed amount  $T$  and the pulses are mixed a second time in the non-linear crystal to generate another SFG signal  $I_2^{SFG}$ . If the SFG signal is zero in the second stage the delayed pulse had originally arrived second at the cross-correlator. If the delayed pulse arrived originally first, then the SFG signal from both stages would be non-zero. In this case, small changes in the timing lead to changes in the SFG signal strength that have opposite signs in the two stages, an increase of the signal intensity in the first stage corresponds to a decrease in the second. Recording the difference signal  $I_1^{SFG}(\tau) - I_2^{SFG}(\tau + T)$  as a function of the delay between the two pulses results in a bipolar signal as plotted in **Figure 6.3** on the right. At the zero-crossing of the difference signal the detectors are perfectly balanced and the zero-crossing is not affected by laser amplitude changes. For small time differences between the two input pulses the difference signal is linearly proportional to their separation in time [131]. Thus, if the OXC is operated near the zero-crossing of the difference signal, the amplitude changes of the input laser pulses can be neglected in a first order approximation [132]. The combination of the SFG signals from the two stages provides an ideal feedback signal which can be applied to the piezo-stretcher to regulate the fiber length. This is possible because the direction of the change in relative

timing between the pulses can be determined independently of intensity fluctuations of the input pulses.

In this kind of OXC, the temporal exchange of the two pulses, which is required for the unambiguous detection, can be accomplished in different ways. Here, in the scheme used for the fiber link stabilization, where the two pulses being compared have the same wavelength, the group delay difference between two orthogonally polarized pulses in a birefringent crystal is exploited. At FLASH the OXC of the fiber link stabilization is based on sum-frequency generation in a type-II phase-matched, periodically-poled titanyl phosphate (PPKTP) crystal that exhibits a large birefringence. For the first stage, the two pulses with perpendicular polarization (one pulse directly from the MLO and the back reflected pulse from the fiber) are focused in the PPKTP to generate the first SFG signal. Then, the temporal exchange for the second stage of the OXC is automatically performed simultaneously with the sum-frequency generation, while the pulses travel inside the PPKTP crystal. In addition, the exit face of the crystal has a dichroic coating, which transmits the sum-frequency but reflects the fundamental input pulses, obviating the need for additional optical elements.

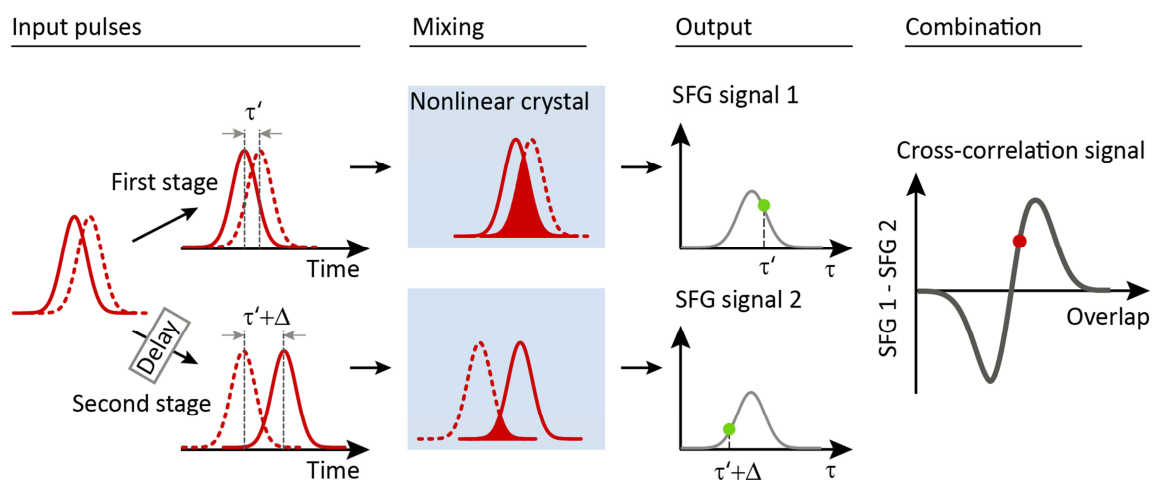


**Figure 6.3:** Illustration of the optical cross-correlator (OXC) principle. In the first stage, two optical pulses with arbitrary temporal overlap are mixed in a nonlinear crystal resulting in a sum-frequency signal that depends on their exact temporal overlap. To determine which pulse arrives first and to balance the cross-correlator, a second stage is used, in which one of the pulses is delayed with respect to the other one by a fixed amount. The rearranged pulses are overlapped again in the nonlinear crystal to generate a second sum-frequency signal. The difference between the two sum-frequency intensities allows the exact input timing to be determined without sign ambiguity. Scanning continuously the relative timing between the two input pulses results in a characteristic OXC curve as illustrated on the right.

Consequently, the second-stage SFG signal is generated as the retro-reflected pulses travel through the PPKTP crystal a second time. This OXC scheme is background-free, as both polarizations states are required for the SFG generation, thus the SFG signal vanishes if the pulses do not overlap in time.

To **characterize the performance of the stabilized fiber link** the arrival time of pulses out of the link is compared to pulses coming directly from MLO. For this purpose the MLO pulses were coupled into a stabilized 400-m-long test fiber. The fiber was placed through the accelerator facility and returned back to the laboratory, where the MLO was located, as shown in **Figure6.4**. Pulses were extracted from the end of the fiber link and their timing with respect to the optical reference pulses directly from the MLO was measured in an independent, calibrated OXC. As shown in **Figure6.4** in the right panel, the fluctuations of the relative laser pulse arrival time in this test were measured to be  $< 1$  fs r.m.s. over a 1-h interval.

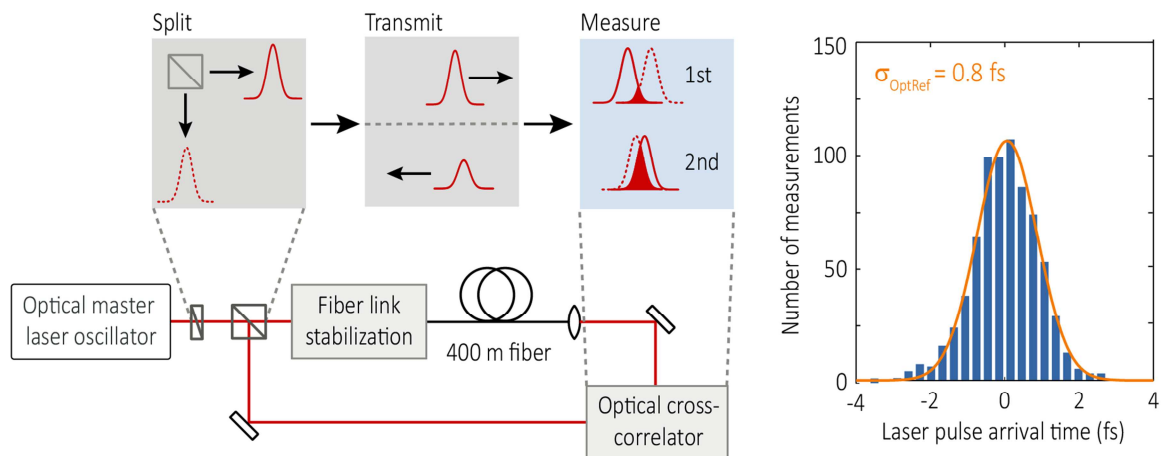


**Figure6.4:** Characterization of the fiber link. For the distribution of relative arrival times measurements between laser pulses from the fiber link and pulses directly from the MLO were performed with an independent out-of-loop optical cross-correlator as depicted on the left. Measurements were made every 5 s for 1 h and for each measurement the average temporal overlap over an interval of 2 ms was taken. The residual timing jitter was found to be 0.8 fs r.m.s., determined from the Gaussian fit to the corresponding distribution depicted on the right.

### 6.3.2 Temporal electron bunch stabilization

Phase and amplitude fluctuations of the accelerating RF field lead to undesired fluctuations of the electron peak current, slice emittance within the electron bunch and arrival time at the undulator. As these electron beam parameters directly affect the FEL photon beam

properties, they need to be controlled and stabilized to ensure a stable and reliable delivery of the generated X-ray pulses from shot to shot.

At FLASH the RF power is generated in several klystrons and transported through a wave-guide system to the main couplers at each cavity of an acceleration module. The RF field amplitude and phase are measured directly inside each cavity by antennas. The measured fields are digitized and evaluated in a low-level radio frequency (LLRF) control system, which provides the signal to correct fluctuations of the RF field by adjusting the amplitude and phase on the input driving the klystron [133]. With this technique of self-regulation, the accelerating field can be controlled with a closed-loop bandwidth of 40 kHz, limited by the intrinsic bandwidth of the superconducting cavities and the maximum possible gain applicable in the feedback loop. At FLASH, under optimum conditions this allows the electron bunch timing jitter to be stabilized to 50 fs r.m.s., measured with respect to the optical reference. Uncorrected, remaining RF field amplitude and phase fluctuations cause energy fluctuations in the accelerated electron bunch, which changes the trajectory and thus the transit time through the bunch compressor section. Furthermore, RF phase fluctuations of the preceding acceleration fields directly influence the bunch compression factor that can be achieved in the two magnetic chicanes.

The electron bunch time structure at FLASH, depicted schematically in **Figure 6.5**, offers the possibility to further improve the stabilization of the electron beam. For normal operation RF pulses with a flat top of 800  $\mu\text{s}$  at a repetition rate of 10 Hz are used. This allows the acceleration of a bunch train (or macro pulse) consisting up to 800 bunches with an intra-train repetition rate of 1 MHz. During the macro pulse relevant beam properties can be measured, like the bunch compression state and the bunch arrival time.

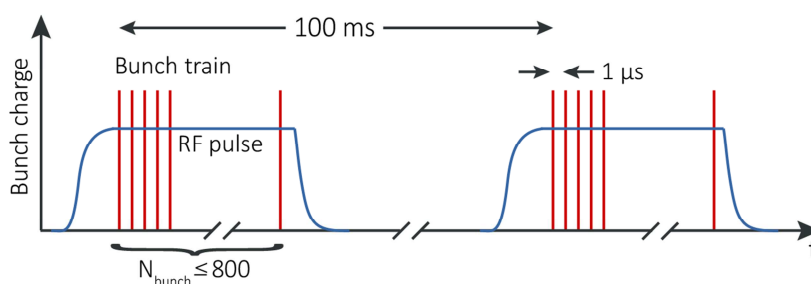


**Figure 6.5:** Electron bunch time structure at FLASH. Due to their low losses and high quality factor the superconducting cavities can be loaded with RF pulses with a flat top of 800  $\mu\text{s}$ , shown in blue. This allows an electron bunch train (or macro pulse) consisting of up to 800 bunches with 1 MHz repetition rate to be accelerated. The repetition rate of the macro pulses is 10 Hz. The intra-train repetition rate can be varied from 1 MHz to 25 kHz with accordingly reduced number of maximum bunches.

This information can be then incorporated into the control loop for the regulation of the phase and amplitude of the accelerating fields to stabilize the later bunches in the macro pulse. The concept of this so-called beam based feedback (BBF) in combination with the optical synchronization scheme within the FLASH facility is depicted in **Figure 6.6**. At different positions of the accelerator bunch arrival-time monitors (BAM) that provide the feedback signal for the RF amplitude regulation and bunch compression monitors (BCM) that provide feedback for the phase regulation, are installed.

In the BCM the intensity of emitted coherent diffraction radiation is used to monitor the longitudinal compression (bunch peak current) of the electron bunches after the two magnetic chicanes. A detailed discussion of the BCMs can be found for example in Ref.[134,135]. The BAMs measure the arrival time of the electron bunches with respect to the optical reference, which is provided by individual length-stabilized fiber links. Since we were interested in the characterization of the optical synchronization system and the improvements of the beam arrival time and thus the FEL photon pulse arrival-time, the BAM operational principle and measurements will be described in the following text.

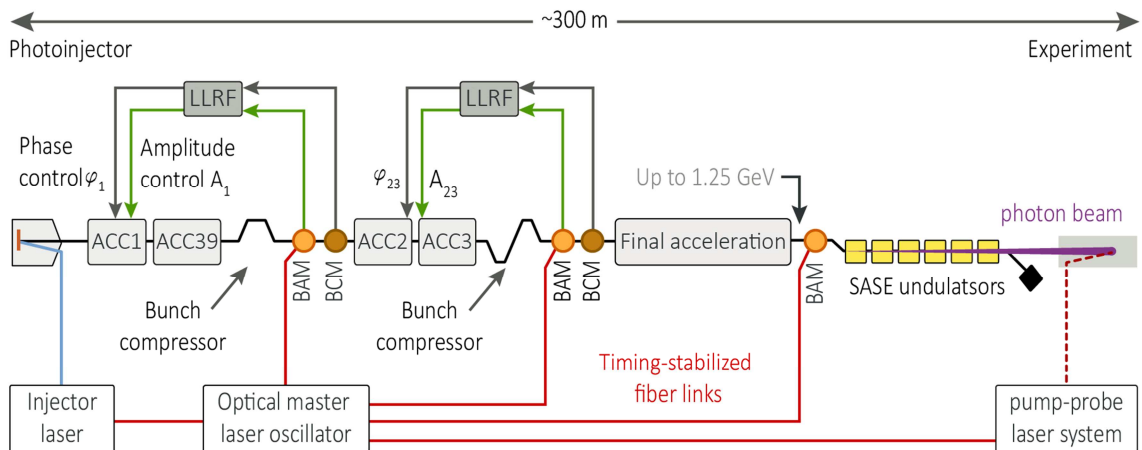


**Figure 6.6:** Schematic of the FLASH FEL with the longitudinal beam based feedback and the optical synchronization. The pulse train from the photoinjector laser is synchronized to the optical reference from the MLO. Bunch compression monitors (BCM) are installed downstream of both compressors for online measurements of the compression strength. The output signals are incorporated in the feedback control loops for the RF phase (LLRF in the sketch) of the accelerating modules in front of the bunch compressors. After each compression stage and after the final acceleration, bunch-arrival-time monitors (BAM) measure the arrival times of the electron bunches with respect to the optical reference. The arrival times measured at the first two locations are integrated into the feedback system, acting on the amplitude of the accelerating RF fields to stabilize the relativistic electron bunches. An external optical laser is synchronized to the MLO, which can be used for pump-probe experiments. This schematic represents the status of the stabilization system at the time when the presented experiments were performed. A complete overview can be found in Ref. [136].

## Bunch arrival-time monitor

The principle of the arrival-time monitor is explained in **Figure 6.7**. To measure the arrival time of the electron bunches at specific locations in the accelerator a pair of antennas is mounted symmetrically around the electron beam path. When the electron bunch passes, its transverse electric field generates a fast transient electronic signal of several GHz bandwidth in each antenna. To reduce the dependency on the electron beam orbit, the signals from the pair of opposing antennas is combined. The zero-crossing of the induced voltage signal is a measure of the arrival-time of the bunch charge center. This signal is coupled into an electro-optic amplitude modulator, where it is mixed with the optical reference pulse, provided by a stabilized fiber link. The relative timing of the optical reference pulse train is set such that one pulse overlaps with the voltage zero-crossing. Timing changes of the electron bunch will cause different modulation voltages experienced by the reference pulse, which results in different laser pulse amplitude modulations. As a result, bunch arrival time changes are encoded in amplitude changes of the reference pulse.

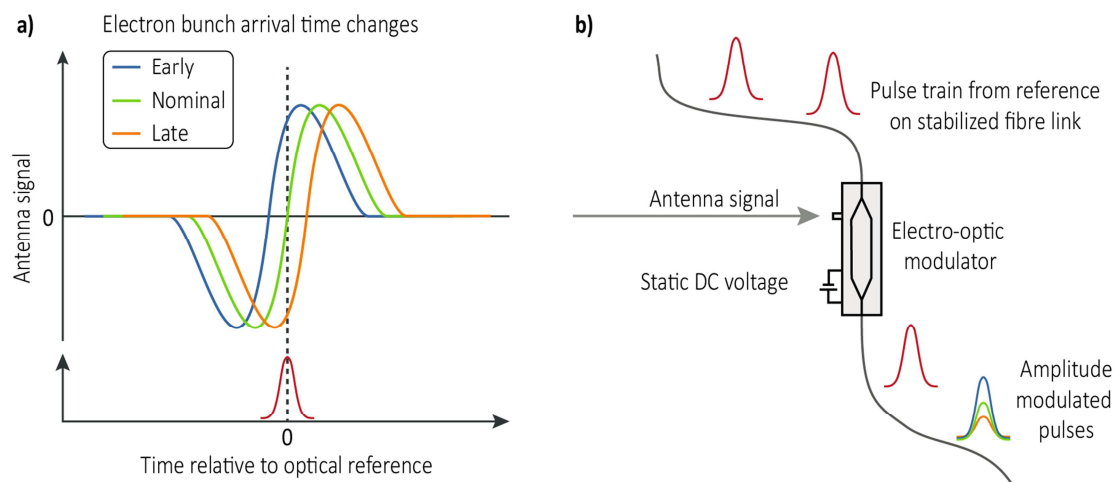


**Figure 6.7:** Principle of the bunch arrival time measurement. **a)** The relativistic electron bunch induces a bipolar transient signal in an antenna. The zero-crossing of the signal is used to measure the bunch centroid arrival time. For this, the timing of the optical reference is set such that one laser pulse coincides with the zero crossing of the antenna signal, as indicated in the picture. **b)** The antenna signal and the pulse train from the optical reference are coupled into an integrated electro-optic modulator. The electron bunch arrival time changes cause different modulation voltages, resulting in different degrees of amplitude modulation of the optical reference pulse, which is subsequently measured in a real-time balanced detection scheme. This illustration is based on figures from Ref. [124, 125].

Comparison of the laser pulse amplitude of the modulated pulse with the amplitude of a reference pulse that is not affected by the electron bunch, one can determine the electron bunch arrival time.

The electro-optic modulator (EOM) makes use of the of the linear electro-optic effect, which is the change of the refractive index of a nonlinear crystal caused by an electric field, as explained already in Chapter 4. The laser pulse that is coupled into a commercial Mach-Zehnder type electro-optic amplitude modulator is split into the two arms of the interferometer. To eliminate the needs for additional optics and associated instabilities, the EOM is realized as a photonic integrated circuit within the optical fiber distribution network. In each arm, the light travels through a waveguide built inside a lithium niobate (LN) crystal. The voltage signal from the pick-up antenna is applied to the two waveguides with opposite polarity. The birefringence in the LN introduces a phase shift between the laser pulses in both arms proportional to the applied electric field strength, which in turn depends on the electron bunch arrival time (see **Figure 6.7a**). Upon recombination the pulses from the two arms interfere depending on their relative phase shift. As a result, the amplitude of the recombined pulses changes with the relative timing between the reference laser pulse and the electron bunch.

The dynamic range of the measurement of several picoseconds is given by the temporal structure of the signal from the antenna, while the measurement accuracy of the single-shot arrival time measurement is determined by observing the arrival time of a single electron bunch at two independent monitors. These two monitors are separated by the final, straight, non-dispersive acceleration section of the accelerator (see **Figure 6.6**). During our experiments the accuracy of the bunch arrival time monitor was  $\sim 5$  fs, as determined by the correlation analysis of the independent arrival time measurements in the accelerator. It should be noted that this value also includes the timing jitter of the reference clock distribution network, as discussed before. A more detailed description of the operational principle can be found in Ref. [125].

### **Evaluation of the beam-based feedback**

With the BBF active, the arrival time jitter for each of the bunches within the macro-pulse is measured over 600 consecutive shots, as depicted in **Figure 6.8a**. The jitter is largest for the first bunches, which are not stabilized due to the feedback latency, and smallest for the last ones where the BBF has been applied to correct the accelerating fields. The jitter in the first few bunches is  $>50$  fs r.m.s. and it is reduced to  $(19 \pm 2)$  fs r.m.s for the last bunch in the

macro-pulse. The error is determined from the Gaussian fit to the distribution, shown explicitly in **Figure 6.8b** for the last bunch in the macro-pulse.

The performance of the beam-based feedback depends, in part, on how quickly the bunch arrival time can be evaluated, on the computation time required to calculate corrections in the accelerating fields and on the time needed to transfer this information to the field controller. All these factors are described by the latency of the feedback loop. With lower latency, corrections to the RF field can be applied faster, and stronger corrections can be made, resulting in a steady-state operation that is reached more rapidly with lower residual beam arrival time jitter [137]. In addition to the computational limits, a physical limit to the strength and speed of the feedback is given by the bandwidth of the accelerator cavities. In practice, steady state conditions are reached in only 15  $\mu\text{s}$  (which corresponds to 15 bunches for the macro-pulse repetition rate used here). This performance is achieved through unique low-latency control algorithms, which involve real-time calculations performed in integrated circuits using modern-field programmable gate arrays.

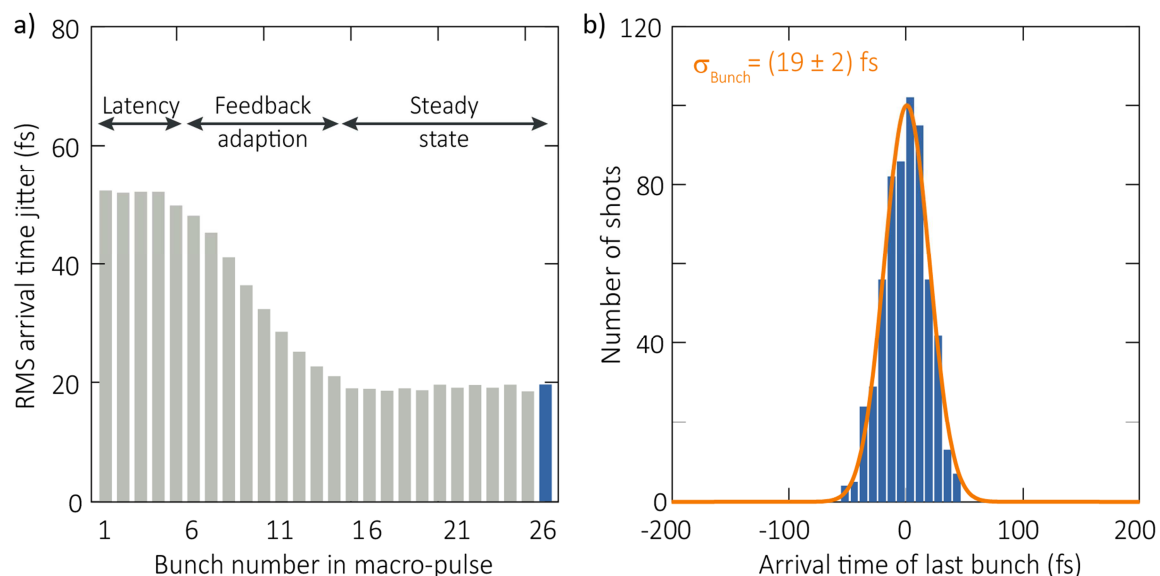


**Figure 6.8:** Bunch arrival-time feedback for accelerator stabilization. The width of the arrival time distribution along the macro-pulse for each bunch over 600 consecutive single shots is shown in panel **a**. The timing jitter without feedback is  $\sim 50$  fs r.m.s, as can be seen for the first few bunches in the macro pulse, which are not stabilized due to the latency of the feedback of about 5  $\mu\text{s}$  (5 bunches). During the feedback adaption period, the effect of the corrections of the accelerating fields according to the arrival times of the first bunches reduces the observed timing jitter to the final steady state value. In **b**) the distribution of the arrival times of the last bunch in the macro-pulse is depicted. It has width of  $(19 \pm 2)$  fs r.m.s. with an accuracy given by the numerical fit.

### 6.3.3 Optical locking of independent lasers at FELs

In general, synchronization of an external laser to the FEL requires locking of the external laser oscillator's repetition rate to the accelerating frequency. Usually, this is realized by comparing electronic RF signals, which have to be generated from the optical pulse train. However, with the optical synchronization scheme at FLASH the relative timing of an external laser and the optical reference can be measured directly using an optical-cross correlator. This represents one of the main advantages of the pulsed optical synchronization scheme, as with nonlinear optical methods the relative timing between the optical reference clock and the external laser can be determined with sub-femtosecond accuracy. The measured signal is then used as a feedback for adjustments of the external laser oscillator cavity length to tune and stabilize its repetition rate, allowing the timing between the external laser and the optical reference (and consequently the FEL pulses) to be controlled.

At FLASH, the external pump-probe laser oscillator is locked to the optical reference clock using the feedback from a two-color OXC. In **Figure 6.9** a schematic of the two-color OXC is shown. The pulses of the optical reference ( $\lambda_1 = 1560 \text{ nm}$ ) and the pump-probe laser oscillator ( $\lambda_2 = 800 \text{ nm}$ ) with different center carrier wavelengths are overlapped collinearly with a dichroic mirror. Then the two pulses are focused into a  $500 \mu\text{m}$  thick type-I phase matched  $\beta$ -barium borate (BBO) crystal, where the sum-frequency ( $\lambda_3 = (\lambda_1^{-1} + \lambda_2^{-1})^{-1} = 528.8 \text{ nm}$ ) of the two pulses is generated. The sum-frequency is separated from the input pulses with another dichroic mirror and an optical bandpass filter and measured with the first detector. For the second stage of the OXC one of the two pulses is delayed with respect to the other by a fixed amount. To accomplish this, the two input pulses are passed twice through a quartz plate after they are reflected by the dichroic mirror, as indicated in **Figure 6.9**. Propagation through the quartz plate introduces a fixed delay, as the group delay is function of the wavelength. After the rearrangement, the two pulses are mixed again in the BBO to generate a second sum-frequency signal, which is filtered and then measured by a second detector. To synchronize the two laser sources to each other, the output signal from the OXC is fed back into an electronic control loop, which controls the repetition rate of the external laser oscillator by adjusting the cavity length with one cavity mirror mounted on a piezoelectric stage. It should be noted that the magnitude of the relative timing change is uncalibrated and that to maintain a fixed temporal overlap between the laser pulses, it is only necessary to keep the sum-frequency signal from the two stages equal.

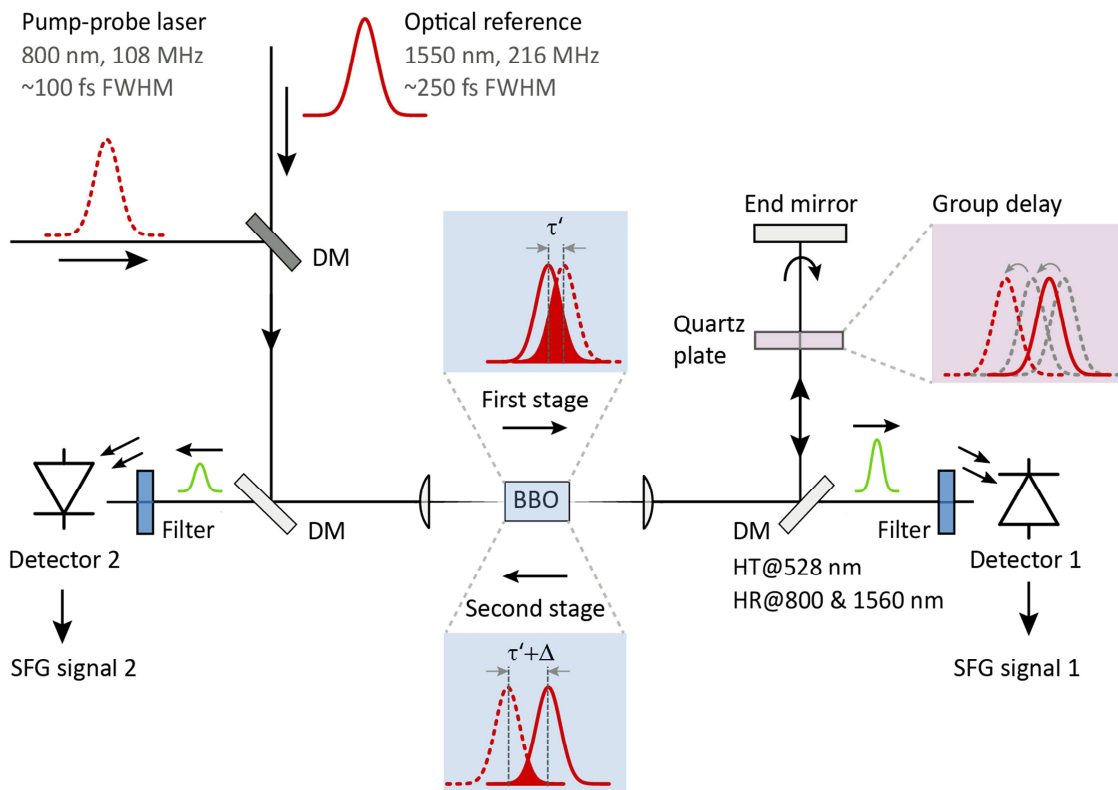


**Figure 6.9:** Schematic of the two-color OXC to measure the relative timing between two independent laser pulses with different central wavelength. The input pulses from the optical reference and the Ti:sapphire oscillator are overlapped collinearly with a dichroic mirror (DM). In the first stage of the OXC the input pulses are focused into a nonlinear crystal (here in a type-I phase-matched BBO), where the pulses generate a sum-frequency component. The strength of the sum-frequency generation (SFG) signal depends on the exact overlap of the pulses. The input pulses and the SFG signal are separated by another DM that transmits the sum-frequency but reflects the input wavelengths. The SFG signal is passed through a bandpass filter and measured by detector 1. Before the inputs pulses are focused a second time into the BBO, they travel twice through a quartz plate, where one of the pulses is delayed by a fixed amount with respect to the other, due to the different group velocities of the different wavelengths in quartz. The SFG component generated in the second stage is measured by detector 2. Combination of the SFG signals from the first and second stage gives a signal proportional to the relative delay between the two input pulses, without sign ambiguity.

For maximum sensitivity of the optical cross-correlator the slope at zero crossing should be maximal. For this, while maintaining sufficient large dynamic range, the thickness of the quartz plate, introducing the delay between the inputs pulses, must be chosen carefully, according to the pulse duration of the optical reference (250 fs) and of the pump-probe laser pulse (100 fs). Here, the plate was chosen to be 6 mm thick.

To characterize the locking between the pump-probe laser and the optical reference an independent balanced optical cross-correlator is used. For its calibration, the relative timing between the locked optical reference and the pump-probe oscillator is scanned across the full range of delays. In **Figure 6.10a** the measured characteristic cross-correlator signal is plotted, exhibiting regions where the detector is saturated (signal exceeding  $\pm 1$  V). The signal is zero when the two pulses overlap perfectly. Away from overlap, the magnitude of the signal increases until a maximum is reached when the pulses are separated by an amount given by their pulse durations. The signal vanishes when the separation increases further and the pulses are no longer overlapped. The time dependence of the cross-correlator output signal is modelled using Gaussian pulses with durations corresponding to the optical reference and the pump-probe laser and the resulting curve plotted also in **Figure 6.10a**. The measurement shows very good agreement with the expected values. The amplitude of the calculated cross-correlator signal can be converted to provide the correct temporal offset for any measured voltage within the dynamic range with sub-femtosecond resolution.

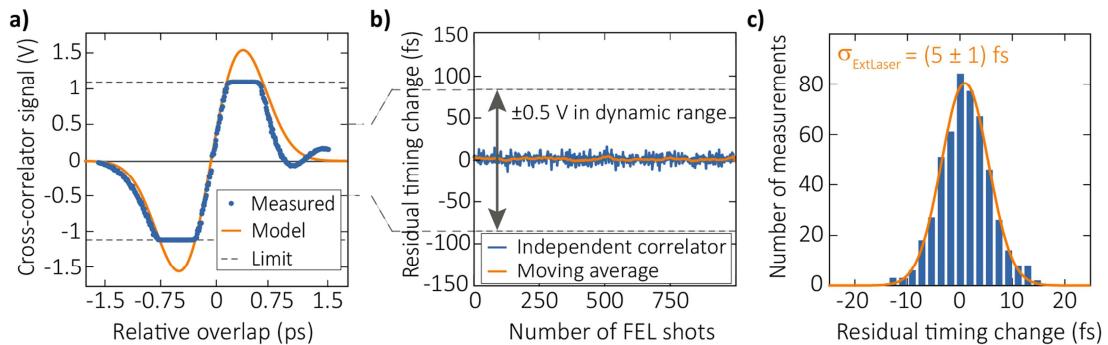


**Figure 6.10:** Characterization of the optical locking between the Ti:sapphire pump-probe laser and the optical reference laser at FLASH. **a)** Here the output signal of a balanced OXC, measured while the relative timing between the optical reference laser and the pump-probe laser was changed continuously, is plotted. Excluding the regions where the detector is saturated ( $\pm 1$  V), the measured curve matches the calculated one, based on the input laser duration. This measurement is used to calibrate the OXC. **b)** Residual timing jitter between the external laser and the MLO reference measured with the independent optical cross-correlator. **c)** The residual timing jitter between the two sources is found to be  $(5 \pm 1)$  fs r.m.s., with accuracy given by the numerical fit to the corresponding distribution.

With the calibrated signal, the performance of the optical synchronization between the external pump-probe laser and the MLO is evaluated. As shown in **Figure 6.10b,c** the residual jitter was found to be  $(5 \pm 1)$  fs r.m.s., when feedback is provided from the optical cross-correlator. This result corroborates the capabilities of the optical synchronization scheme.

For comparison, with the conventional electronic synchronization scheme employed at FELs the residual jitter is typically  $\sim 40$  fs r.m.s., as shown in **Figure 6.11**. The reason for this improvement is the extreme sensitivity of the OXC, where the relative timing between the two pulses is measured with sub-femtosecond accuracy within the  $\sim 400$  fs dynamic range of the cross-correlator. However, due to the limited dynamic range of the optical scheme, the two laser sources are first coarsely locked with conventional electronic phase detection before the all-optical synchronization scheme is engaged. With electronic synchronization the dynamic range of the feedback is given by half the RF accelerating reference period of 385 ps.

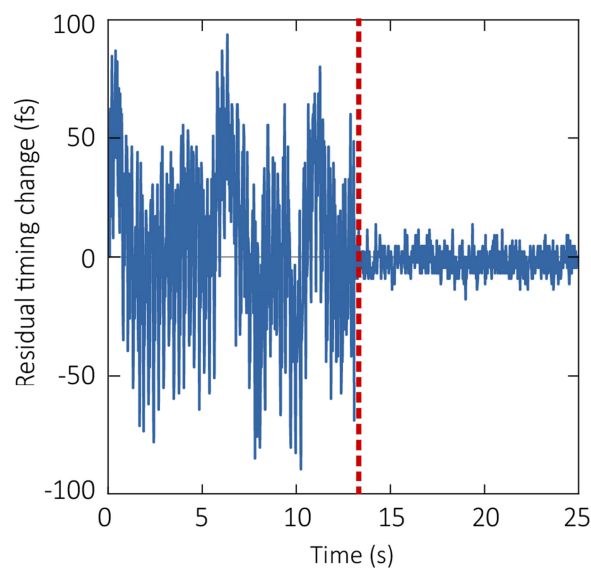


**Figure 6.11:** Comparison between the electronic and optical synchronization between two laser sources. An independent OXC was used to measure the residual timing between the MLO and the pump-probe laser at FLASH. In the first part of the measurement only the electronic synchronization scheme was active, resulting in timing jitter of  $\sim 40$  fs r.m.s. For the second part of the measurement (after 13 seconds) the feedback from the OXC was applied to measure the relative laser pulse arrival time fluctuations and to feed back the cavity length of the pump-probe laser. In this case the jitter between the sources is reduced to  $\sim 5$  fs r.m.s.

## 6.4 Characterization of the complete synchronization system

To evaluate the synchronization system, the method of choice is single-shot, time-resolved photoelectron spectroscopy using single-cycle THz pulses – a technique that simultaneously provides the FEL photon pulse duration and its relative arrival time with respect to the THz pulse. The theoretical background of time-resolved photoelectron spectroscopy is presented in chapter 3. A detailed description of the experimental set-up and measurement procedure is given in chapter 5. Here, the key aspects relevant for the present application will be repeated.

### 6.4.1 Experimental set-up & measurement

**Figure 6.12** sketches the experimental geometry (a photograph of the experimental setup is shown in Appendix C). The FEL photon pulse is focused into a Ne gas target producing a burst of photoelectrons that replicates its temporal profile. An overlapping single-cycle THz pulse modifies the initial kinetic energy of the photoelectrons. An electron TOF spectrometer detects the photoelectron spectrum for every single FEL pulse.

In our experiment, we used the Ti:sapphire NIR FLASH pump-probe laser ( $\sim 3.5$  mJ,  $\sim 60$  fs) to generate THz pulses of  $\sim 2$  ps in duration at a central frequency of  $\sim 0.6$  THz (chapter 5, Figure. 5.3). As the THz pulses are generated by optical rectification of the amplified pump-probe laser, the arrival time of the FEL photon pulse with respect to the THz pulse, retrieved from in the streaking measurement, is nearly equivalent to the arrival time of the FEL pulse with respect to the pump-probe laser pulse. The THz pulse is transported into the vacuum chamber and focused into the interaction region using a telescope consisting of a collimating Teflon lens with 300 mm focal length and a 150 mm focal length  $90^\circ$  off-axis parabolic mirror. The THz pulses were horizontally polarized and the TOF spectrometer was mounted in the same direction.

The FEL was operating at a photon energy of 234 eV (5.3 nm), bunch charge of  $\sim 0.3$  nC and in burst mode with 26 bunches per macro-pulse. The field-free Ne 2p and 2s photoemission spectra were used for the calibration of the TOF. The average energy width of the field-free Ne 2p spectrum in our measurements was  $\sim 3.7$  eV FWHM. Deconvolution of the measured spectrum with the independently measured average FEL bandwidth of 2.5 eV leads to an energy resolution of 2.7 eV [138].

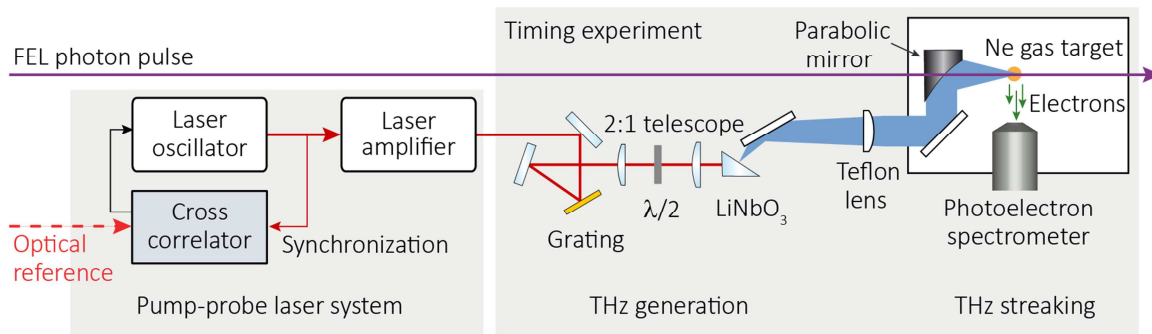


**Figure 6.12:** Experimental set-up for the relative timing measurement between FEL and external laser. An external laser is optically locked to the accelerator reference clock signal and used to generate single-cycle THz pulses by optical rectification in LiNbO<sub>3</sub>. The generated THz pulses and the FEL pulses are then overlapped in a Ne gas jet, where the FEL pulse profile and the relative arrival time of these pulses with respect to the THz field are measured using streaking spectroscopy. Since the THz pulse is phase-locked to the external laser, the relative arrival time between the FEL photon pulse and the THz pulse is nearly equivalent to the relative arrival time between the FEL photon pulse and external laser.

**Figure 6.13** shows the center of mass (COM) of each Ne 2p single-shot photoelectron spectrum versus the set delay between the FEL and THz pulse. On average, the kinetic energy of the streaked Ne 2p photoelectron peak shifts as the average delay between the THz streaking pulse and the FEL pulse is varied continuously over the full range of the THz pulse duration. Since the residual timing jitter is small, in this case the vector potential of the single cycle THz pulse is clearly traced out. The complete set of measurements consists of ~5000 single shots collected over 3 ps of relative delay.

As the jitter between the FEL pulse and the THz pulse is low in comparison to the THz pulse duration, the transformation map from streaked kinetic energy to time can be retrieved directly from the streaking measurements. This was not possible for the measurements presented in chapter 5, because there the timing jitter was large and the transformation map had to be constructed with the independently measured (EO-sampled) THz pulse shape. Constructing the map directly from the streaking measurements eliminates uncertainties that may arise by sampling a portion of the THz focus that does not interact with the FEL pulse in the gas target (see section 5.2.2).

To retrieve the map, the acquired single-shots were binned and averaged in time and interpolated. In **Figure 6.13** the resulting transformation map is plotted in orange color. The furthest upshifted and downshifted single-shot photoelectron spectra were found at 225 eV and 192 eV, respectively, corresponding to a THz peak electric field of ~85 kV/cm.

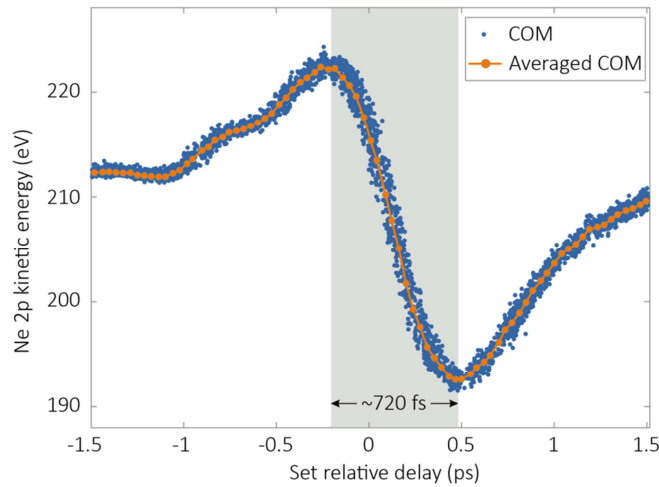


**Figure 6.13:** The center of mass (COM) of single-shot Ne 2p photoelectron peak is plotted as the set delay between the ionizing FEL photon pulse with 234 eV photon energy and the THz streaking pulse is changed gradually. Since the two sources are tightly synchronized, the shift in kinetic energy as a function of temporal overlap can be accurately mapped by averaging the shift over several single-shot measurements while the relative delay is scanned. Interpolating the averaged COM at each delay results in a continuous curve that represents the THz vector potential, plotted in orange. This curve is used to map the streaked photoelectron spectra, generated by an FEL pulse that arrives within the  $\sim 720$  fs single-valued streaking ramp, from kinetic energy to time.

To evaluate the timing jitter, the COM of the 2p photoemission peaks of 600 consecutive FEL pulses arriving near the zero-crossing of the THz vector potential, i.e. where the measurement is most sensitive, were mapped from kinetic energy to time. The arrival time distribution of these 600 single-shot measurements is plotted in **Figure 6.15** and has a width of  $(28 \pm 2)$  fs r.m.s, where the error is determined from the Gaussian fit.

The single-shot arrival-time measurement precision, which is governed by the fluctuations of the mean FEL photon energy (0.3 eV r.m.s for the measurement shown), is determined to be 3 fs r.m.s. The quality of the synchronization system should be evaluated and put into context with the FEL pulse duration, which is simultaneously provided by the THz streaking measurement.

To retrieve the pulse duration each streaked Ne 2p photoelectron spectrum of the corresponding 600 single-shots was first fitted with a Gaussian curve, then deconvolved with the 2.7 eV FWHM energy resolution of the TOF spectrometer, and finally converted to time using the gradient of the THz streaking field. In **Figure 6.14** the averaged streaking spectrogram and some single shots that were evaluated are plotted. The resulting FEL pulse duration distribution is shown in **Figure 6.15b**, yielding a mean value of  $(90 +6/-7)$  fs FWHM. The accuracy of the pulse duration measurements is evaluated from the statistical error in the single-shot photoelectron spectrum, as described in chapter 5.

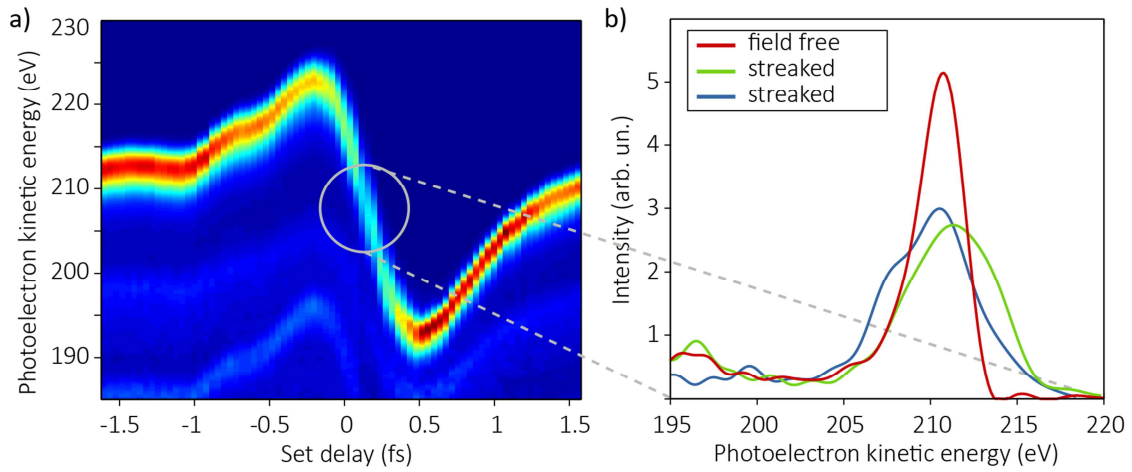


**Figure 6.14:** **a)** An averaged Ne 2p photoelectron streaking spectrogram is plotted. The shots arriving close to time zero can be analyzed to provide the temporal duration. **b)** In this panel photoelectron spectra of 2 FEL pulses arriving near-time zero are plotted. The FEL pulse duration is retrieved from the width of the streaked spectra. The curve in red color shows a field-free photoelectron spectrum.

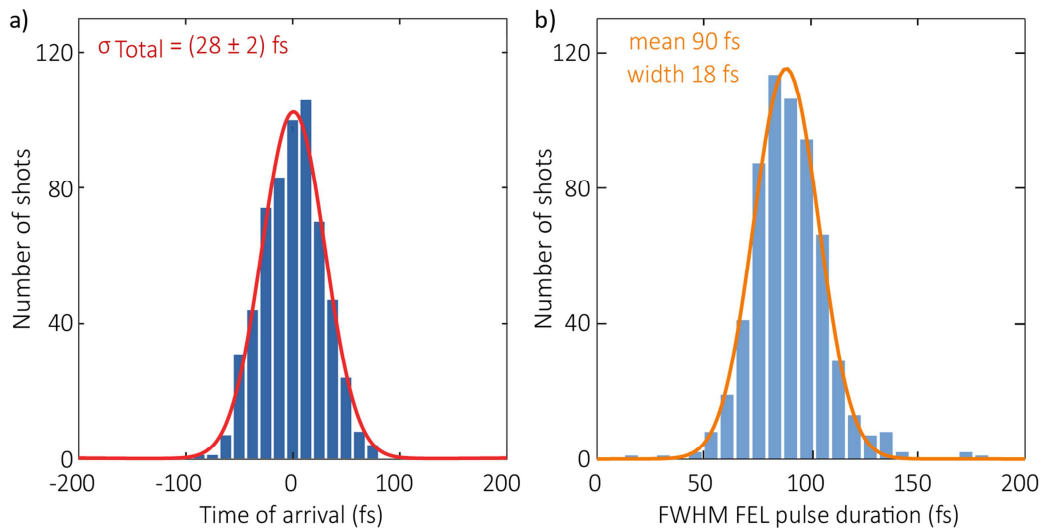


**Figure 6.15:** Total residual timing jitter characterized by THz streaking. The arrival time of 600 consecutive FEL photon pulses recorded at the zero-crossing of the streaking THz vector potential (see Figure 6.13) is evaluated from the streaked Ne 2p photoemission peaks and plotted in panel **a)**. The distribution of the arrival times yields a timing jitter of  $(28 \pm 2)$  fs r.m.s, where the error is determined numerically from the Gaussian fit. In **b)** the distribution of the pulse duration of these 600 consecutive shots is shown. The average pulse duration is  $\sim 90$  fs FWHM. The FWHM of the single-shot duration was determined with an average measurement precision of 7 fs.

## 6.4.2 Jitter analysis

For the all-optical synchronization scheme at FLASH the arrival time jitter between external laser pulses and the FEL pulses was measured to be  $(28 \pm 2)$  fs r.m.s for an average FEL pulse duration of  $(90 \pm 18)$  fs FWHM of the generated FEL pulses. The total jitter can be considered as a cumulative effect of several different sources. To attain better understanding the total jitter can be divided, thereby allowing the sources to be quantified. The known sources are:

- The jitter due to the MLO and its optical distribution  $\sigma_{OptRef}$ . This jitter is determined to be  $\sim 1$  fs r.m.s. from an independent measurement (see **Figure 6.4**).
- The jitter due to the synchronization of the external laser oscillator to the optical reference  $\sigma_{ExtLaser}$ , which is measured to be 5 fs r.m.s. (see **Figure 6.10**).
- The jitter of the electron bunch with respect to the optical reference  $\sigma_{Bunch}$ , that is measured to be 19 fs r.m.s. with an accuracy of  $\sim 5$  fs. After deconvolution, the underlying beam jitter is determined to be 18 fs r.m.s. (see **Figure 6.8**).

Assuming that the sources of jitter are uncorrelated, the measured total jitter is described as:

$$\sigma_{Total}^2 = \sigma_{OptRef}^2 + \sigma_{Bunch}^2 + \sigma_{ExtLaser}^2 + \sigma_{Residual}^2 . \quad (6.2)$$

Hence, we obtain a residual jitter  $\sigma_{Residual}$  of  $\sim 20$  fs r.m.s, which together with the electron beam jitter constitutes the largest contribution to the total jitter of the FEL photon pulses.

To improve the level of synchronization between laser and FEL, the two largest contributions, the electron beam jitter ( $\sigma_{Bunch}$ ) must be reduced and the residual sources ( $\sigma_{Residual}$ ) have to be identified and minimized. One source of jitter is the SASE process itself, as it gives rise to statistical fluctuations that are on the order of the cooperation time, which is a few femtoseconds for soft X-ray FELs. The pump-probe laser amplifier and the beam transport may also contribute to the residual jitter, as only the oscillator seed pulse is synchronized to the optical reference clock. Thus, path length fluctuations within the amplifier system could result in an unaccounted timing instability. In addition, the laser transport from the hutch to the experiment might also contribute to the residual jitter. However, such changes are expected to occur on comparatively slow timescales as they arise mainly from changes of the environmental conditions. In principle, a similar optical cross-correlation technique that is already applied throughout the synchronization network could be applied to stabilize the arrival time of the amplified pulses.

From the measured fluctuations of the photon pulse duration, we can conclude that a significant contribution to the residual jitter most probably results from the variation of the

compressed FEL-driving electron bunch composition. This uncertainty results in changes of the parts of the electron bunch that contribute to the FEL lasing process from shot to shot. If the FEL emission varies between the leading and the trailing edge of the electron bunch, additional jitter up to tens of femtoseconds would be observed in the photon pulse arrival time. As this effect scales with the electron bunch duration, it will naturally decrease for stronger compressed pulses, which are required for even shorter FEL pulses. Furthermore, as the electron bunch is already compressed by a factor of  $\sim 50$  from its initial value at the photoinjector, stronger compression will only have a minor influence on the arrival time jitter of the electron bunch centroid. This claim is also supported by the correlation between the photon pulse and the electron bunch arrival time, which will be discussed in the following.

### **Shot-to-shot comparison of the photon pulse and bunch arrival time monitor data**

A comparison of the single-shot time-of-arrival data of the electron bunch (measured after the second bunch compressor) and the photon pulse arrival time measured with THz streaking is shown in **Figure 6.17**. For the single-shot data there is only a weak correlation observed between the two different measurements, however the correlation is really good when the arrival times are compared on average over a few FEL and optical laser pulses. This discrepancy could arise due to several factors.

Since only the oscillator is synchronized to the optical reference clock, there could be potentially an additional contribution to the jitter introduced by the amplifier system, as discussed earlier. However, since there is a good agreement on average between the arrival times, we believe that the jitter introduced by the amplifier system is smaller than the electron bunch duration.

Another contribution to the residual jitter could be the variation of the lasing region along the electron bunch, which would result in an uncorrelated behavior among the different measured arrival times of the single shots. The reason for this is that in the BAM measurement only the arrival time of the COM of the charge distribution in the bunch is determined, which may not be the lasing part of the bunch. However, as the level of synchronization is better than the FEL photon pulse duration, this timing uncertainty introduced by the variation of the lasing portion would agree with our observation that the arrival times match only on average. The “lasing jitter” within the electron bunch, due to the changing electron bunch composition from shot to shot, may be the dominant contribution to the residual timing jitter. This jitter would naturally decrease for shorter electron bunches.

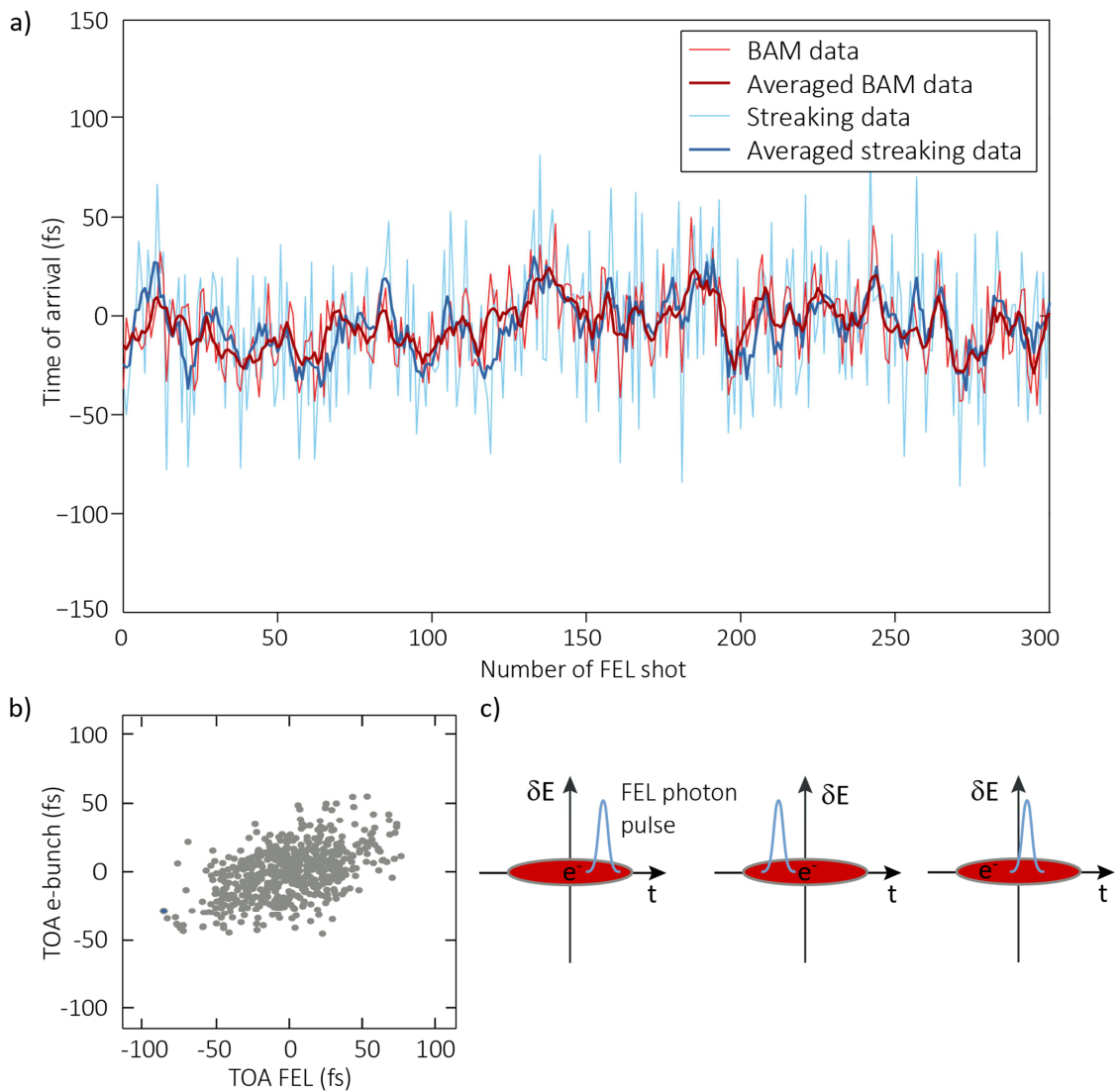


**Figure 6.16:** Correlation plot of arrival time measurements. **a)** Comparison between the time-of-arrival data of the electron bunch and the time-of arrival of the corresponding FEL photon pulse measured with THz streaking. The plot shows the single shot data, as well as the moving average of the data. **b)** Shot-to-shot correlation between the arrival time of the photon pulse and the arrival time of the electron bunch. The correlation between the single-shot data is poor. However, the moving average of the data shows quite good agreement as can be seen in a). The cartoon in **c)** describes one possible reason for the lack of correlation. The BAM measures the arrival time of the electron bunch centroid, which may not be the part of the electron bunch that fulfills the requirements for FEL emission. If the FEL emission alternates from shot-to-shot within the electron bunch, additional jitter will be observed in the arrival time of the photon pulse.

### 6.4.3 Optical versus RF synchronization

Here, we compare the all-optical synchronization over the conventional RF-based synchronization scheme. The measurements presented in chapter 5<sup>4</sup> were performed 2011 with only the RF synchronization active and without beam based feedback, while the data presented in this chapter was recorded 2013 with the all-optical synchronization and the beam stabilization active. **Figure 6.17** shows a comparison between the two streaking measurements taken with RF and with optical synchronization, respectively. The red points correspond to the COMs of the streaked photoelectron spectra with conventional RF synchronization (see also **Figure 5.7**). Around the zero-crossing of the streaking field, the timing jitter between the FEL and the THz pulse, or equivalently the NIR pulse that generates the THz pulse is evident. The central energies of the streaked spectra are widely spread at each set delay between the two pulses. On the other hand, the kinetic energy distribution is substantially narrower for the case of optical synchronization (data from **Figure 6.13**). For this comparison the latter one had to be scaled as the maximal kinetic energy shift was smaller in this measurement due to a weaker THz field strength available, which in turn results from a longer focal length of the parabolic mirror focusing the THz pulses into the interaction region. Interestingly, also far from temporal overlap the data recorded with the electronic synchronization scheme is more spread, which indicates that in addition to the arrival time jitter the photon energy jitter is larger. The lower level of energy jitter in the photon beam for the optical synchronization scheme may result from the improved energy stability and reduced fluctuations of the electron bunch composition with the beam-based feedback engaged. However, it is important to note that, as the measurements were not taken during the same beam time, the differences may originate also from other sources. It is possible that the differences in the photon energy jitter may also arise from a more stable trigger signal and/or a different set up of the accelerator.

---

<sup>4</sup> FEL photon pulse: 258 eV, 10 $\mu$ J, target gas: Helium 1s, THz: NIR  $\sim$ 3 mJ,  $\sim$ 50 fs, THz focusing: 3 inch effective focal length parabolic mirror

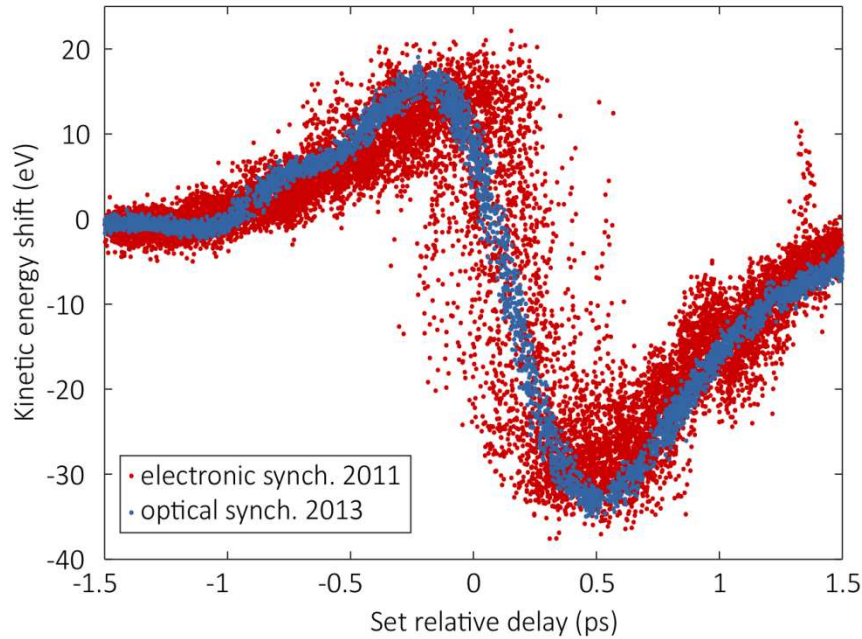


**Figure 6.17:** Comparison of THz streaking data taken with and without the optical synchronization system. The COM of the streaked photoelectron spectra as a function of set delay between the THz streaking pulse and the ionizing FEL pulse are shown. The red data points correspond to the THz streaking measurement that was performed in 2011 at FLASH (see chapter 5, Figure 5.7) with conventional RF synchronization, while the blue data points correspond to the measurement with optical synchronization. In order to compare the two measurements, the kinetic energy shift of the optical-synchronization measurement was scaled, as the THz field amplitude was smaller due to the longer focal length of the parabolic mirror that was focusing the THz into the interaction region during this beam time.

## 6.5 Summary

Using time-resolved THz photoelectron streaking we were able to characterize the all-optical synchronization scheme that was implemented at the FEL FLASH facility. The present synchronization system allows to stabilize the relative arrival times of the FEL photon pulses and external laser pulses to better than 30 fs r.m.s., while delivering  $\sim 90$  fs FWHM FEL pulses.

In addition, we were able to identify and to quantify the different sources of jitter. From our analysis we conclude that it should be possible to improve the overall synchronization to the sub-10 fs level for shortest FEL pulses. In order to obtain this, the residual beam jitter must be identified and minimized and the electron beam jitter has to be reduced. For the latter one, the latency in the feedback system of the beam based stabilization should be reduced. To achieve this at FLASH, one normal conducting cavity is being installed. Normal

conducting cavities have higher bandwidths, which allows for a faster regulation of the accelerating field to stabilize the bunch arrival time. In this way it is expected to stabilize the bunch arrival time to the 5 fs level [139]. Additionally, our jitter analysis indicates that the timing jitter scales with the pulse duration and will automatically decrease as shorter electron bunches are used to produce even shorter X-ray pulses.

As the level of synchronization is better than the average FEL pulse duration, time-resolved experiments can be performed without additional measurements of the relative timing between the pump and the probe pulse with almost optimal temporal resolution. Furthermore, as the timing between the pump and the probe pulse can be controlled better, most of the measurements would be recorded at the desired temporal overlap, which is inherently more efficient than random sampling and post-processing.

Additionally, the achieved level of synchronization might have impact on current FEL developments, such as seeding. This technique aims to overcome the poor temporal coherence and the shot-to-shot statistical fluctuations of the SASE generated X-ray pulses. In self-seeding, for example, a fixed spectral slice from the SASE radiation emitted in the first part of the undulator is used to seed the second part of the undulator. As a result, temporally coherent pulses with tunable pulse duration (by variation of the seed bandwidth) are emitted. To fully exploit those possibilities of such pulses in pump-probe experiments femtosecond synchronization is mandatory. Likewise, the electron energy jitter induced seed power fluctuations, which cause severe intensity fluctuations of the self-seeded FEL emission, might be minimized with a better facility wide synchronization [140]

The FEL radiation process can also be seeded externally by overlapping an independent optical laser pulse with the driving electron bunch. In this so called direct seeding, the seed signal has the same wavelength as the FEL resonance wavelength [141]. The emitted FEL radiation is then fully coherent with temporal and spectral properties given by the seed laser pulse. Currently, the most promising source for short wavelength (in the VUV and XUV region) seed pulses is high-harmonic generation in noble gases. Other external seeding techniques, like high-gain high-harmonic generation or echo-enabled harmonic generation rely on electron beam manipulation by the seed beam. In these techniques, FEL emission occurs at harmonic of the seeding laser wavelength and also here the properties of the FEL output radiation are determined by the seed radiation. In principle, these methods should provide natural synchronization of the FEL pulse and the seed laser pulse. However, successful operation of external seeding techniques relies on the precise temporal and spatial overlap of the seed laser pulses and the electron bunches. Thus, precise synchronization between the driving electron bunch and the external seed laser remains critical in order to ensure consistent temporal overlap.

To summarize, the improved timing stability that is achieved with the optical synchronization scheme will improve the experimental conditions for user experiments and enable new and more advanced developments at FELs. In particular, fully coherent FEL pulses with complete control over the FEL pulse properties is one of the possible most exciting future implementations, which could open up entirely new opportunities for researches.



## 7 X-ray pulse shaping at LCLS

The spectral and temporal properties of FEL X-ray pulses can be tailored to the needs of a specific experiment by directly modifying the FEL driving electron bunch. At the Linac Coherent Light Source (LCLS), X-ray double pulses with a controllable delay can be generated from a single electron bunch. Successful experimental application of the shaped FEL pulses requires precise characterization of their temporal structure. Moreover, accurate measurement of the X-ray temporal properties is essential to provide feedback for these beam-based pulse shaping approaches.

In this chapter, I present the measurement of the separation between the generated double pulses with laser-driven photoelectron spectroscopy. In the first section, the LCLS machine layout and operation parameters are described, while the experimental details and the results of the measurements are discussed in the second part of the chapter.

### 7.1 The Free-Electron Laser LCLS

LCLS at the Stanford Linear Accelerator Center (SLAC National Laboratory) is the first SASE FEL operating in the soft and hard X-ray regime and has been available for user operation since 2009 [16]. **Figure 5.13** shows the machine layout from the electron source up to the 132-m-long undulator, including two electron bunch compressor chicanes BC1 and BC2. The LCLS uses the last kilometer of the original SLAC 3-km-long linac to accelerate the FEL driving electron beam. The electrons are accelerated by an RF wave (2856 MHz) travelling in normal conducting copper cavities. The RF field is derived from a single master oscillator and amplified by klystrons. The X-ray photon wavelength is easily tunable from 22 Å (~540 eV) to 1.2 Å (~10 keV) by varying the electron energy in the range of 3.5 eV to 15 GeV. Moreover, the X-ray pulse length can also be changed from ~500 fs to less than 10 fs. As can be seen in **Table 7.1**, two main operation modes are available at LCLS: the standard mode with an electron bunch charge of 250 pC and the low-charge mode with 20 pC. The numbers for the FEL pulses lengths in the table are derived from simulations [142].

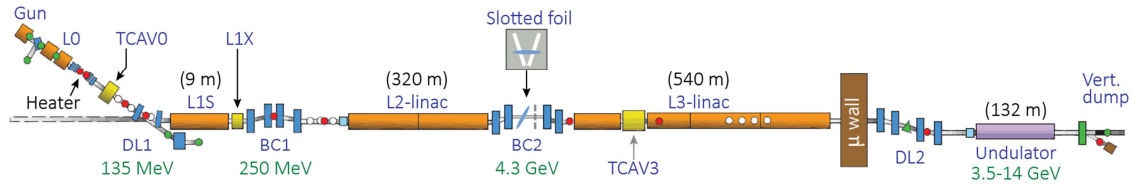


**Figure 7.1:** Schematic layout of the LCLS FEL machine layout. The injector produces single electron bunches with a repetition rate of up to 120 Hz. The two magnetic chicanes (BC1, BC2) compress the electron bunch longitudinally and thereby increase the peak current from the injector by a factor of  $\sim 100$  to  $\sim 3$  kA at the end of the linac. A 132 m long fixed-gap undulator is used for the x-ray generation process through SASE. Note this figure represents the machine status in 2011/12, when the measurements presented in this work were performed. (Figure reproduced from reference [16])

**Table 7.1:** LCLS electron and X-ray beam parameters for the low charge mode at 20 pC and at the more routine setting of 250 pC, according to Ref [142].

Parameter	20 pC	250 pC	Unit
Injector bunch length (rms)	1.3	2.5	ps
Initial peak current	5	30	A
Final bunch length (rms)	$\sim 3$	$\sim 30$	fs
Final peak current	$\sim 3$	$\sim 3$	kA
FEL pulse duration (FWHM) <sup>a</sup>	$\sim 2$	$\sim 60$	fs
FEL Peak power	$\sim 400$	$\sim 20$	GW

<sup>a</sup>Based on simulations at 1.5 Å.

### 7.1.1 Principle of longitudinal compression

At FELs a high peak current (typically kiloampere level) is required to efficiently generate radiation at X-ray wavelengths in an undulator structure and to achieve saturation. High peak currents cannot be generated directly in the electron source, as repulsive forces between the electrons would lead to an increase in transverse emittance resulting in a significant deterioration of the FEL performance. These space charge effects largely cancel at relativistic electron energies. Therefore, low current electron bunches are created and accelerated to higher energies and then temporally compressed in the magnetic bunch compressor chicane, consisting of four bending magnets. The principle of the longitudinal bunch compression is illustrated in **Figure 7.2**. The bunch compressor consists of four

bending magnets. The trajectory of the electrons passing through the magnetic chicane varies with their kinetic energy. Electrons with higher energy travel along a shorter path than electrons with lower energy.

Longitudinal electron bunch compression is achieved in two steps: First, a negative linear energy chirp ( $\Delta E / E \sim -z$ , with  $z$  being the position within the bunch) is introduced by off-crest acceleration in the RF-fields prior to the chicane. In this case, as shown in **Figure 7.2** in the upper left illustration, the energy of the electrons in the tail of the bunch is higher than of those in the head. In the second step, the electron bunch passes through the magnetic chicane. Due to the energy-dependent trajectories, the electrons in the tail take a shorter path and catch up with the electrons in the head of the bunch at the exit of the chicane, thereby compressing the longitudinal bunch length [33]. By adjusting the RF phase in the cavities prior the magnetic chicane, the compression ratio of the electron bunch is changed and thus the electron bunch length can be controlled. This allows to generate electron bunches with durations below 10 fs [142].

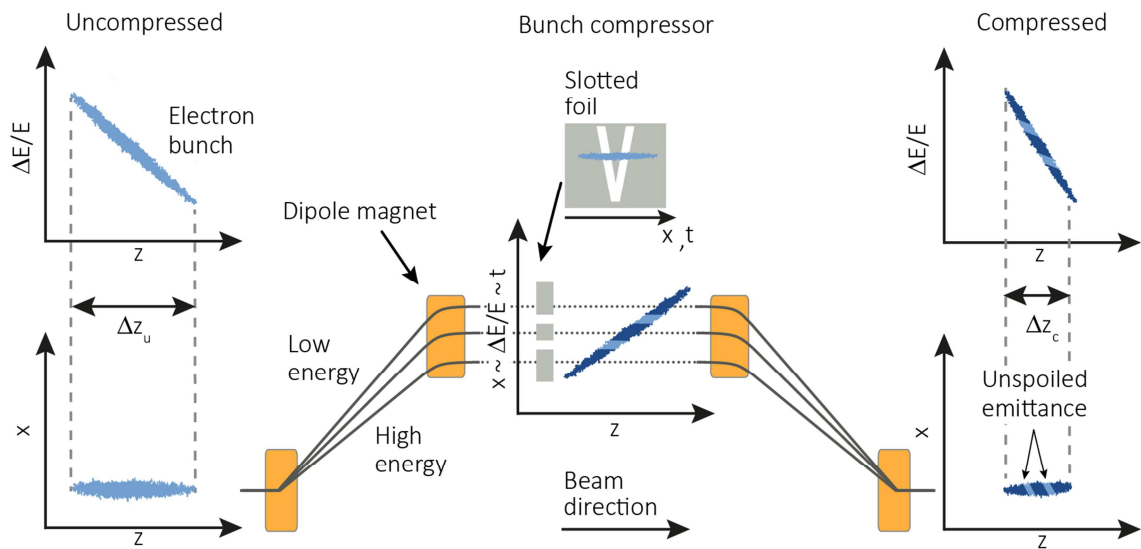


**Figure 7.2:** Longitudinal electron bunch compression and temporal shaping. To compress the electron bunch, first an energy chirp is imprinted on it, as depicted on the left. It is then sent to a magnetic chicane, comprising of four dipole magnets. The electron trajectories in the magnetic chicane are energy dependent. The higher energy electrons at the tail of the bunch travel a shorter distance than the leading lower energy electrons and are thus able to catch up with them. In the center of the magnetic bunch compressor chicane, where the electrons are maximally dispersed in transverse direction, a V-shaped slotted aluminum foil is inserted. The slots in the foil leave two narrow parts in the beam unspoiled to permit only in these parts lasing in the FEL undulator. At the exit of the chicane, where the transverse dispersion is zero, the two unspoiled parts are separated in time and will generate two subsequent X-ray pulses. The separation and duration of the X-ray double pulses is controlled with the slot geometry.

The electron bunch properties determine the corresponding X-ray FEL pulse durations, which have similar or even shorter durations [143,144]. As can be seen in **Table 7.1**, the shortest pulse durations are achieved in the low charge mode at 20 pC, as only in this mode the transverse emittance is reasonably preserved, even near full compression. However, changing the charge requires additional accelerator tuning and X-ray optics alignment [14<sup>4</sup>]. Other methods that promise even shorter pulses, down to the attosecond regime, require significant changes in the design of the FEL, see for example Ref. [145,146,147]. A simple way to generate and to shape short FEL pulses, which requires no changes in the linac, is the emittance-spoiling foil [148].

### 7.1.2 Temporal shaping at X-ray FELS

Temporal shaping of the X-ray FEL pulse can be achieved by modifying the emittance, which is defined as the area occupied by the electrons in the position-momentum phase space, of the driving electron bunch. This scheme relies upon the fact that the SASE gain process is highly dependent on the transverse emittance of the electron beam. A simple and robust implementation is illustrated in **Figure 7.2**. Here, a thin slotted aluminum foil is inserted in the center of the bunch compressor (BC2 at LCLS, see Figure 7.1) chicane in the path of the beam [148]. At this position of the chicane the linear energy chirp of the electron bunch is mapped onto the transverse spatial coordinate  $x$ , resulting in a tilt of the bunch with respect to its direction of propagation. The emittance of most of the beam increases by Coulomb scattering of the electrons passing through the foil, leading to a strong suppression of the FEL gain in the undulator in these fractions of the bunch, while the FEL gain remains practically unaffected in the unspoiled (preserved emittance) slice passing through the slit. By introducing a V-shaped double slotted foil in the chicane, two time slices of the electron bunch remain unspoiled, resulting in the emission of two, time delayed, collinear X-ray pulses. The pulse duration can be controlled by different slot widths, while the separation can be regulated by variation of the insertion depth of the foil, which changes the transverse separation between the unspoiled parts of the electron bunch. For a slot distance of  $\Delta x$  the temporal separation of the two pulses can be estimated from [144]:

$$\Delta t = \frac{\Delta x}{\eta h C c}, \quad (7.1)$$

where  $\eta$  is the momentum dispersion at the middle of the chicane,  $h$  is the linear energy chirp introduced in L2,  $C$  is the bunch compression factor, and  $c$  the speed of light. The linear chirp  $h$  is defined with the electrons' relative energy spread over the longitudinal bunch length coordinate  $z_0$  before compression by:

$$\frac{\Delta E}{E} = h z_0. \quad (7.2)$$

Similarly, the pulse duration can be calculated from the slot width and can be found in Ref. [148]. The main difficulty in these calculations is the accurate knowledge of the initial beam conditions, such as the energy chirp. Moreover, it is also hard to take account of the collective effects and high order optics in these simple calculations.

The X-ray pulses from the emittance-spoiling foil can be as short as few femtoseconds and even reach sub-femtosecond durations [149]. The duration of these ultrashort X-ray pulses was also measured with the photoelectron streaking technique and is reported in Ref. [150].

## 7.2 Experimental implementation and results

In this chapter, I present photoelectron streaking measurements aimed to characterize the double X-ray pulses generated with the V-slotted foil method. In a first beam time at LCLS, we used THz streaking pulses generated with the tilted pulse front method as in the experiments at FLASH discussed previously. The rise time of the THz vector potential in this case is about 650 fs, resulting in a dynamic range that fully accommodates the typical timing jitter at LCLS, and it provides the possibility to measure pulses up to 100 fs in duration. In a second experiment at LCLS, THz streaking fields generated from the organic electro-optic crystal DSTMS were applied. These THz pulses have steeper rise time of less than 200 fs, which in principle can lead to higher resolution measurements, but with reduced dynamic range. Both experiments were performed at the atomic, molecular and optical science (AMO) instrumental end station in a vacuum chamber [151]. The THz streaking fields were characterized by EO-sampling. In order to do this, the THz and a weak NIR beam were focused onto a 100  $\mu\text{m}$  thick GaP crystal placed in the interaction region. We used neon gas supplied by a 50  $\mu\text{m}$  diameter gas nozzle for the streaking measurements. The gas was streaming continuously and the background pressure in the experimental chamber was kept constant at  $\sim 1 \times 10^{-6}$  mbar. To collect the photoelectron spectra, the same electron TOF was used as for the measurements at FLASH [152]. The photon energy was calculated from the electron beam energy and the measured photoelectron spectra were corrected by the corresponding value for each FEL shot to correct for the photon energy jitter. A YAG screen was placed in the interaction region to align the beams to the same spot to ensure spatial overlap of the X-rays with the THz/NIR. Coarse timing was achieved electronically, for that the signals from a fast photodiode in the beam path were observed and synchronized.

Experimental details and results of both experiments are discussed in the following two sections. Here only a short description of the experimental set-up and alignment procedure is given, for more details I refer to chapter 5.

### 7.2.1 Large dynamic range: THz streaking fields from LiNbO<sub>3</sub>

In the first experiment performed at LCLS, the THz pulses were generated by optical rectification in LN similar to the experiments conducted at FLASH. Due to the higher NIR pump pulse energy of up to ~20 mJ, THz pulses with energies of 10  $\mu$ J were generated. The measurement geometry resembled the streaking experiments at FLASH presented previously (see **Figure 5.2**). The THz beam was collimated with a 3 inch Teflon lens of a focal length of 275 mm and focused with a 3 inch, 90° off-axis parabolic mirror with an effective focal length of 3 inch. Electro-optic sampling was used to characterize the THz pulse shape at the position of the gas target. The maximum field-strength determined in the streaking measurements was ~400 kV/cm. **Figure 7.3** shows an averaged streaking spectrogram of ~25000 single-shot streaking spectra of the neon 1s line ( $E_b=870$  eV) recorded with an FEL photon energy of  $E_\gamma \approx 1010$  eV. Here, every single shot spectrum was fitted with a Gaussian and an exponential decay time for the background (which arises from the secondary electrons). In the plotted streaking spectrogram the background is subtracted. As indicated with the arrow, the streaking ramp, which defines the dynamic range of the measurements, was ~660 fs. This is longer than the typical r.m.s time-of-arrival jitter of 200 fs at LCLS. The total kinetic energy shift was ~120 eV.

With these THz pulse parameters we measured the resulting X-ray pulse separation at 5 different double-slotted foil positions with an electron bunch charge of 140 pC, a maximum compression of 600 A after BC2 and with FEL photon energies of ~1010 eV. For these measurements the LCLS gas attenuator transmission was ~6%. For every double slotted foil position, a streaking trace consisting of ~50000 single-shot spectra was recorded. In order to extract the double pulse separation, the spectra resulting from FEL pulses arriving on the main streaking ramp were fitted and mapped from kinetic energy to time with the transformation map. As discussed in chapter 3, the transformation map (or streaking map) was constructed with the independently measured THz electric field waveform to provide the shape of the streaking field and calibrated with the single shot that was maximally shifted in kinetic energy to provide the field strength. The result of the measurements are summarized in **Figure 7.4**, where the distribution of the double-peak separation is plotted. We were able to measure peak separations from ~160 fs to ~50 fs and we found that the separation between the X-ray emission peaks varied approximately

linearly with the insertion depth of the double slotted foil (see **Figure 7.12**). The statistics for the intermediate separation is better than for both the bigger and smaller peak separations. We did not find in every recorded single shot spectrum a double pulse structure and several reasons are suggested to explain this. Firstly, energy jitter in the electron beam may result in a changed deflection in the magnetic chicane and the electron bunch simply may not pass through both slots. Moreover, at big slot separations the amount of recorded double pulses might be substantially reduced due to the poor electron beam quality at the edges of the bunch. In addition, due to the present timing jitter one of the pulses could fall out of the measurement window for some shots. For smaller separations, the double pulse structure can only be resolved for pulses arriving near the middle of the streaking ramp, where the temporal resolution is highest.

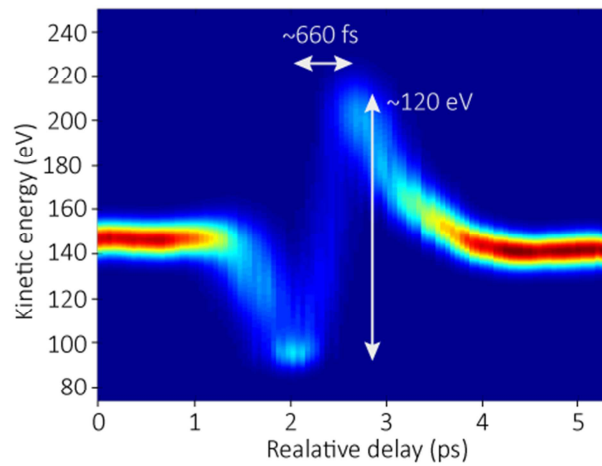
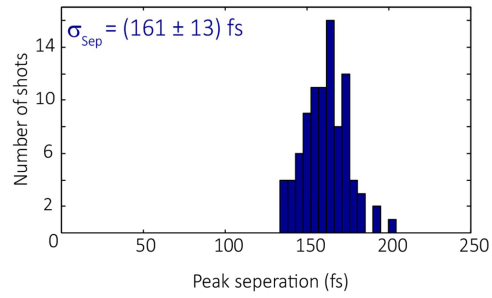
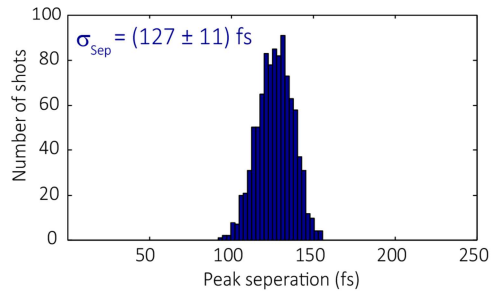


**Figure 7.3:** Fitted and averaged Photoelectron spectra of Ne 1s as function of set delay between the THz streaking pulse and the ionizing FEL pulse at  $\sim 1010$  eV. Coarse synchronization between the FEL pulse and THz pulse was maintained electronically. The streaking ramp of  $\sim 660$  fs is longer than the maximum expected FEL pulse timing jitter.

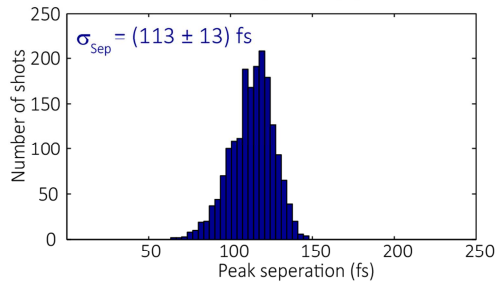
Bunch charge: ~150 pC  
 BC2: 1000 A  
 V-spoiler: -26.5 mm  
 Peak separation energy:  $(28 \pm 2)$  eV



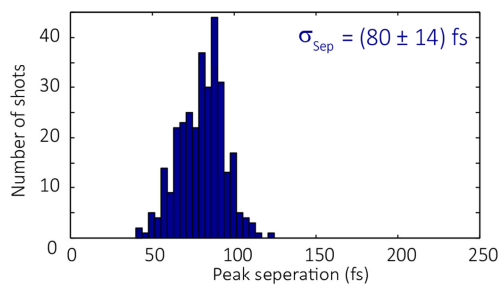
V-spoiler: -24.5 mm  
 Peak separation energy:  $(22 \pm 2)$  eV



V-spoiler: -22.5 mm  
 Peak separation energy:  $(19 \pm 2)$  eV



V-spoiler: -20.5 mm  
 Peak separation energy:  $(16 \pm 2)$  eV



V-spoiler: -18.5 mm  
 Peak separation energy:  $(11 \pm 2)$  eV

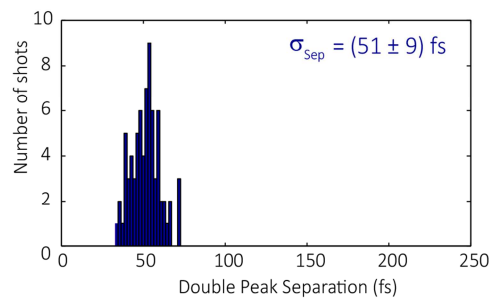


**Figure 7.4:** Measured double pulses generated with the double-slot geometry at a electron bunch charge of 140 pC and compression of 600 A at BC2.S hown are the results of the THz streaking measurements performed with the LN generated THz pulses.

### 7.2.2 High Temporal Resolution: THz streaking fields from DSTMS

To improve the temporal resolution, stronger streaking fields and/or fields with steeper rise time need to be applied. High power single-cycle THz pulses can be generated by collinear optical rectification in the organic ionic crystal DSTMS pumped at infrared wavelengths as described in Sec. 4.2.2 [91]. The optimal pump wavelengths are in the wavelength range from 1400 nm to 1700 nm corresponding to the generation of 1.5 THz and 2.0 THz [91].

#### Experimental details

In our experiments we used a  $\sim 440$   $\mu\text{m}$  thick DSTMS crystal with a diameter of  $\sim 8$  mm pumped by a collimated infrared beam with pulse energy of  $\sim 1.2$  mJ at a wavelength of 1500 nm. The infrared pulses were supplied by a three-stage optical parametric amplifier (OPA) pumped by  $\sim 50$  fs,  $\sim 14$  mJ Ti:sapphire laser pulses at 120 Hz. To block the infrared radiation, black polypropylene was placed after the DSTMS crystal. The THz radiation was coupled through a polymer window into the vacuum chamber, where it was focused with a 3-inch effective focal length  $90^\circ$  off-axis parabolic mirror into the interaction region. At this position the THz temporal waveform was characterized by EO-sampling. This was done by focusing the THz radiation and a weak 800 nm probe beam, split off from the Ti:sapphire pump beam of the OPA, onto a  $100$   $\mu\text{m}$  GaP crystal. In **Figure 7.5**, the temporal and the corresponding spectral characteristics of the THz pulse are shown. With 1.2 mJ pump energy, field strengths of  $\sim 860$  kV/cm were achieved. The generated THz radiation is emitted in forward direction collinear with the pump, which facilitates a much easier alignment than for the THz generation with the tilted pulse front method. Moreover, a well collimated, low divergence THz beam is generated, obviating the need for additional recollimation optics. The THz is polarized in the same direction as the pump, which in this case is horizontal, to be parallel with the electron TOF detector. **Figure 7.6** shows a sketch of the used experimental set-up in the case of THz field generation with DSTMS.

As mentioned previously, only if the timing jitter between the streaking pulse and the X-ray pulse is lower than the streaking field half-cycle, the X-ray pulse will arrive at a uniquely defined position on the streaking ramp, which enables calibrated transformation from streaked kinetic energy shift to time. Since in this second experiment at LCLS, the relative arrival time jitter between the X-ray pulses and an external optical laser was larger than the THz streaking ramp of  $\sim 180$  fs, a jitter correction method was employed in conjunction with the streaking experiment.

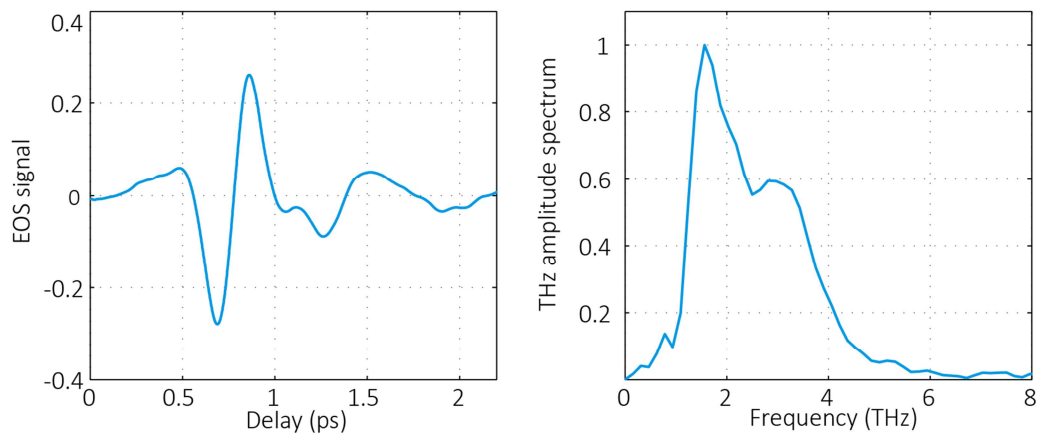


**Figure 7.5:** Single-cycle THz pulse from DSTMS. For the THz generation the  $\sim 440 \mu\text{m}$  thick DSTMS crystal was pumped with 1 mJ pulses at  $1.5 \mu\text{m}$ . A weak probe pulse at  $800 \text{ nm}$  and  $\sim 50 \text{ fs}$  pulse duration is used for the EOS measurement in a  $100 \mu\text{m}$  thick GaP. The resulting temporal shape of the THz pulse is plotted on the left. The spectrum of the THz pulse is shown on the right. The beam path of the THz was pure with nitrogen.

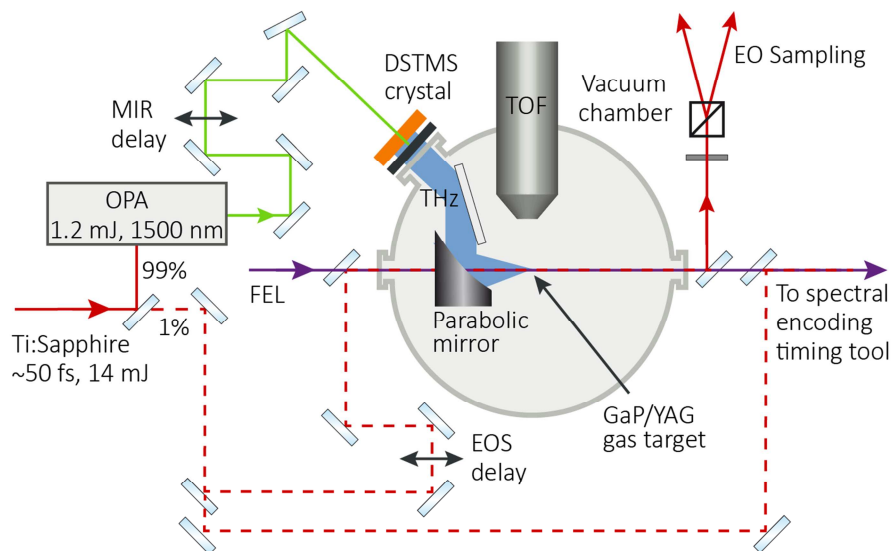


**Figure 7.6:** Experimental set-up at LCLS with DSTMS generated THz streaking pulses. Infrared pulses at  $1500 \text{ nm}$  with  $\sim 1.2 \text{ mJ}$  pulse energy are generated by an optical parametric amplifier, pumped by  $\sim 14 \text{ mJ}$  Ti:sapphire laser pulses. To generate the THz radiation the collimated infrared pump beam is sent through the  $\sim 500 \mu\text{m}$  thick DSTMS crystal at normal incidence. A filter is installed after the DSTMS crystal to block the infrared radiation. The generated phase-stable single-cycle THz pulse is focused with a 90-degree off axis parabolic mirror. The FEL and a weak  $800 \text{ nm}$  beam (originating from the pump of the OPA) are passed through a hole in the parabolic mirror and collinearly overlapped with the THz beam. For the EO-sampling the GaP crystal is placed in the interaction region. Part of the Ti:sapphire pump beam is sent directly to the spectral encoding tool as illustrated.

To correct for the arrival-time jitter, we measure the arrival time of the X-ray pulses with the spectral encoding method for every FEL and laser shot [153]. Here, the X-ray induced changes of the optical properties in a dielectric material are probed with a chirped super continuum to determine the relative arrival time of the X-ray pulse. To achieve this, a part of the NIR pump laser ( $\sim 1 \mu\text{J}$ ) is split off before the OPA and sent to the timing tool as illustrated in **Figure 7.6**. The NIR laser pulse is focused into a 1mm thick C-cut sapphire plate, where a super-continuum is generated through self-phase modulation. This white light is stretched while propagating through several optical components to  $\sim 1.5$  ps. Thus the different spectral components are temporally spread. The white light and the X-ray pulses are passed through a silicon nitride ( $\text{Si}_3\text{N}_4$ ) membrane. The X-ray pulse induces a change in the complex index of refraction of the material and thereby modulates the amplitude and phase of the white light. This modulation manifests itself as an edge in the transmitted spectrum of the super-continuum. The arrival time of the X-ray pulse is encoded as the position of the edge in the transmitted spectrum. For more details see for example Ref. [153, 154].

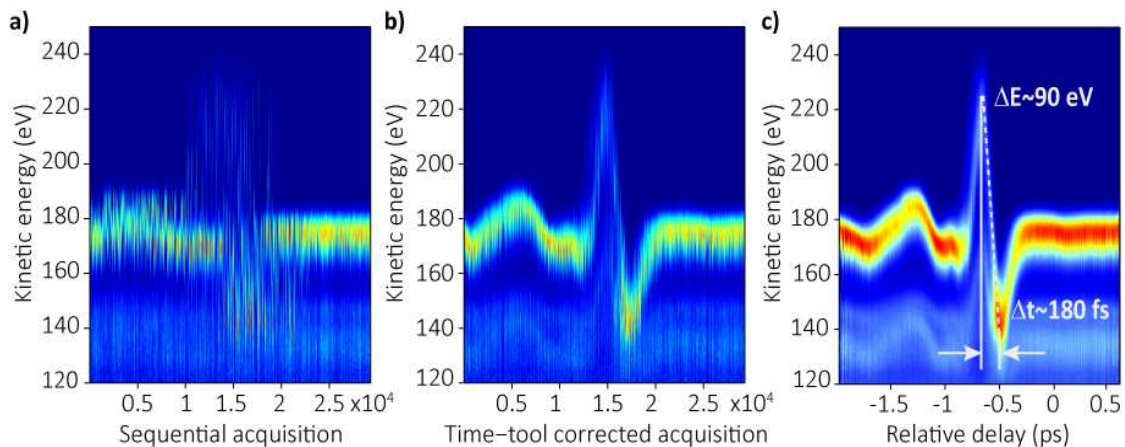


**Figure 7.7:** DSTMS streaking at LCLS in conjunction with the timing tool. In all three pictures the same photoelectron spectra of Ne 1s (870.2 eV), recorded as the delay between the THz pulse and the ionizing FEL pulse ( $E_\gamma = 1050$  eV) was continuously changed, are shown. Coarse synchronization between the ionizing FEL pulse and THz pulse was maintained electronically. In **a)** a single-shot spectrogram is shown, where the photoelectron spectra are plotted in the sequence as they were recorded. The timing jitter between the FEL and the THz is larger than the streaking field half-cycle which leads to a smeared spectrogram and the vector poetical of the THz streaking pulse cannot be identified. In **b)** the arrival-time of the FEL X-ray pulse was corrected according to the data retrieved from the spectral encoding measurement. Here the streaking field is clearly observed. **c)** Corresponding time tool sorted and averaged streaking spectrogram. The streaking ramp is  $\sim 180$  fs long with a total kinetic energy shift of  $\sim 90$  eV.

For our measurements, the LCLS was working with an electron bunch charge of 150 pC and beam energy of 4.8 GeV. The peak current after BC2 was about  $\sim 1$  kA. The expected FEL pulse durations for these machine settings is 150 fs. We used X-ray pulses at a photon energy of  $E_\gamma=1050$  eV with an independently measured bandwidth of  $\sim 6$  eV and pulse energy of approximately 0.2 mJ to ionize the Neon 1s core level ( $E_b=870.2$  eV). In **Figure 7.7** a streaking spectrogram measured with the DSTMS generated THz pulse is depicted. The Ne 1s line was recorded as function of set delay between the THz streaking pulse and the ionizing FEL pulse. On the left graph, a single-shot spectrogram in the sequence as it was recorded is plotted. The plot in the middle shows the same single-shot spectrogram, but sorted according to the arrival-time data of the X-ray pulse with respect to the NIR pulses as measured with the spectral encoding timing tool. While in the sequential unsorted spectrogram the THz streaking field cannot be observed, it can be clearly recognized in the timing-tool sorted data. Thus, with the timing tool, each X-ray pulse can be assigned to the correct position within the THz vector potential. This allows for a unique energy to time transformation to retrieve the FEL pulse profile and to increase the accuracy of the arrival time measurement.

The THz streaking ramp is  $\sim 180$  fs long and the total kinetic energy shift is about 90 eV, which corresponds to a THz electric field strength of  $\sim 860$  kV/cm. When using the modulation measured in the EOS measurement, the resulting electric field strength is  $\sim 440$  kV/cm. This big discrepancy could be due to several reasons. The efficient detection of the THz radiation by means of the Pockels effect requires, among other things, correct crystal orientation with respect to the linear polarization of the THz and the probe beam and an EO crystal with low levels of impurities and structural defects. Moreover, the mismatch of the THz phase velocity and the probe beam group velocity at 800 nm in GaP might also lead to a reduction of the detected signal at these THz frequencies [155]. In addition, the electro-optic coefficient also depends on the THz frequency, and we might not have the correct value for our calculations.

### **Double-slotted foil measurements**

With the same machine settings as described above, we measured the X-ray double pulses generated with the V-slotted foil at three different insertion depths. The results of these measurements are summarized in the next three figures. **Figure 7.8** shows the measurement for the maximum separation between the unspoiled parts of the electron

bunch, and therefore the maximum delay between the peaks. In panel a) the sorted and averaged streaking spectrogram composed of  $\sim 50000$  single-shot spectra is plotted. To determine the precise peak separation the single shots arriving on the main streaking ramp were fitted. The separation of the peaks in energy was found to be  $(53 \pm 4)$  eV, which corresponds to a peak separation of about  $(66 \pm 4)$  fs, where the error is determined numerically from the Gaussian fits. In panel d) an example of a measured single shot photoelectron spectrum and the corresponding X-ray pulse profile is plotted. For the measurements in **Figure 7.9**, the separation between the unspoiled parts was reduced slightly, resulting in X-ray double pulses separated by 56 fs. Here, the splitting of the streaking curve can be clearly observed, as depicted in the averaged streaking spectrogram in panel a). In the panels b) and c) the histograms of the peak separation in energy and time extracted from the single shots are shown. For the narrowest separation that we measured, displayed in **Figure 7.10**, the distinct X-ray emission peaks are separated by  $(38 \pm 6)$  fs. Also here the double streaking curve can be observed.

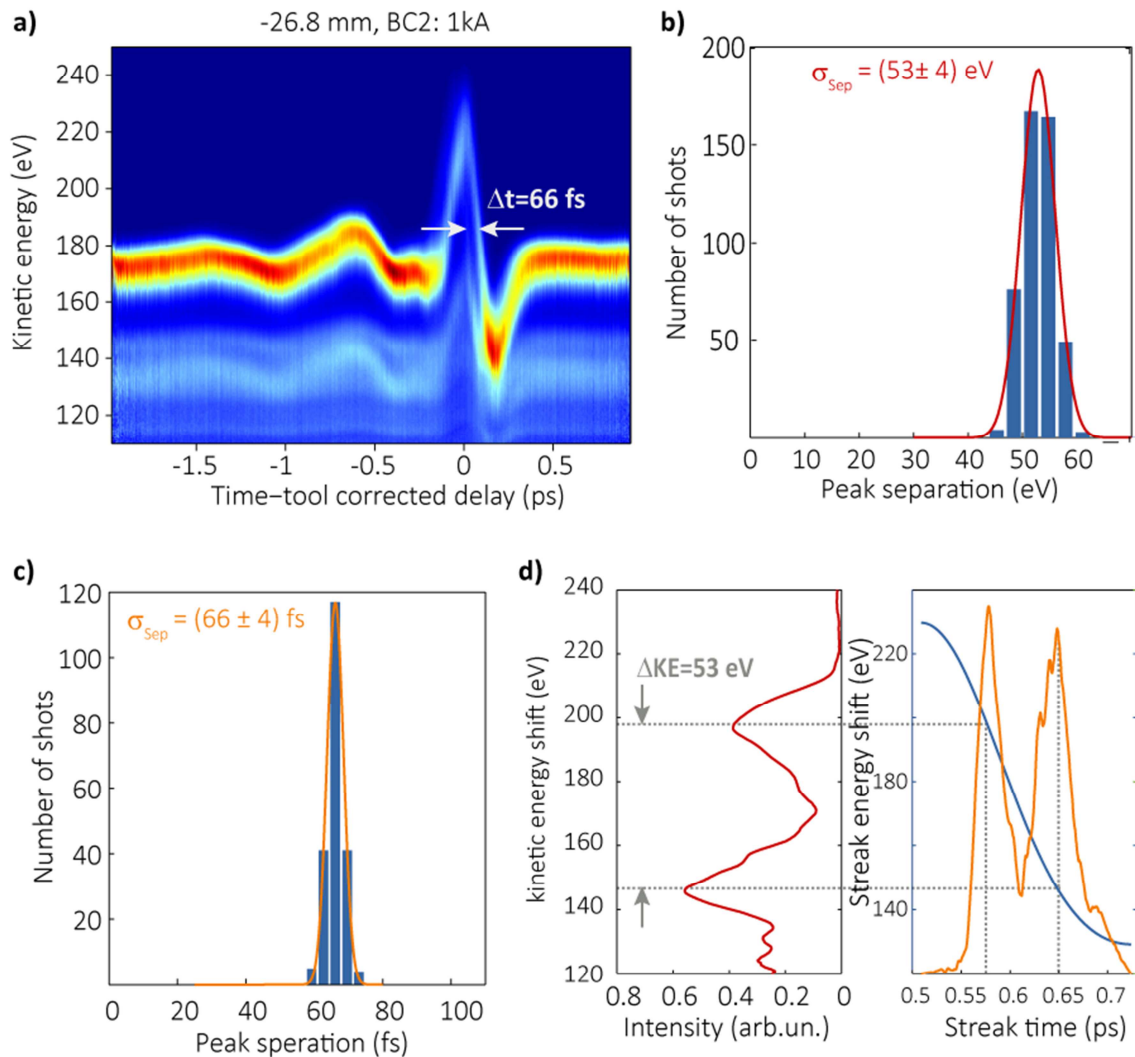


**Figure 7.8:** **a)** Timing tool sorted and averaged DSTMS streaking spectrogram measured with the double-slotted foil at -26.8 mm and a peak current of 1 kA after BC2. The complete scan consists of  $\sim 60000$  single shots. On the main streaking ramp the X-ray double peak manifest itself as a double line with distance in time corresponding to the average double peak separation, as indicated with the arrows. To precisely determine the peak separation the shots arriving on the main streaking ramp were analyzed. The resulting peak separation in energy is  $(53 \pm 4)$  eV as shown in the histogram in **b)**. In **c)** the corresponding distribution in time is plotted, here the peak separation is  $(66 \pm 4)$  fs, with the error determined from the Gaussian fit to the distribution. In panel **d)** a single-shot example in energy and time and the transformation map (blue) are plotted.

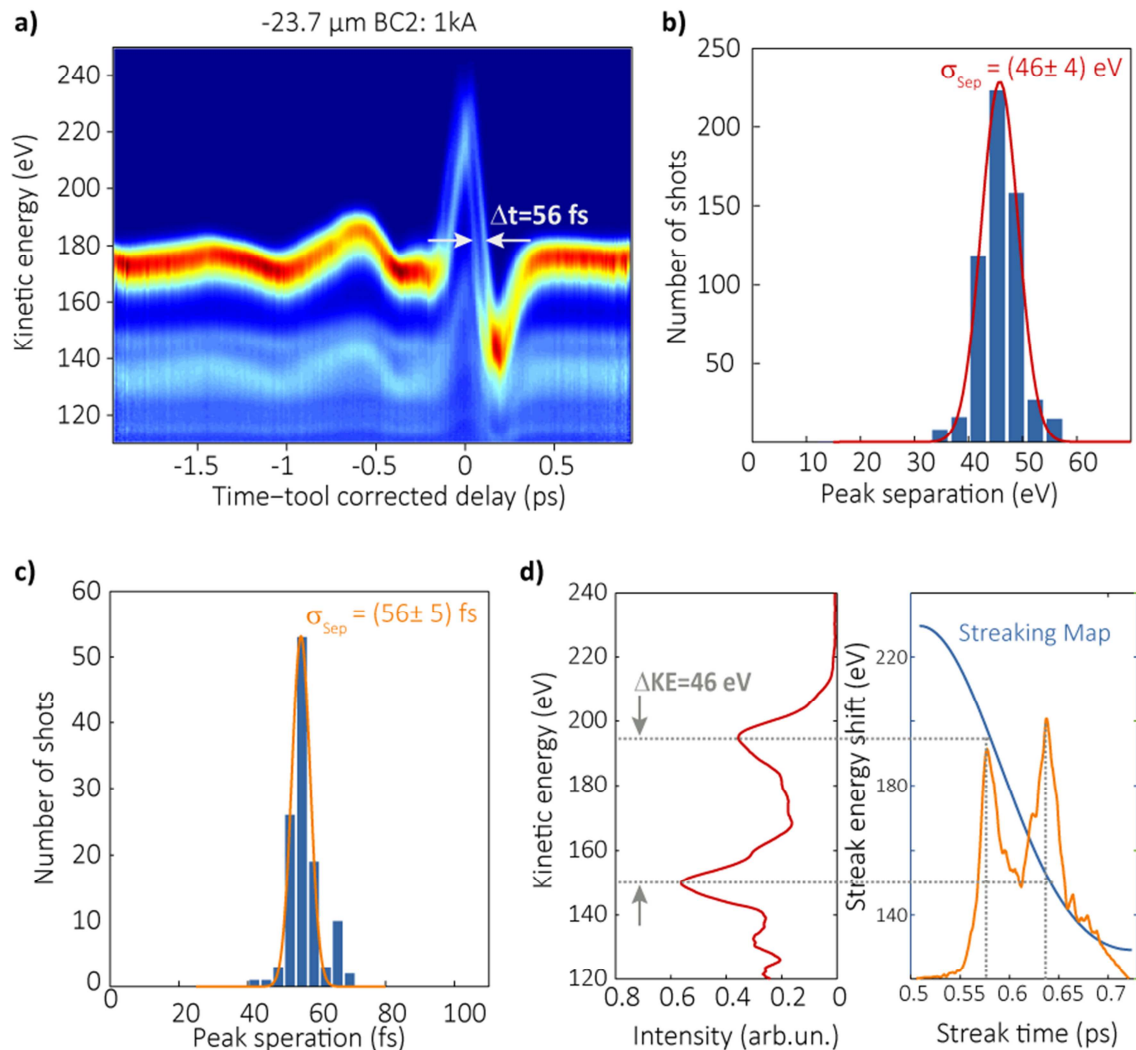


**Figure 7.9:** **a)** Timing tool sorted and averaged DSTMS streaking spectrogram measured with the double-slotted foil at  $-23.7 \text{ mm}$  and a peak current of 1 kA after BC2. The complete scan consists of  $\sim 60000$  single shots. The splitting of the streaking curve is clearly observed. To precisely determine the peak separation the shots arriving on the main streaking ramp were analyzed. The resulting peak separation in energy is  $(46 \pm 4) \text{ eV}$  as shown in the histogram in **b)**. In **c)** the corresponding distribution in time is plotted, here the peak separation is  $(56 \pm 5) \text{ fs}$ , with the error determined from the Gaussian fit to the distribution. In panel **d)** a single-shot example in energy and time and the transformation map (blue) are plotted.

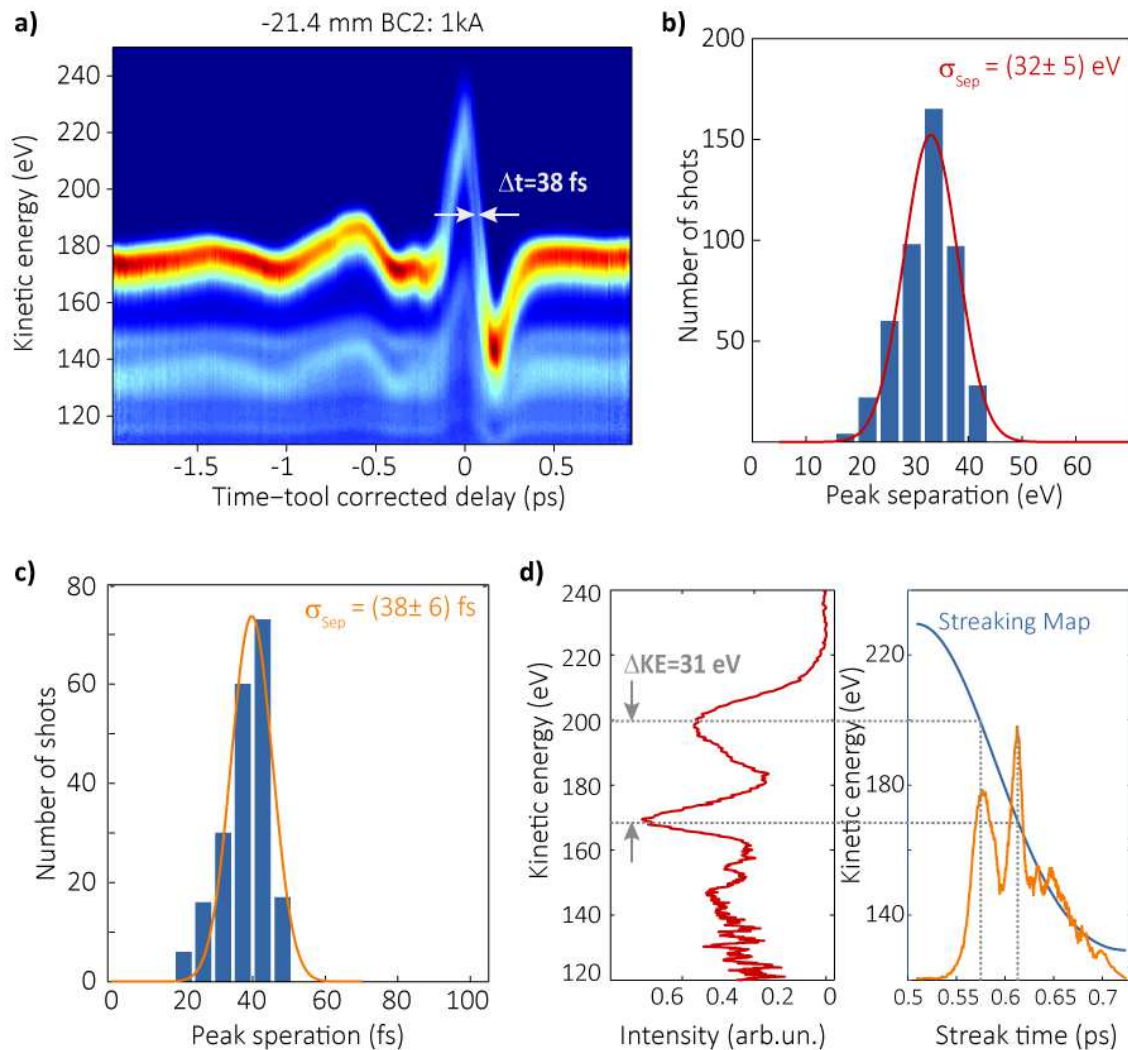


**Figure 7.10:** Timing tool sorted and averaged DSTMS streaking spectrogram measured with the double-slotted foil at -21.4 mm and a peak current of 1 kA after BC2. The complete scan consists of  $\sim 60000$  single shots. Again, the pulses arriving on the streaking ramp were analyzed. The resulting peak separation in energy is  $(32 \pm 5)$  eV as shown in the histogram in **b)**. In **c)** the corresponding distribution in streaked time is plotted, here the peak separation is  $(56 \pm 5)$  fs, with the error determined from the Gaussian fit to the distribution. In panel **d)** a single-shot example in energy and time and the transformation map (blue) are plotted.

### Comparison of the experimental measurements with calculations

To conclude, we measured the separation of the delivered X-ray pulse profile as the V-slotted aluminum foil was inserted in the middle of the magnetic chicane BC2. The separation between the FEL X-ray emission peaks varies approximately linearly with the insertion depth of the V-slotted foil, as depicted in **Figure 7.11**. The figure shows the measurements performed with the LN generated THz (streaking power:  $\sim 6$  fs/eV) and the DSTMS generated THz ( $\sim 2$ fs/eV). The calculations were performed by Yuntao Ding using Eq. 7.24 [144]. The retrieved X-ray peak separations agree well with the calculated data for the measurements performed with DAST. For the largest separation, the measured double-peak separation is smaller than the calculated one. In Ref. [156] this is explained by the non-uniform peak current distribution across the electron bunch. While the calculations assume an uniform peak current, the actual beam current exhibits a double horn profile [157]. Close to the bunch head and tail the peak current is higher, however in the calculations the compression factor and the chirp near the horns is under estimated. For the LN measurements, the measured peak separations differs more from the calculated data. Here, the slope of the measured data agrees well with the calculated line if the two biggest separations are ignored. However an offset in the data is present. The offset in the measured data might be a result of an overestimation of the streaking field strength.

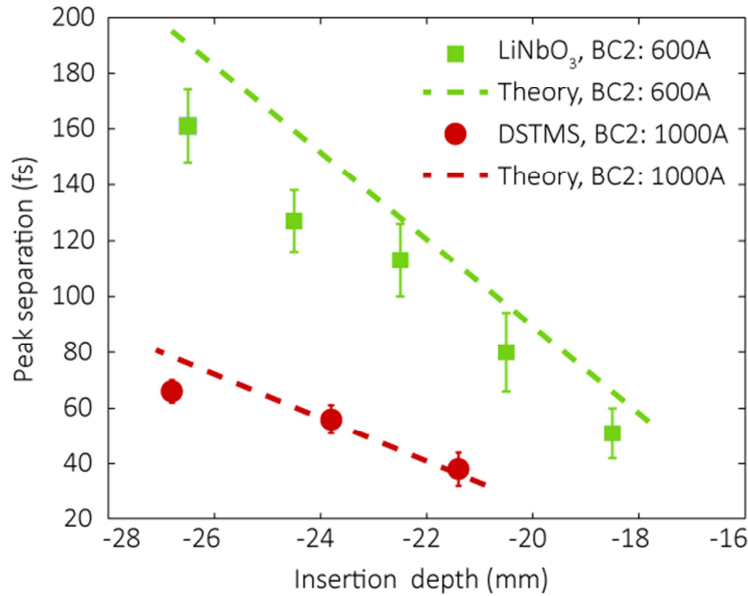


**Figure 7.11:** THz streaking measurements and calculations of the double pulse separation versus the insertion depth of the double-slotted foil. The calculations were performed by Yuntao Ding at SLAC.

### 7.2.3 Complete X-ray pulse Characterization

As explained in chapter 3, to determine the spectral phase of the ionizing FEL pulse at least two measurements at two opposite slopes of the THz streaking pulse are required. THz generation in DSTMS offers the possibility to reverse the THz streaking ramp by rotating the c-axis of the crystal by  $\pi$ . The reason for this is that the nonlinear tensor  $\chi^{(2)}$  changes the sign under rotation and thus also the polarization P and the generated THz field. In **Figure 7.12**, an averaged streaking spectrogram with a rotated axis compared to the other DSTMS measurements presented here is depicted. This offers the possibility to detect the average phase of the ionizing FEL pulse. For this however, the resolution of the electron spectrometer should be improved.

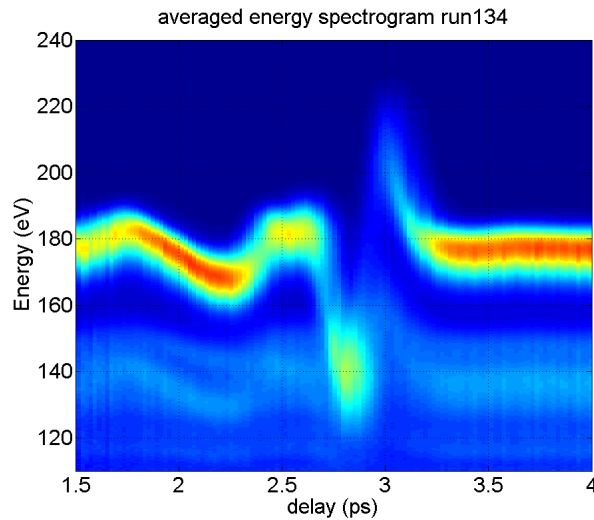


**Figure 7.12:** DSTMS THz streaking at LCLS for average spectral phase reconstruction. Rotation of the DSTMS crystal by  $180^\circ$ , results in an inverted streaking ramp, which consequently enables determination of the average spectral chirp of the ionizing FEL pulses.

### 7.3 Summary

The achievements of the THz streaking measurements performed at LCLS are two-fold. Firstly, our measurements provide experimental verification of the emittance-spoiling foil concept for X-ray pulse shaping at FELs. We observed that the separation between X-ray emission peaks varies approximately linearly with the insertion depth of the foil, as predicted by the simulations of the FEL process. These double-pulses enable X-ray pump and X-ray probe measurements without timing jitter [158]. Secondly, these experiments have been important to evaluate the temporal resolution limit and performance of our measurement apparatus. Double pulse structures with separation down to  $\sim 60$  fs could be resolved with the THz pulses generated in LN. Using THz streaking pulses with a steeper rise time, generated by optical rectification in DSTMS, the temporal resolution was improved to better than  $\sim 38$  fs.

With the THz pulses generated from DSTMS, we achieved average streaking power of  $\sim 2$  fs/eV. In principle, this corresponds to sub-10 fs temporal resolution with 1% relative bandwidth photoelectron spectrometer resolution. To reach this resolution, the interaction zone has to be reduced to minimize the smearing due to the Gouy phase shift. Furthermore, future DSTMS-based measurements might also provide access to the average X-ray pulse spectral phase, as here the slope of the streaking ramp can easily be flipped.

The temporal resolution can be further improved with shorter streaking wavelengths in the IR and mid-IR regime generated using optical parametric amplification and nonlinear frequency conversion [159]. Ultimately, the temporal resolution may reach a level to resolve the underlying time structure of the SASE FEL pulses that would verify theoretical predictions experimentally. FEL theory expects a pulse temporal profile composed of a train of individual coherent intensity spikes that vary from shot to shot [160]. The duration of these spikes is determined by the cooperation length, which in turn is related to the radiation-electron slippage in one gain length [161]. Indeed, first photoelectron streaking experiments performed at LCLS with a streaking wavelength of 2.4  $\mu\text{m}$  showed evidence for the existence of the ultrashort intensity spikes in the SASE temporal pulse profile [150].

## 8 Conclusion & Outlook

X-ray FELs have led to an explosion of activities in both fundamental and applied research. Many potential techniques require single-shot characterization of the X-ray pulse duration, temporal profile and time of arrival with high accuracy. This knowledge is especially important at current-generation FELs, which are primarily based on SASE and radiate with parameters that fluctuate strongly from pulse to pulse.

The present work describes the experimental realization of laser-based THz photoelectron spectroscopy (“THz streaking”) as a tool for temporal diagnostics of FEL photon pulses. This non-invasive and reliable technique allows simultaneous measurement of the FEL pulse temporal profile and of the relative arrival time with respect to an external pump-probe laser pulse. To the best of our knowledge, optical laser-driven THz streaking is currently the only method that can provide full and accurate temporal characterization of FEL pulses.

This technique is implemented with state-of-the-art laser technology and the apparatus does not require dedicated accelerator infrastructure. It can be used as a standard diagnostic between the FEL source and the user experiment because the measurement is made in transmission geometry and does not affect the FEL pulse. As a result, it is possible to perform experiments with an improved temporal resolution and also to post-process arbitrary experimental data based on the measured single-shot FEL photon pulse intensity analysis. In addition, this method is ideally suited as a diagnostic tool for machine studies and for FEL optimization of specific lasing parameters and pulse shapes, as it is fully decoupled from the FEL parameters.

We have successfully demonstrated laser-based THz-streaking at two of the currently operating FEL facilities, namely FLASH in Hamburg and LCLS in Stanford.

In the first proof-of-principal experiment at FLASH, we characterized soft X-ray FEL pulses at 4.8 nm (258 eV). The short-term timing jitter between the pump-probe laser and the FEL was measured to be 87 fs r.m.s. Furthermore, we observed that the temporal profile of the pulses changes drastically from shot to shot, hence modifying the peak power significantly. This result is especially important for all studies exploring non-linear X-ray

processes, where the pulse intensity plays a prominent role in accessing different regimes. These experiments require precise knowledge of the FEL pulse's temporal intensity profile to evaluate and interpret the acquired data correctly. In addition, a short and temporally well-defined X-ray pulse is crucial for biological imaging, where data must be recorded before the onset of radiation damage that is expected to occur within the first few femtoseconds of FEL exposure.

In a second experiment at the FLASH facility, we used THz-streaking to characterize the recently installed all-optical synchronization system. This timing system is based on an ultralow-noise optical pulse train from a mode-locked laser, which is distributed to the remote locations of the facility by a length stabilized fiber network. The timing information is contained in the high accuracy of the repetition rate of the optical pulse train. Using THz streaking measurements, we demonstrated the facility-wide timing to be better than 30 fs r.m.s. with a mean FEL pulse duration of 90 fs FWHM. Hence, the temporal jitter between X-ray pulses and optical pump-probe laser pulses is lower than the FEL pulse duration. This facilitates time-resolved experiments with nearly optimal time resolution, obviating the need for additional arrival time measurements. Furthermore, FEL seeding techniques will benefit from the demonstrated improved level of synchronization, as here consistent temporal overlap of the optical seed laser pulse with the driving electron bunch is mandatory for stable operation. Ultimately, a combination of these advanced techniques, that is, external seeding and femtosecond optical synchronization, will allow for pulse shaping in the spectral and temporal domain, which will have an impact on the emerging field of nonlinear X-ray science. Furthermore, we identified and quantified the different sources of jitter. Our results indicate that the performance of this optical synchronization is limited primarily by the free-electron laser pulse duration, and should naturally decrease as shorter FEL pulses are delivered.

The THz streaking technique can also be extended to characterize pulses with higher photon energy. This thesis presents successful implementation of the streaking technique at LCLS for pulses at 1 keV. At LCLS, temporal shaping of the X-ray FEL pulses can be achieved by manipulation of the FEL driving electron beam. Amongst other things, it is possible to generate X-ray double pulses with variable delay. This double-pulse structure was useful to evaluate the temporal resolution of the streaking measurements. We were able to measure a delay between the double pulses as small as 38 fs.

Several limitations might affect the practical implementation of laser-based THz streaking for characterization of FEL pulses in the hard X-ray regime ( $>5$  keV). Firstly, the photoionization cross section and the photoelectron yield decreases with increasing X-ray energy as  $\sigma \sim 1/(h\nu)$ . Therefore, a proper choice of an ionizing material, which has a sharp

photoemission line with high enough photoelectron yield, is required. Secondly, the bandwidth of the X-ray pulses increases with the X-ray energy, and this is intimately connected to the generation of short X-ray pulse durations of few femtoseconds. Therefore, a better time resolution than presented here will be required.

In general, the ability to measure even shorter FEL pulses and their substructure down to the femtosecond or even attosecond region will strongly depend on the progresses in the generation of THz pulses and in photoelectron spectroscopy. Indeed, single-shot photoelectron detection at FELs has been demonstrated with a relative energy resolution of  $\Delta E / E = 0.4\%$ , an improvement of nearly one order of magnitude compared to what was achieved in the experiments presented in this thesis [162]. For an increased streaking strength, stronger and steeper streaking fields can be achieved by decreasing the rise time of the streaking ramp, i.e. decreasing the streaking wavelength, or by scaling up the THz field strength with stronger driving optical laser pulses. With the tilted pulse-front technique and improved focusing geometry, THz field strength of 1 MV/cm is reported [97]. For comparison, the maximal field strength in our measurements was determined to be  $\sim 400$  kV/cm for the LN generated THz with  $\sim 20$  mJ driving pulses. At the LCLS we were able to use THz fields with a peak-to-peak rise time of  $\sim 180$  fs, generated by optical rectification in organic crystal DSTMS [163]. This is about a factor of three faster than the  $\sim 650$  fs rise time typically achieved with the tilted pulse front technique in LN. In the future, the streaking wavelength may even be decreased to the mid-infrared (for example 25 fs half-cycle for 15  $\mu\text{m}$  wavelength) in order to increase the temporal resolution even further.

A secondary effect that degrades the temporal resolution is the evolution of the THz through focus, which results in a dephasing between the THz and the X-ray pulses. This effect leads to a false broadening and consequently to a degradation of the temporal resolution. To minimize the spatial averaging, the interaction length between the THz and the X-ray pulses should be limited to within a fraction of the focal volume and the TOF acceptance angle should be minimized. Here, a pulsed high density gas jet would be advantageous, rather than the continuous diffusive gas nozzle used during the experiments presented in this thesis. This is particularly important for shorter X-ray pulse durations.

Besides these technical developments that will improve the THz streaking resolution, one could think of the following future goals that might become feasible:

**X-ray Chirped Pulse Amplification (XCPA)** at FELs promises even shorter pulses with peak powers up to the terawatt level, which could facilitate the promise of single molecule imaging. In general, the number of delivered photons is limited by the density of electrons

cooperating in the coherent FEL emission process. The density of these electrons, in turn, is restricted by space charge effects that degrade the electron beam brightness and emittance. To avoid beam degradation, the electron bunch length can be increased while keeping the electron bunch charge density constant. In XCPA, the driving FEL bunches are temporally-stretched and spectrally-chirped, producing long chirped X-ray pulses with a high number of photons. To achieve the highest peak power, the generated FEL pulses need to be temporally compressed to compensate for the initial chirp [164]. A compressor can be realized with asymmetric-cut multilayer mirrors, which act as X-ray gratings to provide variable dispersion [165]. The accelerator can be tuned to generate chirped electron bunches, which emit FEL pulses with dispersion properties that match the grating compressor settings. This development requires an independent characterization of the temporal structure of the generated pulses, and it can be achieved with THz streaking as feedback for tuning the electron beam parameters

The ability to compress and to shape the X-ray pulse profile would not only have a tremendous impact on imaging experiments but would also revolutionize the field of X-ray FEL science.

**Tandem streaking:** To improve the resolution of the streaking measurements to a sub-femtosecond level, streaking pulses with a shorter rise time with wavelengths in the IR spectral region might be used. In this case, however, it is not possible to control the streaking field amplitude and phase due to the temporal jitter at FELs and without defined streaking parameters it would not be possible to perform a calibrated transformation from energy to time. This problem can be solved by recording two streaked photoelectron spectra of the same pulse using a phase-shifted streaking pulse as illustrated in **Figure 3.6**. In the first stage, the X-ray pulse overlaps with a maximum of the streaking field, while in the second one the overlap occurs at a zero crossing of the pulse. The first stage measurement provides the streaking strength for the second stage, which enables a calibrated and unambiguous transformation from energy to time of the streaked spectrum acquired in the second stage. As the streaking shift in the first stage is sensitive to the intensity of the streaking field, it is also possible to determine where the emission occurred within the streaking pulse envelope, providing the arrival time of the pulse. The  $\pi/2$  phase shift between the two streaking measurements can be realized by taking advantage of the Gouy phase shift, which occurs when a Gaussian beam is focused. If the first and the second stages of the streaking measurements are performed at one Rayleigh length on either side of the optical focus, the streaking pulse will be phase shifted by exactly  $\pi/2$ .

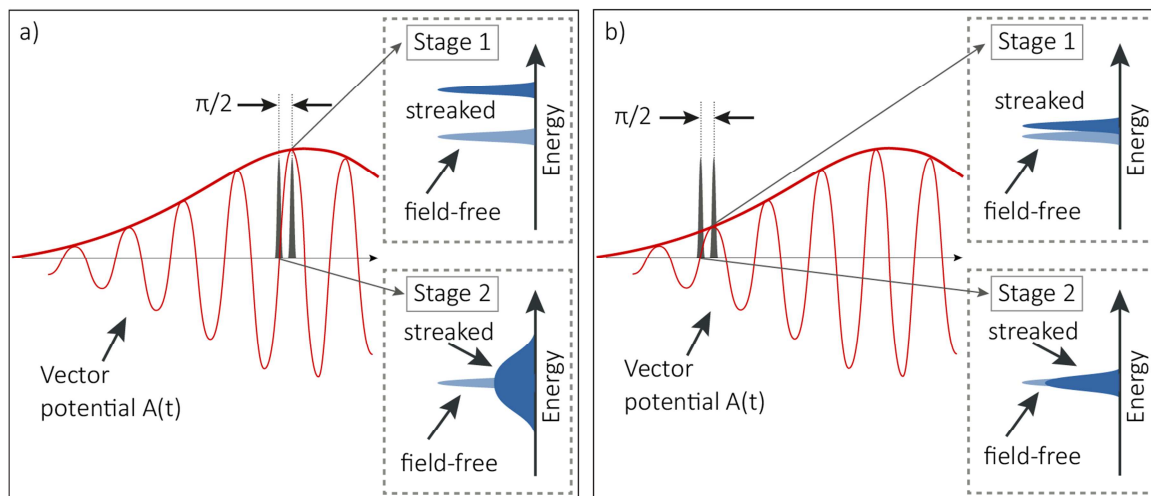


**Figure 8.1:** Tandem streaking for self-calibrated measurements with two TOF spectrometers located at the Rayleigh distance on both sides of the focal position. **a)** In the first stage the X-ray pulse overlaps with a maximum of the vector potential, resulting in a maximal energy shift of the streaked photoelectron spectrum by an amount proportional to the instantaneous vector potential. In the second stage the photoemission occurs at a zero-crossing of the vector potential, resulting in a maximally broadened photoelectron spectrum. The first stage measurement recovers the gradient of the vector potential in the second stage measurement, which enables a calibrated transformation of the second stage measurement from energy to time. **b)** The photoelectron spectrum is only slightly upshifted, indicating that the streaking strength (gradient) in the second stage is weaker.

Beside pulse characterization, the streaking technique may also be used to study **few femtosecond electron dynamics** at FELs. The interaction of matter with high-fluence X-ray pulses of durations of few femtoseconds triggers complex dynamics in matter that are not yet fully understood. Photoelectron streaking spectroscopy provides the possibility to study these dynamics on a femtosecond time scale. As a first approach, Auger decay lifetime of simple gas-phase molecules could be measured directly in the temporal domain. Synchrotron sources have been used to measure the lifetime of core holes from the spectral width of the electrons emitted during the decay of the excited state. However, these measurements fail to provide details of the temporal evolution of the excited state, when multi-electron dynamics are involved. In contrast, at FELs with photoelectron streaking spectroscopy the temporal evolution of highly excited states and corresponding relaxation dynamics can be studied.

In conclusion, time-resolved photoelectron spectroscopy applied at FELs is a versatile technique. In this thesis, we demonstrated that streaking spectroscopy is a reliable tool for single-shot temporal characterization of the delivered X-ray photon pulse and of their arrival time. The measurement is direct, self-calibrated and does not rely on any assumption

of the lasing process itself and does not affect the FEL pulses. In the future, this technique can even serve as a standard diagnostic for user experiments, allowing for more comprehensive analysis of all observed phenomena. Moreover, streaking spectroscopy has the potential to explore complex electron dynamics in matter with an unprecedented resolution at atomic scales.

## Appendix A

### Wave-Equation of nonlinear optics

As described in chapter 4, an intense laser can induce a polarization in a nonlinear medium with frequency components that are not present in the incident electromagnetic radiation. If the polarization is changing in time, it can act as the source for emission of electromagnetic radiation with these new frequency components. In order to calculate the form of the generated radiation, we start with the Maxwell equations. The mathematical description presented here follows the text book from Boyd [87]. The Maxwell equations in Si units are:

$$\nabla \cdot D = \rho \quad (\text{A.1})$$

$$\nabla \cdot B = 0 \quad (\text{A.2})$$

$$\nabla \times E = -\frac{\partial B}{\partial t} \quad (\text{A.3})$$

$$\nabla \times H = j + \frac{\partial D}{\partial t} \quad (\text{A.4})$$

Where  $\rho$  and  $j$  are electric charge and current. The dielectric displacement  $D$  is defined as:

$$D = \epsilon_0 E + P, \quad (\text{A.5})$$

here  $\epsilon_0$  is the vacuum permittivity and  $P$  is the macroscopic polarization of the medium.

The magnetic field  $B$  and the magnetizing field  $H$  are related by

$$B = \mu\mu_0 H, \quad (\text{A.6})$$

where  $\mu_0$  is the vacuum permeability and  $\mu$ , the permeability of the medium, which is 1 for a nonmagnetic material. In the following we assume that the material is nonmagnetic and that no free charges and no free currents are present:

$$\mu = 1, \quad (\text{A.7})$$

$$\rho = 0, \quad (\text{A.8})$$

$$j = 0. \quad (\text{A.9})$$

Now to form the wave equation, we take the curl of equation (A.3) and exchange the order of the time and space derivatives on the right hand side:

$$\nabla \times \nabla \times E = \nabla \times \left( -\frac{\partial B}{\partial t} \right) = -\frac{\partial}{\partial t} (\nabla \times B) \quad (\text{A.10})$$

Now we can use (A.4) of the Maxwell equations to express the left hand side of equation (A.10) in terms of  $D$  and together with (A.6), (A.7) and (A.9) we can write:

$$\nabla \times \nabla \times E = -\mu_0 \frac{\partial^2 D}{\partial t^2} \quad (\text{A.11})$$

If we replace in this equation  $D$  with the definition (A.5), we can write the wave equation thereby:

$$\nabla \times \nabla \times E + \mu_0 \epsilon_0 \frac{\partial^2 E}{\partial t^2} = -\mu_0 \frac{\partial^2 P}{\partial t^2}. \quad (\text{A.12})$$

This is the general form of the wave equation used in optics.

The first term on the left hand side can be rewritten using the vector identity:

$$\nabla \times \nabla \times E = \nabla (\nabla \cdot E) - \nabla^2 E. \quad (\text{A.13})$$

For a linear medium, where the induced polarization and the electric field are related by:

$$P = \epsilon_0 \chi^{(1)} E, \quad (\text{A.14})$$

the quantity  $\chi^{(1)}$  is the linear susceptibility and it is a material property. In general  $\chi^{(1)}$  is a 2nd-order tensor but it reduces to a scalar for an isotropic medium. For the electric displacement we can write:

$$D = \epsilon_0 E + \epsilon_0 \chi^{(1)} E = \epsilon_0 E (1 + \chi^{(1)}) = \epsilon_0 \epsilon^{(1)} E. \quad (\text{A.15})$$

Here  $\epsilon_r$  is the relative permittivity of a medium, which is in general a tensor and it reduces to a scalar for a isotropic medium. For a linear, isotropic medium the displacement vector  $D$  and the applied electric field  $E$  are parallel, and therefore  $\nabla \cdot D = 0$  implies that  $\nabla \cdot E = 0$ . With this the first term on the right hand side of equation (A.13) disappears and the wave equation reduces to:

$$\nabla^2 E - \frac{1}{c^2} \frac{\partial^2 E}{\partial t^2} = \frac{1}{c^2 \epsilon_0} \frac{\partial^2 P}{\partial t^2}, \quad (\text{A.16})$$

Here  $c = 1/\sqrt{\mu_0 \epsilon_0}$  is the speed of light. In general, in nonlinear optics the first term of (A.13) on the right hand side does not vanish, even for an isotropic medium, but usually the contribution from this term is very small and it can be neglected. Therefore it will be assumed, that the wave equation has the form of (A.16.)

The dependence of the polarization  $P$  upon the electric field  $E$  is in general nonlinear as presented in chapter 4:

$$\begin{aligned} P &= \epsilon_0 \left[ \chi^{(1)} E + \chi^{(2)} E^2 + \chi^{(3)} E^3 + \dots \right] \\ &\equiv P^{(1)} + P^{(2)} + P^{(3)} + \dots \\ &\equiv P^{(1)} + P^{NL} \end{aligned} \quad (\text{A.17})$$

The quantity  $\chi^{(n)}$  is the  $n$ th-order nonlinear optical susceptibility. Often it is convenient to split the polarization into a linear  $P^{(l)}$  and nonlinear  $P^{NL}$  part, as done in equation A.17.

With this, the dielectric displacement can be written like:

$$\begin{aligned} D &= \epsilon_0 E + P^{(1)} + P^{NL} = D^{(1)} + P^{NL}. \\ D^{(1)} &= \epsilon_0 E + P^{(1)} \end{aligned} \quad (\text{A.18})$$

With (A.18) the wave equation can be expressed in terms of:

$$\nabla^2 E - \frac{1}{\epsilon_0 c^2} \frac{\partial^2 D^{(1)}}{\partial t^2} = \frac{1}{c^2 \epsilon_0} \frac{\partial^2 P^{NL}}{\partial t^2}, \quad (\text{A.19})$$

Using (A.15), the equation (A.19) for an isotropic medium can be rewritten as:

$$\nabla^2 E - \frac{\epsilon^{(1)}}{c^2} \frac{\partial^2 E}{\partial t^2} = \frac{1}{c^2 \epsilon_0} \frac{\partial^2 P^{NL}}{\partial t^2}. \quad (\text{A.20})$$

This expression is an inhomogeneous wave equation. Here the nonlinear polarization, acts as a source term of the electric field. When the right-hand side of equation (A.20) is nonzero, charges are being accelerated in the medium and accelerated charges generate electromagnetic radiation. Without this source term, equation (A.20) is being solved by free propagating waves with the velocity  $c/n$ , where  $n$  is the linear refractive index with  $n^2 = \epsilon^{(1)}$ . Note that Eq. (A.20) just holds true for a non-dispersive medium. In a dispersive medium the relative permittivity will be frequency depended and each frequency component of the field must be considered separately. The electric field, linear displacement and polarization field are presented as the sum of the different frequency components. The individual frequency components can be expressed with:

$$E_n(r, t) = E_n(r) e^{-i\omega_n t} + c.c., \quad (\text{A.21})$$

$$D_n^{(l)}(r,t) = D_n(r)e^{-i\omega_n t} + c.c., \quad (\text{A.22})$$

$$P_n^{NL}(r,t) = P_n^{NL}(r)e^{-i\omega_n t} + c.c. \quad (\text{A.23})$$

Here *c.c.*, is the complex conjugated. In the representation above the electric field is separated in its fast varying part  $e^{-i\omega t}$  and its complex amplitude  $E_n(r,t)$ . If we assume a lossless medium, the dielectric displacement of one frequency component can be written as:

$$D_n^{(l)} = \epsilon_0 \epsilon^{(l)}(\omega_n) \cdot E_n(r,t) \quad (\text{A.24})$$

$$\nabla^2 E_n - \frac{\epsilon^{(l)}(\omega_n)}{c^2} \frac{\partial^2 E_n}{\partial t^2} = \frac{1}{c^2 \epsilon_0} \frac{\partial^2 P_n^{NL}}{\partial t^2}. \quad (\text{A.25})$$

In general for a dissipative medium, the dielectric tensor is complex. In this case the complex amplitudes of dielectric displacement and the electric field can be related.

## Appendix B

### Derivation of the pulse front tilt introduced by an angular dispersive medium

In this section, a simple derivation of the relation between angular dispersion and pulse front tilt is given [166,167].

Let us consider a light pulse propagating towards the spectroscopic device. The pulse is composed of monochromatic plane waves with distinct wavelengths, which can be expressed as:

$$E(\lambda) = E_0(\lambda) \sin(\omega t - \vec{k}\vec{r} + \varphi_0) = E_0(\lambda) \sin \varphi \quad (\text{B.1})$$

Where  $\vec{k}$  is the wave vector and  $\varphi_0$  represents a phase constant. Suppose the wave is travelling in the x-z plane and the angular dispersion is in the same plane, then the argument of the sin function in (A.1) is:

$$\varphi = \omega t - k_x x - k_z z + \varphi_0 \quad (\text{B.2})$$

With the definition of the angle  $\varepsilon$  as shown in **Figure B.1**, we can write  $k_x = k \sin(\varepsilon)$  and  $k_z = k \cos(\varepsilon)$ . The phase front of a waveform is the surface where phase  $\varphi$  is constant:

$$\omega t - k_x x - k_z z + \varphi_0 = \text{constant} \quad (\text{B.3})$$

Equation (A.3) is the mathematical description of a straight line, hence in the x-z plane the phase front of the pulse is a line with the slope:

$$m = -\frac{k_x}{k_z} = -\tan \varepsilon \quad (\text{B.4})$$

The gradient of the pulse front, which is the surface determined by the instantaneous spatial position of the maximum intensity of the pulse, can also be calculated from equation (B.3).

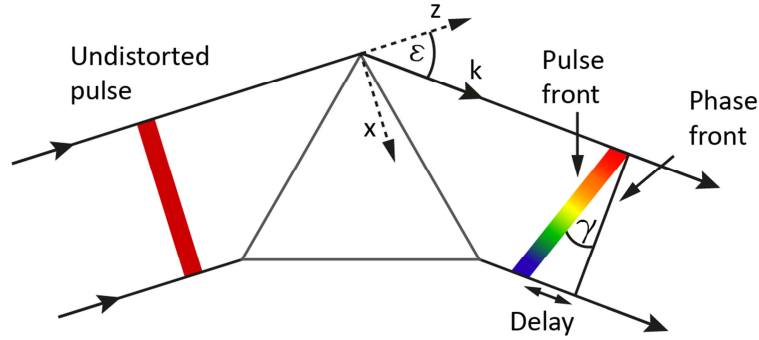


**Figure B.1:** Pulse front tilt imparted on to the propagating beam through an angular dispersive device, i.e. a prism. Before the prism the phase front and the pulse front are parallel to each other and perpendicular to the propagation direction of the pulse. After passing the prism the pulse front is tilted by an angle  $\gamma$  to the phase front.

In this surface the different wavelength components of the plane wave are in phase, i.e. the frequency derivative of the phase is zero:

$$\frac{d\varphi}{d\omega} = t - \frac{dk_x}{d\omega} x - \frac{dk_z}{d\omega} z = 0 \quad (\text{B.5})$$

Like before, this equation describes a straight line in the  $x$ - $z$  plane with a different slope  $m_t$ :

$$m_t = -\frac{dk_x}{dk_z} = -\frac{d(k_z \tan \varepsilon)}{dk_z} = -\left( \tan \varepsilon + k_z \frac{1}{\cos^2 \varepsilon} \frac{d\varepsilon}{dk_z} \right) \quad (\text{B.6})$$

The coordinate system can be chosen so that  $\varepsilon=0$  for the mean wavelength  $\bar{\lambda}$  of the pulse. Then the wavevector is  $k_z = k = 2\pi/\bar{\lambda}$  and the slope of the pulse front reduces to:

$$m_t = -k_z \frac{d\varepsilon}{dk_z} = \bar{\lambda} \frac{d\varepsilon}{d\lambda} \quad (\text{B.7})$$

Comparison with figure B.1 shows that the tilt angle  $\gamma$  of the pulse front can be written as:

$$\tan \gamma = -m_t = -\bar{\lambda} \frac{d\varepsilon}{d\lambda} \quad (\text{B.8})$$

Equation (B.8) is a generalized expression, showing, that the tilt angle is only related to the wavelength and angular dispersion, while it does not contain any parameters of the spectroscopic device, which means that it does not matter how the angular chirp is introduced.

Till now the material dispersion is not taken into account and equation (B.8) is valid for pulses in either free-space or in nondispersive materials ( $dn/d\omega=0$ ). The equation can be

generalized by including the wavelength dependence of the wavevector  $k(\lambda) = 2\pi n(\lambda)/\lambda$  in equation (B.7):

$$m_i = -k \frac{d\varepsilon}{dk} = \frac{n}{\left(n - \bar{\lambda} \frac{dn}{d\lambda}\right)} \bar{\lambda} \frac{d\varepsilon}{d\lambda} = \frac{n}{n_g} \bar{\lambda} \frac{d\varepsilon}{d\lambda} \quad (\text{B.9})$$

where  $n_g$  is the group index.



## Appendix C

### Derivation of the kinetic energy of photoelectrons released into a strong laser field

An X-ray pulse and a strong, long-wavelength streaking pulse are collinearly overlapped and focused onto a rare gas target. The X-ray pulse ionized a fraction of the atoms and photoelectrons, with an initial kinetic energy of  $E_i$ , are released. After ionization, the Coulomb potential of the ion can be neglected and the electron is treated as a free particle that is instantaneously accelerated in the oscillating streaking field. Let us assume that the electron is ejected at the instant  $t_0$  into the linearly polarized streaking light field given by  $E_L(t) = E_0(t) \cos(\omega_L t + \varphi)$ , where  $\omega_L$  is the streaking field frequency and  $E_0$  is the envelope. According to Newton's laws of motion, the influence of the external electric field on a free electron with charge  $-e$  and mass  $m_e$  can be expressed as

$$m_e \ddot{\mathbf{x}} = -e\mathbf{E}_L(t). \quad (\text{C.1})$$

Integration of this equation yields:

$$\begin{aligned} \mathbf{p}(t) - \mathbf{p}(t_0) &= -e \int_{t_0}^t \mathbf{E}_L(t') dt' \\ \mathbf{p}(t) &= \mathbf{p}(t_0) + e \int_{t_0}^t \frac{d\mathbf{A}(t')}{dt'} dt' , \\ \mathbf{p}(t) &= \mathbf{p}(t_0) + e[\mathbf{A}(t) - \mathbf{A}(t_0)] \end{aligned} \quad (\text{C.2})$$

where  $\mathbf{A}(t)$  given by  $\mathbf{E}_L(t) = -d\mathbf{A}/dt$ , is the vector potential of the streaking field. For  $t \rightarrow \infty$ ,  $\mathbf{A}(t)$  can be set to zero and the final momentum change after the end of the streaking pulse is given by

$$\Delta\mathbf{p}(t_0) = -e\mathbf{A}(t_0). \quad (\text{C.3})$$

Hence, the momentum change of a photoelectron is proportional to the vector potential of the streaking field at the instant of ejection. The dashed circle in **Figure C1.a** shows the initial momentum distribution of the photoelectrons in the  $xy$ -plane without an external

field. In this case, the electron final momentum is independent of the observation angle  $\Theta$ . Here we assume the streaking field to be polarized along the x-direction. The influence of the field on the momentum distribution at a given ionization time  $t_0$  is represented by the solid circle in **Figure C1.a**, whose center is shifted by  $\Delta p_x = -eA(t_0)$  with respect to the dashed circle. This circle oscillates along the polarization axis of the streaking laser field as  $t_0$  varies. The final momentum of the electron can be calculated from the trigonometric relation

$$p_i^2 = \Delta p^2 + p_f^2 - 2\Delta p p_f \cos\Theta, \quad (\text{C.4})$$

where  $\Theta$  is the angle between the laser polarization and the initial momentum  $p_i$  of the photoelectron. Solving the quadratic equation for the final momentum  $p_f$  results in a final kinetic energy given by:

$$E_f(t_0) = \frac{p_f^2}{2m_e} = E_i + 2U_p \cos 2\theta \sin^2(\omega_L t_0 + \phi) \pm \cos \theta \sin(\omega_L t_0 + \phi) \sqrt{8U_p E_i \left(1 - \frac{2U_p}{E_i} \sin^2 \theta \sin^2(\omega_L t_0 + \phi)\right)}, \quad (\text{C.5})$$

where  $E_i$  is the initial kinetic energy and  $U_p$  the ponderomotive potential. Furthermore the slowly varying envelope approximation  $dE_0/dt \ll E_0 \omega_L$  was applied. For  $U_p < E_i/2$  only the positive sign has physical meaning.

Eq. C.5 clearly indicates the dependence of the final kinetic energy on the ionization time  $t_0$  and on the chosen observation angle  $\theta$ . An observation angle perpendicular ( $\Theta = 90^\circ$ ) to the laser polarization results in a final kinetic energy of

$$E_{f,\perp}(t_0) = E_i - 2U_p \sin^2(\omega_L t_0 + \phi). \quad (\text{C.6})$$

In this observation geometry, the influence of the streaking field on the electron momentum distribution results in a downshift of the kinetic energy oscillating with twice the laser frequency [58], as represented by the green curve in **Figure C1.b**. The curves in this figure were calculated with a similar THz intensity and initial photoelectron kinetic energy as employed in the pulse characterization measurements discussed in this thesis. As depicted in **Figure C1**, the energy shift in the perpendicular direction is negligible and a spectrum measured can be considered as field-free spectrum. This detection geometry is not feasible for THz streaking based FEL pulse temporal diagnostic.

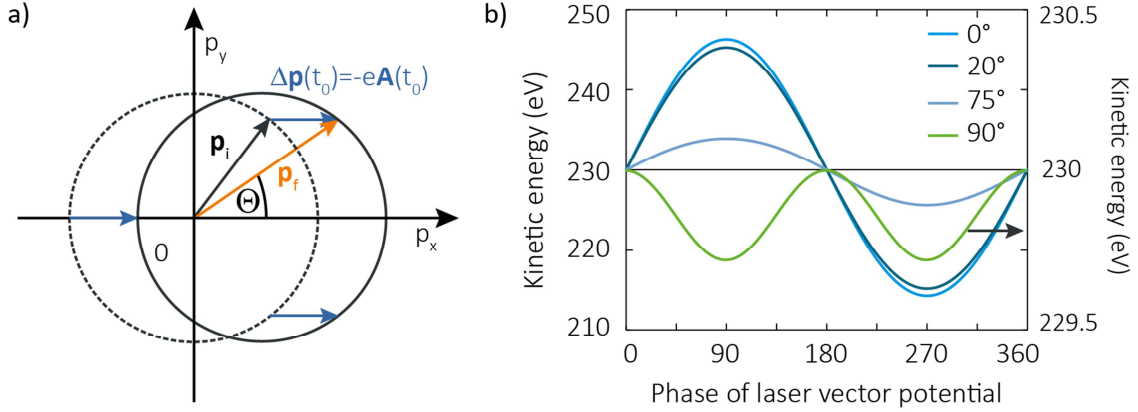


**Figure C.1:** **a)** The dashed circle shows the initial photoelectron momentum distribution after ionization by the X-ray pulse without streaking field. The solid circle, shifted by  $\Delta\mathbf{p}(t_0) = -e\mathbf{A}(t_0)$ , represents the momentum distribution under the influence of a streaking laser field polarized along the x-axis for electrons liberated at a given time  $t_0$  within the pulse. Both, the electron kinetic energy and the direction of motion are altered. The measured photoelectron spectrum depends on the observation angle  $\Theta$  and their release time, as shown in **b)**. In **b)** the final kinetic energy as function of the phase of the streaking field at the time of ionization for 4 different observation geometries is plotted. The streaking pulse parameters are chosen similar to the measurement conditions (0.5 THz, energy = 1.5  $\mu\text{J}$ , duration = 2 ps, focus diameter = 1.2 mm).  $\Theta=0^\circ$  corresponds to an observation angle along the streaking field polarization. The resolution of the kinetic energy measurement degrades with a larger acceptance angle. However, in the parallel detection direction the energy smearing due to the finite collection angle is marginal. The energy shift in the perpendicular direction ( $\Theta=90^\circ$ ) represented by the green curve is negligible (note the different energy scale on the right axis).

Detection along the laser polarization ( $\Theta = 0^\circ$ ) results in

$$E_{f,\parallel}(t_0) = E_i + 2U_p \sin^2(\omega_L t_0 + \varphi) + \sqrt{8E_i U_p} \sin(\omega_L t_0 + \varphi). \quad (\text{C.7})$$

This geometry provides the largest energy shift and the final kinetic energy is periodically shifted up-and-down as shown in **Figure C1.b**. In the experiments that are presented in this thesis, the second term can be neglected, as  $U_p$  is much smaller than the initial kinetic energy. Thus, Eq. C.5 can be simplified to:

$$\Delta E_{f,\parallel}(t_0) = \sqrt{8E_i U_p} \sin(\omega_L t_0 + \varphi) = e \sqrt{\frac{2E_i}{m_e}} A(t_0). \quad (\text{C.7})$$

Hence, the observed energy shift of the electrons is directly proportional to the vector potential of the streaking laser field at their instant of release. This implies that for parallel detection, the vector potential  $A(t)$  of the streaking field can be directly accessed by measuring the energy shift as function of delay between the streaking pulse and the ionizing

X-ray pulse, provided that the timing jitter between the two pulses is small and that the streaking pulse is reproducible.

In addition, it is important to note, the final kinetic energy of electrons does not change much within a detection cone of tens of degrees, as shown in **Figure C1.b** for observation angles of  $\Theta = 0^\circ$  and  $\Theta = 20^\circ$  with respect to the laser polarization axis. This result is of practical importance for measurements at FELs, as a larger collection angle (acceptance angle of the electron spectrometer used in our experiments is on the order of tens of degrees) results in an improved signal-to-noise ratio.

## Appendix D

### Measurement Apparatus at FLASH

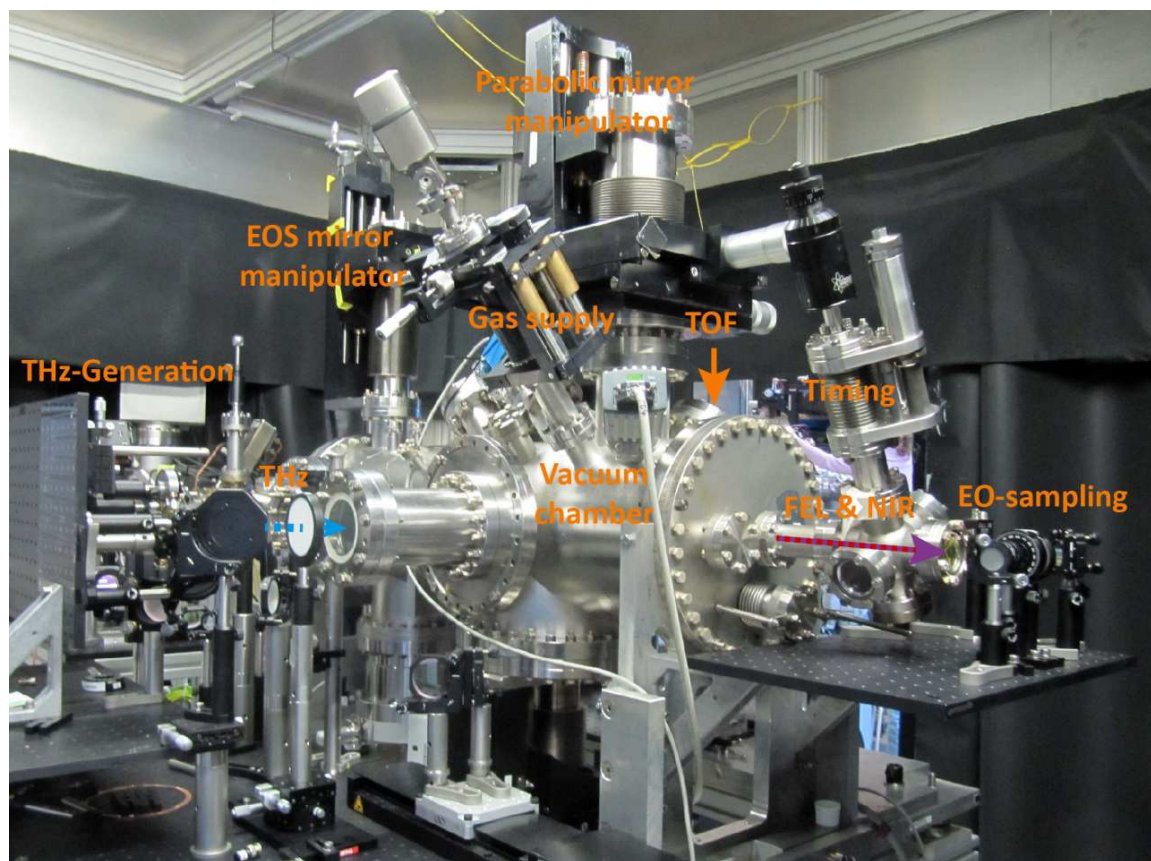


**Figure D.1:** Picture of the THz-streaking measurement set-up at the beam line at FLASH for the all-optical synchronization beam time in 2012. The TOF spectrometer cannot be seen on this photograph, but its position is indicated with the arrow.



## Bibliography

1. Röntgen, W. C. On a New Kind of Rays. *Nature* **53**, 274–276 (1896).
2. Friedrich, W., Knipping, P. & Laue, M. Interferenzerscheinungen bei Röntgenstrahlen. *Ann. Phys.* **346**, 971–988 (1913).
3. Bragg, W. H. X-rays and Crystals. *Nature* **90**, 219 (1912).
4. Bragg, W. L. The Structure of Some Crystals as Indicated by Their Diffraction of X-rays. *Proc. R. Soc. Lond. Ser. Contain. Pap. Math. Phys. Character* **89**, 248–277 (1913).
5. Watson, J. D. & Crick, F. H. C. Molecular Structure of Nucleic Acids: A Structure for Deoxyribose Nucleic Acid. *Nature* **171**, 737–738 (1953).
6. Iwanenko, D. & Pomeranchuk, I. On the Maximal Energy Attainable in a Betatron. *Phys. Rev.* **65**, 343–343 (1944).
7. O'Neill, G. K. Storage-Ring Synchrotron: Device for High-Energy Physics Research. *Phys. Rev.* **102**, 1418–1419 (1956).
8. Motz, H. Applications of the Radiation from Fast Electron Beams. *J. Appl. Phys.* **22**, 527–535 (1951).
9. Deisenhofer, J., Epp, O., Miki, K., Huber, R. & Michel, H. Structure of the protein subunits in the photosynthetic reaction centre of *Rhodospseudomonas viridis* at 3[[angst]] resolution. *Nature* **318**, 618–624 (1985).
10. Bressanelli, S. *et al.* Crystal structure of the RNA-dependent RNA polymerase of hepatitis C virus. *Proc. Natl. Acad. Sci.* **96**, 13034–13039 (1999).
11. Maiman, T. H. Stimulated Optical Radiation in Ruby. *Nature* **187**, 493–494 (1960).
12. Schmäser, P., Rossbach, J., Behrens, C. & Dohlus, M. *Free-Electron Lasers in the Ultraviolet and X-Ray Regime: Physical Principles, Experimental Results, Technical Realization.* (Beschleunigerphysik, Forschung Linear Accelerator, 2009). at <<http://bib-pubdb1.desy.de/record/207370>>
13. Barletta, W. A. *et al.* Free electron lasers: Present status and future challenges. *Nucl. Instrum. Methods Phys. Res. Sect. Accel. Spectrometers Detect. Assoc. Equip.* **618**, 69–96 (2010).
14. Madey, J. M. J. Stimulated Emission of Bremsstrahlung in a Periodic Magnetic Field. *J. Appl. Phys.* **42**, 1906–1913 (1971).
15. Ackermann, W. *et al.* Operation of a free-electron laser from the extreme ultraviolet to the water window. *Nat. Photonics* **1**, 336–342 (2007).
16. Emma, P. *et al.* First lasing and operation of an ångstrom-wavelength free-electron laser. *Nat. Photonics* **4**, 641–647 (2010).
17. Allaria, E. *et al.* Highly coherent and stable pulses from the FERMI seeded free-electron laser in the extreme ultraviolet. *Nat. Photonics* **6**, 699–704 (2012).
18. Neutze, R., Wouts, R., van der Spoel, D., Weckert, E. & Hajdu, J. Potential for biomolecular imaging with femtosecond X-ray pulses. *Nature* **406**, 752–757 (2000).
19. Young, L. *et al.* Femtosecond electronic response of atoms to ultra-intense X-rays. *Nature* **466**, 56–61 (2010).

20. Ding, Y. *et al.* Measurements and Simulations of Ultralow Emittance and Ultrashort Electron Beams in the Linac Coherent Light Source. *Phys. Rev. Lett.* **102**, 254801 (2009).
21. Zholents, A. & Fawley, W. Proposal for Intense Attosecond Radiation from an X-Ray Free-Electron Laser. *Phys. Rev. Lett.* **92**, 224801 (2004).
22. Saldin, E. L., Schneidmiller, E. A. & Yurkov, M. V. Scheme for attophysics experiments at a X-ray SASE FEL. *Opt. Commun.* **212**, 377–390 (2002).
23. Emma, P. *et al.* Femtosecond and Subfemtosecond X-Ray Pulses from a Self-Amplified Spontaneous-Emission-Based Free-Electron Laser. *Phys. Rev. Lett.* **92**, 074801 (2004).
24. Kienberger, R. *et al.* Atomic transient recorder. *Nature* **427**, 817–821 (2004).
25. Ribic, P. R. & Margaritondo, G. Status and prospects of x-ray free-electron lasers (X-FELs): a simple presentation. *J. Phys. Appl. Phys.* **45**, 213001 (2012).
26. Elder, F. R., Gurewitsch, A. M., Langmuir, R. V. & Pollock, H. C. Radiation from Electrons in a Synchrotron. *Phys. Rev.* **71**, 829–830 (1947).
27. Schwinger, J. On the Classical Radiation of Accelerated Electrons. *Phys. Rev.* **75**, 1912–1925 (1949).
28. Huang, Z. & Kim, K.-J. A Review of X-ray Free-Electron Laser Theory. *Phys. Rev. Spec. Top.* **10**, (2007).
29. Saldin, E., Schneidmiller, E. A. & Yurkov, M. V. *The Physics of Free Electron Lasers.* (Springer Science & Business Media, 2000).
30. John David Jackson. *Classical Electrodynamics.* at <http://archive.org/details/ClassicalElectrodynamics>
31. Duke, P. *Synchrotron Radiation: Production and Properties.* (Oxford University Press, USA, 2009).
32. Attwood, D. *Soft X-Rays and Extreme Ultraviolet Radiation: Principles and Applications.* (Cambridge University Press, 2007).
33. Schmüser, P., Dohlus, M. & Rossbach, J. *Ultraviolet and Soft X-Ray Free-Electron Lasers: Introduction to Physical Principles, Experimental Results, Technological Challenges.* (Springer, 2008).
34. Galayda, J. N., Arthur, J., Ratner, D. F. & White, W. E. X-ray free-electron lasers-present and future capabilities [Invited]. *Opt. Soc. Am.* **27**, B106–B118 (2010).
35. Bonifacio, R., Pellegrini, C. & Narducci, L. M. Collective instabilities and high-gain regime in a free electron laser. *Opt. Commun.* **50**, 373–378 (1984).
36. Kondratenko, A. M. & Saldin, E. L. Generation of Coherent radiation by a relativistic electron beam in an undulator. *Particle Accel.* **10**, 207–216 (1980).
37. Deacon, D. A. G. *et al.* First Operation of a Free-Electron Laser. *Phys. Rev. Lett.* **38**, 892–894 (1977).
38. Behrens, C. Characterization and control of femtosecond electron and X-ray beams at free-electron lasers. (Hamburg, 2012).
39. Saldin, E. L., Schneidmiller, E. A. & Yurkov, M. V. Statistical and coherence properties of radiation from x-ray free-electron lasers. *New J. Phys.* **12**, 035010 (2010).

40. Bonifacio, R., De Salvo, L., Pierini, P., Piovella, N. & Pellegrini, C. Spectrum, temporal structure, and fluctuations in a high-gain free-electron laser starting from noise. *Phys. Rev. Lett.* **73**, 70–73 (1994).
41. Krinsky, S. & Gluckstern, R. L. Analysis of statistical correlations and intensity spiking in the self-amplified spontaneous-emission free-electron laser. *Phys. Rev. Spec. Top. - Accel. Beams* **6**, 050701 (2003).
42. Behrens, C. *et al.* Constraints on photon pulse duration from longitudinal electron beam diagnostics at a soft x-ray free-electron laser. *Phys. Rev. Spec. Top. - Accel. Beams* **15**, 1–12 (2012).
43. Düsterer, S. *et al.* Femtosecond x-ray pulse length characterization at the Linac Coherent Light Source free-electron laser. *New J. Phys.* **13**, 093024 (2011).
44. Behrens, C. *et al.* Constraints on photon pulse duration from longitudinal electron beam diagnostics at a soft x-ray free-electron laser. *Phys. Rev. Spec. Top. - Accel. Beams* **15**, 030707 (2012).
45. Ding, Y. *et al.* Femtosecond x-ray pulse temporal characterization in free-electron lasers using a transverse deflector. *Phys. Rev. Spec. Top. - Accel. Beams* **14**, 120701 (2011).
46. Behrens, C. *et al.* Few-femtosecond time-resolved measurements of X-ray free-electron lasers. *Nat. Commun.* **5**, (2014).
47. Riedel, R. *et al.* Single-shot pulse duration monitor for extreme ultraviolet and X-ray free-electron lasers. *Nat. Commun.* **4**, 1731 (2013).
48. Cavalieri, A. L. *et al.* Clocking Femtosecond X Rays. *Phys. Rev. Lett.* **94**, 114801 (2005).
49. Bionta, M. R. *et al.* Spectral encoding of x-ray/optical relative delay. *Opt. Express* **19**, 21855–21865 (2011).
50. Schorb, S. *et al.* X-ray–optical cross-correlator for gas-phase experiments at the Linac Coherent Light Source free-electron laser. *Appl. Phys. Lett.* **100**, 121107 (2012).
51. Harmand, M. *et al.* Achieving few-femtosecond time-sorting at hard X-ray free-electron lasers. *Nat. Photonics* **7**, 215–218 (2013).
52. Grguraš, I. *et al.* Ultrafast X-ray pulse characterization at free-electron lasers. *Nat. Photonics* **6**, 852–857 (2012).
53. Itatani, J. *et al.* Attosecond Streak Camera. *Phys. Rev. Lett.* **88**, 173903 (2002).
54. Christov, I. P., Murnane, M. M. & Kapteyn, H. C. High-Harmonic Generation of Attosecond Pulses in the “Single-Cycle” Regime. *Phys. Rev. Lett.* **78**, 1251–1254 (1997).
55. Gagnon, J., Goulielmakis, E. & Yakovlev, V. S. The accurate FROG characterization of attosecond pulses from streaking measurements. *Appl. Phys. B* **92**, 25–32 (2008).
56. Quéré, F., Mairesse, Y. & Itatani, J. Temporal characterization of attosecond XUV fields. *J. Mod. Opt.* **52**, 339–360 (2005).
57. Kienberger, R. *et al.* Steering Attosecond Electron Wave Packets with Light. *Science* **297**, 1144–1148 (2002).
58. Drescher, M. *et al.* X-ray Pulses Approaching the Attosecond Frontier. *Science* **291**, 1923–1927 (2001).
59. Hentschel, M. *et al.* Attosecond metrology. *Nature* **414**, 509–513 (2001).

60. Yakovlev, V. S., Gagnon, J., Karpowicz, N. & Krausz, F. Attosecond Streaking Enables the Measurement of Quantum Phase. *Phys. Rev. Lett.* **105**, 073001 (2010).
61. Schins, J. M. *et al.* Observation of Laser-Assisted Auger Decay in Argon. *Phys. Rev. Lett.* **73**, 2180–2183 (1994).
62. Glover, T. E., Schoenlein, R. W., Chin, A. H. & Shank, C. V. Observation of Laser Assisted Photoelectric Effect and Femtosecond High Order Harmonic Radiation. *Phys. Rev. Lett.* **76**, 2468–2471 (1996).
63. Meyer, M. *et al.* Two-color photoionization in xuv free-electron and visible laser fields. *Phys. Rev. A* **74**, 011401 (2006).
64. Kienberger, R. *et al.* Atomic transient recorder. *Nature* **427**, 817–821 (2004).
65. Goulielmakis, E. *et al.* Direct Measurement of Light Waves. *Science* **305**, 1267–1269 (2004).
66. Gagnon, J. & Yakovlev, V. S. The direct evaluation of attosecond chirp from a streaking measurement. *Appl. Phys. B* **103**, 303–309 (2011).
67. Mairesse, Y. & Quéré, F. Frequency-resolved optical gating for complete reconstruction of attosecond bursts. *Phys. Rev. A* **71**, 011401 (2005).
68. Frühling, U. *et al.* Single-shot terahertz-field-driven X-ray streak camera. *Nat. Photonics* **3**, 523–528 (2009).
69. Yeh, K.-L., Hoffmann, M. C., Hebling, J. & Nelson, K. A. Generation of 10 $\mu$ J ultrashort terahertz pulses by optical rectification. *Appl. Phys. Lett.* **90**, 171121 (2007).
70. L.G. Gouy. Sur une propriete nouvelle des ondes lumineuses. *Acad Sci Paris* **110**, (1890).
71. Wellhöfer, M. *et al.* Photoelectron spectroscopy as a non-invasive method to monitor SASE-FEL spectra. *J. Instrum.* **3**, P02003 (2008).
72. Schins, J. M. *et al.* Observation of Laser-Assisted Auger Decay in Argon. *Phys. Rev. Lett.* **73**, 2180–2183 (1994).
73. M. O. Krause, M. O. K. Atomic Radiative and Radiationless Yields for K and L Shells. *1979* **8**, 307
74. Drescher, M. *et al.* Time-resolved atomic inner-shell spectroscopy. *Nature* **419**, 803–807 (2002).
75. Auston, D. H. & Smith, P. R. Generation and detection of millimeter waves by picosecond photoconductivity. *Appl. Phys. Lett.* **43**, 631–633 (1983).
76. Bartel, T., Gaal, P., Reimann, K., Woerner, M. & Elsaesser, T. Generation of single-cycle THz transients with high electric-field amplitudes. *Opt. Lett.* **30**, 2805–2807 (2005).
77. Xie, X., Dai, J. & Zhang, X.-C. Coherent Control of THz Wave Generation in Ambient Air. *Phys. Rev. Lett.* **96**, 075005 (2006).
78. Shen, Y. *et al.* Nonlinear Cross-Phase Modulation with Intense Single-Cycle Terahertz Pulses. *Phys. Rev. Lett.* **99**, 043901 (2007).
79. You, D., Dykaar, D. R., Jones, R. R. & Bucksbaum, P. H. Generation of high-power sub-single-cycle 500-fs electromagnetic pulses. *Opt. Lett.* **18**, 290–292 (1993).
80. Dai, J., Xie, X. & Zhang, X.-C. Detection of Broadband Terahertz Waves with a Laser-Induced Plasma in Gases. *Phys. Rev. Lett.* **97**, 103903 (2006).

81. Leitenstorfer, A., Hunsche, S., Shah, J., Nuss, M. C. & Knox, W. H. Detectors and sources for ultrabroadband electro-optic sampling: Experiment and theory. *Appl. Phys. Lett.* **74**, 1516–1518 (1999).
82. Kojima, S., Tsumura, N., Kitahara, H., Takeda, M. W. & Nishizawa, S. Terahertz Time Domain Spectroscopy of Phonon-Polaritons in Ferroelectric Lithium Niobate Crystals. *Jpn. J. Appl. Phys.* **41**, 7033 (2002).
83. Dougherty, T. P., Wiederrecht, G. P. & Nelson, K. A. Impulsive stimulated Raman scattering experiments in the polariton regime. *JOSA B* **9**, 2179–2189 (1992).
84. Blanchard, F. *et al.* Generation of 1.5  $\mu$ J single-cycle terahertz pulses by optical rectification from a large aperture ZnTe crystal. *Opt. Express* **15**, 13212–13220 (2007).
85. Ding, Y. J. Efficient generation of high-power quasi-single-cycle terahertz pulses from a single infrared beam in a second-order nonlinear medium. *Opt. Lett.* **29**, 2650–2652 (2004).
86. Hebling, J., Yeh, K.-L., Hoffmann, M. C., Bartal, B. & Nelson, K. A. Generation of high-power terahertz pulses by tilted-pulse-front excitation and their application possibilities. *JOSA B* **25**, B6–B19 (2008).
87. Boyd, R. W. *Nonlinear Optics, Third Edition.* (Academic Press, 2008). at <<http://dl.acm.org/citation.cfm?id=1817101>>
88. Hoffmann, M. C., Yeh, K.-L., Hebling, J. & Nelson, K. A. Efficient terahertz generation by optical rectification at 1035 nm. *Opt. Express* **15**, 11706–11713 (2007).
89. Xing, Q. *et al.* The effect of two-photon absorption and optical excitation area on the generation of THz radiation. *Opt. Commun.* **267**, 422–426 (2006).
90. Mutter, L., Brunner, F. D., Yang, Z., Jazbinšek, M. & Günter, P. Linear and nonlinear optical properties of the organic crystal DSTMS. *JOSA B* **24**, 2556–2561 (2007).
91. Stillhart, M., Schneider, A. & Günter, P. Optical properties of 4-N,N-dimethylamino-4'-N'-methyl-stilbazolium 2,4,6-trimethylbenzenesulfonate crystals at terahertz frequencies. *JOSA B* **25**, 1914–1919 (2008).
92. Nahata, A., Weling, A. S. & Heinz, T. F. A wideband coherent terahertz spectroscopy system using optical rectification and electro-optic sampling. *Appl. Phys. Lett.* **69**, 2321–2323 (1996).
93. Hebling, J., Almasi, G., Kozma, I. & Kuhl, J. Velocity matching by pulse front tilting for large area THz-pulse generation. *Opt. Express* **10**, 1161–1166 (2002).
94. Bor, Z., Racz, B., Szabo, G., Hilbert, M. & Hazim, H. A. Femtosecond pulse front tilt caused by angular dispersion. *Opt. Eng.* **32**, 2501–2504 (1993).
95. Martinez, O. E. Pulse distortions in tilted pulse schemes for ultrashort pulses. *Opt. Commun.* **59**, 229–232 (1986).
96. Fülöp, J. A., Pálfalvi, L., Almási, G. & Hebling, J. Design of high-energy terahertz sources based on optical rectification. *Opt. Express* **18**, 12311–12327 (2010).
97. Hirori, A. D. Single-cycle THz pulses with amplitudes exceeding 1 MV/cm generated by optical rectification in LiNbO<sub>3</sub>. *Appl. Phys. Lett.* **98**, (2011).
98. Fülöp, J. A., Pálfalvi, L., Almási, G. & Hebling, J. Design of high-energy terahertz sources based on optical rectification. *Opt. Express* **18**, 12311–12327 (2010).

99. Yang, Z. et al. Large-Size Bulk and Thin-Film Stilbazolium-Salt Single Crystals for Nonlinear Optics and THz Generation. *Adv. Funct. Mater.* **17**, 2018–2023 (2007).
100. Kaindl, R. A. et al. Generation, shaping, and characterization of intense femtosecond pulses tunable from 3 to 20  $\mu\text{m}$ . *JOSA B* **17**, 2086–2094 (2000).
101. Ventalon, C. et al. Generation and complete characterization of intense mid-infrared ultrashort pulses. *JOSA B* **23**, 332–340 (2006).
102. Wu, Q. & Zhang, X.-C. Free-space electro-optic sampling of terahertz beams. *Appl. Phys. Lett.* **67**, 3523–3525 (1995).
103. Valasek, J. Properties of Rochelle Salt Related to the Piezo-electric Effect. *Phys. Rev.* **20**, 639–664 (1922).
104. Yeh, K.-L. The generation of high field terahertz radiation and its application in terahertz nonlinear spectroscopy. (MASSACHUSETTS INSTITUTE OF TECHNOLOGY).
105. Planken, P. C. M., Nienhuys, H.-K., Bakker, H. J. & Wenckebach, T. Measurement and calculation of the orientation dependence of terahertz pulse detection in ZnTe. *JOSA B* **18**, 313–317 (2001).
106. Dexheimer, S. L. *Terahertz Spectroscopy: Principles and Applications*. (CRC Press, 2007).
107. Schneider, J. R. FLASH—from accelerator test facility to the first single-pass soft x-ray free-electron laser. *J. Phys. B At.* **43**, (2010).
108. Schmüser, P. Superconductivity in High Energy Particle Accelerators. *2002* **49**,
109. Free-electron laser FLASH. at <<http://flash.desy.de/>>
110. P. Nicolosi, L. P. Grazing-incidence spectrometer for the monitoring of the VUV FEL beam at DESY. *J. Electron Spectrosc. Relat. Phenom. - J ELECTRON SPECTROSC RELAT PH* **144**, 1055–1058 (2005).
111. Planken, P. C. M., Nienhuys, H.-K., Bakker, H. J. & Wenckebach, T. Measurement and calculation of the orientation dependence of terahertz pulse detection in ZnTe. *J. Opt. Soc. Am. B* **18**, 313 (2001).
112. Azima, A. et al. Time-resolved pump-probe experiments beyond the jitter limitations at FLASH. *Appl. Phys. Lett.* **94**, 144102 (2009).
113. Ravi, K., Huang, W. R., Carbajo, S., Wu, X. & Kärtner, F. Limitations to THz generation by optical rectification using tilted pulse fronts. *Opt. Express* **22**, 20239–20251 (2014).
114. Akturk, S., Gu, X., Zeek, E. & Trebino, R. Pulse-front tilt caused by spatial and temporal chirp. *Opt. Express* **12**, 4399–4410 (2004).
115. Stepanov, A. G., Bonacina, L., Chekalin, S. V. & Wolf, J.-P. Generation of 30 ?J single-cycle terahertz pulses at 100 Hz repetition rate by optical rectification. *Opt. Lett.* **33**, 2497–2499 (2008).
116. Fülöp, J. A., Pálfalvi, L., Hoffmann, M. C. & Hebling, J. Towards generation of mJ-level ultrashort THz pulses by optical rectification. *Opt. Express* **19**, 15090–15097 (2011).
117. Hebling, J., Stepanov, A. G., Almási, G., Bartal, B. & Kuhl, J. Tunable THz pulse generation by optical rectification of ultrashort laser pulses with tilted pulse fronts. *Appl. Phys. B* **78**, 593–599 (2004).

118. Vicario, C. *et al.* High efficiency THz generation in DSTMS, DAST and OH1 pumped by Cr:forsterite laser. *Opt. Express* **23**, 4573–4580 (2015).
119. Monoszlai, B., Vicario, C., Jazbinsek, M. & Hauri, C. P. High-energy terahertz pulses from organic crystals: DAST and DSTMS pumped at Ti:sapphire wavelength. *Opt. Lett.* **38**, 5106–5109 (2013).
120. Feng, S. & Winful, H. G. Physical origin of the Gouy phase shift. *Opt. Lett.* **26**, 485–487 (2001).
121. Ruffin, A. B., Rudd, J. V., Whitaker, J. F., Feng, S. & Winful, H. G. Direct Observation of the Gouy Phase Shift with Single-Cycle Terahertz Pulses. *Phys. Rev. Lett.* **83**, 3410–3413 (1999).
122. Lindner, F. *et al.* Gouy Phase Shift for Few-Cycle Laser Pulses. *Phys. Rev. Lett.* **92**, 113001 (2004).
123. Schulz, S. *et al.* Femtosecond all-optical synchronization of an X-ray free-electron laser. *Nat. Commun.* **6**, (2015).
124. Schulz, S. Implementation of the Laer-Based Femtosecond Precision Synchronization System at FLASH. (University of Hamburg, 2011).
125. Bock, M. K. Measuring the Electron Bunch Timing with Femtosecond Resolution at FLASH. (2012).
126. Löhl, F. Optical Synchronization of a Free-Electron Laser with Femtosecond Precision. (Hamburg, 2009).
127. Kim, J., Cox, J. A., Chen, J. & Kärtner, F. X. Drift-free femtosecond timing synchronization of remote optical and microwave sources. *Nat. Photonics* **2**, 733–736 (2008).
128. Kim, T. K. *et al.* Sub-100-as timing jitter optical pulse trains from mode-locked Er-fiber lasers. *Opt. Lett.* **36**, 4443 (2011).
129. Winter, A. *et al.* Towards high-performance optical master oscillators for energy recovery linacs. *Nucl. Instrum. Methods Phys. Res. Sect. Accel. Spectrometers Detect. Assoc. Equip.* **557**, 299–304 (2006).
130. Kim, J. *et al.* Long-term femtosecond timing link stabilization using a single-crystal balanced cross correlator. *Opt. Lett.* **32**, 1044 (2007).
131. Schibli, T. R. *et al.* Attosecond active synchronization of passively mode-locked lasers by balanced cross correlation. *Opt. Lett.* **28**, 947–949 (2003).
132. Loehl, F. *et al.* Sub-10 femtosecond stabilization of a fiber-link using a balanced optical cross-correlator. in *IEEE Particle Accelerator Conference, 2007. PAC* 3804–3806 (2007). doi:10.1109/PAC.2007.4439912
133. Pfeiffer, S., Lichtenberg, G., Schmidt, C., Schlarb, H. & Werner, H. Design of an optimal and robust controller for a free-electron laser exploiting symmetries of the RF-system. in *2012 IEEE 51st Annual Conference on Decision and Control (CDC)* 4253–4258 (2012). doi:10.1109/CDC.2012.6425991
134. Koprek, W. *et al.* Intra-train Longitudinal Feedback for Beam Stabilization at FLASH. (Forschung Linearbeschleuniger-Technologien, M-Bereich, 2010). at <<https://bib-pubdb1.desy.de/record/93318>>

135. Behrens, C., Schmidt, B., Wesch, S. & Nicoletti, D. Upgrade and evaluation of the bunch compression monitor at the free-electron laser in Hamburg (FLASH). in *Proc. IPAC'10* 912–914 (2010).
136. Schulz, S. & Bousonville. *PAST, PRESENT, AND FUTURE ASPECTS OF LASER-BASED SYNCHRONIZATION AT FLASH*. (2013).
137. Löhl, F. *et al.* Electron Bunch Timing with Femtosecond Precision in a Superconducting Free-Electron Laser. *Phys. Rev. Lett.* **104**, 144801 (2010).
138. P. Nicolosi, L. P. Grazing-incidence spectrometer for the monitoring of the VUV FEL beam at DESY. *J. Electron Spectrosc. Relat. Phenom. - J ELECTRON SPECTROSC RELAT PH* **144**, 1055–1058 (2005).
139. Fakhari, F., Floettman, K., Pfeiffer, S., Schlarb, H. & Rossbach, J. *Design of a Normal Conducting Cavity for Arrival Time Stabilization*.
140. Amann, J. *et al.* Demonstration of self-seeding in a hard-X-ray free-electron laser. *Nat. Photonics* **6**, 693–698 (2012).
141. Ackermann, S. *et al.* Generation of Coherent 19- and 38-nm Radiation at a Free-Electron Laser Directly Seeded at 38~nm. *Phys. Rev. Lett.* **111**, 114801 (2013).
142. Ding, Y. *et al.* Measurements and Simulations of Ultralow Emittance and Ultrashort Electron Beams in the Linac Coherent Light Source. *Phys. Rev. Lett.* **102**, 254801 (2009).
143. Behrens, C. *et al.* Constraints on photon pulse duration from longitudinal electron beam diagnostics at a soft x-ray free-electron laser. *Phys. Rev. Spec. Top. - Accel. Beams* **15**, 030707 (2012).
144. Ding, Y. *et al.* Femtosecond X-Ray Pulse Characterization in Free-Electron Lasers Using a Cross-Correlation Technique. *Phys. Rev. Lett.* **109**, 254802 (2012).
145. Saldin, E. L., Schneidmiller, E. A. & Yurkov, M. V. Scheme for attophysics experiments at a X-ray SASE FEL. *Opt. Commun.* **212**, 377–390 (2002).
146. Reiche, S., Emma, P. & Pellegrini, C. Pulse length control in an X-ray FEL by using wakefields. *Nucl. Instrum. Methods Phys. Res. Sect. Accel. Spectrometers Detect. Assoc. Equip.* **507**, 426–430 (2003).
147. Zholents, A. A. & Fawley, W. M. Proposal for Intense Attosecond Radiation from an X-Ray Free-Electron Laser. *Phys. Rev. Lett.* **92**, 224801 (2004).
148. Emma, P. *et al.* Femtosecond and Subfemtosecond X-Ray Pulses from a Self-Amplified Spontaneous-Emission-Based Free-Electron Laser. *Phys. Rev. Lett.* **92**, 074801 (2004).
149. Emma, P., Huang, Z. & Borland, M. Attosecond x-ray pulses in the LCLS using the slotted foil method. 333–338 (2004).
150. Helml, W. *et al.* Measuring the temporal structure of few-femtosecond free-electron laser X-ray pulses directly in the time domain. *Nat. Photonics* **8**, 950–957 (2014).
151. Bozek, J. D. AMO instrumentation for the LCLS X-ray FEL. *Eur. Phys. J. Spec. Top.* **169**, 129–132 (2009).
152. TIME-OF-FLIGHT SPECTROMETERS by STEFAN KAESDORF Geraete fuer Forschung und Industrie. at <<http://www.kaesdorf.de/>>

153. Bionta, M. R. *et al.* Spectral encoding of x-ray/optical relative delay. *Opt. Express* **19**, 21855–21865 (2011).
154. Bionta, M. R. *et al.* Spectral encoding method for measuring the relative arrival time between x-ray/optical pulses. *Rev. Sci. Instrum.* **85**, 083116 (2014).
155. Leitenstorfer, A., Hunsche, S., Shah, J., Nuss, M. C. & Knox, W. H. Detectors and sources for ultrabroadband electro-optic sampling: Experiment and theory. *Appl. Phys. Lett.* **74**, 1516–1518 (1999).
156. Ding, Y. *et al.* Flexible control of femtosecond pulse duration and separation using an emittance-spoiling foil in x-ray free-electron lasers. *SLAC-PUB-16312* June 2015
157. Arthur, J. *Linac Coherent Light Source (LCLS) Conceptual Design Repor.* (2002).
158. Bostedt, C. *et al.* Ultra-fast and ultra-intense x-ray sciences: first results from the Linac Coherent Light Source free-electron laser. *J. Phys. B At. Mol. Opt. Phys.* **46**, 164003 (2013).
159. Brida, D. *et al.* Few-optical-cycle pulses tunable from the visible to the mid-infrared by optical parametric amplifiers. *J. Opt.* **12**, 013001 (2010).
160. Krinsky, S. & Gluckstern, R. L. Analysis of statistical correlations and intensity spiking in the self-amplified spontaneous-emission free-electron laser. *Phys. Rev. Spec. Top. - Accel. Beams* **6**, 050701 (2003).
161. Bonifacio, R., De Salvo, L., Pierini, P., Piovela, N. & Pellegrini, C. Spectrum, temporal structure, and fluctuations in a high-gain free-electron laser starting from noise. *Phys. Rev. Lett.* **73**, 70–73 (1994).
162. Düsterer, S. *et al.* Femtosecond x-ray pulse length characterization at the Linac Coherent Light Source free-electron laser. *New J. Phys.* **13**, 093024 (2011).
163. Hauri, C. P., Ruchert, C., Vicario, C. & Ardana, F. Strong-field single-cycle THz pulses generated in an organic crystal. *Appl. Phys. Lett.* **99**, 161116 (2011).
164. Pellegrini, C. High power femtosecond pulses from an X-ray SASE-FEL. *Nucl. Instrum. Methods Phys. Res. Sect. Accel. Spectrometers Detect. Assoc. Equip.* **445**, 124–127 (2000).
165. Bajt, S., Chapman, H. N., Aquila, A. & Gullikson, E. High-efficiency x-ray gratings with asymmetric-cut multilayers. *J. Opt. Soc. Am. A Opt. Image Sci. Vis.* **29**, 216–230 (2012).
166. Hebling, J. Derivation of the pulse front tilt caused by angular dispersion. *Opt. Quantum Electron.* **28**, 1759–1763 (1996).
167. Bor, Z., Racz, B., Szabo, G., Hilbert, M. & Hazim, H. A. Femtosecond pulse front tilt caused by angular dispersion. *Opt. Eng.* **32**, 2501–2504 (1993).



## Acknowledgement

Finally, I want to thank all the people that contributed to the success of this work.

I would like to express my gratitude to Prof. Adrian Cavalieri for the opportunity to work on interesting projects and for providing me guidance and support in realizing challenging experiments.

I would like to thank Dr. Matthias Hoffmann for shearing all his THz knowledge.

Moreover, I am thankful to Dr. Christoph Bostedt, Hubertus Bromberger, Dr. Ryan Coffee, Prof. J.T. Costello, Dr. Gilles Doumy, Dr. Stefan Duesterer, Dr. Wolfram Helml, Sebastian Huber, Dr. Markus Ilchen, Prof. Reinhard Kienberger, Dr. Haiyun Liu, Dr. Jia Liu, Dr. Tommaso Mazza, Dr. Marc Messerschmidt, Dr. Michael Meyer, Dr. Paul Radcliffe, Dr. Wolfgang Schweinberger, Dr. Sebastian Schorb and Ulrike Wegner for the excellent and pleasant cooperation at the various beamtimes at FLASH and the AMO beamline at LCLS. I would like to thank especially Dr. Andreas Maier, Dr. Sebastian Schulz and Dr. Christopher Behrens for the help with the analysis of the data and for the great discussions.

I also would like to thank Prof. Andrea Cavalleri, Regina Brodowski, Jörg Harms and all the other group members for providing a nice work environment.

For a variety of reasons I am indebted to Michael Först, Hauke Höppner, Cassie Hunt, Roman Mankowsky, Francesca Moglia, Michaela Petrich, Alberto Simoncig, Nikola Stojanovic and Alaska Subedi.

I am very thankful to Srivats for his immeasurable patience and for providing calmness.

Hvala mojim dragim roditeljima, bratu i Marini što su bili potpuna podrška u svim mojim odlukama!